Universitá degli Studi di Napoli "Federico II"

Universitá degli Studi di Napoli "Parthenope"

Characterization of the DUSTER instrument for stratospheric dust collection and Raman analysis of stratospheric samples

Submitted for the degree of

Philosophiae Doctor (PhD) in Aerospace Engineering

Simone De Angelis

Advisor: prof. Pasquale Palumbo

Co-Advisor: Ing. Vincenzo Della Corte

Coordinator: Prof. Antonio Moccia

Introduction

The direct collection of cosmic interplanetary dust in the Earth stratosphere is a unique tool for the understanding of the structure, formation and evolution of our planetary system; the collection and study of rare interstellar grains, that penetrate in terrestrial stratosphere (Grun et al., 2001), can give insights about the interaction of the Solar System and its neighbourhood, the Local Interstellar Medium. Global atmospheric dynamics causes air masses to descent from the mesosphere to the stratosphere, in correspondence of the polar vortex (Russell et al., 1993), hence extraterrestrial particles that enter the Earth atmosphere can reach the stratosphere where they settle gravitationally.
The terrestrial stratosphere (from an altitude of 15 to 50 km approximately) is a suitable environment where to collect extraterrestrial samples, especially the upper stratosphere, above 25-30 km of altitude: it is close to the frontier between the Earth and the space, but at the same time it is not necessary the use of space vehicles to reach these altitudes, thanks to the use of stratospheric balloons. In the upper stratosphere the contamination due to terrestrial material is very minimum, and the concentration of cosmic particles is increased of a factor about 10^6 with respect to the concentration in space, due to the deceleration and conservation of the cosmic particles flux.
The Interplanetary dust particles (IDPs) are a unique source of fragile and volatile cometary materials directly collectable in the stratosphere, because these friable and volatile materials cannot survive the hypervelocity atmospheric entry when they are in large meteorites (Brownlee, 1985). Cosmic particles as IDPs represent poor altered extraterrestrial material that can be collected in stratosphere, because they generally suffer a minimum thermal heating during the atmospheric entry. The IDPs contain a record of the physical, chemical and mineralogical compositions and processes that occurred during the early phases of the Solar System formation; dust particles were embedded into icy protoplanets during the accretion of planetesimals (Rietmeijer, 2002), and remained stored at low temperatures (10-50 K) until suitable dynamics

configurations (i.e. collisions) allowed the release of embedded debris, that finally can penetrate the Earth atmosphere. Hence IDPs represent the transition phase between interstellar, pre-solar dust and circumstellar dust. The understanding of hierarchical accretion of IDPs can give insights about planetesimals accretion mechanisms. The various populations of interstellar dust grains and interplanetary dusts, their sources and properties are described in the chapter 1.

IDPs have typically sizes in the range $0.1 - 100\ \mu m$; cluster-IDPs and superclusters can be as large as $500\ \mu m$; the collection of IDPs in the range $10 - 100\ \mu m$ on board NASA U2 aircrafts at an altitude of 20 km and on board stratospheric balloons has been performed in the past decades (Brownlee et al., 1973, 1976, 1980; Brownlee, 1985; Testa et al., 1990), so IDPs in this size range have been largely studied (see the chapter 2 for a brief review of *sampling return* experiments in stratosphere); at the same time, larger extraterrestrial samples such as meteorites (> 10 cm) have been extensively studied; on the other side IDPs in the subμm and μm range are poorly studied, they have been collected only in the space; small IDPs suffer a lower flash heating during the atmospheric entry, and moreover they are the most abundant in the size distribution.
The study of interplanetary dust particles can help to solve scientific questions not also in planetology, for example to obtain information about the different populations of IDPs, or in astrophysics, in order to determine the flux of interstellar dust grains in the Solar System; their study is relevant for the astrobiology, because they could contain pre-biotic molecules, and for the atmospheric sciences, because it contributes to the understanding of the global atmospheric circulation and dynamics, and of different properties of stratospheric aerosols, such as chemical composition, abundance, optical properties.
The DUSTER project (Dust in the Upper Stratosphere Tracking Experiment and Retrieval) has been designed and realized to collect refractory dust particles in the sub$\mu m - \mu m$ range in the upper stratosphere, with the aim to collect cosmic dust particles (Palumbo et al., 2008; Della Corte et al., 2011). In the chapter 2 the different populations, terrestrial and extraterrestrial, of stratospheric aerosols are described.

Collected samples are then analyzed in laboratory with several techniques, using scanning electron microscope (SEM), field-emission scanning electron microscope (FESEM), energy dispersive X-rays (EDX), infrared spectroscopy (Ciucci et al., 2011), micro-Raman spectroscopy (De Angelis et al., 2011). Transmission electron microscope (TEM) and isotopic analyses are also planned for the future. Differently from other sampling return experiments, the DUSTER project reduces the steps of

manipulation of collected samples in the laboratory; the samples are indeed analyzed at the electron microscope directly on the collection substrates. The sampling on board stratospheric balloons, with low relative velocities between the substrate and the particles, is non-destructive and non-contaminant, respect to the collection on board aircrafts; moreover, sticking materials and oils are not used.

The DUSTER instrument and the various measurements and tests performed are described in the chapter 3. In the chapter 4, the calibration of DUSTER, consisting of *collection efficiency* measurements, performed at the Cosmic Physics Laboratory of the Applied Sciences Department, "Parthenope" University of Naples, are described. Finally, in the chapter 5, micro-Raman analyses on samples collected during the DUSTER-2008 flight campaign (from Svalbard Islands, Norway), are explained. Moreover, a NI-LabVIEW tool, developed for the automatized compute of fits of numerous Raman spectra, is presented.

Chapter 1

Cosmic matter

The luminous matter in our Galaxy is essentially present in two forms, stars and interstellar medium (ISM). The density of stars in the neighbourhood of the Sun is about 0.08 pc^{-3}, where 1 pc = 3.083×10^{16} m. The average mass density due to stars is about $\rho_\star = 3 \times 10^{-21}$ kg m^{-3}, assuming a mean stellar mass $M_\star = 0.5\ M_\odot$. The interstellar medium is in turn constituted by gas and dust, it has a somewhat lumpy structure, with dense clouds and large empty bubbles with low density; the mean density is of the order of 10^{-21} kg m^{-3}. The gas component has a mass $M_{gas} = 4 \times 10^9\ M_\odot$, assuming a galactic disk radius of 15 kpc. The gas is mainly constituted by hydrogen and helium, with *cosmic* abundances, relative to silicon, $a_H/a_{Si} = 3.18 \times 10^4$ and $a_{He}/a_{Si} = 2.21 \times 10^3$; oxygen and carbon have cosmic abundances $a_O/a_{Si} = 22.1$ and $a_C/a_{Si} = 11.8$. The total mass fraction due to H and He is 98%. The dust is a minority component, in mass, being $M_{dust} = 1 - 2\%\ M_{gas}$. Interstellar medium and stars are not absolutely separate of course, but the cosmic matter cyclically passes from one phase to another: stars form starting from the matter present in the ISM, dust has a role in star formation regions, and the stars in turn inject gas, ions and dust particles in the interstellar space during their lifetime and at the end of their life. In the following we will focus on the dust component of the cosmic matter.

1.1 Interstellar grains

Interstellar dust plays an important role in the thermal, dynamical and chemical evolution of many environments of our Galaxy. One reason of that, is the large cross section of micrometer and submicrometer-sized dust particles with respect to interaction processes with electromagnetic radiation. The absorption, extinction and scattering efficiencies due to dust grains are very large, more than if only gas were present in the interstellar medium; dust has a fundamental role, though its overall mass is almost negligible, being $M_{dust}/M_{gas} \sim 10^{-2}$. The chemical composition and evolution of the interstellar dust also influences the elemental cosmic abundance; the mass of the dust is proportional to the interstellar metallicity. Dust contains about 40% of all heavy elements in the interstellar medium, and most of refractory elements such as Fe, Mg, Si, C and O; about 90% of interstellar Fe, which is injected into the space by supernovae explosions, is contained into dust grains.
There are many observational evidences of the existence of the interstellar medium (ISM) (see for example the reviews of Salpeter, 1977; Dorschner and Henning, 1995; Grun et al., 2001). The stellar extinction has been measured in the spectral range $0.1 - 100\ \mu m$; the main caracteristic of the extinction profile measured in the UV is the *extinction bump* at 217.5 nm, which is attributed to interstellar graphite grains. Molecular hydrogen clouds have been detected in the ISM thanks to microwave and ultraviolet spectroscopy. From UV absorption lines it has been found that more refractory elements are depleted from the gaseous phase, and thus these heavy elements have formed refractory solids. For example the Fe abundance in the ionized gas (HII regions) within the Orion nebula is about 20 times lesser than the cosmic abundance (assuming as *cosmic abundance* that relative to solar photosphere, corona and meteorites). Abundances obtained from galactic cosmic rays are consistent with the cosmic abundance within a factor 4, and from O and B stars comparable. Assuming an initial cosmic abundance in the ISM, the depletion in Fe abundance is attributed to the formation of solid refractory iron grains. Underabundances have been observed for Mg and Si; large depletion of Fe is also observed in planetary nebulae, with an iron abundance about 30 times lesser than cosmic abundance, thus indicating the presence of Fe-rich solid grains. Infrared spectra of cold and bright stars show emission features at 10 μm and 18 μm; these bands are attributed to Si-O stretching and O-Si-O bending respectively; while absorption features are caused by surface photospheric layers projected on the disks of stars, these emission bands are due to solid dust grains in stellar envelops, that absorb, re-emit and scatter the starlight; these grains, that evidently formed in regions where they previously lacked, are mainly constituted by silicates.

The interstellar dust can be subdivided on the basis of the different regions in which grains form in the interstellar space (see review of Dorschner and Henning, 1995): (a) stardust; (b) diffuse ISM; (c) molecular clouds; (d) young stellar objects (YSO).

1.1.1 Dust from the stars

The main contribution to dust grains in the interstellar space is provided by stars; dust formed in dense clouds or in the diffuse ISM is at the most comparable with stardust. The mass loss rate of a star can reach values as high as $10^{-4}\ M_{\odot}\ yr^{-1}$, and for each star about 1 $M_{\odot}$ of its original mass returns to the interstellar space; the total stellar mass (gas plus dust) that returns to the interstellar space is estimated $\sim 1.5\ M_{\odot}\ yr^{-1}$, assuming a stellar death rate of $\sim 2\ yr^{-1}$, for stars with original mass in main sequence $M_{\star} \sim 1-4\ M_{\odot}$, and a galactic disk radius of 15 kpc. Circumstellar matter is detected, as already said, by IR emission bands at ~ 10 and $\sim 18\ \mu m$, due to silicate grains; moreover circumstellar grains absorb starlight and emit in the infrared region. Dust refractory grains can form in stellar atmospheres for $T \leq 2000$ K, within a few stellar radii, and then they are transported in the interstellar space by radiation pressure. Evolved stars, in advanced stages, can inject dust grains in the interstellar space. Most of these stars, about 90%, are asymptotic giant branch (AGB) stars; about 10% consists of planetary nebulae, novae, supernovae, supergiant stars, Wolf-Rayet (spectral type WC, carbon rich, with $T_W = 10^5$ K). Some isotopic anomalies, such as that relative to Xe or ^{44}Ca found in grains embedded in meteorites or in interplanetary dust particles (IDPs), suggest that these materials formed within supernovae explosions. Supernovae are the main source of elements heavier than C in the space, though the injection rate of material by SN is about 1/20 of that relative to giant, supergiant stars and planetary nebulae.

Oxygen to carbon ratio in evolved stars

The chemical composition and mineralogy of dust grains that can form in stellar atmospheres substantially depend on the relative abundances of oxygen and carbon, that is on the ratio O/C; it is assumed thermodynamic equilibrium and a pressure in the range $10^{-2} - 10^{-7}$ hPa. In this environment the CO molecule is extremely stable, even at temperature values 1000-2000 K. Thus the element with minor abundance between oxygen and carbon is all bonded inside the CO molecule and will not be available to form solid grains, while the excess element will be. Generally O-rich stars (M-type stars, with $T_M = 3000 - 3600$ K, TiO bands present) with O/C$>$ 1

produce silicate grains or metal oxides. For example alumina (Al_2O_3) has been detected in stellar spectra thanks to a band at 13 μm, and it has been also found inside meteorites. On the other side C-rich stars, such as cold giant and supergiant, with a ratio O/C$<$ 1, have a carbon excess, and so they mainly produce organic molecules and carbonaceous grains. Generally the spectra of these stars don't show silicate features, but a black body profile at $T \sim 1000$ K, that can be due to graphite and SiC grains.

Condensation of minerals and nucleation

The growth of grains occurs in the temperature range 700-1300 K; in non-equilibrium regions clusters of heteroatoms can form and be stable, such as silicate grains Fe-SiO and Mg-SiO; oxygen is bonded in H_2O molecule up to temperatures $T \sim 2500$ K, N in molecular form, Si is in oxides, Mg, Fe and Ca in monatomic form. For example, considering the forsterite (olivine, Mg_2SiO_4), for temperatures greater than the condensation temperature T_{cond}, only gaseous Mg, SiO and H_2O exist; forsterite grains begin to form when the temperature decreases below T_{cond}. Refractory elements like Ca, Ti, Al have abundances about 10 times lesser than elements like Mg, Si, Fe; nevertheless the former constitute solid grains earlier, that is at higher temperatures: for $T > 1300 - 1500$ K perovskite ($CaTiO_3$), alumina (Al_2O_3) and gehlenite ($Ca_2Al_2SiO_7$) begin to form. Magnesium silicates (forsterite and enstatite, $MgSiO_3$) form at lower temperatures, Na-rich and K-rich silicates (feldspars) form at more lower temperatures (around 1000 K). Below 1000 K sulfides and oxides (troilite, FeS, and magnetite, Fe_3O_4) begin to form, and hydrated silicates form below 500 K. The homogeneous nucleation theory (Salpeter, 1977, review) provides the frame within solid grains can grow. Thermodynamic equilibrium is assumed, while the temperature slowly decreases. Gas phase monomers (atoms or molecules) are indicated with A, with number concentration c_1, and a cluster of N monomers is A_N (that is a macroscopic solid grain), which concentration is c_N. The equilibrium implies that:

$$A_N + A \rightleftarrows A_{N+1} \tag{1.1}$$

If an atom/molecule is added to the cluster A_N, then the concentration is:

$$\frac{c_{N+1}}{c_N} = c_1 \exp\left[-\frac{\Delta F_N(T)}{kT}\right] \tag{1.2}$$

where $\Delta F_N(T)$ is the free-energy difference between the two states. The parameter η indicates the number of *sticking collisions* that a surface site on a grain experiments during the cooling time. Then the final number of atoms/molecules in a solid grain is:

$$N_{fin} \sim \left(\frac{\eta}{\ln \eta}\right)^3 \tag{1.3}$$

The final grain abundance is $f_{fin} = f/N_{fin}$:

$$f_{fin} \sim f^{-2}(\ln f)^3 \tag{1.4}$$

where f is the initial abundance of the species A. Typically at the beginning cluster containing 10-100 atoms form, that successively act as nuclei, onto which gaseous species can condensate, leading to the growth of macroscopic grains. Refractory cores generally coagulate inside the internal regions of circumstellar envelopes, while icy mantles can condensate on grain surfaces in external and cold regions. The growth of pure crystalline or amorphous grains depends on factors such as accretion time-scale, number density and η. Fast accretion leads to amorphous grains, while a slow accretion can produce crystalline grains. Moreover, for large values of η and number density (many sticking collisions, large thermal mobility, high T_{cond}) pure crystalline grains can form, with Mg-silicates separated from Fe-minerals, and pure graphite grains in C-rich atmospheres; for small values of η and number density, amorphous mixtures of silicates, oxides, sulfides grow; amorphous silicates (glasses) are characterized by distorted SiO_4 tetrahedra; amorphous carbon mixed with hydrocarbons form in C-rich envelopes (see below). In reducing, oxygen-deficient, interstellar environments, O-free grains can also form, like sulfides of magnesium and iron; FeS grains are more stable in the interstellar space, and they have also been found within primitive meteorites.

Pure carbon and carbonaceous grains

Pure carbon grains can only grow within stellar atmosphere in which hydrogen is lacking; indeed in presence of hydrogen, C and H atoms bond with each other and carbonaceous grains form; base molecules for carbonaceous grains growth are acetylene, C_2H_2. In C-rich environments far from the equilibrium, pure amorphous carbon

grains form, while in environments in thermodynamical equilibrium the most abundant material is graphite. Amorphous carbon grains typically consist of mixtures of sp^2/sp^3 hybridization states, such as aromatic sp^2 islands joined by sp^3 bonds. Typical sources of pure carbon grains are the Wolf-Rayet (WC) stars, with no hydrogen; the band at 7.7 μm is attributed to stretching vibrations in aromatic C-C bonds in soot grains. Laboratory experiments concerning soot grains, performed in an atmosphere with and without hydrogen, compared with data from stellar UV spectra, have showed that most of emitted stardust grains are hydrogenated amorphous carbons (HAC). Soot grains produced in an atmosphere without hydrogen are characterized by a UV absorption band at 240-260 nm, while in a H-rich atmosphere, this band disappears; after annealing the UV band appears. Probably HAC grains in the interstellar space are subject to dehydrogenation and graphitization, so graphite nanograins form, which are responsible of the extinction bump at 217.5 nm. Other materials that are produced in stars and injected in the interstellar space are *polycyclic aromatic hydrocarbons* (PAHs); unlike the HAC grains, the PAHs are not properly solid grains, but structured molecules; they consist in planar hexagonal rings of C atoms, sp^2 bonded, containing H atoms at each vertex; they represent a transition stage from molecular gaseous to solid phase. Unidentified Infrared Bands (UIB) detected, for example, in stellar spectra in the range 3-13 μm, are attributed to PAHs, especially in spectra of C-rich stars; laboratory experiments with carbonaceous materials and PAH mixtures give bands similar to the observed UIBs. The intensity of UIBs is correlated with the O/C ratio, while the width of these bands is correlated with the number of atoms in PAHs. In the interstellar space PAHs are destroyed in $< 5 \times 10^7$ yr; they can survive in molecular phase or form solid grains (AC, HAC): thus UIBs can be due to aromatic islands inside amorphous carbon grains. The nucleation of pure carbon solid grains can be onset by PAH molecules or by SiC grains. Amorphous SiC grains have been detected thanks to emission features in many stellar spectra, while absorption bands have not been found; the emission band at 11.3 μm is attributed to SiC grains, probably condensed in stellar winds. Silicon carbide grains can also exist in oxidized form or coated with carbonaceous mantles, but the fact that these grains have been found in several meteorites, implies that they must also exist in the interstellar space.

1.1.2 Dust in the diffuse ISM

The main spectral bands that characterize the interstellar medium are the UIBs, that are mostly seen in emission in the infrared range 3.28-13 μm; there are the two IR

emission silicate bands, at 10 μm (Si-O stretching) and 18 μm (O-Si-O bending); the two bands at 3.3 μm (aromatic C-H) and at 3.4 μm (aliphatic C-H). The structure of the ISM is schematized with a three-stage model. It consists of clouds of gas and dust, embedded within *HIM* (*hot ionized matter*); each cloud is constituted by a cold and dense core (*CNM, cold neutral matter*) and a warm envelop (*WNM, warm neutral matter*); finally the *WIM* (*warm ionized matter*) surrounds these clouds. The neutral zones are HI regions, while the warm and hot ionized matter constitute HII regions. In this frame supernovae explosions are the main source of energy. The neutral regions consist of cold and dense clouds ($c_N > 10^3/cm^3$ and $T = 30 - 80$ K), linked by HI regions with filament structures ($T > 500$K); the warm surrounding HI regions are at $T = 5000 - 8000$ K; about 90% of the matter in the ISM is in the form of HI regions, while only 10% is in the form of HII regions. Absorption bands of reddened stars arise in cold dense clouds, while absorption bands of non-reddened stars arise in warm neutral regions. The local interstellar medium (LISM) has a patch structure, with dust clouds having different radial velocities, embedded in the local interstellar cloud (LIC), that is actually an inter-cloud medium. The local interstellar cloud surround the whole solar heliosphere, with a Sun-relative velocity of 26 km/s; calcium depletion in the LISM is index of the presence of dust grains; the temperature of 7000 K, the low number density $c_N = 0.05 - 0.1/cm^3$, SN shock velocities in the range 20-200 km/s, and the non-Maxwellian velocity distribution of gas clouds indicate that there is not thermodynamic equilibrium; in some regions there is large depletion in gas species. Observational evidences of the existence of dust in the ISM are given by extinction curves, absorption profiles, scattering, luminescence and thermal emission by solid grains.

Extinction curves

Extinction curves of starlight are characterized by the extinction parameter $R = A_V/E(B-V)$, where A_V is the total extinction and $E(B-V)$ is the colour excess; the typical value for the diffuse ISM is $R = 3.1$, while it is larger in stellar formation regions and dense clouds; a greater value of R indicates larger dust grains. Several absorption bands are superimposed onto the extinction profile; the main band is the UV *extinction bump* observed at 217.5 nm, due to graphite grains with diameter 0.04 μm. While the bump position is constant, its width varies with different line-of-sights, and its intensity decreases and disappears in HII regions; the disappearance of the bump is attributed to the destruction of its carriers, while the FWHM variation is attributed to icy PAH mantles with different thicknesses covering graphite grains.

Diffuse interstellar bands (DIBs) in the VIS-NIR range 400-1300 nm are probably due to PAHs; absorption lines in IR spectra of intrinsically bright stars, different from *young stellar objects* and without circumstellar envelopes, are due to dust grains in the diffuse ISM. Infrared spectra obtained for different sources show several bands due to the presence of dust in the diffuse ISM, such as the 3.3 and 3.4 μm features due to aromatic and aliphatic C-H stretching, and the 9.7 and 18.7 μm absorption features due to silicate grains. The CH_2/CH_3 ratio equal to 2.5 is consistent with the value measured for the Murchison meteorite. The continuum profile in the visible is essentially due to SiC grains of diameter 0.2 μm, while extinction in the range 1200-1800 $\mathring{A}$ is due to silicate grains with diameter 0.1 μm. The size distribution is dominated by small grains < 0.1 μm, while large uncertainties remain on the distribution of greater grains.

Scattering and thermal emission

The diffuse galactic light in the UV-NIR range is a clue of the existence of dust grains in the ISM, being due to scattering of light from stars in the galactic disk, by dust in the ISM. Moreover dark clouds can show bright edges due to the starlight scattering by dust grains. Scattering is characterized by the grain albedo $\gamma(\lambda) = Q_{sca}/Q_{ext}$ and asymmetry factor $g = \langle \cos \alpha \rangle$, where Q_{sca} and Q_{ext} are scattering and extinction efficiencies, and α is relative to scattering direction. Typical values in the visible are $\gamma = 0.6$ and $g = 0.6$ for 0.1 μm grains. Beyond the visible emission caused by grains that scatter the starlight from stars in the galactic plane, an infrared diffuse emission is observed: solid grains absorb interstellar radiation and re-emit it in the FIR; the bands at 60 and 100 μm are due to large grains, while bands at 12 and 25 μm are due to nano-grains in non-equilibrium, that are heated at $> 10^2$ K by UV sources in HII regions.

Dust processing in the ISM

The matter in the ISM evolves passing cyclically from the solid phase (dust grains) to the gas phase, due to several mechanisms. Dust grains are altered in the interstellar space by processes such as collisions, destruction, fragmentation, sputtering, irradiation, growth, vaporization within stellar formation regions. Processes as grain-grain collisions are fundamentally caused by shock waves from supernovae explosions in the *WNM* or *WIM* phases; in the *HIM* this fact does not occur because of the low density. Collision between grains can lead to four different results: elastic scattering,

coagulation, shattering or vaporization, depending on the relative velocity. Total vaporization occurs at high velocities, $V_{rel} > 20$ km/s; coagulation is possible at low velocities, $V_{rel} < 1$ km/s; shattering (fragmentation) occurs at intermediate velocities. Particle-cluster collisions can lead to compact aggregates, while cluster-cluster collisions can lead to fluffy aggregates; condensation and coagulation produce small grains, with a narrow size distribution, while cluster-cluster collisions produce large grains, with a broadened size distribution. Grain erosion is caused by physical and chemical sputtering; physical sputtering can be thermal, when gas phase atoms impinging on grain surface have a thermal distribution of temperature and velocity; non-thermal sputtering is due to impinging flows of atoms with the same velocity and flow direction; high velocity impinging atoms lead to the release of atoms and molecules from grain surfaces; the most efficient projectiles are He-atoms, with a high sputtering efficiency for $V_{sputt} = 200$ km/s. Sputtering only removes surface atoms and molecules, while grain cores remain intact, but if grains experiment destructive collisions, the cores remain exposed to sputtering. Chemical sputtering consists of the release of surface molecules, formed subsequently to the chemical reaction of surface C-atoms with incident O and H atoms. Supernova shock waves can produce phase transitions of dust grains from solid to vapour phase; SN shocks can also bring to the formation of amorphous silicates and cause transitions from graphite to nanodiamond. Grain irradiation is produced by UV radiation from stars, X-rays, cosmic rays; they cause photolysis, photodesorption, radiation damages, dehydrogenation of carbonaceous grains. Photolysis of icy mantles of dusts can produce refractory organic residues, and UV irradiation of these organics can bring to dehydrogenation (destruction of C-H bonds) and formation of pure amorphous carbon residues; graphite arise from large grains, while small grains produce nanodiamonds, that have been found in meteorites. The sp^2/sp^3 fraction depends on the amount of UV irradiation, hence the different ~ 3 μm bands depend on the absorbed UV dose; the absorption band at 3.4 μm of aliphatic C-H should be due to cold mantles in HAC grains, while the emission feature at 3.3 μm of aromatic C-H should be due to warm mantles.

Life cycle of dust grains in the ISM

Carbonaceous grains have typical lifetimes of about 4×10^8 yr, while silicate grains have lifetimes of the order of 2.2×10^8 yr (see reviews of Dorschner and Henning, 1995 and Grun et al., 2001). Comparing the mean grain lifetime in the interstellar space with the time required to form new grains from stardust, about 2.5×10^9 yr,

it is deduced that formation of grains must also occur directly in the diffuse ISM. Contributions to the replenishing of solid grains in the ISM are the disintegration of dense clouds in stellar formation regions, and condensation mechanisms in the interstellar gas phase. During the whole lifetime a dust grain can cyclically pass several times from one region to another of the interstellar space, characterized by very different environments such as inter-cloud space ($c_N = 10^{-1} - 10^2\ cm^{-3}$), HII regions ($c_N = 10^2 - 10^3\ cm^{-3}$), dark and molecular clouds ($c_N = 10^4 - 10^6\ cm^{-3}$). Dusts in the interstellar space are not only modified and processed, but they also modify and influence their environment; for examples solid grains screen from UV radiation the internal zones of diffuse clouds, thus facilitating the birth or stars; moreover, the formation of molecular hydrogen can only occur on solid grain surfaces. The growth of grains is accompanied by the condensation of gaseous species on grain surface, and by coagulation of small particles; even if the vapour condensation is faster than coagulation, due to the competition with destructive mechanisms, the coagulation is more efficient than condensation in order to cause growth; however during the lifetime of a molecular cloud (10^7 yr) an icy mantle of 20 nm thickness can condensate on the grain surface. The grain destruction dominates in *WIM* regions in the ISM, while it is negligible in *HIM* because the density is too low. Material exchanges between the molecular gas phase and the inter-cloud medium characterize the dust evolution; comparing the mean lifetime of molecular clouds ($< 2 \times 10^7$ yr) with the photo-ionization timescale (10^7 yr), it seems that diffuse clouds are converted in *WIM*. Again the warm gas in the *WIM* is converted into cold dense clouds within about 10^6 yr. Icy mantles form in molecular clouds, and then are photo-processed within the diffuse ISM.

1.1.3 Dust in molecular clouds

The observed molecular clouds require the presence of solid grains, because the formation of molecular hydrogen occurs on the surface of dust particles. In star formation regions the grains are subject to thermal metamorphism, consisting in mantle evaporation and photoprocessing of the cores; shock waves due to new-born stars modify grains, and also cloud-cloud collisions can alter or destroy dust particles. There are some differences between dusts in molecular clouds and in diffuse ISM, for example in their size distributions; moreover grains in molecular clouds have icy mantles, that can form within $\sim 10^5$ yr, small if compared with the 10^7 yr lifetime of molecular clouds. Infrared spectroscopy, using as IR sources background stars beyond dark clouds or YSO embedded in clouds, has evidenced the presence of icy

mantles in dust grains with several chemical compositions, such as H_2O, CO, CO_2, CH_3OH. Water ice mantles are characterized by the IR band at 3.08 μm, due to O-H stretching, at 6.0 μm, due to O-H bending, and at $12.5 - 14$ μm, due to H_2O libration. The icy carbon monoxide shows the band at 4.67 μm due to solid C-O stretching. Mantles of icy carbon dioxide show a band at 15 μm (O-C-O bending), and frozen methanol mantles have a band at 3.53 μm. In these clouds the molecular accretion leads to formation of solid grains and depletion in gaseous species: from the comparison between the accretion time and the free-fall timescale, it results that for densities $> 10^5/cm^3$ the accretion of molecules can start. The formation of H_2 occurs on solid grain surfaces, because H+H reactions in the gas phase are not efficient, and a third (solid) body can dissipate the reaction heat; the construction of other compounds containing O, C, N depends on the H/H_2 ratio. If $H/H_2 > 10^{-3}$ then compounds as CH_4, NH_3, H_2O, H_2CO, CH_3OH and H_2O_2 form. If the hydrogen has a number density $> 10^4/cm^3$ then H is in molecular form, and icy CO, N_2 and O_2 mantles can grow. As in diffuse ISM, also in molecular clouds collisions among grains can lead to different results, such as coagulation, fragmentation or vaporization, depending on relative velocity. Sticking collisions leading to the growth of grains depend on the *coagulation critical velocity*, over which coagulation does not occur; turbulence is the more efficient process for sticking collisions when density is $< 10^8$ H-atoms/cm^3, while at higher hydrogen density the dominant process is Brownian motion. Hot molecular cores consist of thermally modified grain cores: their detection is related to observed NH_3 and CH_3OH overabundance, attributed to the evaporation of icy mantles subsequently to the irradiating action from stars (UV radiation, stellar winds, shock waves). The UV irradiation, ion bombardment and cosmic rays bombardment of icy mantles cause the evaporation of volatiles, leading to the formation of refractory organic residues, essentially HAC grains, and then dehydrogenation produces amorphous carbon grains. Several desorption mechanisms counterbalance the accretion processes of grains: gas species are desorbed from the grain surface by (a) thermal evaporation of atoms and molecules; (b) desorption caused by cosmic rays; (c) excitation and disexcitation of H_2 molecules causing UV emission and so dissociation of surface molecules; (d) the formation of CO is inhibited in regions of H_2 reactions on H_2O-ice.

1.1.4 Dust in young stellar objects (YSO)

Dust grains are also associated to young stellar objects, such as T-Tauri and Herbig Ae/Be stars (with emission lines), HII regions and BN-type objects, or Becklin-

Neugebauer objects (extremely luminous and obscured stars with $L > 10^4 L_\odot$ and $A_V \sim 15$). The continuum infrared emission observed in circumstellar environments is due to the presence of solid grains, that are altered and processed by UV radiation and shock waves from forming stars. Infrared bands of aromatic PAHs have been detected in high-UV-flux regions as planetary nebulae and HII regions, while IR features of aliphatic PAHs have been observed in BN-type objects, with some differences with respect to those observed in the diffuse ISM. Differently from the diffuse ISM, in circumstellar materials, CH_3 and CH_2 groups have not been found. Moreover solid grains in circumstellar disks (around T-Tauri and Herbig Ae/Be) can have larger sizes than grains in the ISM, from 1 μm even to submillimetric diameters. The *Vega phenomenon*, for which prototypes are α-Lyrae and β-Pictoris, consists of main sequence stars with circumstellar disks containing dust grains at $T \sim 100$ K; the thermal emission from these dusts dominates the stellar spectra in the IR range $\lambda > 25 \mu m$. Detected infrared bands at 10 μm and 11.2 μm reveal the presence of Mg-rich silicates and olivines in these environments.

1.2 Interplanetary dust

The formation of our planetary system has occurred in three stages: (1) the *formation stage*, with a time-scale of about 10^5 yr; the protostar was embedded in a collapsing nebula, with a flat disk consisting of gas and dust ($M_{dust} \approx 1 - 2\%$ by mass); (2) the *viscous stage*, with a time-scale of $10^5 - 10^6$ yr; the protostar was not yet visible within the optically thick gas, and in the rotating disk the matter was transferred inwards, while angular momentum was transferred outwards; (3) the *cleaning stage*, lasting about 10^7 yr; the gas was removed, the star became optically visible, the new-born star was a T-Tauri type.
The planetary formation begins in the viscous stage; the grains are initially coupled with the gas streams (Brownian motion and turbulence) in the protostar nebula. Fluffy aggregates first coagulate by collisional sticking, and grains grow into kilometre-sized planetesimals: these are the building blocks of planets; collisions between planetesimals and self-gravity finally lead to planets. The Sun contains about 99.86% of the total mass of the Solar System, while all other bodies of our planetary system (planets and minor bodies) contribute for about 99% to its whole angular momentum.
During the gravitational collapse the dust grains in the solar nebula were heated by shocks; most of the original interstellar grains vaporized and then recondensed, and this fact explains the similar isotopic compositions of interplanetary dusts; interstel-

lar grains in the outer solar nebula experienced a minor thermal heating, and some of these pre-solar grains survived until today embedded within solar system materials such as meteorites, comets, asteroids and IDPs (interplanetary dust particles). Nanodiamonds (2 nm in size) and graphite grains of pre-solar origin have been found within meteorites; pre-solar grains amount to $5-10\%$ of total meteoritic mass.

1.2.1 Sources of interplanetary dust

Many environments in our Solar System host cosmic dust grains, such as cometary tails and comas, asteroidal regolith, interplanetary dust cloud, Earth's stratosphere (and other planets atmospheres) and polar ices. The interplanetary dust cloud is continuously replenished by comets, asteroids and interstellar dust.
The main source of interplanetary dust is given by comets (within 3 AU from the Earth): sublimation of volatile ices trapped in the comet nuclei produces the ejection of surface grains, that are released into the space; this dust has been frozen into comets for 4.5×10^9 yr; it is important to study their size distribution and chemical composition in order to gain insights to the accretion mechanisms and chemical composition of the Solar nebula.
Asteroids constitute another important source of interplanetary dust (within 2-3 AU from the Earth): collisions between asteroids in the Main Belt produce fragments in a very wide size range; the spatial distribution of dust in the Solar System has indeed a significant increase in correspondence of the Main Belt of asteroids. Asteroidal dust particles are mainly compact grains composed by silicates and metals. Finally dust particles can originate in the Kuiper Belt (within 30-100 AU from the Earth) due to collisions between minor bodies beyond the orbit of Neptune.

1.2.2 Interplanetary Dust Particles (IDPs)

Interplanetary Dust Particles (IDPs) are a very distinctive and characteristic type of cosmic dust; they are typically in the size range $10 < d < 100\ \mu m$; particles $< 10\ \mu m$ in diameter usually vaporize after flash heating. These particles are the product of many processes such as aggregation and accretion, parent-body residence and alteration, ion irradiation in interplanetary space, heating, ablation and melting during atmospheric entry [71, 73]. IDPs are first of all classified depending on their bulk composition: chondritic, non-chondritic and clusters. Following a morphological criterion the first two classes are subsequently subdivided into aggregates or non-

aggregates (chondritic), and in refractory aggregates or fragments (non-chondritic). Moreover IDPs can be spherical or non-spherical. A classification scheme of IDPs is in fig. 1.1. Aggregate or non-aggregate IDPs are typically $10 - 15\ \mu m$, while cluster are $\sim 60 - 100\ \mu m$ (Rietmeijer 2000, 2002) [71, 73].

Chondritic aggregate IDPs have densities in the range $0.1 \div 4.3$ g/cm^3: they consist of a matrix of *principal components*, with embedded grains like silicates (olivine and pyroxenes), Fe,Ni sulfides and iron oxides; embedded grains are $\sim 5\ \mu m$. The matrix is constituted by principal components (PCs), that are small spherical particles $\sim 100 - 1000$ nm in size. The PC units have the following mineralogy:

1. *Carbonaceous PCs*: this carbonaceous matrix contains refractory hydrocarbons, amorphous vesicular carbon, poorly graphitized carbon and pre-graphitic carbon, often grouped into patches;

2. *Carbon-bearing ferromagnesiosilica PCs*: ultrafine grains composed of olivines (forsterite, Mg_2SiO_4, and fayalite, Fe_2SiO_4), pyroxenes (enstatite, $MgSiO_3$), Fe,Ni sulfides and Fe-oxides; these ultrafine grains (2 - 50 nm) are mixed into a matrix consisting of refractory hydrocarbons and amorphous carbon;

3. *Pure ferromagnesiosilica PCs* occur as:

   - Coarse grained PCs: these are Mg-rich units, $\sim 10 - 410$ nm in size, with bulk composition $(Mg,Fe)_6Si_8O_{22}$ (*smectite dehydroxylate*); the *fe* ratio for these particles is Fe/(Fe+Mg)$\approx 0 - 0.33$; it is a material containing olivines, pyroxenes and amorphous aluminasilicates;

   - Ultrafine grained PCs: these are Fe-rich units, < 50 nm in size, with bulk composition $(Mg,Fe)_3Si_2O_7$ (that is *serpentine dehydroxylate*, *serpentine* being $Mg_3Si_2O_5(OH)_4$); the *fe* ratio is Fe/(Fe+Mg)$\approx 0.3 - 0.83$; it is an amorphous matrix with embedded olivines, pyroxenes, Fe,Ni-sulfides, magnetite and *kamacite* grains [α-(Fe,Ni), with $\sim 90\%$ Fe and $\sim 10\%$ Ni]. This Fe-rich grain matrix sometimes can include grains of unknown origin, such as Ca-silicates and Fe,Ni sulfides $\sim 100 - 500$ nm in diameter.

Typically the matrix of an aggregate IDP consists of a mixture of all types of PC: carbonaceous, C-bearing and pure ferromagnesiosilica PCs. The similarity of matrix principal components within IDPs and CHON (carbon, hydrogen, oxygen and nitrogen) grains within comets like Halley suggests a link between the IDPs and the icy protoplanets [73].

Embedded non-chondritic grains can occur in the chondritic aggregate matrix. These

grains can contain minerals like silica (tridymite: SiO_2), olivine (forsterite and fayalite), Ca-free pyroxene (enstatite), Ca-pyroxene [$Ca(Mg,Fe)Si_2O_6$ like *pigeonite* (low Ca) and *diopside*], Fe,Ni and Fe-sulfides (*pyrrhotite*, Fe_7S_8) and Fe,Ni-metals (kamacite). Embedded non-chondritic grains also can include amorphous silicates like plagioclase (*albite*, $NaAlSi_3O_8$ and *anorthite*, $CaAl_2Si_2O_8$), alkali-feldspar [*orthoclase*, $KAlSi_3O_8$] and other aluminasilicates.

Chondritic non-aggregate IDPs occur as CI or CM meteorites types. Most of these particles resemble debris of the phyllosilicate matrix of the CI and CM meteorites. Chondritic IDPs can be "unaltered" or "heated": unaltered IDPs have not suffered a severe thermal heating, while heated IDPs occur with morphological surface features that reveal heating, like platy lobes, fringes, rings, disks or skirts. Chondritic IDPs have solar abundances of main elements within a factor of 2, even if non-chondritic abundances on small scale could occur.

Non-chondritic particles can be refractory aggregate or fragments.
Non-chondritic refractory aggregates occur as Ca, Ti, Al-rich IDPs. Refractory oxides aggregates are typically $\sim 5-15\ \mu m$ in diameter, and are constituted by small ($< 500nm$) grains. The main common minerals are *hibonite* [$CaAl_{11}Ti_{0.5}Mg_{0.5}O_{19}$], *gehlenite* [$Ca_2Al_2SiO_7$], *perovskite* [$CaTiO_3$], *diopside* [$CaMgSi_2O_6$], Ti-diopside, *corundum* [Al_2O_3], *spinel* [$MgAl_2O_4$], *melilite* [that is a Na,Mg,Fe-bearing gehlenite] and plagioclase (*anorthite*, $CaAl_2Si_2O_8$).

Non-chondritic fragments are silicate IDPs (olivine or pyroxenes; unmelted or spheres); Fe,Ni sulfide IDPs (troilite FeS or pyrrhotite with low Ni; unmelted or spheres). Unmelted silicate and sulfide IDPs are likely fragments of low density and fluffy aggregates, that survived the strong heating due to the atmospheric entry; they are characterized by S and Zn depletions [71]. Sometimes chondritic aggregates can appear adhering to the surface of non-chondritic IDPs. Non-chondritic IDPs can also occur as mixture of all these previous types.

Cluster IDPs can be as large as $\sim 60-100\ \mu m$, they have a minor matrix mass and appear as agglomerates of chondritic aggregate and non-chondritic IDPs. They include olivine, Ca-poor and Ca-rich pyroxene, Fe,Ni-sulfides, and amorphous and crystalline plagioclase and feldspar.

Spherical IDPs instead lose a significant mass fraction. The spheres have experimented complete melting subsequent to flash heating; during a $5-15$ s flash heating the temperature reaches $300-1000$°C, while the melting temperature for chondritic IDPs is ~ 1500°C. Spherical IDPs are usually non-chondritic quenched-melt spheres, consisting in Mg,Fe-silicates, Mg,Fe,Ca-silicates and Mg,Ca,Al-silicates, and

also Fe,Ni,S or Fe-spheres. Spherical non-chondritic IDPs are related to unmelted non-chondritic silicates and sulfides. Ablation spheres are rare in the stratosphere, they amount to less than 10% of particles 10 μm in size [10].

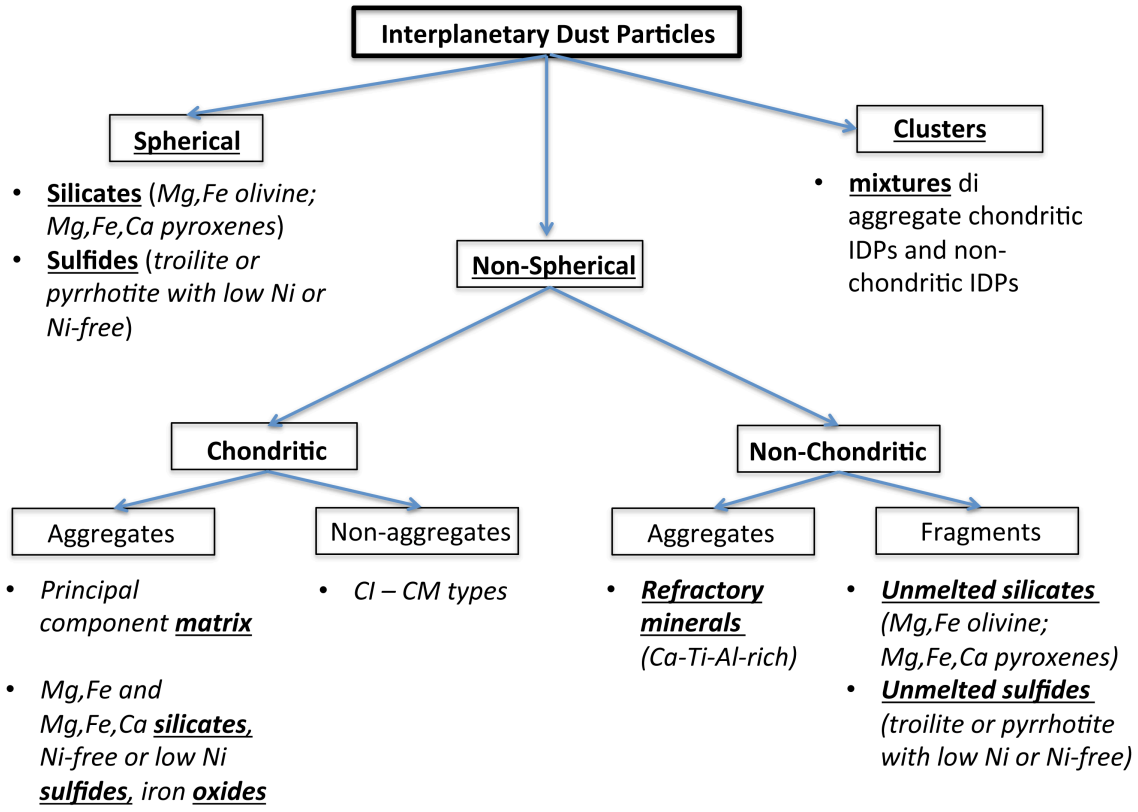

Figure 1.1: *Interplanetary Dust Particles classification [71, 73].*

The average iron-to-nickel ratio in IDPs is Fe/Ni = 20.5, very similar to the cosmic value Fe/Ni = 20. Nevertheless the Fe/Ni ratio in IDPs varies in a wide range, and this could indicate a certain mixing of constituents materials and thermal alteration and processing. For comparison the terrestrial (crustal, basaltic, volcanic) value is Fe/Ni $\sim 2-750$. The meteoric value is Fe/Ni $\sim 7-35$, consistent with cosmic values [71]. Thus the determination of the iron-to-nickel ratio in stratospheric collected materials could provide clues for a cosmic origin of the particles. During ablation meteoroids are depleted in volatile elements, for example Na and K. Therefore the measured Na/Ca and Mg/Na ratios in meteoroids can be too low and too high respectively than the original values. Typical values for aggregate and cluster IDPs

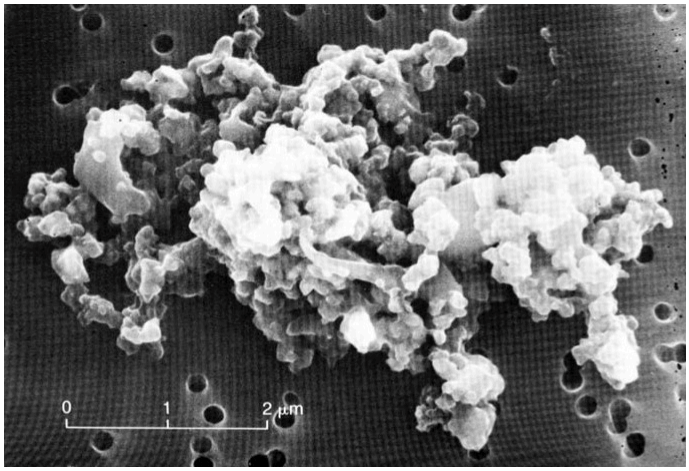

Figure 1.2: *A typical aggregate Interplanetary Dust Particle (IDP) [NASA].*

are Na/Ca $\approx 1-2$ and Mg/Na $\approx 5-10$; these values are between the meteor and mesospheric metal and the CI-CM values [71].

Large porous aggregates IDPs have typically chondritic bulk composition, even if the single small grains can have different composition and mineralogy. *Troilite* (FeS) has also been detected in stratospheric particles, and also *Augite*, a mineral containing Ca, Mg, Fe, Al, Ti, Si, O (Testa et al. (1990)) [87]. Some particles can contain high percents of Ti and TiO; the presence of barium could be due to volcanic emissions, but could also be intrinsic. High concentrations of Br have also been detected in many IDPs; it is not definitely clear if the bromine is intrinsic of the extraterrestrial particles or if it is produced by chemical reactions with atmospheric gases. Rietmeijer (1992) shows that the bromine content of several chondritic porous interplanetary dust particles (CP IDPs) has a linear correlation with the residence times in stratosphere calculated for the particles: that is, IDPs with larger residence times in stratosphere have a major Br content, while IDPs having little residence times show a minor Br content; this fact could be an evidence for a stratospheric bromine contamination of IDPs [69].

Aggregate IDPs $\sim 5\ \mu m$ in size host non-chondritic grains ~ 100 nm in diameter, mixed with the PCs of the matrix; aggregate IDPs of $10-15\ \mu m$ have embedded non-chondritic grains typically of $\sim 5\ \mu m$; cluster IDPs of $\sim 60-100\ \mu m$ host embedded non-chondritic grains as large as $> 10\ \mu m$, that are mixed with aggregate IDPs. All these recurrences of non-chondritic dust grains embedded within larger aggregates could be evidence supporting the hypothesis of hierarchical accretion (Ri-

etmeijer, 2002) [73]. Following this sequence, cluster IDPs should agglomerate into *super clusters*, and these super clusters should agglomerate to form *giant clusters*. Finally these super and giant clusters IDPs could represent the pebbles and boulders from which the icy protoplanets could have formed. For example, Mg-rich olivine grains ($\sim 50 - 150\ \mu m$) and Fe,Ni-sulfide grains ($\sim 50 - 500\ \mu m$) that are found within the matrix of undifferentiated meteorites could be an analogue of these super and giant cluster IDPs, from which started the accretion sequence [73]. Thus it could be interesting to search for super or giant cluster IDPs entering the terrestrial atmosphere for stratospheric collection, though seems very unlikely that such large aggregate particles (up to $\sim 500 - 1000\ \mu m$) could survive the strong heating due to atmospheric entry. Nevertheless Rietmeijer (2001) calculates that a meteoroid coming from the Leonids shower could penetrate the atmosphere as a millimeter-sized particle, composed by a 575-μm sized dustball ($\rho = 1\ \mathrm{g}/cm^3$) and a $\sim$ 500-μm sized Mg-rich or pyrrhotite grain: that is, a giant cluster [73].

1.2.3 Evolution of interplanetary dust

Several processes influence the orbital motion of dust particles: (a) solar radiation pressure sweeps away in the outer Solar System micrometer and sub-micrometer sized particles, being more effective than gravity; (b) the Lorentz force sweeps away, or concentrates in the inner Solar System, small dust grains with some surface electrical charge, depending on the phase of the solar magnetic cycle; (b) because of the Poynting-Robertson effect, micrometer-sized particles spirals towards the Sun due to non-radial radiation pressure; the P-R effect is however important also for larger grains (up to centimeter or meter-sized bodies). A grain orbiting the Sun absorbs solar radiation in a radial direction, and if it is in thermal equilibrium, then the radiation is re-emitted at the same rate; the radiation is emitted isotropically in the reference frame of the grain, but in the Sun's reference frame the radiation emission is no longer isotropic because of grain motion and rotation; there is a preferential direction of emission tangentially to the motion. The rate of exchange of momentum (tangential force) of a grain due to solar radiation absorption is:

$$F_t = L_\odot \frac{a^2 v}{4 r^2 c^2} \tag{1.5}$$

where $L_\odot = 3.86 \times 10^{26}$ W is the Sun luminosity, a is the grain radius, r the distance from the Sun, v the grain velocity and c the velocity of light. The time necessary for

the grain of density ρ to move from an orbit at distance r_0 to an orbit at distance $r_f < r_0$ is given by:

$$t = \frac{4\pi a c^2 \rho}{3 L_\odot}(r_0^2 - r_f^2) \tag{1.6}$$

This implies that because of the non-isotropic emission of radiation small grains loss angular momentum, they are slowed down, their orbits are modified and they spiral toward the Sun, where they are destroyed, in timescales that are small if compared with the lifetime of the Solar System. For example a spherical grain with density $\rho = 3 \times 10^3$ kg/m^3 at a distance of 1 AU from the Sun, will spiral into the Sun in a time of 2×10^3 yr if it has a radius $a = 1$ μm, in a time of 2×10^7 yr if its radius is $a = 1$ cm; a grain of ~ 10 cm will spiral into the Sun within 2×10^8 yr; these timescales are much smaller than the lifetime of the Solar System.

The interplanetary dust cloud (the "Zodiacal dust cloud", responsible of the Zodiacal light), which lies along the ecliptic plane, is thus homogeneously filled with dust particles of cometary, asteroidal, Kuiper-Belt and interstellar origin. Meteoroid streams, initially associated to comets, are embedded in this cloud, even if these particles disperse and spread with time because of the described effects.

1.2.4 Pre-solar grains in interplanetary particles

During the formation of our planetary system, there was a temperature gradient from the proto-Sun to the external regions, with the inner parts being warmer and the outer regions being colder. Thus in the innermost solar nebula the loss of volatile elements is consistent with the formation of the internal terrestrial planets (mainly constituted by rocks and metals); in the outer solar nebula the volatile "icy" species survived and gaseous giant planets formed. In this frame, the comets, which are thought to be originated in the cold regions of the outer solar nebula (approximately in the range $5-100$ AU), are the least altered objects of the Solar System: they carry information about the primordial conditions of the Solar System during its formation, and moreover often contain pre-solar inclusions. Meteorites also carry chemical and isotopic information about the solar nebula, though they suffered thermal heating and modifications due to collisions between their parent bodies, the asteroids. The environments in which comets formed, differing by temperatures, densities and chemical compositions, are reflected in different size distributions and chemical-physical properties of dust grains. Refractory components in cometary grains consist mainly

of silicates, typically mixtures of crystalline (olivines and pyroxenes) and amorphous grains, and carbonaceous grains. Interstellar inclusions like GEMS (Glass with Embedded Metal and Sulfides) and isotopic anomalies of H, N, O in IDPs are clues of an interstellar origin for these materials. The GEMS inclusions in cometary IDPs are characterized by non-stoichiometric ratios, Mg and Si depletion respect to O, inclusions of Fe-Ni metals and Fe-sulfides. Pre-solar grains have been also detected inside primitive meteorites; these are essentially nanodiamonds, SiC and graphitic grains. Nanodiamonds are the most abundant pre-solar grains (400 ppm), characterized by the Xe isotopic anomaly: this is a mark of their formation within supernovae explosions. Nanodiamonds in meteorites have a density 30% lesser than terrestrial diamond; they are enriched in H and D, with C-atoms essentially in surface. Pre-solar graphitic grains in meteorites (1 ppm) consist in spherical shells constituted by graphitic layers, containing other refractory materials of stellar origin between the layers, such as TiC.

1.2.5 Interstellar dust in the Solar System

Because of the motion of the Solar System across the interstellar medium, interstellar atoms and grains can penetrate into our planetary system. Dust particles with a sufficiently low charge-to-mass ratio can penetrate into the Solar System because their interaction with the heliosphere is negligible. Interstellar grains in the Solar System have been identified, by the Ulysses and Galileo probes, thanks to three distinctive features: (a) their retrograde motion, opposite to that of interplanetary particles, that move around the Sun in the same sense as the planets; moreover the trajectory directions coincide with that of the inflow of interstellar gas; (b) interstellar grains are distributed at all latitudes respect to the ecliptic plane, while interplanetary dust is concentrated on the ecliptic plane; (c) interstellar grains are observed to move at velocities $V \gg V_{esc}$, and thus they are not bound to the Solar System. Indeed interstellar grains are observed in the Solar System with velocities of $V \sim 100$ km/s, while the escape velocity is $V_{esc} \approx 42$ km/s. Interstellar grains are assumed to have a mean mass $m_{IS} \sim 3 \times 10^{-13}$ g, corresponding to particles with diameters in the range $0.1 - 1.0$ μm depending on density, in the range 1-3 g/cm^3, but very small particles of about 0.005 μm can exist. Ulysses and Galileo probes measured the interstellar grains flux $F_{IS} = 1.5 \times 10^{-8}$ $cm^{-2}s^{-1}$; the velocity of the Sun is 26 km/s, hence the mean number density in the Solar System is approximately $c_{IS} = F/v = 5.8 \times 10^{-15}$ cm^{-3}, corresponding to a mean mass density of about 1.7×10^{-27} g/cm^3 due to interstellar grains.

Chapter 2

Dust in terrestrial stratosphere

2.1 Stratospheric particles

Dust particles are present in terrestrial stratosphere in great quantity as they are continuously replenished from many different sources. Stratospheric aerosols span in a wide range of physical and chemical properties, mineralogical compositions, morphologies and dimensions: they range from nanometric to few hundreds micrometers in size. These particles can have a terrestrial as well as an extraterrestrial origin. Aerosol particles can originate directly in the stratosphere due to condensation processes (section 2.1.1). Dust particles with a terrestrial origin are produced by volcanoes, by human activities or by other biological processes and subsequently are injected in the atmosphere where they can rise up to the stratosphere (section 2.1.2). Particles of extraterrestrial origin are interplanetary dust particles or interstellar dust particles that enters the Earth atmosphere and settle down to the stratosphere, where they remain for few weeks (section 2.1.3).

2.1.1 Background stratospheric aerosol

The stratospheric background aerosol layer was for the first time directly observed and sampled in the 1961 by Junge et al. [47] with balloon-borne experiments. Before that date only indirect measurements indicated the presence of a stratospheric aerosol layer, such as the observation of noctilucent clouds, sodium in atmosphere, twilight phenomenons, electrical conductivity measurements, the assessment that volcanic

eruptions inject dust particles in the stratosphere and the observation of a decrease of atmospheric transparency during meteor showers. Junge et al. (1961) performed different types of measurements up to 30 km relatively to different particle size ranges; in particular aerosols in the size range $0.01 < r_p < 0.1\ \mu m$ were counted using an Aitken nuclei counter; solid aerosols in the size range $0.1 < r_p < 1.0\ \mu m$ were collected using inertial jet impactors (cascade impactor technique, see section 2.2). The number of collected particles with radius $> 1.0\ \mu m$ was very low. Vertical concentration profiles were determined for the two size ranges.

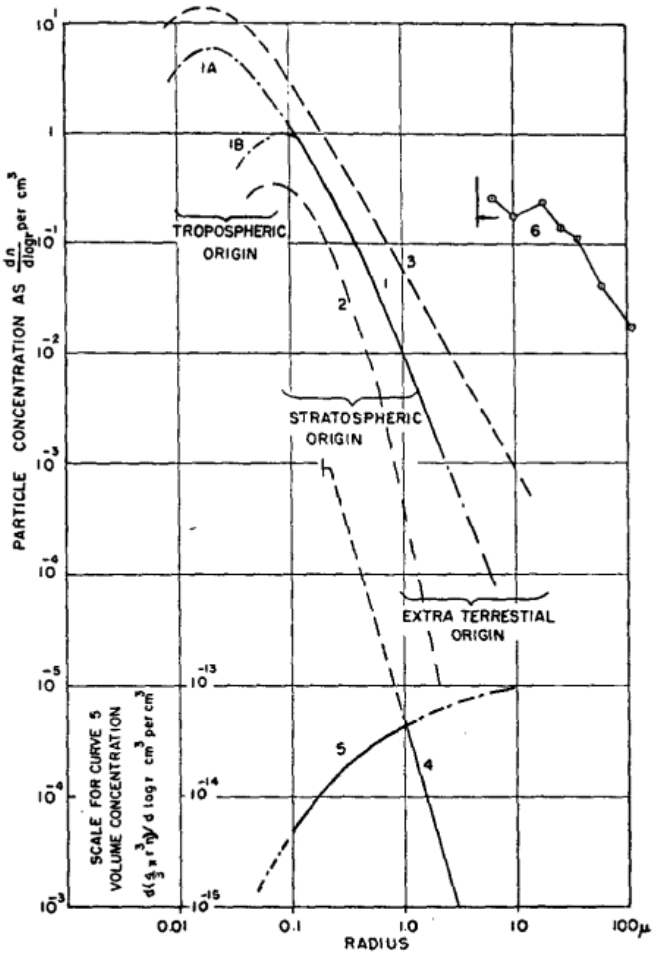

Figure 2.1: *Size distribution of aerosols as measured by Junge et al. (1961) [47].*

The vertical profile of particles of size $0.01 < r_p < 0.1\ \mu m$ shows a decrease with increasing altitude: the concentration is 500 cm^{-3} at 5 km altitude, 100 cm^{-3} at

the tropopause (15 km altitude), then drops down to 0.1 cm^{-3} at 30 km altitude. The particles in this range are thought to be of tropospheric origin, diffusing to the stratosphere because of vertical air mixing and horizontal exchange. From these measurements appears evident that the vertical aerosol distribution has a layered structure: main horizontal layers occur at altitudes of 8 km and 10 km. The vertical profile of particles of size $0.1 < r_p < 1.0\ \mu m$ has a quite different shape: the concentration increases from 1 cm^{-3} at the tropopause, to 5 cm^{-3} at 22 km altitude, then decreases down to 0.5 cm^{-3} at 30 km altitude. The size distribution of particles in the range $0.01 < r_p < 10\ \mu m$ has a sharp decrease with increasing size, from 1 to 10^{-4} cm^{-3}; in the range $0.1 < r_p < 1.0\ \mu m$ the concentration varies roughly as $\propto 1/r^2$ (fig. 2.1). From chemical analyses (Electron Microprobe Analyzer) the most abundant element constituting aerosol particles appears to be sulfur, besides the water vapour; sulfur occurs mainly in the form of sulfate. Sulfates can form starting from H_2S and SO_2 in the upper troposphere and then diffuse into the stratosphere because of vertical mixing [47]. Bigg et al. (1970) performed aerosols measurements from balloon at altitudes from 20 to 37 km. They collected aerosol particles (see section 2.2 for the technique used) and first tried to state a classification of aerosols [4]. The particle sizes are $0.1 < d_p < 2\mu m$ (mean diameter) and the measured concentrations are in the range 2-400 l^{-1}. The aerosol classification (Bigg et al., 1970) comprises three large classes of aerosols based on particle morphology as they appear on collection substrate under the electron microscope:

- type 1: central particle surrounded by a circle of small discrete particles (satellites)
- type 2: central particle surrounded by a ring
- type 3: simple particles without ring or satellites

These types are then divided into classes that take into account other features such as liquid or solid central particles, single or aggregate particles; for example we have the sub-classes L (liquid central particle), F (flattened central particle), M (mixed central particle), D (electron-dense nature), X (crystalline centre). The morphologies of the types 1 and 2 clearly indicate an impact of a liquid droplet onto the collection substrate (fig. 2.2). Particles classified as $3DC$ consist of aggregate chains of small spheres, very similar to *soot*, that is to combustion products (fig. 2.3).

Renard et al. (2005) [66] report the results of measurements carried with the balloon-borne instrument SALOMON (*Spectrometrie d'Absorption Lunaire pour l'Observation des Minoritaires Ozone et NOx*), a spectrometer that performs aerosol extinction

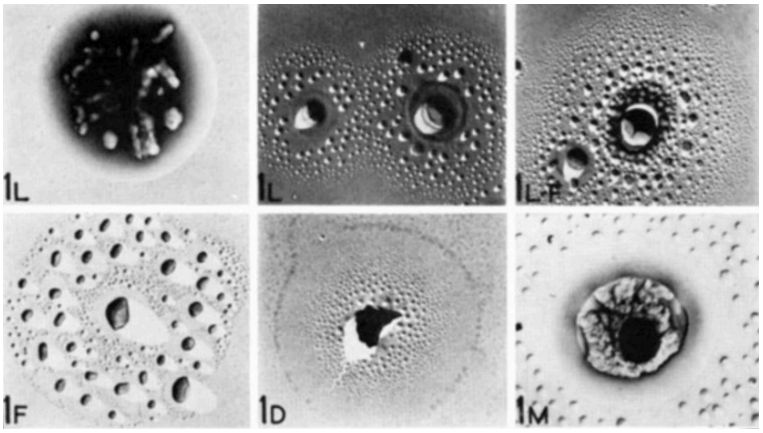

Figure 2.2: *Aerosols collected between 20 and 37 km by Bigg et al [4]. Particles are of type 1; the sub-classes are: L = liquid central particle; F = flattened central particle; D = electron-dense nature; M = mixed central particles.*

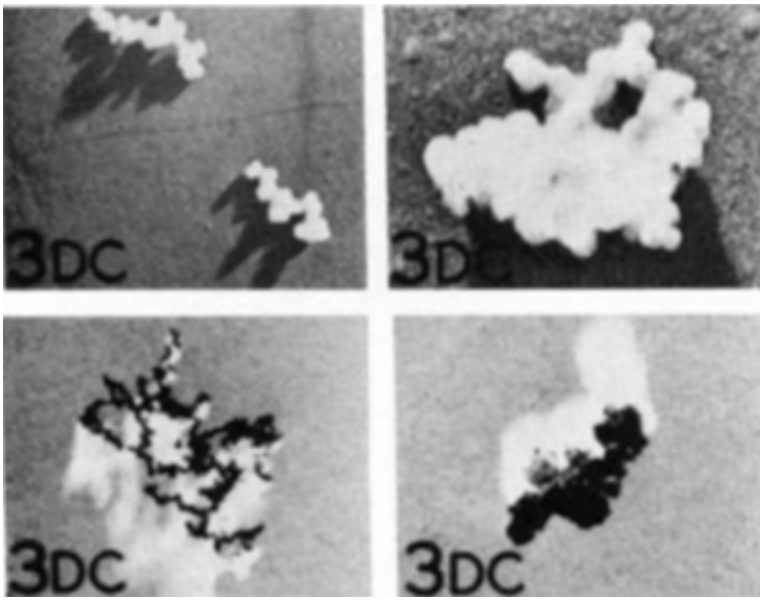

Figure 2.3: *Aerosols collected between 20 and 37 km by Bigg et al [4].*

measurements using the Moon as a light source during the balloon ascent, up to float altitude of $30 \div 40$ km. The spectra acquired by SALOMON correspond to profiles of optical depth with varying wavelength. These extinction profiles are characterized by a feature at ~ 650 nm that can't be explained by the presence of liquid sulfate aerosols alone; moreover it is believed that liquid sulfate aerosols are very rare in middle and upper stratosphere. Renard et al. (2005) suggest that soot particles can amount to a small fraction of detected aerosols. They show that the extinction profiles are well fitted by a distribution of background aerosols, soot and solid grains of extraterrestrial origin (micrometeorites). In particular they find that micrometer-sized solid grains originated from asteroidal regolith are characterized by UV-vis spectra having a large absorption band at ~ 650 nm, so they conclude that the main population of solid aerosols in the middle and upper stratosphere consists of interplanetary dust particles [66]. Renard et al. (2008) performed aerosol measurements using different ballon-borne instruments and different techniques, aimed at the systematic analysis of the content and various properties of background aerosols in the unperturbed stratosphere, that is free of volcanic dusts [67]. One of the instruments is STAC (*Stratospheric and Tropospheric Aerosol Counter*), an optical particle counter that performs particle counting from the troposphere up to above 30 km, during the balloon ascent, at floating altitude and during the descent. Another instrument is the spectrometer SALOMON [66, 67]. GOMOS (*Global Ozone Monitoring by Occultation of Stars*) is a satellite-borne UV-vis spectrometer for the measure of vertical profiles of ozone, NO_2, NO_3 and the acquisition of spectra of aerosol extinction using stars as light source. MicroRADIBAL (*Micro Radiométre Balloon*) is a NIR five-channels radiometer for the collection of the sunlight scattered by gas and particles in the atmosphere. STAC measured a solid aerosol concentration of $\sim 10^{-4} cm^{-3}$ for particles in the range $1.3 < d_p < 2.0\ \mu m$ in the middle stratosphere above 15 km, consistently with theoretical assessments regarding the population of interplanetary dust particles. STAC also detected several local enhancements of aerosol concentration during the ascent at 25 km, interpreted as aerosol layers with a ~ 4 km vertical thickness and a $2 \div 8$ km horizontal extension. SALOMON detected four layers between 28 and 33 km; below 22 km the extinction increases as the wavelength decreases, it is greater in the blue than in the red: this fact is attributed to the presence of small liquid sulfate aerosols (sulfuric acid + water droplets). Between 22 and 30 km the extinction is almost constant and independent from the wavelength: this could indicate the presence of small soot particles. Finally above ~ 30 km the non-monotonous wavelength dependence of the extinction reveals the presence of large solid dust particles, likely of extraterrestrial origin and possibly due to disintegration of large meteoroid (see section 2.1.3). The GOMOS spectra confirm the results of

SALOMON, detecting several aerosol layers and revealing a similar vertical structure as SALOMON. MicroRADIBAL radiance measurements evidence the presence in lower and middle stratosphere of both soot and sulfate aerosols; above $\sim$ 24 km $>$ 90% of aerosol extinction is due to soot particles, while below $\sim$ 20 km $>$ 50% of aerosol extinction is due to sulfate droplets. All these measurements suggest that the vertical structure of the unperturbed stratosphere comprises a layer of liquid droplets of sulfate below $\sim$ 20 km (the Junge aerosol layer); a layer consisting of soot particles between 20 and 30 km; above 30 km and in the upper stratosphere the major population consists of micrometer sized solid grains likely of extraterrestrial origin [67, 87]. In another study, followed to recent measurements of the aerosol counter STAC, Renard et al. (2010) confirmed the existence of a large layer between 20 and 10 hPa (26 - 31 km), and revealed the presence of several thinner layers, with a vertical width of a few hundred meters, above 50 hPa. The large layer has a large size grain population, and it has been attributed to the disintegration of some large meteoroid; the thinner layers are instead thought to be constituted of small particles that are electrically charged and uncoupled from atmospheric air masses, perhaps solid soots and meteoritic debris [68].

It is accepted today that background stratospheric aerosols consist of liquid droplets constituted by a mixture of 75% sulfuric acid and 25% water; this composition was estabilished by Rosen (1971) using a balloon-borne photoelectric particle counter and performing boiling point measurements, heating the instrument inlet up to $100°C$ [77]. The sulfur constituting aerosol droplets is injected in atmosphere by volcanoes; eruptions with a volcanic explosivity index (VEI) ≥ 4 typically inject particles into the stratosphere [22]. Eruptions with VEI > 4 can inject particles up to $>$ 20 km, while eruptions with VEI > 5 can inject particles up to $>$ 25 km. The sulfur injected in troposphere/stratosphere is oxidized into SO_2 and then transformed into sulfuric acid within a few weeks; another source of sulfur is the inert S-bearing molecule carbonyl sulfide OCS [22]. The formation of sulfuric acid + water aerosol particles occurs likely directly in the stratosphere (see below), while reactions between sulfur dioxide and ammonia that don't involve atomic oxygen or ozone take place at the minimum of temperature, that is at the tropopause. A considerable fraction of stratospheric aerosols originate in the upper troposphere and lower stratosphere, because of spontaneous processes of particle formation starting from nucleation in the gas or liquid phase. The initial processes are *binary homogenous nucleation* (BHN), concerning the aggregation of sulfuric acid - water nanometer sized droplets (H_2SO_4, H_2O), or *ternary homogenous nucleation* (THN), concerning the agglomeration of sulfuric acid - ammonia - water droplets (H_2SO_4, H_2O, NH_3). Lee et al. (2003) have suggested that particle formation by nucleation can be initially induced

by ionization due to the interaction between cosmic rays and atmospheric molecules [51]. The ion-induced particle nucleation is thermodynamically favoured because of the greater electrical stability of clusters and the higher growth rate due to electrostatic forces. From airborne *in-situ* measurements performed at $\sim$ 20 km it has been found that aerosol particles newly formed (within 2-3 days) in the size range $4 < d_p < 2000$ nm have a concentration of $\sim 5 \cdot 10^2\ cm^{-3}$, while preexisting particles in the same size range have a concentration of $\sim 2 \cdot 10^2\ cm^{-3}$ [51]. Particle formation by nucleation is highly accelerated by a long sun exposure and a low preexisting particle surface area. Because of global atmospheric dynamics particle nucleation in upper troposphere and lower stratosphere is a likely source of aerosol particles in the stratosphere both at low and polar latitudes [51]. The static and quasi-permanent character of the background aerosol size distribution in the unperturbed stratosphere is the result of the interaction of many processes, starting from the evolution of atomic sulfur into sulfuric acid; the subsequent nucleation, condensation, coagulation and growth takes place from newly formed acid molecules or from pre-existing particles. Aerosols are then subject to atmospheric circulation, through extratropical downwelling or equatorial upwelling; the removal of stratospheric aerosols is mainly due to stratosphere/troposphere exchange processes, but in minor amount also to gravitational settling and diffusional growth [22]. Fueglistaler et al. (2004), on the basis of trajectories simulations, have suggested for example that $\sim$ 80% of the trajectories ascending from troposphere to stratosphere enter the tropopause over the western Pacific; they conclude that the western Pacific area is the dominant source of stratospheric air [35]. Background stratospheric aerosols have an important role in radiative and chemical balance of the atmosphere. The influence of stratospheric aerosols on radiative balance concerns the stratospheric warming and tropospheric cooling, even if the influence is small. Aerosols also affect chemical reactions in atmosphere: when the aerosol loading is high, after volcanic eruptions, trace gases as NO_x decrease, while the activated chlorine is more abundant; during quiescent periods the low aerosol loading leads to an increase of NO_x species and this induces ozone loss [21, 22].

Besides their direct effect on climate due to absorption and scattering of solar and infrared radiation in atmosphere, aerosols also affect the cloud formation and the efficiency of precipitation. An increase in the aerosol concentration can influence the number density of cloud droplets, and can decrease the efficiency of precipitation. Aerosol with dry diameters in the range $0.1 < d < 1.0\ \mu m$ are most important both for radiative forcing and for heterogeneous chemistry; these particles can hydrate and become as large as 2 μm. Indeed smaller particles are removed by fast coagulation, while larger particles are removed by nucleation to cloud droplets [62].

Above the sulfate aerosol layer ($\sim$ 20 km) aerosol enhancements could occur, especially in Polar Winter stratosphere (Iwasaka et al. 1992). Such aerosol enhancements, or Polar Stratospheric Clouds (PSC), contain nitric acid trihydrate crystals (NAT, type-I PSCs) or ice crystals (type-II PSCs). It is believed that NAT crystals originate above the sulfate layer, in the upper stratosphere, then descend in the middle and lower stratosphere. NAT crystals can form through condensation of nitric acid vapour (HNO_3), and then coagulation of NAT particles brings to μm-sized particles [42]. Such particles play a role in heterogeneous chemistry and in ozone depletion mechanisms. Sulfate aerosol layer and NAT layer appear to be quite separate in the stratosphere, so sulfates are not the unique nuclei of NAT particles.

2.1.2 Stratospheric aerosol of terrestrial origin

Dust from volcanic activity

Volcanic eruptions not only contribute to the background stratospheric aerosol layer, through the injection in stratosphere of atomic sulfur from which nucleation and growth of aerosols take place, but also inject in stratosphere solid dusts and ashes. During a volcanic eruption a great amount of dust particles are inlet into the atmosphere. Many studies evidence and demonstrate the permanence in stratosphere of aerosols of volcanic origin, their influence on atmospheric dynamic and chemistry and on climate. Volcanic eruptions emit particles with a large grain size distribution; the emitted particles range from diameters $> 10 \div 10^2$ mm (pyroclasts) to micrometer ashes. Volcanic ashes are divided into *fine ash*, with $d < 1000$ μm, and *very fine ash*, with $d < 30$ μm. Rose and Durant (2009) have found that major mass proportions of very fine ash (30% to $> 50\%$) follow silicic eruptions (Mount St Helens, 1980 and El Chichón, 1982), while lower mass proportions ($< 4\%$) of these smaller particles follow basaltic eruptions (Fuego, 1974) (see [76]). Very fine ashes can reach the upper troposphere or the lower stratosphere and then can be transported by the winds through the atmosphere, where they have residence times at least weeks to months depending on size and shape [76]. Particles with $d < 30$ μm fall in the *laminar flow* regime and settle according to Stokes Law. Mateshvili et al. (2005) performed measurements of twilight sky brightness [57] in the period 1989-1993 across the Mt Pinatubo eruption (1991) and evidenced strong differences in the sky brightness pre- and post-eruption. Sky brightness versus solar zenith angle profiles, measured when the sun is below the horizon, contain contributions both from the lower layers of stratosphere and from the stratospheric aerosol layer; this

brightness is due to scattering of sunlight from atmosphere molecules and aerosol particles; it has been demonstrated that after great volcanic eruptions, such as Mt Pinatubo (Philippines), twilight sky brightness profiles show variations and large peaks (*humps*) due to an enhancement of the stratospheric aerosol loading. Particles with different sizes settle at different altitudes, the size increasing with decreasing altitude: indeed sky brightness profiles show that light extinction maximum occurs at longer wavelengths with decreasing altitude, and so it is caused by bigger particles [57]. Lin and Saxena (1997) in their study report an increase of the values of aerosol parameters such as extinction efficiency, particle radius, aerosol surface and mass loading subsequent to Pinatubo eruption [52]. Vertical profiles of aerosol extinction also show evident increases in the period after the eruption, with respect to the period before eruption, especially at $20 \div 30$ km of altitude, but the plume can penetrate into the stratosphere up to 40 km [52]. Lin and Saxena have found moreover that, after the eruption, the number density of aerosol particles in the size range $< 0.2\ \mu m$ is one order of magnitude larger than that of background aerosol; for greater particles the number density has an increase of order of $> 10^3$: this strong enhancement of larger dust particles is due to Pinatubo eruption [52]. Mateshvili et al. (2002) showed that typically one month after an eruption most particles of radius $\sim 1\ \mu m$ are volcanic ash, while a few months after an eruption the predominant particles are large sulfuric acid aerosols; a period of one year after a great eruption is sufficient to remove all dust particles $> 2\ \mu m$ from lower stratosphere [56]; they performed combined twilight sky brightness measurements (TSM) and dust collections in the period 1981-1985, during which were observable the consequences of large eruptions such as Mt S.Helens (1980), El Chichón (1982) and minor eruptions such as Alaid (1981), Nyamuragira (1981/1982) and Bezymianny (1985): these measurements evidence that while minor eruptions produce small dust clouds, large eruptions produce a great stable aerosol layer in stratosphere [56]. Successively large particles decay and remains a volcanic ash background of micrometer sized dust particles, replenished by minor eruptions; dust particles inlet by volcanoes at the tropics are transported northward in the stratosphere up to polar latitudes.

Deshler et al. (2003) carried on measurements with balloon-borne optical particle counters from University of Wyoming (Laramie, 41°N) in the period 1971-2001, during which the three major volcanic eruptions occurred: Fuego (1974), El Chichón (1982) and Pinatubo (1991): they showed that while the impact of Fuego was primarily below 20 km, the effects of El Chichón and Pinatubo were preminent above 25 km [21].

Aerosol particles produced by volcanoes have a not negligible influence on global

climate; Qun (1995) has calculated that after Pinatubo eruption the aerosol clouds caused a sensible drop in global mean temperature and the expansion of climatically cool regions [64]. After large eruptions such as El Chichón and Pinatubo a mean decrease of $0.1-0.2$°C in surface temperature for both hemispheres has been inferred for two years subsequent the eruptions [75, 85]. As suggested by Saxena et al. (1997) the stratospheric volcanic aerosol layer absorbs and scatters the solar radiation incoming on Earth, increasing planetary albedo and causing a decrease in the daytime maximum temperature (*shortwave forcing*); moreover the aerosol layer absorbs and scatters the infrared radiation outgoing from Earth, producing an increase of nightly minimum temperature (*longwave forcing*) [85]. As a consequence stratospheric volcanic aerosol loading also contributes to the decrease of the atmospheric parameter DTR (defined as the difference between the minimum and maximum temperatures) [85]. Labitzke and McCormick (1992) have shown that a temperature increase of 2.5°C with respect to previous 26-years mean has followed the Pinatubo eruption for several months, with peaks of 3.5°C higher than the mean, in the region between the equator and 30°N [50]. Dutton and Christy (1992) have calculated that, in the first year following the Pinatubo eruption, the global and northern hemispheric tropospheric temperatures decreased of 0.5°C and 0.7°C respectively [26].

Dust from anthropogenic activity

A fraction of aerosol particles in stratosphere is produced by human activities such as industrial processes, power plants, environmental pollution, burning processes. Other sources can be aircrafts and spacecrafts exhaust particles. Concerning industrial processes, for example, Jablonska et al. (2001) have found that carbonaceous particles emitted by power plants (*coal fly ash*) can contain micrometric or nanometric barite grains [43]. Barite ($BaSO_4$) is a chemically inert and thermally stable mineral with melting point at 1580°C; barite grains in aerosol particles are typically $< 0.1 \div 25\ \mu m$ in size constituted by $20 \div 160$ nm nanocrystals. Primary barite grains are originated when volcanogenic elemental Ba dissolved in aqueous environments mixes with coal deposits; domestic coal burning at $800 - 900$°C do not reach the melting temperature, so it produces coal fly ash containing unmelted primary barite grains. Industrial coal burning processes instead reach the melting temperature and so can inject in atmosphere secondary barite grains: the primary barite is thermally decomposed into BaO, then this can react with stratospheric sulfuric acid aerosol to form secondary barite [43]. Generally aspherical particles will have longer residence time in atmosphere than spherical coal fly ash. Performing particle

collection in the troposphere above an industrial region in Poland, Rietmeijer and Janeczek (1997) have shown that there are many types of particles that are injected into atmosphere because of industrial processes [70]. While spheres are extremely rare, silica shards are very common and can also contain Al_2O_3, and traces of Mg and Fe. Silica shards can also appear as clusters held together by carbonaceous material. Thin sheet carbonaceous materials, that are the cement of the clusters and to which single graphitic layers are attached, can contain silica single crystal grains, traces of Mg and Fe, Al_2O_3, CaO, MgO, FeO, ZnO, BaO, Na_2O, K_2O, SO_3, barite, $CaSO_4$ and NaCl. Amorphous spherical soot particles are very common and form chains or fluffy clusters; the soot units are $8 \div 68$ nm in size. Both silica shards and carbonaceous sheets contain sulfur in the form of SO_3. The presence of many salts indicates that this type of particles are the product of coal combustion [70]. Charlson et al. (1992) have shown that anthropogenic sulfate aerosols adduce a major perturbation to the global radiative forcing. This contribution to climate forcing due to anthropogenic sulfate has been estimated to be -1 to -2 watts per square meter, globally averaged [14]. Estimates of source strength for dust particles of industrial origin are in the range $100 \div 200$ Mt/yr [62].
Jackman et al. (1998) have estimated the impact of alumina particles emitted in the exhausts by solid rocket motors on atmospheric chemistry and ozone depletion [44]. During the launch of solid rocket motors (SRM) several types of compounds are injected into the stratosphere: hydrogen chloride, water vapour, molecular nitrogen, carbon monoxide and alumina particles (Al_2O_3). Alumina particles are in the range $0.01 < r < 5\mu m$, and play a role in atmospheric chemistry both through heterogeneous chlorine activation reaction ($ClONO_2$+HCl$\rightarrow$$HNO_3$+$Cl_2$), and through the coating with H_2SO_4. Alumina particles indeed can become coated with sulfuric acid, thus increasing the background aerosol layer, the increase being $\sim 1\%$. If alumina particles are not coated then they have a higher potential in ozone depletion, because chlorine activation reaction is facilitate on alumina surface. The annually averaged ozone depletion due to Al_2O_3 particles is about 3-4 times smaller than the depletion due to HCl emissions [18, 44].

Dust from biological and terrestrial sources

Generally carbonaceous aerosols are originated from biomass and fossil fuel burning, and from oxidation in atmosphere of volatile organic compounds (VOC). Estimates of the global emission of organic aerosol from biomass burning are $45 \div 80$ Mt/yr, while for aerosol originated from fossil fuel burning we have $10 \div 30$ Mt/yr. Sec-

ondary organic aerosols (SOA) are formed from atmospheric oxidation of biogenic hydrocarbons; these low volatility particles are in the sub-micrometer range [62]. Emission estimates are $30 \div 270$ Mt/yr. The oxidation of VOC in atmosphere is due to oxygen compounds such as O_3, NO_3 and primarily to OH.
Several studies have showed that large amounts of smoke particles and organic compounds originated from forest fires can reach the lower stratosphere and thus increase the background stratospheric aerosol. Fromm and Servranckx (2003) calculated trajectories of air parcels showing that an extreme convection mechanism can bring forest fires-originated particles from troposphere to stratosphere [34]. Ray et al. (2004) observed aerosols produced by biomass burning over Florida during a period of frequent forest fires in western United States and eastern Canada; they deduce that this is due to convective injection of tropospheric air into lower stratoshere [65]. Jost et al. (2004) detected high amount of particulate and gases (carbon monoxide and dioxide) in stratosphere up to 16 km; in particular they measured 193 ppb CO (while typical values at these altitudes are < 50 ppb); they observed particle concentrations of up to 140 cm^{-3}, about 5 times greater than the background aerosol concentration, in the range $90 \div 2000$ nm; they showed that these increases in gases and aerosols were due to US forest fire plumes penetrating deep in the stratosphere [45]. Other authors (Goldstein et al. 2009) suggest that besides anthropogenic aerosols also biogenic aerosols have to be considered when modeling the radiative forcing, in particular secondary organic aerosols (SOA): their contribution is estimated as $\sim 12-70$ $TgC \cdot yr^{-1}$ [36]. In general primary biogenic aerosols are theoretically originated from plant debris and microbial particles such as bacteria, fungi, spores, pollen, algae, viruses, but very little information is available [62].
Immler et al. (2005) performed lidar observations of a lower stratospheric aerosol layer at 13 km altitude, measuring a particle concentration of $500 \div 2000$ cm^{-3} and detecting an inelastic scattering signal originating from the aerosol layer, interpreted as laser induced fluorescence from aerosol particles. They conclude that this fluorescence signal could be attributed either to polycyclic aromatic hydrocarbons (PAH) adsorbed to soot particles, or to sulfuric acid droplets contaminated with organic compounds, or to bacteria and fungal spores, and suggest that similar particles are originated from forest fires [41].
Other terrestrial sources of atmospheric aerosols are soil dusts and sea salt particles [62]. Soil dusts are originated mainly in tropical and subtropical regions from deserts, dry lake beds and semiarid desert fringes. Dust detachment from desert soils can happen when the wind speed exceeds a threshold value, and this fact depends on soil surface roughness, grain size and soil moisture. Anthropogenic activities over these regions can enhance dust mobilization. Soil dust particles are in the size range

$2 < d < 4$ μm. Their atmospheric lifetimes depend on particle size: smaller grains can have atmospheric residence times of several weeks.
Soil dust source strength has been estimated to be $1000 \div 5000$ Mt/yr. Sea salt particles in the range $0.05 < d < 10$ μm are produced from bursting of air bubbles during whitecap formation and then are moved into atmosphere up to the stratosphere: Xu et al. (2001) collected sea salt particles in stratosphere at 18 km [92]. These particles are very efficient cloud condensation nuclei; their source strength is estimated to be ~ 3000 Mt/yr.

2.1.3 Stratospheric particles of extraterrestrial origin

Cosmic particles are dispersed all around the Solar System, and they enter the terrestrial atmosphere because of their relative motion with respect to the Earth. (fig. 2.4).

The meteoric materials that penetrate into the Earth atmosphere come essentially from four sources. Sporadic meteors originate from the Zodiacal dust cloud. The Zodiacal cloud is constantly replenished with dust: grains released subsequently to ice sublimation in active cometary nuclei during perihelion passages, debris from collisions between main-belt asteroids and near-Earth asteroids. A second source consists in annual meteor showers, that are residual trails of periodic comets, which the Earth encounters annually. The third source arises from sporadic meteor showers (Leonids for example), streams of meteoroids residual of perihelion passages of long period comets [71]. Finally interstellar grains can also penetrate into the Solar System and hence into the terrestrial atmosphere (see the end of this section).

The total flux of extraterrestrial particles entering the Earth atmosphere has been estimated as $\sim 10^{-16}$ $g \cdot cm^{-2}s^{-1}$ or 44 tons per day on the whole Earth (Hunten et al. 1980, Brownlee 1985) [40, 10]. That is, the annual extraterrestrial mass influx on the Earth is $\approx 1.6 \times 10^4$ ton/year. Other authors report the ranges $0.2 - 4 \times 10^4$ ton/year (Murphy et al. 1998) and $0.8 - 3.8 \times 10^4$ ton/year (Cziczo et al. 2001). This amounts to $0.3 - 9\%$ of total stratospheric aerosol [58]. Considering that 10 μm cosmic particles entering the atmosphere are decelerate from ~ 10 km/s to ~ 1 cm/s, the deceleration factor is $\approx 10^6$; if we assume that the particle influx is conserved, then there is an enhancement of concentration of a factor $\approx 10^6$ for 10 μm particles in terrestrial stratosphere. The flux of particles 10 μm in size is ~ 1 $m^{-2}day^{-1}$, while the flux of particles 100 μm in size is ~ 1 $m^{-2}yr^{-1}$. The number concentration of 10 μm particles in stratosphere is estimated $\sim 3 \times 10^{-4}$ particles$\cdot m^{-3}$ [10], while

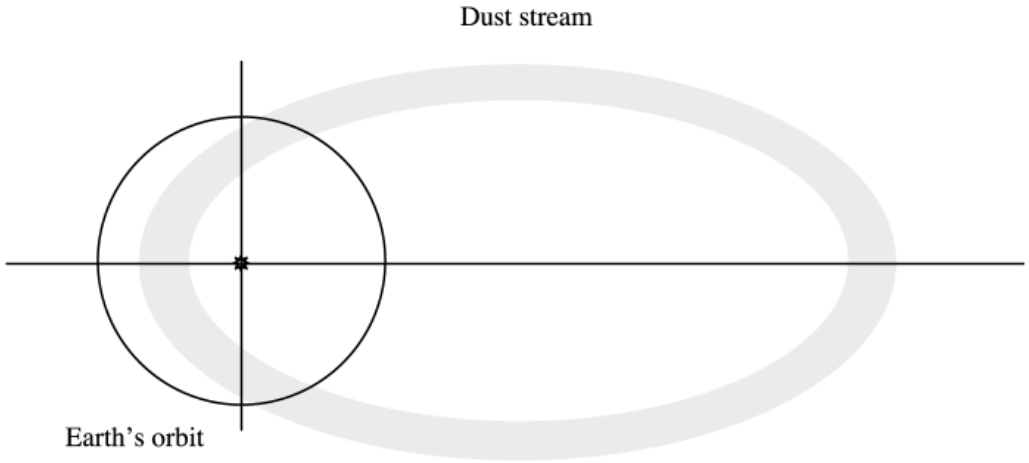

Figure 2.4: *During the motion around the Sun, the Earth intersects interplanetary dust streams. The orbits intersect in only one point because they have different inclinations.*

for > 100 μm particles it is even smaller, $\sim 10^{-7}$ particles·m^{-3} [9]. Interstellar grains can also penetrate the Earth atmosphere, because of the relative motion of the Solar System with respect to the local interstellar medium (see the end of the section); the flux of interstellar grains entering the Solar System has been estimated of the order of $\sim 10^{-4}$ $m^{-2}s^{-1}$ [37]. Rare interstellar grains can be embedded within interplanetary dust particles, and so collected in terrestrial stratosphere or on Earth. Roughly on a stratospheric collection in the free-volcanic atmosphere, the amount of extraterrestrial particles > 5 μm can be $\sim 30\%$.

Meteor ablation and theory of micrometeorites

When an extraterrestrial particle penetrate the terrestrial atmosphere, it is subject to a strong friction caused by air molecules impacting onto the forward surface and transferring energy to the particle, and it suffers atmospheric drag and a very intense heating, which in turn results in an internal temperature increase of the grain. If the particle is able to reirradiate the energy gained, then the temperature does not increase above the melting temperature T_m of the meteoritic material and the particle is slowed by the atmosphere without melting: it descends down to the stratosphere almost unaltered. Otherwise if the particle is not able to efficiently irradiate the energy gained, then the temperature increases above the melting point, and the grain

vaporizes completely. The efficiency of irradiation depends on the critical parameter m/B, that is the ratio of the mass to the effective surface of the particle (Whipple, 1951):

$$\frac{m}{B} = \frac{3e\beta\sigma D(T_m^4 - T_0^4)}{\alpha b \cos(Z) v_\infty^3} \tag{2.1}$$

in which m is the particle mass; $B = 4\pi r^2$ is the effective irradiating surface; $e = 2.718$; $\alpha \sim 1$ is the accomodation coefficient, which represents the fraction of kinetic energy of air molecules that is transferred to the particle surface; it is assumed to be almost unity because at most velocities the air molecules will penetrate into the grain surface for several molecular layers; β is the emissivity factor; D is the drag coefficient; $\sigma = 5.67 \times 10^{-8}\ W \cdot m^{-2} K^{-4}$, is the Stefan-Boltzmann constant; Z is the zenith angle; v_∞ is the initial velocity; T_0 and T_m are the initial equilibrium and the melting temperatures respectively; typically $T_m = 1200 \div 1700$ K; finally b is the inverse of scale height, arising from the assumed atmospheric density profile $\rho(h) = \rho_0 e^{-bh}$.

Smaller particles irradiate more efficiently than larger ones because they have a greater ratio of irradiating surface to the volume. Thus it follows that there is a maximum radius r_{max} below which the particle does not reach the melting temperature; instead a particle with radius $r > r_{max}$ will vaporize completely during the atmospheric entry. The maximum radius is given by Whipple (1951):

$$r_{max} = \frac{9e\beta\sigma D(T_m^4 - T_0^4)}{\alpha \rho_s b \cos(Z) v_\infty^3} \tag{2.2}$$

where:

- $\rho_p = 2 \times 10^3\ kg/m^3$, particle density

Cosmic particles in the size range $0.1 < d < 100\ \mu m$ entering the terrestrial atmosphere are able to irradiate almost all of the gained energy due to thermal heating: these are micrometeorites, they are slowed by atmospheric drag without melting and slowly descend from the mesosphere to the stratosphere where they have long residence times.
It has been calculated (MacKinnon et al. 1984) that μm-sized particles of irregular shape have a settling time from 26 to 18 km of about 10 years; sub-micrometer sized irregular particles can have similar settling rates in the upper stratosphere [54, 87].

Cosmic particles in the size range between $\sim 100\ \mu m$ and ~ 1 m instead are subject to a very strong ablation and total vaporization during atmospheric entry. Larger meteoroids, with diameters ~ 1 m, experience ablation and partial vaporization but some fragments reach the Earth surface. Extraterrestrial dust particles can be detected in stratosphere by several indirect effects. It is believed that they are a likely source for the terrestrial sodium layer; sodium atoms can originate both from meteoroids ablation around 90 km and from meteor smoke evaporation. This meteoric sodium could be the source of stratospheric NaOH. Meteoric debris and smoke particles can also act as condensation nuclei for noctilucent clouds and as solid sites for heterogeneous chemical reactions with atmospheric ions and neutrals.

Meteor smokes and meteoric dust

Stratospheric extraterrestrial particles of diameters $< 0.1\ \mu m$ are dominated by particles recondensed from meteor smokes, subsequent to the total vaporization of large meteoroids ($100\ \mu m - 1$ m) entering the atmosphere; the vaporization of meteoroids occurs in mesosphere at altitudes of $80 \div 120$ km [78, 87]. The condensation of smoke particles in stratosphere from total vaporization of meteoroids occurs at pressure values similar to those believed to have occurred in the early stages of the solar nebula, thus the study of these particles of extraterrestrial origin can improve our comprehension of the processes of formation of the Solar System. The condensation mechanism has been investigated by numerous authors.

Rosinski and Snow (1961) first investigated the process of meteor ablation, vaporization and recondensation into tiny particles [78]. They calculate, for example, that when a meteoroid containing Fe or Si is heated during atmospheric entry, iron or silicon atoms can collide both between them or with oxygen atoms; but for one collision between two iron atoms, there are $\sim 10^3$ collisions between iron and oxygen atoms; indeed at 85 km altitude ($T = 210$ K) the rate of collision between iron atoms is $\sim 2 \times 10^{12}$ collisions $\cdot\, cm^{-3}s^{-1}$, while the rate of collision between iron and oxygen atoms is $\sim 1.5 \times 10^{15}$ collisions $\cdot\, cm^{-3}s^{-1}$ [78]. Thus the formation of FeO is highly probable, and once formed this molecule is thermodynamically stable even at temperature above 2000 K. Rosinski and Snow suggest that after the vaporization of a meteoroid most of vapour could rapidly recondense into small particles, of the order of nanometers: this process would occur in mesosphere between 120 and 80 km, then these smoke particles settle down in the upper stratosphere, between 30 and 80 km where their concentration increases. The vaporization of a 100 mg meteoroid produces $\sim 1.5 \times 10^3$ particles $\cdot\, cm^{-3}$ in the range $80 \div 30$ km, in a time

interval of ~ 30 days; the vaporization of a few grams meteoroid instead produces ~ 25 particles $\cdot\, cm^{-3}$ in the same conditions; a meteor shower vaporization can produce $\sim 5 \times 10^4$ particles $\cdot\, cm^{-3}$, in which condensed particles (smokes) are in the size range $0.5 \div 10$ nm. Such nanometric smoke particles act as condensation nuclei for aerosol sulfates in the stratosphere, while in the mesosphere constitute a sink of atoms and ions.

Fuchs (1964) studied the coagulation and growth of generic aerosol particles, assuming that coagulation leads to compact particles with unity sticking coefficient. Stephens and Kothari (1978) suggest that coagulation rather leads to fluffy aggregates, loose structures with low coagulation coefficient [86]. These chain-like structures are constituted by nanometer sized particles, and form in many vapour condensation processes in low pressure environments such as stellar atmospheres ($10^{-7} \div 10^{-2}$ mbar), protostellar nebulae (1 mbar) and terrestrial mesosphere ($0.1 \div 1$ mbar). For submicrometer particles (< 1000 nm) the rate of thermal coagulation is independent on temperature and size, and is given by:

$$\frac{dn}{dt} = -kn^2 \tag{2.3}$$

where n is the particle number concentration and $k = 10^{-9} \div 10^{-10}\ cm^3 s^{-1}$ the coagulation coefficient. For a pressure $\sim 10^{-2}$ mbar, assuming 1 nm particles, the number concentration is $\sim 10^8\ cm^{-3}$ and the growth rate is $\sim 10^6 \div 10^7\ cm^{-3} s^{-1}$. For a fixed partial pressure the growth rate has a strong dependence on particle size:

$$\frac{dn}{dt} \propto r^{-6} \tag{2.4}$$

thus for example assuming 25-nm particles the coagulation rate drops down to 1 $cm^{-3} s^{-1}$.

Hunten et al. (1980) developed the work done by Rosinski and Snow (1961) investigating the mechanism of further agglomeration of the tiny smoke particles. They assume an extraterrestrial mass influx of $10^{-16}\ g \cdot cm^{-2} s^{-1}$ into Earth atmosphere, and a mass median weight of 10 μg (corresponding to a particle of radius 100 μm and density $\rho = 2.0$ g/cm^3). They calculate ablation vertical profiles for several values of entry velocities of meteoroids, in the range $12 < v < 70$ km/s, assuming a mean boiling temperature of 2100 K; when the meteoroid reaches the boiling temperature

during atmospheric entry, the mass loss becomes appreciable; smoke particles with radii 1.3 nm are produced; this value is a bit greater than that estimated by Rosinski and Snow (1961) of 0.5 nm; Hunten et al. (1980) assume for smoke particles a lower limit of 0.2 nm. The ablation profiles show that the maximum production rate of smoke particles occurs at an altitude between 70 and 90 km; the peak of mass loss shifts at higher altitudes for increasing entry velocity: for a 14 μg meteoroid entering the atmosphere at 15 km/s the vaporization occurs at 85 km; for a meteoroid with the same mass and entry velocity 40 km/s the vaporization occurs at 100 km; below 15 km/s a large fraction of the meteoroid does not vaporize [40]. The maximum radius for which a meteoroid does not vaporize, that is for which the temperature reached is lower than the vaporization (melting) temperature T_m is given by Whipple (1951), eqn. 2.2 [40, 89]. For a meteoroid with $v_\infty = 12$ km/s we have $r_{max} = 111$ μm, while for a meteoroid with $v_\infty = 20$ km/s we have $r_{max} = 24$ μm. Smoke and dust concentration have been also calculated by Hunten et al. (1980): they assume that below 35 km dust concentration may be depleted by aerosol scavenging. The net flux of aerosol particles from troposphere to stratosphere is estimated as 2×10^{-15} g$\cdot cm^{-2}s^{-1}$, while the meteoric mass influx is estimated as 10^{-16} g$\cdot cm^{-2}s^{-1}$, so meteoric mass might amount to about $\sim 5\%$ of total aerosol mass. Assuming initial smoke particles of ~ 1 nm the concentration in mesosphere and upper stratosphere is of the order of $10^3 \div 10^4$ particles$\cdot cm^{-3}$, in agreement with Rosinski and Snow (1961) [40, 78]. The further agglomeration and coagulation of 1 nm smoke particles can be affected by several physical factors. If the smoke particles are singly charged then the coagulation is highly inhibited, while if they are not charged the coagulation occurs. Van Der Waals forces may enhance the coagulation, and also the presence of micrometeorites can facilitate the agglomeration, but only for smoke particles > 10 nm. On the contrary eddy diffusion hinders coagulation. Hemenway et al. (1961) in their work describe the collection in stratosphere (at 18 km) of numerous nanometer-sized particles, to which they attribute an extraterrestrial origin [39]. These *nanometeorites* have a mean size of 7.5 nm, are clustered and are mainly composed by nickel monoxide (NiO) and taenite γ-(Ni,Fe); a background material composed of NiO and FeO was collected together with nanometeorites. Such particles seem to be the meteor smoke particles described by Rosinski and Snow (1961) and Hunten et al. (1980).

More recently Mateshvili et al. (1999), using the twilight sounding method (TSM) have possibly detected condensed meteor dust, likely correlated to the 1998 Leonids meteor shower. From the detection of two meteor dust layers at altitudes of 93 km and 30 km they infer that dust particle sizes are in the range 20-80 μm for the layer at 30 km, and in the range 6-60 nm for the layer at 93 km, depending on the

assumptions made on the particle density [55].

Testa et al. (1990) suggest that besides the vaporization of meteoroids and recondensation into sub-micrometer particles, another contribution to particles $< 0.1\ \mu m$ arises from the breakup in atmosphere of interplanetary dust particles (IDPs); indeed a major class of IDPs consist of porous, fluffy and loose aggregates of sub-micron grains, that breakup during the atmospheric entry [87].

The vaporization of extraterrestrial materials inject in mesosphere meteoric metals which fate is not clear yet. For example meteoric metals could aggregate into small ($<$ 10 nm) grains and act as condensation nuclei for ice particles in noctilucent clouds at $\sim$ 85 km altitude; moreover these injected metals could react with atmospheric components or produce sporadic mesospheric Ca^+, Na and Fe layers [72]. Recondensed particles from meteoric vapours as predicted by Rosinski and Snow (1961) are very difficult to detect. Such meteoric dust could also be collected by IDPs that descent through the mesosphere and stratosphere, and so they can act as terrestrial contamination (of extraterrestrial origin) of cosmic particles. Rietmeijer (2001) suggests a scenario in which mesospheric iron of meteoric origin could have contaminated IDPs collected by the NASA Cosmic Dust Program, using aircrafts in the lower stratosphere (17-19 km), and stratospheric particles collected by Testa et al. (1990) in the upper stratosphere (34-36 km). Analyzing these IDPs Rietmeijer (2001) found goethite (α-FeOOH) laths and nanocrystals, maghémite (γ-Fe_2O_3) and hematite (α-Fe_2O_3) nanocrystals, whose possible origin is the following. After the vaporization of meteoroids, the reaction of meteoric iron with ozone rapidly produces FeO. The iron oxide reacts with ozone, oxygen, carbon monoxide and water to give the products:

$$\mathrm{FeO} + \mathrm{O_3} \implies \mathrm{FeO_2} + \mathrm{O_2} \tag{2.5}$$
$$\mathrm{FeO} + \mathrm{O_2} + \mathrm{N_2} \implies \mathrm{FeO_3} + \mathrm{N_2} \tag{2.6}$$
$$\mathrm{FeO} + \mathrm{CO_2} + \mathrm{N_2} \implies \mathrm{FeCO_3} + \mathrm{N_2} \tag{2.7}$$
$$\mathrm{FeO} + \mathrm{H_2O} + \mathrm{N_2} \implies \mathrm{Fe(OH)_2} + \mathrm{N_2} \tag{2.8}$$

but the iron bi-hydroxide $Fe(OH)_2$ is also converted into iron hydroxide by:

$$\mathrm{Fe(OH)_2} + \mathrm{H} \implies \mathrm{FeOH} + \mathrm{H_2O} \tag{2.9}$$

All these iron species, FeO_2, FeO_3, FeOH and $Fe(OH)_2$ can condensate and act as

condensation nuclei, onto which water ice can agglomerate. Condensation experiments from a mixture of Fe, SiO, H_2 and O_2 vapours show the formation of FeO·SiO crystals and maghémite crystals (γ-Fe_2O_3) 50 nm in size [72]. These maghémite nanocrystals react with water ice and produce goethite:

$$\gamma\text{-}Fe_2O_3 + H_2O_{(ice)} \Longrightarrow 2FeOOH \tag{2.10}$$

The goethite is converted into hematite:

$$2\alpha\text{-}FeOOH \Longrightarrow \alpha\text{-}Fe_2O_3 + H_2O \tag{2.11}$$

Thus meteoric iron can be enclosed in goethite and then in iron oxides as maghémite and hematite; the fact that these iron species nanocrystals have been found attached to stratospheric IDPs could be evidence of stratospheric contamination: IDPs have residence times of weeks or months, thus during the slow descent trough the mesosphere and stratosphere they can "collect" atmospheric contamination such as meteoric dust [72].

Murphy et al. (1998), using a laser ionization mass spectrometer (PALMS) on board a high altitude aircraft, have detected meteoritic material in aerosol layers up to 19 km, mostly meteoritic iron. Their aerosol measurements are consistent with very homogeneous small particles, similar to what is expected from meteor smoke condensation [58]. Cziczo et al. (2001) have used the same instrument (PALMS) to obtain stratospheric aerosol spectra; moreover they reproduced in laboratory stratospheric aerosol analogues, dissolving in two different H_2SO_4 solutions chondritic meteorites and 'artificial meteorites' containing iron and other elements. These laboratory simulations, consisting with in-situ measurements on aerosol, showed that a great amount of stratospheric aerosols ($\sim$ 50%) contain $\sim$ 0.75 wt% of iron of meteoritic origin [17].

Interplanetary Dust Particles (IDPs) in the stratosphere

IDPs entering the Earth atmosphere are decelerate from few km/s to few m/s, at altitudes 120-80 km, then slowly descent ($\sim$ cm/s) through the mesosphere and settle in upper and middle stratosphere. Brownlee et al. (1976) collected stratospheric particles and identified essentially two types of extraterrestrial particles, in the range $2 < d < 20\ \mu m$, the identification being based upon both grain morphology and

composition [8]. FSN particles are iron sulfides with a percent of nickel, and are in the range $> 5\ \mu m$; about 50% of these particles are spherical, and they could be meteor ablation debris. The composition of these iron sulfides is consistent with troilite or pyrrhotite (FeS) with $1 - 5\%$ of Ni, and is similar to primitive meteorites (CM and CV meteorites). Meteor ablation droplets are characterized by a spherical shape, sulphur depletion and the presence of small magnetite grains or rims, similar to meteorite fusion crusts. Other grains are chondritic particles, which abundance of Fe, Si, Ca, Mg, Ni and S are similar to that of chondritic meteorites (carbonaceous chondrites, CI). Only 10% of chondritic particles are spherical, while most of them are irregular aggregates of very small spherical grains ($100 < d < 1000$ nm); this fact suggests that these particles could have not been subject to a strong thermal heating, thus they might have not been altered. These fluffy and irregular grains are often filled with a carbonaceous content, which gives them a very dark appearance under the optical microscope. The agreement between chondritic particles and chondritic meteorites is an evidence that these grains could really be extraterrestrial, though if not with the same origin.

Based upon measurements of the morphology of microcraters observed on lunar rocks, Brownlee et al. (1973, 1976) suggest that micrometeorites are mainly spherical and have density in the range $1 < \rho < 4$ g/cm^3, excluding both non-spherical irregular micrometeorites and low density (< 1 g/cm^3) particles [7, 8]. It is instead accepted today that IDPs are mainly irregular and aggregate particles, and also very low density particles (< 0.6 g/cm^3) have been detected [9, 46].

Chondritic particles with low content of filling material between grains have large porosity and density ~ 1 g/cm^3, while aggregates with a sufficient content of filling carbon have density ~ 2 g/cm^3. The abundance of fine dispersed carbon filling the small grain aggregates is $\geq 4\%$. The fact that interplanetary dust particles and CI-CM meteorites could have similar elemental abundances does not imply a common origin, but could be a clue that both these type of particles have been condensed starting from a gas of cosmic composition [8, 10].

For example primitive meteorites contain inclusions such as chondrules, calcium aluminum inclusions, glass and olivine that are believed to be formed in the inner and hotter Solar Nebula within ≤ 5 AU from the Sun. Most of interplanetary particles instead are believed to be of cometary origin, and if so they condensed and aggregated in the outer regions of the Solar System; thus the search for such inclusions could be a distinctive criterion [8, 10].

Meteoroids from objects with high eccentricity and high inclination orbits, like comets, Oort Cloud objects and near-Earth asteroids (Aten-Apollo-Amor) usually enter the Earth atmosphere with high velocity, > 20 km/s. These high velocity me-

teoroids ablate mainly in the lower termosphere and upper mesosphere. Typically meteoroids from objects on circular and low inclination orbits, such as main-belt asteroids and Kuiper belt objects, penetrate in the Earth atmosphere with low velocity, < 11 km/s. These small entry velocity objects ablate lower in the atmosphere, mainly in lower mesosphere and upper stratosphere [71].

Flynn & Sutton (1991) have measured the density of 12 cosmic dust particles collected in stratosphere by the NASA JSC Cosmic Dust Collection Program. These IDPs show a bimodal density distribution, with the evidence of two populations of cosmic dust particles, having mean densities 0.6 g/cm^3 and 1.9 g/cm^3. Higher density particles are subject to a slower orbital evolution in the interplanetary space, because of the Poynting-Robertson effect ($t_{evol} \propto a\rho$, see eq.1.6); low density particle orbits instead evolve more rapidly. Thus high density particles have major probabilities of being trapped into gravitational resonances, while low density particles are expected to fall in the Sun and also to arrive at Earth sooner. Moreover, high density particles will experience a strong atmospheric heating; on the contrary low density and fluffy particles will not be subject to total melting during atmospheric entry [32]. Main-belt asteroid IDPs are usually heated up to 700°C during atmospheric entry, comets with perihelion at > 1.2 AU are heated at $600 - 800$°C, and comets with perihelion at < 1.2 AU are heated at > 800°C [31]. Determining solar flares tracks (which are deleted above 600°C), the noble gases abundance and the presence of volatile elements can give clues for the peak temperature experimented by the IDPs during atmospheric entry, and thus it is possible to obtain information about the sources of IDPs (Flynn, 1989). Nier and Schlutter (1990) using the Flynn model (1989), have observed a high ^{4}He concentration in several stratospheric IDPs, consistent with a low peak temperature experimented by particles during the descent in atmosphere. Entry velocities of IDPs can be determined measuring the step He-release profile for each particle; He ions are indeed implanted by the solar wind into the structure of IDPs during their sojourn in the interplanetary space; when these are heated during atmospheric entry, they stepwise release He at several temperatures. Thus measuring in laboratory the He-release profile for IDPs, it is possible to establish the peak temperature that particles have experimented, and so to determine their entry velocities [59]. They conclude that these IDPs could have low entry velocities, likely of asteroidal origin [59]. Joswiak et al. (2007), analyzing 31 stratospheric IDPs and following the Flynn model (1989, 1991), suggest a quantitative criterion to discriminate between asteroidal and cometary IDPs entering the atmosphere. Particles with low entry velocities (< 14 km/s) are of *asteroidal* origin, while particles with high entry velocities (> 18 km/s) are of *cometary* origin. Asteroidal IDPs originate from collisions between main-belt asteroids: these particles then

orbit on circular orbits with low inclination, thus they encounter the Earth at low average relative velocity. Cometary IDPs originate from the surface of comet nuclei during outgassing and sublimation because of the heating of the Sun. Joswiak et al. (2007) also determined the densities for such 31 stratospheric IDPs. The mean density for cometary IDPs is 1.0 g/cm^3, while the mean density for asteroidal IDPs is 3.3 g/cm^3. This measure is consistent with an asteroidal IDPs mineralogy characterized by hydrated Fe,Mg-silicates, whose structure is not porous and more compact; and it is consistent with a cometary IDPs mineralogy characterized by anhydrous silicates and GEMS, with a porous structure.

Interstellar grains in the stratosphere

Because of the motion of the Solar System across the interstellar medium, interstellar atoms and grains can penetrate into our planetary system and thus into the Earth atmosphere, where they have residence times of about 6-8 weeks.
Considering that the heliocentric velocity of the Earth is 30 km/s, the velocity of the flux of interstellar grains in the Solar System has to be added or subtracted to the Earth velocity depending on the period of the year; the two velocities must be subtracted when the Earth is moving in the same direction as the interstellar flux, and thus the relative velocity is minimum; hence the entry velocity of interstellar grains in the Earth atmosphere is modulated during the year, of a factor ± 30km/s. The Earth velocity varies as $\cos\theta t$, where $\theta = 360°/yr$.

The atmospheric entry velocity of interstellar grains can be estimated as follows, using the measurements from Ulysses and Galileo spacecrafts. The grain heliocentric velocity at 1 AU is obtained from the conservation of energy between 4 AU and 1 AU from the Sun, and is:

$$v_{1AU} = [v_{4AU}^2 + 2GM_\odot(1/r_1 - 1/r_4)]^{1/2} = 44.8\ km/s \tag{2.12}$$

The minimum geocentric velocity is:

$$v_{geo} = v_{1AU} - 30\ km/s = 14.8\ km/s \tag{2.13}$$

Finally the atmospheric entry velocity is given by:

$$v_{entry} = (v_{geo}^2 + v_{esc}^2)^{1/2} = 18.6\ km/s \tag{2.14}$$

where $v_{esc} = 11.2$ km/s is the escape velocity from Earth. The atmospheric entry velocity of interstellar grains is lesser than the typical entry velocity of many IDPs. In a period of about 6-8 weeks centered at August the relative velocity is minimum and almost constant, and the interstellar grains suffer a minor thermal heating during the atmospheric entry; silicate grains in the size range 0.5-1 μm, density 1-3 g/cm^3, emissivity $\epsilon = 1$ entering the atmosphere with $v = 18.6$ km/s, show that they are not heated at temperatures $T > 600$ K; at this temperature silicate grains are subject to minimum thermal modifications. When the emitted radiation has a wavelength comparable to the particle size, $\lambda \sim a$, the emissivity ϵ decreases and becomes < 1: the grains don't emit efficiently the stored heat during the atmospheric entry and can alter thermally. Nevertheless also assuming $\epsilon = 0.1$ as a lower limit, the grains are not heated above 1200 K; moreover smaller entering grains are further decelerated by the solar radiation pressure. Assuming an interstellar grain flux in the Solar System, at 4-5 AU, $F_{IS} = 1.5 \times 10^{-8}\ cm^{-2}s^{-1}$, an average grain mass $m \sim 3 \times 10^{-13}$ g and a diameter of 0.5 μm, a mass influx of 4.2×10^{-21} g$\cdot cm^{-2}s^{-1}$ is obtained as incident on the Earth projected disk ($\pi R_{\oplus}^2$), that is, an interstellar mass influx of 5.75×10^{-3} g/s. The total influx of cosmic (interplanetary and interstellar) particles of size $\sim 10^{-13}$ g entering the Earth atmosphere has been estimated as ~ 0.02 g/s, thus comparing this value with the amount of interstellar grains we can infer that approximately 25% of the cosmic particles entering the Earth atmosphere have an interstellar origin. The concentration of interstellar grains in the Earth stratosphere can be estimated as follows. The concentration of interstellar grains in interplanetary space is:

$$c_{space} = 5.8 \times 10^{-9}\ m^{-3}$$

as measured by Ulysses and Galileo probes, see section 1.2.5. These grains, assuming a size of 0.5 μm, have a velocity in space, at 4-5 AU, $v_{space} = 26$ km/s, while in the stratosphere at 35-40 km have the settling velocity $v_{settl} = 6.9 \times 10^{-4}$ m/s; thus the deceleration factor from 100 to 35-40 km of altitude is $v_{space}/v_{settl} \approx 3.8 \times 10^7$, and hence the number density of interstellar grains in stratosphere is obtained multiplying the deceleration factor by the concentration in space:

$$c_{strato} \approx 0.22\ m^{-3}$$

Large meteoroids

Klekociuk et al. (2005) report the disintegration of a very large meteoroid in the upper stratosphere on 3 September 2004, with physical parameters, estimated by satellite observations, $d \approx 10$ m, $\rho \approx 3500$ kg/m^3 and $m \sim 10^6$ kg. The meteoroid was detected at an altitude of 75 km, and two disintegration features were revealed at an altitude of 32 and 25 km. Lidar observations at Davis Station in Antarctica detected an anomalous cloud (too warm and at higher altitude compared to typical PSCs) that was associated to the disintegration of the meteoroid. Klekociuk et al. (2005) suggest that the disintegration of meter-sized meteoroids in the upper stratosphere produce large amounts of debris mainly in the micrometer-size range, than in the sub-micrometer one, which then settle in the stratosphere with residence times of weeks to months, and so this process could yield the major contribution of micrometer-sized cosmic dust in the stratosphere [49].

Borovicka and Charvát (2009) analyzing the satellite observation of the fireball due to the disintegration at 45 km of the meter-sized asteroid 2008 TC_3, found that two dust clouds deposited at 44 and 36 km. From the IR spectra these dust clouds, of total mass 3×10^3 kg, appeared to be consisting of nanometer-sized recondensed silicate smokes [6].

Clues for an extraterrestrial origin

There are several criterions to discriminate between the terrestrial or extraterrestrial origin of a particle collected in stratosphere.

Morphology. A preliminary morphological observation of collected particles could be useful to discriminate, in some cases, terrestrial from extraterrestrial particles, for examples it is possible to distinguish soot, IDPs, smooth fragments, ablation spheres.

Iron to nickel ratio. The average cosmic Fe/Ni ratio is 20; chondritic IDPs have an average Fe/Ni ratio ~ 20; the range of cosmic values is between 18.3 (interstellar dust) and 26.4 (solar photosphere). For comparison, values of Fe/Ni ratio for volcanic samples are in the range $2 - 126$, while the average ratio for Earth crust is ~ 750 [71, 74].

CI-Chondritic composition. The CI-chondritic composition today is accepted to be the bulk composition of the solar nebula. Collected particles with a chondritic bulk

composition thus are likely of extraterrestrial origin. Most of collected stratospheric particles have carbonaceous chondritic CI and CM composition, while only $< 3\%$ of meteorites have CI-CM composition; this could be ascribed to a major alteration for meteorites than for IDPs [10, 73]. Although an IDP can have a non-chondritic bulk composition, there can be chondritic material adhering to the surface: this is a clue for extraterrestrial origin.

Isotopic ratios. Several isotopic ratios can give clues for an extraterrestrial origin [59]. For example the average $^3He/^4He$ ratio for collected IDPs is 2.4×10^{-4}, for the solar wind is 4.3×10^{-4}, for lunar soil samples is 4.0×10^{-4}; the atmospheric helium instead has the abundance 1.4×10^{-6}, and for meteorites it is ~ 0.3. The average $^{21}Ne/^{22}Ne$ measured for IDPs is ~ 0.03, similar to the solar value; for meteorites it is ~ 1. The average $^{20}Ne/^{22}Ne$ measured for IDPs is 12.0, similar to the average solar wind value of 13.7. Isotopic anomalies measured for the elements O (^{16}O, ^{17}O, ^{18}O ratios), Mg (^{24}Mg, ^{25}Mg, ^{26}Mg) and Al (^{26}Al and ^{27}Al) in collected particles could be clues for an extraterrestrial origin.

Solar flare tracks and ions. Because of their sojourn in the interplanetary space, collected IDPs can show solar flares tracks due to the interaction with solar wind and energetic particles; ions and atoms are implanted into the voids of the grain structure [31, 46, 59]. Solar flare tracks are recorded in Mg-rich olivines, pyroxenes; they disappear when heating the IDPs above 600°C. The dissipation of kinetic energy can also produce amorphous rims, amorphization of crystals and magnetite (Fe_3O_4) [73]. Rare gases (He, Ne, Ar) are typically implanted into IDPs by this interaction [10, 73]. Since usually solar wind ions are implanted into a few angstroms depth on the surface of interplanetary dust particles, this is also a clue that most of IDPs are not fragments of larger bodies but individual cosmic particles [9].

Flash heating. During the $5 - 15$ s flash heating due to atmospheric entry, on the surface of an IDP several morphological features can form, such as a 100-nm thick rim of Fe-oxides (for example magnetite) or melting [73].

2.2 *Sample return* experiments

The first direct collection of stratospheric aerosols was performed in 1961 by Junge. The collector consisted in inertial jet impactor (cascade impactor); the collection area was a specially coated gummed slide, and the cascade impactor allowed the size grading through successively finer jets. The instrument was constituted substantially

by a motor-driven rotary air pump, that drew air and particles through the jet impactors. Several large diameter inlet tubes were mounted vertically upon the instrument; the collector used was suitable for microscopy examination and chemical investigation of collected samples. Junge collected aerosol particles in the range $0.1 < r_p < 10\ \mu m$ at an altitude of up to 30 km using a stratospheric balloon [47].

Hemenway et al. (1961) reported the sampling of stratospheric nanometeorites (see section 2.1.3), using four collection surfaces exposed on a U-2 aircraft at 18 km altitude. The collection surfaces were coated with a *Formvar* film 7 nm thick, supported by a copper screening with 200 mesh/in, and were suitable for direct electron microscope analysis without any chemical treatment after exposure [39].

In the 1970's many *sample return* experiments were performed. Bigg et al. (1970) collected aerosol particles using a balloon-borne instrument between 20 and 37 km. A solenoid operated vacuum pump, with constant flow rate above 25 km, drew air and particles through a 1 mm diameter inlet onto a 3 mm diameter electron microscope grid; the collection grid was coated with carbon film and thin nitrocellulose, and was protected by baffle plates from contamination. The pump was turned on when the balloon was at float altitude, then was turned off once the payload was cut down. A 35 mm camera photographed the horizon in order to monitor the altitude at which sampling occurred.

Brownlee et al. (1973, 1976, 1979) performed several collections in low and middle stratosphere, using a balloon-borne inertial impactor for collection up to 34 km, and mounting the collector on a NASA U-2 aircraft for collection at 20 km. The stratospheric particles were deposited onto an oil-coated collection surface [8].

Testa et al. (1990) sampled stratospheric particles at $34 \div 36$ km using balloon-borne collectors [87]. Collected particles were in the range $0.045 < r_p < 10.0\ \mu m$. The collector consisted of several "stacks", each formed by a 25 mm diameter Nucleopore Membrane Filter (NMF) used as impact surface and a 0.2 μm pore NMF used as a filter; a "Battelle" impactor of 2.63 mm diameter allowed the air jet to flow onto the impact surface (fig. 2.5). Three stacks were used: a "SEM stack", for Scanning Electron Microscopy analyses, a "TEM stack", for Transmission Electron Microscopy, and a "Blank stack", for the contamination control; the SEM and TEM stack were attached to pumps, while the Blank stack was not. The SEM stack and Blank stack comprised an NMF used as impact surface and an NMF used as filter; the TEM stack consisted of nine berillium TEM grids, coated with holey carbon film and attached to an NMF impact surface. All the stacks were placed inside the stainless

steel "Cosmic Dust Collector", and sealed by a plate that was opened only at float altitude for sampling. These collectors were suitable to perform direct analysis on samples with SEM/TEM, thus allowing minimization of post-flight manipulation, handling and contamination [87].

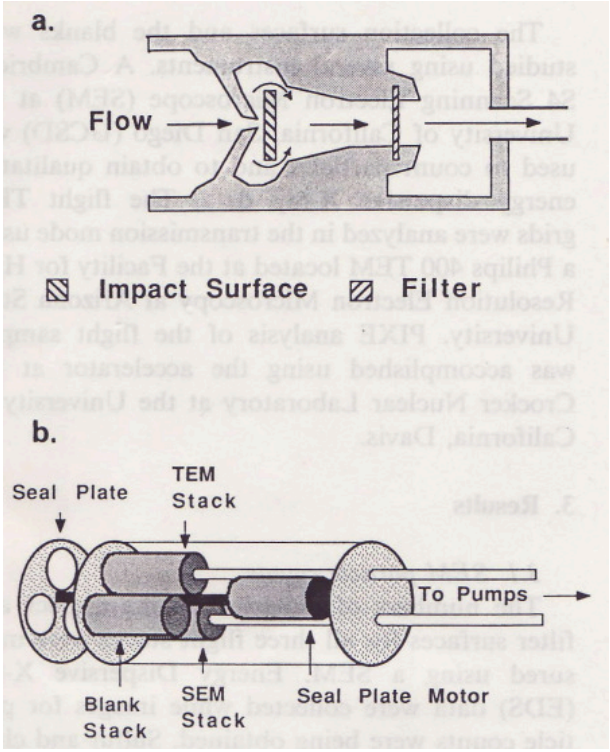

Figure 2.5: *The collector used by Testa et al. (1990). a) the air flow, the NMF impact surface and the NMF filter; b) the SEM, TEM and Blank stacks [87].*

Iwasaka et al. (1992) collected stratospheric particles with a balloon-borne impactor, in the Polar Winter stratosphere from Kiruna (North Sweden), in the altitude range from 10 km (troposphere) to 30 km (middle stratosphere). The impactor consisted in a 2 mm diameter jet nozzle, and the air was sampled with a 10 l/min flow rate. They collected mainly sulfate aerosols, with the typical droplet-satellites morphology of sulfuric acid particles (Junge et al. (1961), Bigg et al. (1970)), and also NAT particles [42].

Wu et al. (1994) reported collections of stratospheric aerosol particles carried in 1993 over Japan, two years after the Pinatubo volcanic eruption. They used a 0.5 mm diameter jet impactor, the collection substrate being a carbon-covered nitrocellulose

film. Collected particles were analyzed by analytical electron microscope equipped with EDX analyzer. The particles were sampled at altitudes up to 25.8 km. Most of collected particles were in the size range $d < 2\ \mu m$, were characterized by the typical morphology of liquid droplets surrounded by satellite rings and contained sulphur, thus were identified as sulfuric acid droplets; an aerosol layer between 16 and 21 km was confirmed by lidar measurements. Laboratory irradiation of these collected particles with an intense electron beam showed that they had not solid nuclei, thus suggesting homogeneous nucleation as origin [91].

Okada et al. (1997) developed a small and light balloon-borne particle sampler, which collected aerosols in the troposphere and lower stratosphere up to 28.6 km. The sampler (< 1 kg) comprised two impactors, each consisting of a 0.5 (or 1.0) mm diameter impact jet; below the impact jet an electron microscopic grid was kept by a holder; the two impactors were connected to a diaphragm pump, whose measured flow rate was 3.1 l/min at 20 km. The grids, used as collection substrates, consisted of a nitrocellulose thin film coated with carbon, and were suitable for direct analysis with electron microscope equipped with an energy dispersive X-ray analyzer (EDX). In order to perform sampling at different altitudes from ground up to lower stratosphere, 16 grids were mounted upon a 30-mm diameter disk, whose rotation was temporized allowing the collection on each grid at every atmospheric layer of 2 km thickness for a few minutes; the total sampling time was about 100 min. The timer for temporization was activated by a second disk containing 16 sticks whose rotation, synchronous with the grid disk, interrupted a light signal between a LED and a sensor; the electrical signal from the light sensor was used by the timer. Another timer controlled the total sampling time, determining the switching on/off of the pump and of the valve for sealing the impactors. They collected 552 and 71 particles on the substrates of the two impactors (0.5 and 1.0 mm diameter jets respectively), finding that particles collected in the lower stratosphere in the size range $0.03 < r < 1.0\ \mu m$ are predominantly sulfuric acid droplets [60].

Xu et al. (2001 paper) performed collection of stratospheric aerosols over China in 1993, using a balloon-borne impactor. The substrate for the collection was a TEM grid supporting a carbon-coated nitrocellulose thin film. The jet diameter of the impactor was 2 mm and the flow rate was 22 l/min; the collection from balloon lasted 90 min from 2 to 34 km. An optical particle counter was used to obtain vertical profiles of aerosols from troposphere to middle stratosphere. Collected particles were analyzed with transmission electron microscope, EDX analyzer and scanning electron microscope for morphology; before the TEM analysis the particles were coated with a Pt/Pd alloy, to obtain a shadow of the particles in order to determine their size.

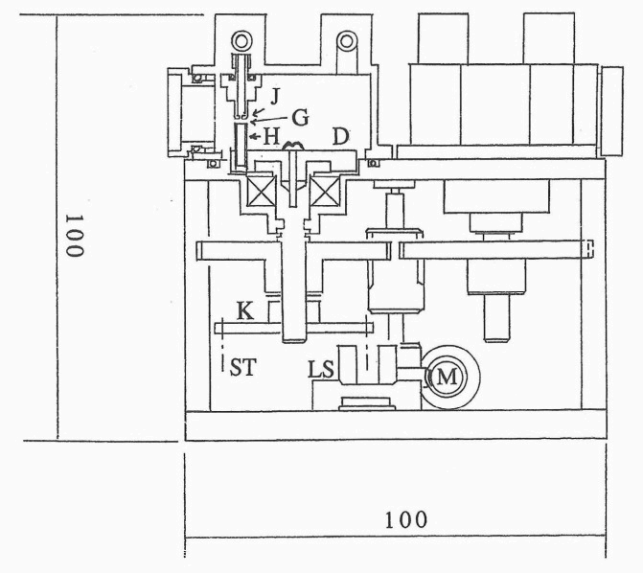

Figure 2.6: *The collector used by Okada et al. (1997), size section. J: impactor jet; G: electron microscopic grid; H: grid holder; D: grids disk; K: second disk for temporization; ST: stick; LS: light sensor; M: valve motor [60].*

They collected several types of particles in the size range $0.07 < r < 15\ \mu m$; particles collected were sulfuric acid droplets with satellite rings, mineral particles embedded in sulfuric acid, minerals, soot and also sea salt particles at 16-18 km altitude. Most of collected particles both in troposphere and in stratosphere (up to $21.2 km$) were S-rich particles and minerals ($\sim$ 97% in number). They also found "S+K" rich particles in troposphere and lower stratosphere, perhaps originated from burning processes [92].

Chapter 3

DUSTER project: Dust in the Upper Stratosphere Tracking Experiment and Retrieval

3.1 The project

The DUSTER instrument (*Dust in the Upper Stratosphere Tracking Experiment and Retrieval*) has been designed to perform *sample return* of stratospheric solid aerosols [15, 16, 20, 61]; after collection dust particles are returned in laboratory for subsequent analyses with different techniques. The main goal of this project is the collection of stratospheric dust particles of extraterrestrial origin, that is, interplanetary dust particles and interstellar dust. DUSTER collects particles in the upper stratosphere, at an altitude of $30 \div 40$ km ($3 \leq p \leq 6$ mbar). It is a balloon-borne instrument: it is designed to flight on board a stratospheric balloon, both for dedicated flights, with light balloons, and as *piggyback* instrument, hosted on large gondolas carrying on many scientific instruments, with great balloons. The size range of particles is about $0.1 \div 100$ μm. The measured flow rate is $Q \geq 1$ m^3/h (see section 3.5), so it needs some hours to sample $10 \div 20$ m^3 of air in order to collect few hundreds of aerosols (and finally few tens of cosmic particles). The balloon flight assures sampling at stratospheric altitudes (≈ 40 km) higher than those reachable by aircraft (≈ 20 km): in this way it is possible to collect micrometeorites in a smaller size range and in higher fraction with respect to terrestrial aerosols. The sampling on-board balloon moreover is non-destructive, because of the low relative velocity between the

particles and the collector, and non-contaminant, because of the lack of fuel exhaust. Several and complementary laboratory analyses are planned to study collected samples: FE-SEM (*Field Emission Scanning Electron Microscopy*) imaging for particles morphology and EDX (*Energy Dispersive X-ray*) Spectroscopy for elemental analysis [15, 16]; IR and Raman spectroscopy for mineral detection and chemical composition (see chapter 5 and also [19]): these are non-destructive analyses that still preserve the samples; finally destructive analyses are scheduled such as TEM (*Transmission Electron Microscopy*) and isotopic analyses. Analyses on collected particles can give informations about size distribution, physical structure, chemical composition, isotopic abundance, stratospheric residence times of solid aerosols; data are also useful for a better characterization of solid aerosols as they influence the homogeneous and heterogeneous reactions in atmospheric chemistry and hence the climate evolution (see chapter 2). The DUSTER instrument has been realized at the "Cosmic Physics Laboratory" of Applied Science Department, "Parthenope" University, Naples. Several versions of the instrument have been realized: the prototype instrument, for a test flight in the 2006, and three versions DUSTER-2008, DUSTER-2009 and DUSTER-2011, that performed scientific flights (see section 3.8).

3.2 Instrument description: hardware

The instrument uses the *inertial deposition* mechanism to collect particles; its main part is a pumping system, thanks to which the instrument aspirates air from the surrounding ambient. Particles contained in the air are collected on a substrate, which looks towards the direction of the air flux. Particles that are suspended in the aspirated air can be collected by the instrument if they are in a suitable size range: they must be small enough to follow the air flux when it enters the inlet tube; nevertheless they have to be large enough and must have sufficient inertia to decouple from the air flux when it encounters the collection substrate, so that the particles can impact on it, while the air flux moves around the substrate surface. This kind of substrate is called *inertial impactor*. The hardware of the instrument [20, 61] consists of (see fig. 3.1):

- pumping system
- collection chamber
- inlet duct
- pumping line

- gate and butterfly valve
- step motors for valves
- collection and blank substrates
- temperature and pressure sensors
- control electronics
- battery pack and solar panels
- aluminium protection structure

The whole instrument (photo in fig. 3.5) has a mass $m \leq 35$ kg and is enclosed in an aluminum box of $(410 \times 310 \times 310)$ mm^3, covered with five teflon panels in order to minimize the internal heating.

3.2.1 Pumping system

The pumping system consists of six pumps connected in parallel. They are 6 carbon vane volumetric micropumps, mounted on a flange: each micropump consists of a cylinder divided into two equal separate parts along its axis; both parts behave like two empty semicylindrical adjacent chambers (*vanes*). When a micropump is supplied with $V_{supply} = 5 \div 12$ V the whole cylinder rapidly oscillates about its axis thanks to a solenoid. The external cylindrical fixed structure of the micropump has two symmetric ducts on the bottom base, each of them communicates alternatively with one of the two vanes above. The two rotating vanes move alternatively an air volume from one duct (the *vacuum* duct) to the other (the *pressure* duct or *exhaust*): the final result is that the micropump aspirates air from the vacuum duct and get out air off the exhaust. The ambient air aspirated by the pumping system enters the inlet, then follows the pumping line through the collection chamber and finally it exits through the pump exhaust. In DUSTER-2009 we used *Fur Gut* micropumps, while in DUSTER-2011 we used *Thomas, G 12/04 EB* ones. A micro-electrovalve is connected to each micropump; we used *SIRAI Z070D* electrovalves in both instruments, with $V_{supply} = \pm 12$ V. Generally an electrovalve coupled to a micropump and placed between the pumping line and the micropump itself assures that in case of malfunction of the pump, it can be switched off; in this case the other five pumps would continue to work without great loss of flow rate (see section 3.5 for tests on pumping system). We used two relative configurations of micropumps and electrovalves (see fig. 3.2).

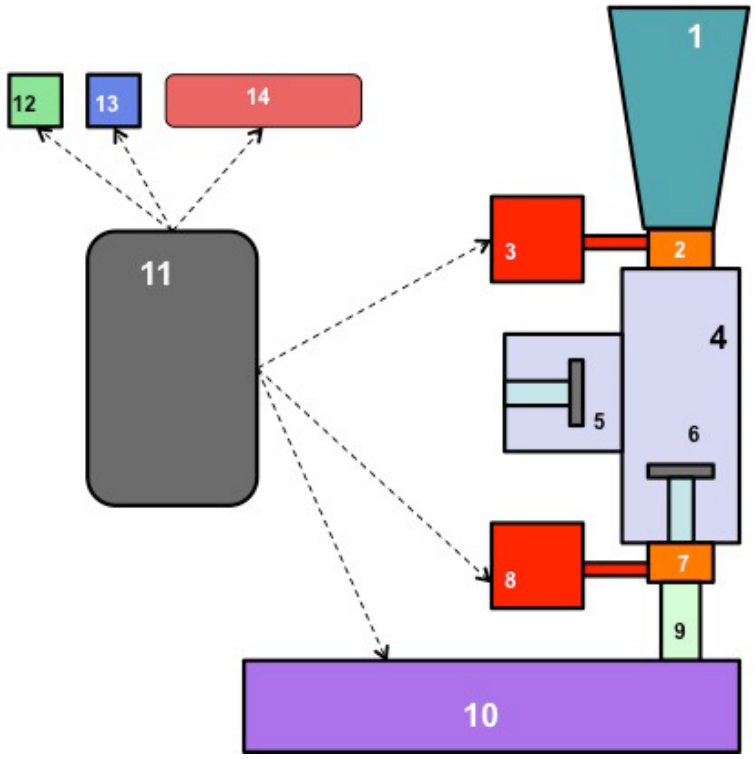

Figure 3.1: *Scheme of the DUSTER instrument as used for 2009 and 2011 flights. 1: inlet; 2: Gate valve; 3: Gate motor; 4: Collection chamber; 5: Blank substrate; 6: Collection substrate; 7: Butterfly valve; 8: Butterfly motor; 9: Corrugated tube; 10: Pumping system; 11: Main electronics; 12: Pressure sensors; 13: Temperature sensors; 14: Modem Iridium (only for 2009 flight).*

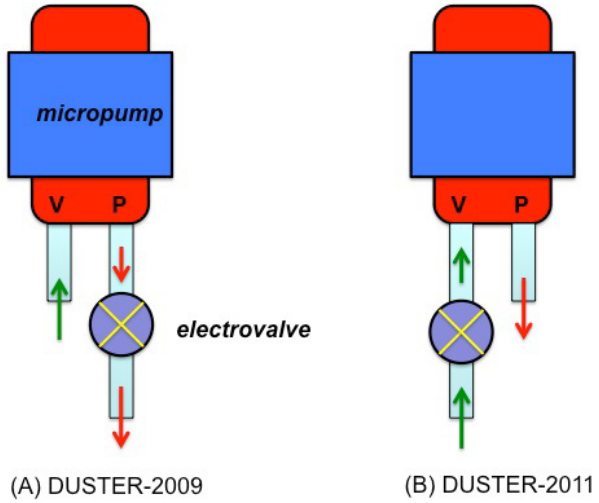

Figure 3.2: *Micropumps-electrovalves relative configuration: (A) DUSTER-2009: electrovalve on the pressure duct (output); (B) DUSTER-2011: electrovalve on the vacuum duct (input).*

In the configuration of fig. 3.2 (A) each electrovalve was connected to the pressure duct of a micropump, i.e. to its output. A malfunctioning micropump, with the electrovalve connected to the output duct and closed, would continue to pump with the total group through the inlet duct. The configuration (A) has been used in the DUSTER-2009 flight. In the new configuration, fig. 3.2 (B), each electrovalve was connected directly to the vacuum duct of a micropump, that is to its input. In this way, because of the possible malfunction of a micropump, this can be completely isolated closing the corresponding electrovalve directly on the input, so avoiding any contribution of this single pump to the total group. The configuration (B) has been used in the DUSTER-2011 flight.

3.2.2 Collection chamber

The collection chamber is realized in Ultra High Vacuum materials and standards; it is constructed in Ergal, an Al-Zn alloy. The chamber is closed at both sides by gate valves and butterfly valves; in order to minimize any contamination, these two valves are only open when the instrument reaches the sampling altitude. Inside the chamber two identical substrate are placed; one substrate, the *collector*, faces the sampled air flux, and it is used to collect particles; the other substrate, the *blank*,

lies in a secondary chamber connected on the side of the main chamber, in a direction perpendicular to the air flux; so the *blank* substrate is not directly exposed to the sampled air flux and it is used to monitor any contamination. The collection chamber is connected to the pumping system through a flexible steel fitting and a butterfly valve; on the other side, the chamber is connected to the inlet conical duct through a gate valve. These two valves are open and closed by two step motors controlled by a dedicated board of the main electronics.

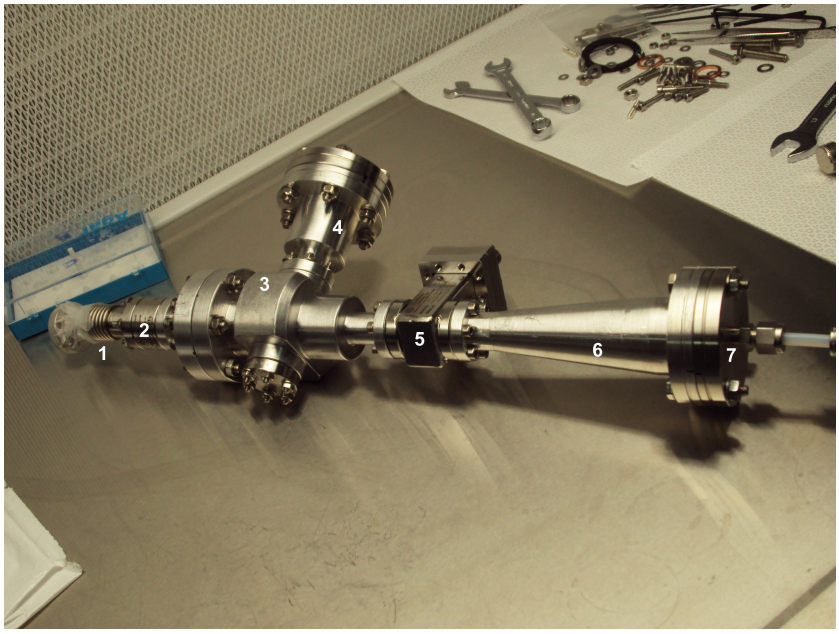

Figure 3.3: *DUSTER collection system. 1: flexible steel fitting; 2: Butterfly valve; 3: collection chamber; 4: blank chamber; 5: Gate valve; 6: inlet; 7: single shot valve.*

3.2.3 Collection substrate

The substrate (sample holder, fig. 3.4) used for DUSTER-2009 and DUSTER-2011 consists of a stainless steel round stub as base, whose dimensions are 5 mm in thickness and 23 mm in diameter; the base has a pin that allows the accommodation of the sample holder in the FE-SEM chamber of the electronic microscope; the stub holds 13 gold TEM grids, which are kept fixed by two thin plates (0.5 mm thickness) perforated with 13 holes; this configuration allows a simple assembly and disassembly procedure [15]. The gold TEM grids are covered with a holey carbon film coating,

on which collected particles are deposited. This kind of sample holder is suitable to perform laboratory analyses directly on the particles deposited on the TEM grids, avoiding any manipulation, because the sample holder only has to be removed from the collection chamber of the instrument and to be placed in the electronic microscope.

Figure 3.4: *The sample holder used for DUSTER-2009 and -2011 flights; the collection substrates are 13 gold TEM grids, covered with holey carbon film, visible inside the round holes.*

3.2.4 The inlet

The inlet pipe is the interface between the instrument and the ambient air, it sticks out of the box for few centimeters; because we want the sampling to be performed only at stratospheric altitude, and in order to minimize contamination, the inlet (at ground and during the ascent) is closed by a single shot valve, which is kept by the low pressure inside the inlet, and only move away at stratospheric external pressure.

3.2.5 Sensors

Several sensors are displaced on many parts of the instrument, both temperature and pressure sensors. Temperature sensors (*LM135*) are mounted on pumps, electrovalves, gate and butterfly valves, motors, inlet, electronics and collection chamber; they monitor the temperature level of each component of the hardware; indeed some

parts could be subject to an excessive cooling or freezing during the flight, like valves and motor, and so there could be some malfunction; the thermal monitoring allows an eventual heating of these components through heaters. On the contrary the CPU could reach a temperature too high and so has to be controlled. Two pressure sensors (*HPA - Honeywell*) read the external pressure level during the ascent, floating and descent phases of the flight, with a working range of $0 \div 121$ kPa and a precision of $\pm 0.03\%$; based on these data the instrument begin to sample only above a certain altitude, that is, below a specified threshold pressure. To monitor the flow rate through the pumping system a micro electro-mechanical systems (MEMS) pressure gauge sensor is used; it has a sensibility of 0.1 mbar. The whole instrument and sensors are managed by the main electronics, which is described in section 3.3. The power consumption of the instrument is 20 W; in DUSTER-2009 configuration a rechargeable battery used in parallel with four solar panels assured the power supply; in DUSTER-2011 configuration we did not use solar panels, but only a Li battery pack, because of the low elevation of the Sun with respect to the horizon, the planned 2011-flight being a winter one from North Sweden (see section 3.8).

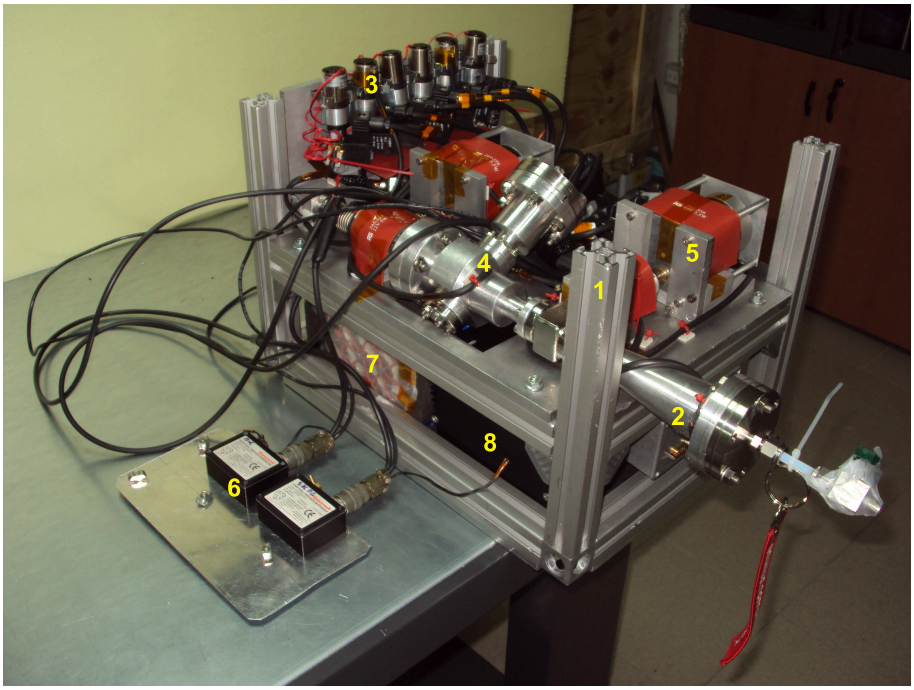

Figure 3.5: *DUSTER instrument. 1: aluminum box; 2: inlet; 3: pumping system; 4: collection chamber; 5: valve motor; 6: pressure sensors; 7: battery pack; 8: electronics box.*

3.3 Electronics

The instrument electronics consists of several boards, each dedicated to the control of some electromechanical components of the instrument hardware. The main on-board computer controls and manages all other boards: it is an SBC PC-104 (*Single-Board Computer*). SBC is a computer with a custom PC-104 small form factor, that integrates an embedded pc with a data acquisition circuit into a single board; it is larger than the PC-104-PCB format on three sides but uses the PC-104 mounting method and interface specifications. Main features of the SBC with low power CPU are:

- 4 serial ports (115.2 kbaud max);
- 4 USB 1.1 ports;
- 16 single-ended / 8 differential analog inputs, 16-bit resolution;
- 4 analog outputs, 12-bit resolution;
- 24 programmable digital I/O lines;
- needs +5 V DC power supply.

All other boards are connected to the main SBC. Two boards, PC-104 *AIM-MOTION-104*, are used to control the two step motors of gate and butterfly valves. Each AIM-MOTION board is an 8-bit PC-104 module that assures the control of single-axis movement of the motor. Another board, a pc-104 relay module, is used to switch on/off the pumps. This is a *Diamond Systems* IR104-PBF High Density Optoisolated Input + Relay Output PC-104 module, and it is based on 20 optoisolated digital inputs and 20 relay outputs to switch on/off the pumps. Finally we realized two custom boards:

- a PC-104 module for the temperature sensors conditioning and control (fig. 3.12)
- a PC-104 module for the power supply of the electrovalves (fig. 3.14)

3.3.1 PC-104 for thermometer and pump conditioning

This PC-104 module contains several circuits:

- temperature sensor conditioning;

- micropumps conditioning;
- battery and solar panels conditioning;
- multiplexer control;
- amplification circuitry.

Temperature sensor conditioning

The temperature conditioning circuit uses an LM134 as current regulator coupled to the LM135 temperature sensor (fig. 3.6). In the current regulator circuit the LM134 has a terminal connected to +5 V, and the other two terminal joined through a resistor, which is connected to the temperature sensor. The terminal of each LM135 which is connected to the conditioning circuit is then also connected to the pc for temperature reading.

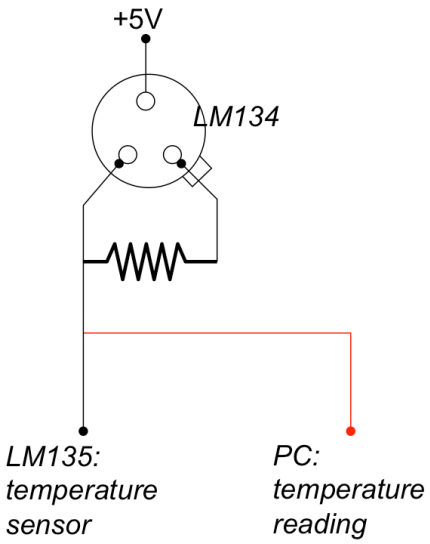

Figure 3.6: *Temperature sensor conditioning circuit.*

Pump current conditioning

The circuitry for the pumps current conditioning is in fig. 3.7. Each micropump has two terminals for power supply: one terminal is connected to $+V_{supply}$. The

negative terminal of each micropump is connected to a precision resistor (0.5 Ω) and to an input channel of the multiplexer through a fuse. The precision resistor is then connected at ground.

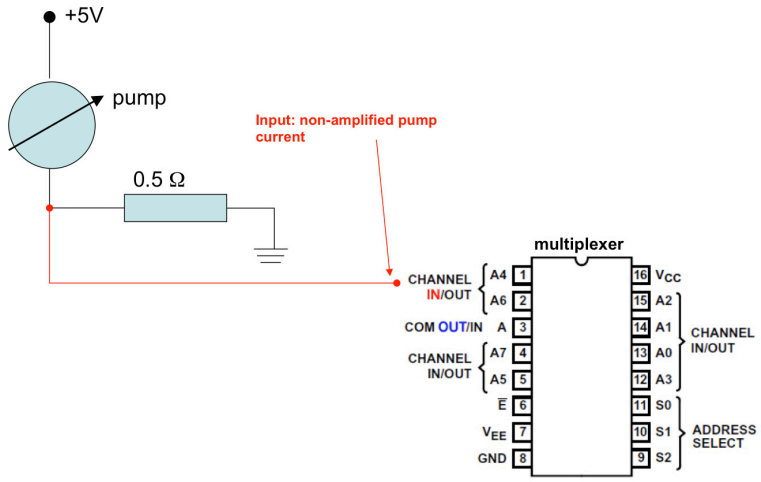

Figure 3.7: *Pump current conditioning circuit.*

Battery and solar panels conditioning

An input channel of the multiplexer is used for solar panels and battery voltage reading, thanks to a voltage divider (see fig.3.8). With reference to the two voltage dividers in figure, using $R_1 = 330\ k\Omega$ and $R_2 = 3.9\ k\Omega$ the input voltages into the multiplexer are:

$$V = V_{batt}\frac{R_2}{R_1 + R_2} \approx \frac{V_{batt}}{100} \tag{3.1}$$

$$V = V_{sol-pan}\frac{R_2}{R_1 + R_2} \approx \frac{V_{sol-pan}}{100} \tag{3.2}$$

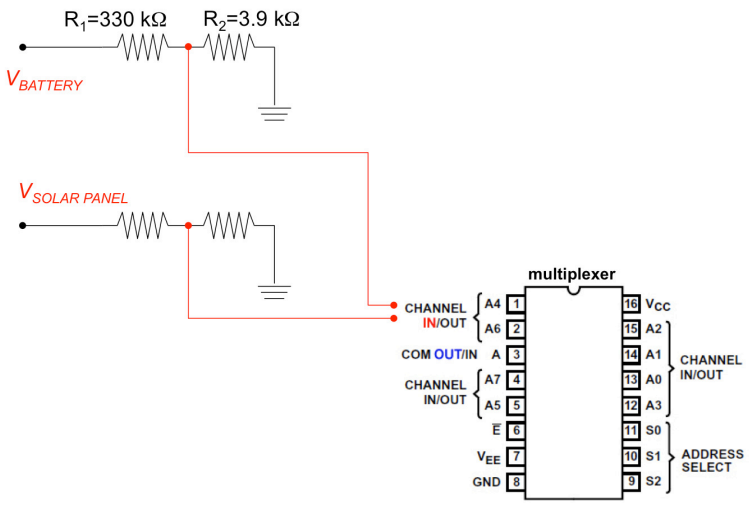

Figure 3.8: *Battery and solar panels conditioning circuit.*

Multiplexer control

The multiplexer (*CD74HC4051, Texas Instrument*) has several inputs and one output channel: four more channels $(S_0, S_1, S_2, \overline{E})$ are used, through a low-high level logic, to select the desired output; the control of the multiplexer is performed from the pc. The logic of functioning of the multiplexer is schematized in fig. 3.9.

Amplification circuit

The output of the multiplexer is then connected to the positive input terminal of an operational amplifier (*Analog Devices, AD820*), which is used in non-inverting configuration: the amplified output voltage is:

$$V_2 = 1 + \left(\frac{R_2}{R_1}\right) \cdot V_1 \tag{3.3}$$

where $R_1 = 180\ \Omega$ and $R_2 = 2.7\ k\Omega$. Finally the output of the AD820 is connected to the pc. The amplification circuit is fig. 3.10.

On the thermometers board 12 circuits for temperature conditioning and 6 circuits for pump current conditioning are mounted. A block diagram of the whole module for thermometers conditioning and of its external connections with hardware is

A

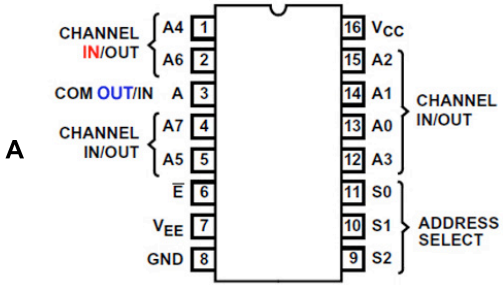

B

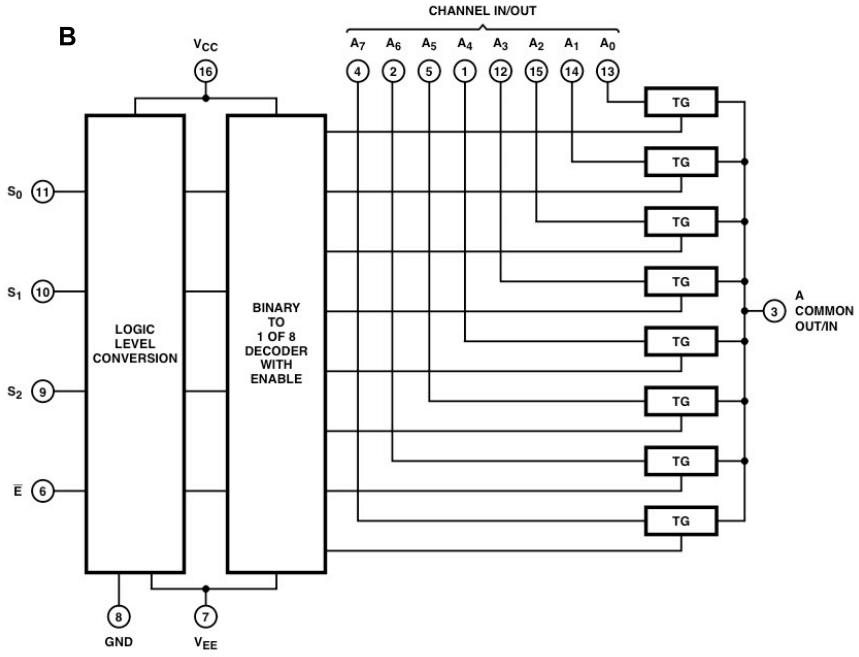

C

TRUTH TABLE
CD54/74HC/HCT4051

INPUT STATES				"ON" CHANNELS
ENABLE	S_2	S_1	S_0	
L	L	L	L	A0
L	L	L	H	A1
L	L	H	L	A2
L	L	H	H	A3
L	H	L	L	A4
L	H	L	H	A5
L	H	H	L	A6
L	H	H	H	A7
H	X	X	X	None

X = Don't care

Figure 3.9: *A: multiplexer; B: functioning logic; C: table of low-high levels for channel selection.*

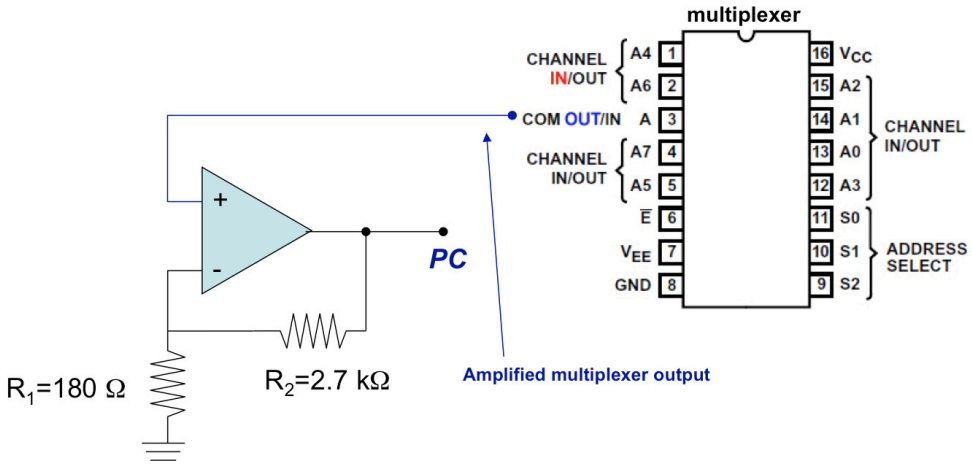

Figure 3.10: *Amplification circuit of the output of the multiplexer.*

schematized in fig. 3.11. This module has the following external hardware connections:

- a cable to 12 temperature sensors LM135,
- battery pack,
- solar panels,
- 6 micropumps,
- SBC PC-104.

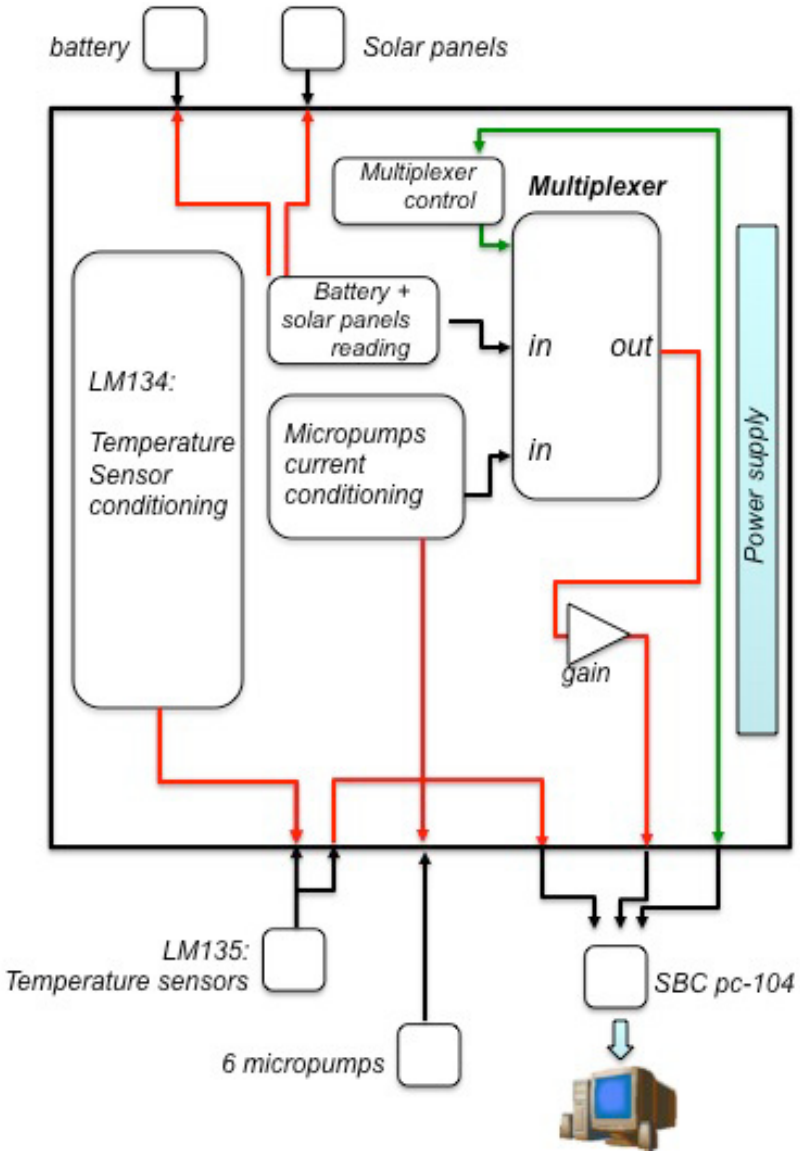

Figure 3.11: *Block diagram of the PC-104 module for thermometer and pump conditioning, and external hardware connections.*

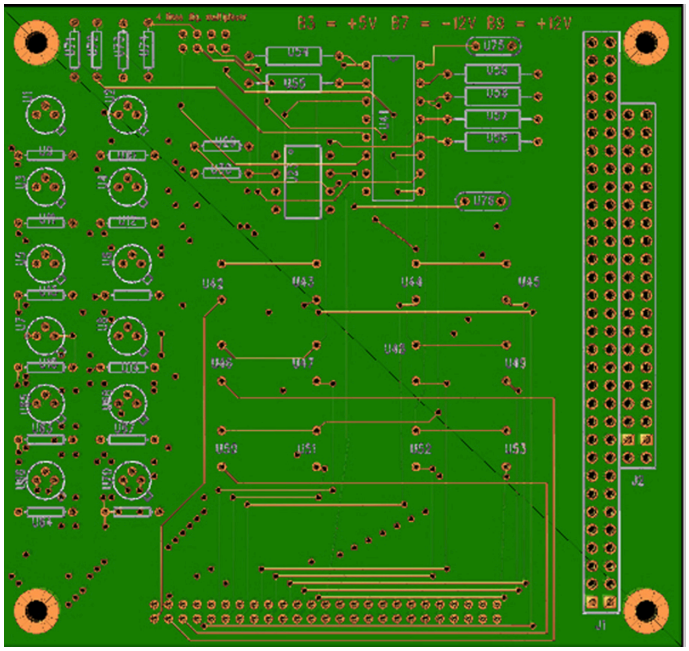

Figure 3.12: *The board with circuitry for temperature and pumps current conditioning.*

3.3.2 PC-104 for power supply of electrovalves

The PC-104 module for the power supply of the electrovalves contains 24 solid state relays that can manage 12 microvalves: two relays are needed to control a single electrovalve, one to switch on and one to switch off, sending ∓ 12 V respectively (see circuit in fig. 3.13). The relays are managed through 24 digital lines, so sending $V_{in} = +5$ V from the pc to a relay makes it to connect a microvalve to ± 12 V. In both DUSTER2009 and DUSTER2011 we used only 6 electrovalves instead of 12, although the PC-104 module has been implemented for the management of 12 electrovalves. This PC-104 module has the following external hardware connections:

- power supply, ± 12 V,
- a cable to SBC, with 24 digital lines for control of relays,
- a cable to 6 electrovalves.

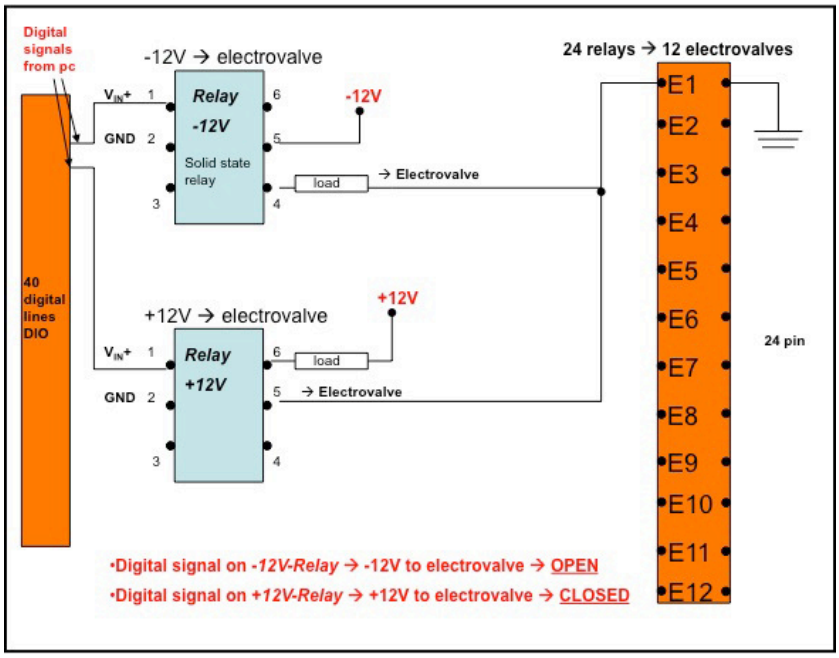

Figure 3.13: *The circuit for the power supply of the electrovalves.*

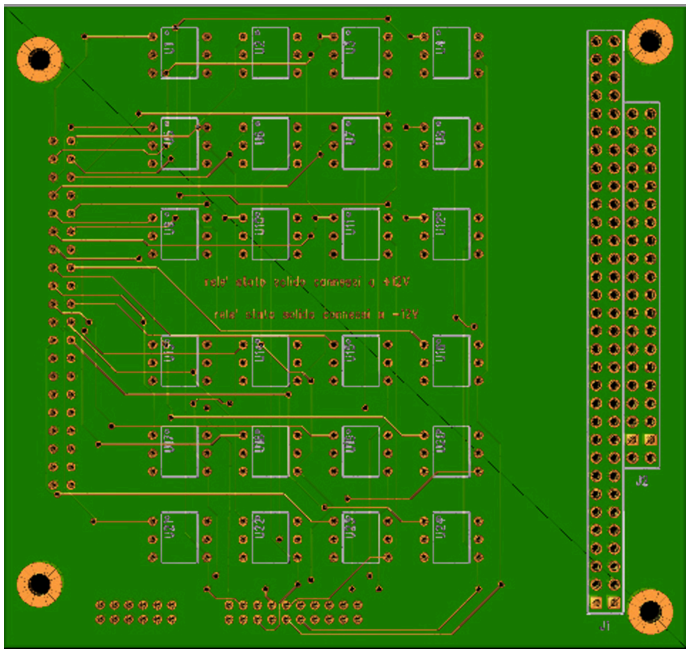

Figure 3.14: *The board with circuitry for microvalves managing.*

3.4 Instrument software

The instrument can be totally controlled by the experimenter (via TC/TM, see sections 3.6.4 and 3.6.5) or by the board pc. It can be configured in *slave* mode or in *auto* mode: in the former case each action is commanded by the user, in the latter case an ad-hoc software [20] manage all the operations and the instrument is autonomous; when it is in *auto* mode the instrument can only accept the telecommand to switch in *slave* mode. In *auto* configuration the on-board software periodically reads the data from pressure and temperature sensors; when the ambient pressure decreases below a threshold pressure (specified by the experimenter and stored onboard) then the instrument has reached the sampling altitude, the software opens the gate and butterfly valves and switches on the pumping system, starting the collection operations. If the software reads too low values of temperatures from sensors mounted on pump flange or on valve motors, then it switches on the heaters. When the instrument begins the descent, once the ambient pressure increases above the threshold value the software switches off the pumping system and closes the valves.

3.5 Flow rate measurements

In order to estimate the mean number of stratospheric particles per volume unit (the stratospheric dust concentration at a certain altitude) and then to suggest a size distribution of stratospheric solid aerosols, we had to determine the total amount of air that the instrument could pump during the flight, that is, we had to determine the *flow rate* of the pumping system. Once we know the pumping group flow rate, the total sampling time (depends on the particular flight conditions), the total number of collected particles (by FE-SEM analyses) and the collection efficiency of the instrument (see chapter 4) we can infer the mean concentration of stratospheric dust. First of all we discuss the physical laws that allow the determination of the flow rate; then we will describe the experimental setup used for flow rate measurements for DUSTER-2009 and DUSTER-2011 instruments.

Let's assume that the air in the environmental chamber, both at P_{amb} and P_{strato}, behaves like a perfect gas, so we can use the perfect gas law:

$$Pv = nRT \tag{3.4}$$

Assuming that the ambient is isothermal and that the volume v of the chamber A does not change, then the time variation of the number of moles is:

$$\dot{n} = \frac{v}{RT}\frac{dP}{dt} \tag{3.5}$$

If we multiply by the molecular mass of the air M we obtain:

$$\dot{n}M = \frac{Mv}{RT}\frac{dP}{dt} \tag{3.6}$$

that is the mass flow rate:

$$\dot{m} = \frac{Mv}{RT}\frac{dP}{dt} \tag{3.7}$$

being $m = nM$. But we are interested in the volume flow rate, so we have to divide by air density ($m = \rho v$):

$$\frac{\dot{m}}{\rho} = \frac{Mv}{RT\rho}\frac{dP}{dt} \tag{3.8}$$

then we obtain the volume flow rate:

$$Q = \dot{v} = \frac{Mv}{RT\rho}\frac{dP}{dt} \tag{3.9}$$

In the equation 3.9 the density depends on the altitude z and hence on the pressure P; so:

$$Q = \frac{Mv}{RT\rho(z)}\frac{dP}{dt} \tag{3.10}$$

Using the Boyle law:

$$\frac{P}{\rho} = cost \tag{3.11}$$

we can obtain the density for each value of stratospheric pressure:

$$\frac{P(z)}{\rho(z)} = \frac{P_0}{\rho_0} \tag{3.12}$$

from which:

$$\rho(z) = \rho_0 \frac{P(z)}{P_0} \tag{3.13}$$

When we acquire waveforms from the oscilloscope we actually get plots of dV/dt vs time, that's voltage data, so we need to convert dV/dt to dP/dt. The conversion factor of the differential pressure sensor is 4.5 V = 2.54 mbar and so:

$$\frac{dP}{dt} = \frac{dP}{dV}\frac{dV}{dt}$$

then

$$\frac{dP}{dt} = \frac{2.54mbar}{4.5V}\frac{dV}{dt}(V/ms)$$

Let's express the pressure in $Pascal$:

$$\frac{dP}{dt} = \frac{2.54 \cdot 10^{-3}bar}{4.5V}\frac{dV}{dt}(V/(10^{-3}s))$$

so

$$\frac{dP}{dt} = \frac{2.54 \cdot 10^{5}Pa}{4.5V}\frac{dV}{dt}(V/s)$$

and finally:

$$\frac{dP}{dt} = \frac{2.54 \cdot 10^{5}}{4.5}\frac{dV}{dt}(Pa/s) \tag{3.14}$$

where dV/dt is expressed in V/ms.

So measuring dV/dt we can obtain dP/dt and finally we can determine the volume flow rate Q.

3.5.1 DUSTER-2009 flow rate measurements

First of all we used a simpler version of the DUSTER instrument, only constituted by the pumping group connected to a small UHV chamber and an inlet, but representative of the fluidodynamics aspects. The pumping group included six micropumps and six corresponding electrovalves (for description see section 3.2.1). The small chamber B was sealed with gate valves. Both pumping group and small chamber were placed in a greater environmental chamber A (see fig. 3.15), in order to set the pressure at stratospheric values; flow rate measurements have been performed at pressure values $4 < P_{strato} < 10mbar$. The micropumps were *Fur Gut* type, with power supply $V = +5V$ and current consumption $I \approx 300mA$ at $P = 1013mbar$ and $I \approx 220 \div 250mA$ at $P = 6mbar$ for each pump. The electrovalves were *SIRAI, Z070D, V12* type, with power supply $V = \pm 12V$. A differential pressure sensor was used to measure the pressure difference between the inlet and the chamber B. The sensor we used was of the type *1 INCH, D1-4V, R7A4-4 MINI*.

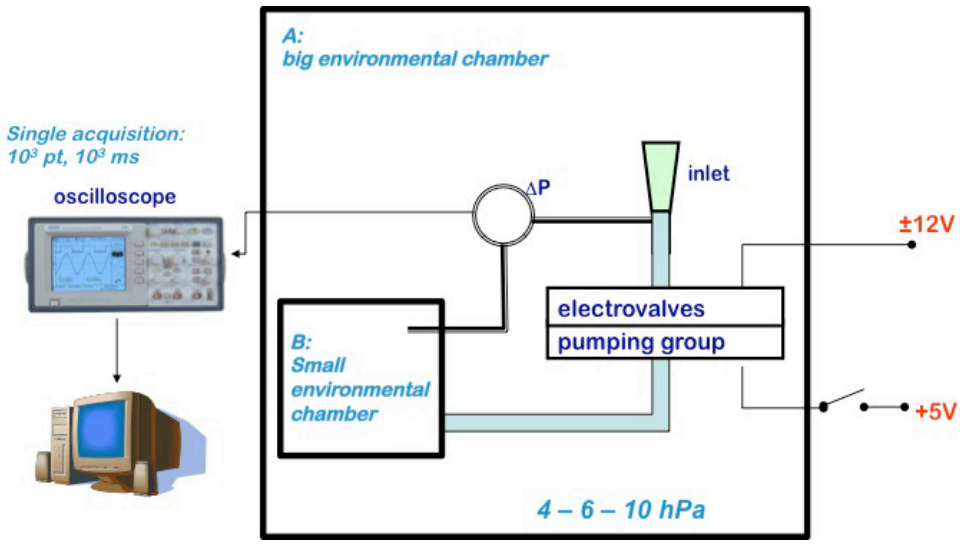

Figure 3.15: *DUSTER-2009 flow rate measurements: experimental setup.*

Once we obtained the desired stratospheric pressure in the environmental chamber A, using a turbopump, we switched on the micropumps, keeping the corresponding electrovalves open and with the differential pressure sensor connected to the oscilloscope. In order the measure to be valid, the differential pressure sensor musts measure $\Delta P = 0$ initially between the inlet and the chamber B. Using the oscilloscope in single acquisition mode, we acquired a waveform for each value of pressure,

each waveform being characterized by a rise of P with time and so by a value of dV/dt.

We first performed measurements using the whole pumping group (6 micropumps), and successively we made measurements excluding one or more pumps from the group, thus measuring the flow rate of each single pump and of groups of 2, 3, 4 and 5 pumps; in tab. 3.1 are listed pressure values and corresponding density values, and are summarized the results of these measurements. For example, the mean flow rate of a single micropump and of the total pumping group at $P = 6$ mbar is:

$$Q_{pump} = 0.25\ m^3/h \tag{3.15}$$

$$Q_{group} = 1.04\ m^3/h \tag{3.16}$$

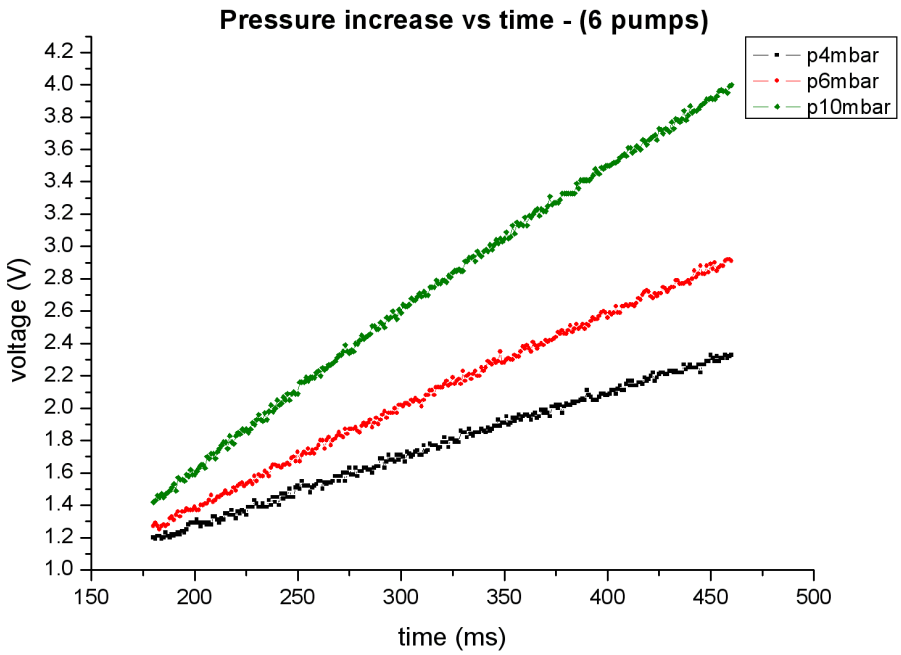

Figure 3.16: *DUSTER-2009 flow rate measurements at stratospheric values: pressure increase (oscilloscope acquisition).*

3.5.2 Estimate of the error on the measure of Q

From the eq.3.10 we can determine the standard deviation of the flow rate measure for each pump and for the whole pumping group:

$$\sigma_{Qi} = \left(\frac{M}{RT}\right)\left\{\frac{1}{\rho^2}\left(\frac{dP}{dt}\right)^2\sigma_v^2 + \frac{v^2}{\rho^4}\left(\frac{dP}{dt}\right)^2\sigma_\rho^2 + \frac{v^2}{\rho^2}\sigma_{dP/dt}^2\right\}^{1/2} \tag{3.17}$$

where the maximum error on the measure of the volume of the small chamber B is $\Delta v = 1.05\ cm^3$; we assume $\sigma_v = \frac{1}{3}\Delta v$. From the Boyle Law, eq.3.13, assuming an uncertainty of 10% about the measure of the pressure sensor, we obtain the standard deviation:

$$\sigma_\rho = \frac{1}{3}\frac{\rho_{amb}}{P_{amb}} \times 10\% P(z) \tag{3.18}$$

The standard deviation of the pressure increase is obtained from the eq.3.14:

$$\sigma(dP/dt) = \frac{2.54 \cdot 10^5}{4.5}\sigma(dV/dt) \tag{3.19}$$

The value of $\sigma(dV/dt)$ has been calculated as:

$$\sigma(dV/dt) = \left(\frac{1}{t_i^2}\sigma_V^2 + \frac{V_i^2}{t_i^4}\sigma_t^2\right)^{1/2} \tag{3.20}$$

The values (V_i, t_i) are taken from the waveforms acquired from the oscilloscope; the standard deviations are:

$$\sigma_V = \frac{1}{3}\Delta V = \frac{1}{3} \cdot 100\ mV$$

and

$$\sigma_t = \frac{1}{3}\Delta t = \frac{1}{3} \cdot 10\ ms$$

Inserting the values obtained into the eq.3.17 we finally obtain the standard deviation of the flow rate for each single pump and for the whole pumping group. The mean standard deviation averaged over the six pumps is:

$$\langle \sigma_Q \rangle = \left[\frac{1}{n^2} \sum_n \sigma_{Qi}^2 \right]^{1/2} \tag{3.21}$$

The values are listed in tab.3.1.

P	**1013**	**10**	**6**	**4**	***mbar***
ρ	1.204	0.0119	0.0071	0.0047	kg/m^3
dV/dt		0.0093	0.0059	0.0041	V/ms
dP/dt		524.933	333.022	231.422	Pa/s
Q_1		4.0	3.8	3.6	$\cdot 10^{-5}\ m^3/s$
σ_1		0.3	0.4	0.6	$\cdot 10^{-5}\ m^3/s$
Q_2		6.0	6.6	8.0	$\cdot 10^{-5}\ m^3/s$
σ_2		0.3	0.4	0.7	$\cdot 10^{-5}\ m^3/s$
Q_3		8.0	8.2	8.9	$\cdot 10^{-5}\ m^3/s$
σ_3		0.4	0.5	0.6	$\cdot 10^{-5}\ m^3/s$
Q_4		7.8	7.3	7.2	$\cdot 10^{-5}\ m^3/s$
σ_4		0.4	0.5	0.6	$\cdot 10^{-5}\ m^3/s$
Q_5		7.7	7.8	9.1	$\cdot 10^{-5}\ m^3/s$
σ_5		0.3	0.5	0.6	$\cdot 10^{-5}\ m^3/s$
Q_6		6.9	7.7	7.4	$\cdot 10^{-5}\ m^3/s$
σ_6		0.3	0.5	0.6	$\cdot 10^{-5}\ m^3/s$
Q_{group}		2.8	2.9	3.1	$\cdot 10^{-4}\ m^3/s$
σ_{group}		0.1	0.1	0.1	$\cdot 10^{-4}\ m^3/s$

Table 3.1: *DUSTER-2009 flow rate measurements: results.*

3.5.3 DUSTER-2011 flow rate measurements

Flow rate measurements have been performed for two distinct pumping groups, one from the DUSTER-2009 flight and a new one, in order to decide which pumping group was better to use. Moreover, the 2009-pumping group has been tested with two different hydraulic configurations, that is, using two different patterns of connection between electrovalve and micropump (see 3.2.1). We will call the two pumping groups "DUSTER-2009" (old) and "DUSTER-2011" pumping group (new). These measurements have been performed in the Cosmic Physics Laboratory at the "Parthenope" University of Naples. For each of the two pumping groups, flow rate was measured at ambient pressure ($P_{amb} = 1013$ mbar) and at stratospheric pressure, that is for several values of pressure between 100 and 3 mbar; we were really interested in pressure values below 10 mbar.

Experimental setup

For both pumping groups the experimental apparatus (schemes in fig. 3.17 and 3.18, photos in fig. 3.19 and 3.20) and the measurement procedure were the same. The pumping group description is in section 3.2.1. A microelectrovalve (*SIRAI, Z070D, V12*) was connected to each pump and supplied with ± 12 V (for the two different hydraulic configurations see below). This pumping group (6 micropumps and 6 electrovalves) pumped air from the small chamber B, which was closed by a flange and connected to the group through a duct; the pumped air was then inlet in the greater chamber A; finally, a differential pressure sensor D_p measured the pressure difference between small and big chamber. We used a turbopump (*Pfeiffer Vacuum - HiCUBE*) to obtain stratospheric pressure in the environmental chamber A, in which vacuum was assured by a check valve C_v and a gate manual valve G_v. The differential pressure sensor (*GE Druck, LPM 9481 series*) was supplied with $10 \div 30$ V DC, and had an output voltage $V_{out} = 0 \div 5$ V, corresponding to a 0 to 20 mbar working range. A digital oscilloscope (*Gw Instek, GDS 2202 series*) was used to analyze the output signal from the differential pressure sensor.

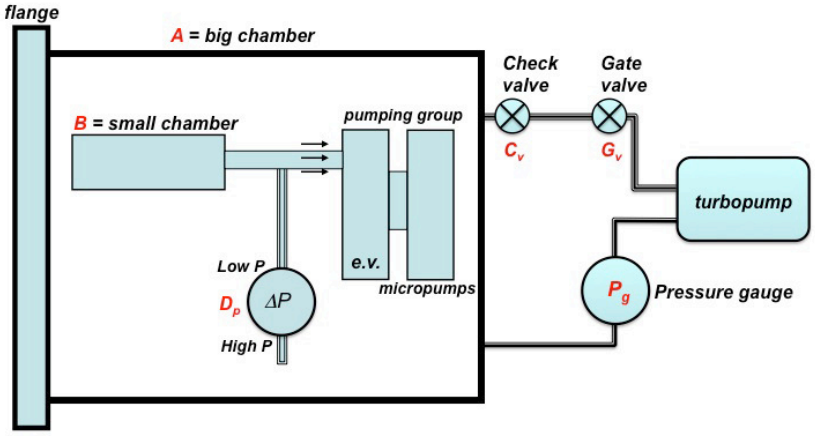

Figure 3.17: *DUSTER-2011 flow rate measurements experimental setup: hydraulic scheme.*

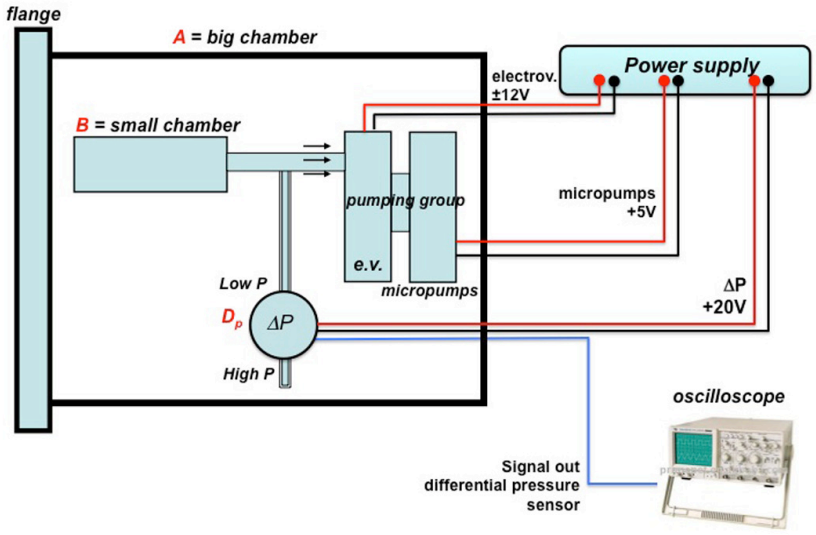

Figure 3.18: *DUSTER-2011 flow rate measurements experimental setup: electric scheme.*

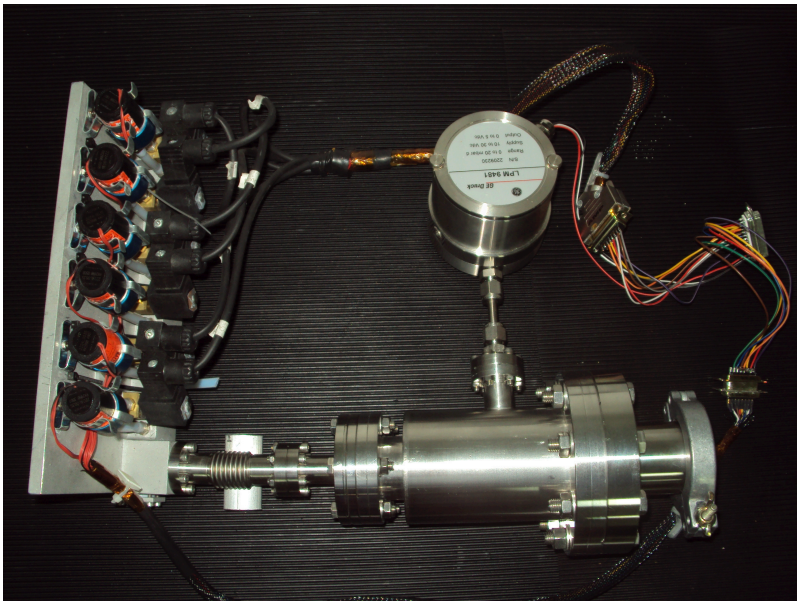

Figure 3.19: *Picture of the pumping system used to measure the flow rate: pumping group, small chamber B and differential pressure sensure.*

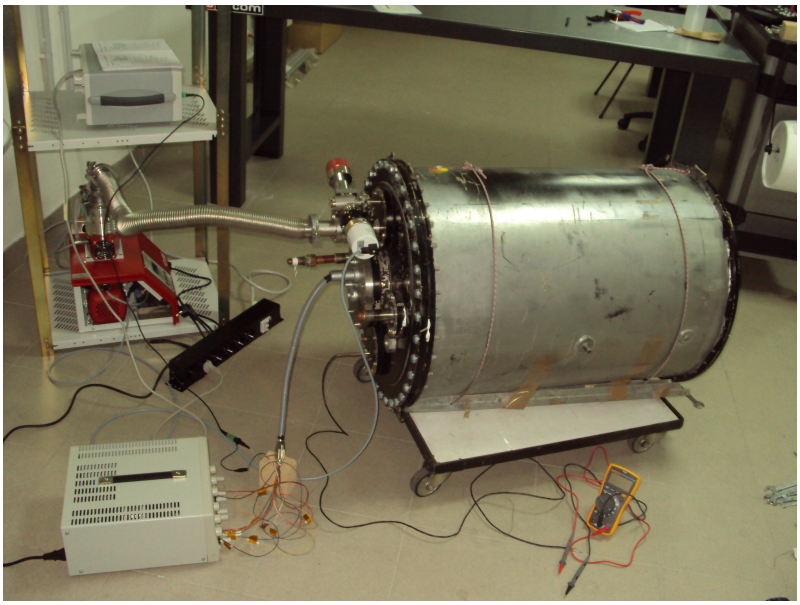

Figure 3.20: *Picture of the experimental setup. Turbopump, oscilloscope, power supply and big enviromental chamber A. The whole pumping system is inside A.*

Measure procedure

First of all it is necessary to set up the pumping system; each electrovalve has to be connected to a micropump (in configuration (A) or (B)). This pumping group has to be connected through a duct to the small chamber B. The differential pressure sensor must be connected to the duct. The whole pumping system has to be placed into the environmental chamber A.

The measurement procedure at $P_{amb} = 1013$ mbar is the following:

- connect the pressure gauge, the oscilloscope and all electric cables to the chamber A;
- the oscilloscope and all electric cables have to be connected respectively to the differential pressure sensor and to the pumping system (power supply) inside A;
- keep open the electrovalves, then switch on the micropumps and switch on the oscilloscope for each single acquisition.

The measurement procedure at $P_{strato} = 100 \div 3$ mbar is the following:

- connect the turbopump, the pressure gauge, the oscilloscope and all electric cables to the chamber A;
- the oscilloscope and all electric cables have to be connected respectively to the differential pressure sensor and to the pumping system (power supply) inside A;
- close the flange, open the valves C_v and G_v and pump in the chamber A;
- once the pressure in A has reached the value $P = 100$ mbar, keep switched on the turbopump;
- switch on the oscilloscope, keep open the electrovalves, then switch on the micropumps connecting to V_{supply};
- while the pressure inside A slowly decreases from 100 mbar to 3 mbar, take a single acquisition with the oscilloscope for each of the selected pressure values in the chamber A.

For each single acquisition, the oscilloscope saved a waveform as a *csv* file. A tool in LabVIEW 2010 environment was developed to analyze all the waveforms: this

program plotted all these waveforms, computing a linear fit for each rise of a waveform, determining the slope of each rise and saving all the results in a single file. In the single acquisition mode, the oscilloscope recorded a waveform for each measurement, namely for each pressure value; keeping the pressure sensor constantly supplied with 20 V DC, every acquisition started simultaneously with the switching on of the pumps and lasted $1s$; so, the waveform profile was characterized by three segments (see fig. 3.21, 3.23 and 3.24):

- a constant part, at initial ΔP_i value, when micropumps were switched off;
- a linear rising part, during the pumping;
- a constant part, at final ΔP_f value, when the pumps are switched off again.

Because $V_A \gg V_B$ we can assume $\Delta P \approx P$, and so each waveform had:

- a constant part, at initial P_i value, when micropumps were switched off;
- a linear rising part, during the pumping;
- a constant part, at final P_f value, when the pumps are switched off again.

The air pressure in chamber A remained almost constant, so P_i and P_f refer to the pressure in chamber B. Indeed the volumes of the two chambers here utilized (fig. 3.17) are $V_A = 157079.63\ cm^3$ and $V_B = 420.64\ cm^3$; so the pressure difference in A with respect to B is:

$$\frac{\Delta P_A}{\Delta P_B} = \frac{V_B}{V_A} \approx 0.3\%$$

The oscilloscope recorded P data as voltage vs time, so voltage data had to be converted into pressure data; it was necessary to measure the value of dP/dt for each waveform, in order to obtain the flow rate. For ambient pressure values in A and B we had $\Delta P_f \gg \Delta P_i$ and the rise was fast and steep, while for stratospheric pressure we had $\Delta P_f \geq \Delta P_i$ with a slow rise and a very small slope.

DUSTER-2009 pumping group

We used six micropumps (*Fur Gut*), each supplied with +5 V DC; the current consumption for each pump was ≈ 300 mA during air pumping at ambient pressure and $\approx 220 \div 250$ mA at stratospheric pressure. We performed the following measurements:

- P_{amb} = 1013 mbar, configuration (A) (fig. 3.2 (A)); 3 acquisitions; results in tab. 3.2;
- P_{amb} = 1013 mbar, configuration (B) (fig. 3.2 (B)); 2 acquisitions; results in tab. 3.3;
- $P_{strato} = 100 \div 3$ mbar, configuration (A) (fig. 3.2 (A)); 7 acquisitions; results in tab. 3.4;
- $P_{strato} = 100 \div 3$ mbar, configuration (B) (fig. 3.2 (B)); 8 acquisitions; results in tab. 3.5;

An example of waveform obtained at stratospheric pressure is plotted in fig. 3.21.

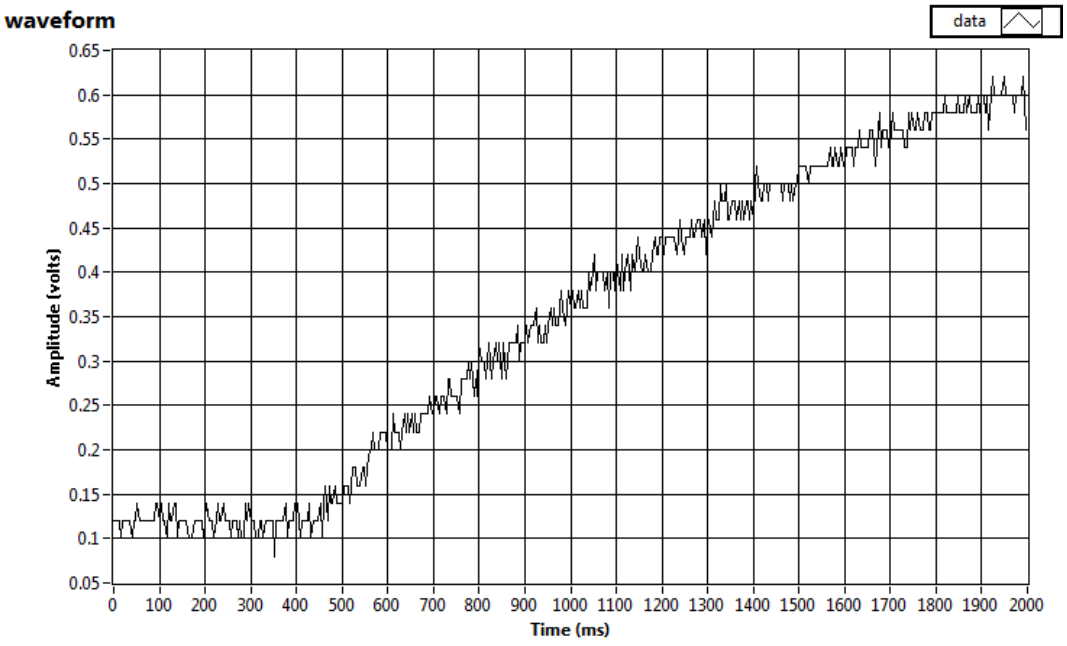

Figure 3.21: *Waveform at stratospheric pressure (Fur Gut micropumps).*

Data conversion

For measurements at P_{amb} = 1013 mbar with configuration (A) each saved waveform had a length memory of 500 points on the horizontal scale, with a sampling time Δt_{sampl} = 2 ms, so a single acquisition corresponded to a measurement time t_{meas} = 1 s. On the vertical scale (voltage) 25 points for each division were recorded. To convert

the data from dV/dt (V/ms) to dP/dt (Pa/s) we considered that the application field of the differential pressure sensor is $0 \div 20$ mbar with an output of $0 \div 5$ V. Thus the conversion factor is:

$$\frac{dP}{dt}(Pa/s) = \frac{dP}{dV}(mbar/V) \cdot \frac{dV}{dt}(V/ms) \cdot \frac{10^5 Pa}{10^3\ mbar} \cdot \frac{10^3\ ms}{1s}$$

so we obtain:

$$\frac{dP}{dt}(Pa/s) = \frac{20\ mbar}{5V} \cdot \frac{dV}{dt}(V/ms) \cdot \frac{10^5 Pa \cdot ms}{mbar \cdot s}$$

$$\frac{dP}{dt}(Pa/s) = 4 \times 10^5 (Pa/s) \cdot \frac{dV}{dt} \tag{3.22}$$

The volumetric flow rate is given by:

$$Q = \dot{v} = \frac{Mv}{RT\rho}\frac{dP}{dt} \tag{3.23}$$

in which:

- $v = 4.206 \times 10^{-4}\ m^3$ is the volume of the small chamber B;
- $M = 0.02884\ kg/mol$ is the molecular mass of the ambient air;
- $R = 8.314\ J/mol \cdot K$ is the gas constant;
- $T = 293$ K is the ambient temperature of the room;
- $\rho = 1.204$ kg/m^3 is the air density at $P_{amb} = 1$ bar.

For measurements at P_{amb} with configuration (B) each waveform had a memory length of 500 points and $\Delta t_{sampl} = 4$ ms, so each acquisition lasted for $t_{meas} = 2$ s.

For measurements at stratospheric pressure values, each waveform was characterized by 500 points, $\Delta t_{sampl} = 4ms$ and $t_{meas} = 2$ s, for both configurations (A) and (B) of fig. 3.2.

Here we used the relation:

$$Q(z) = \dot{v} = \frac{Mv}{RT\rho(z)} \frac{dP}{dt} \tag{3.24}$$

where z is the altitude; with increasing altitude, almost to the stratosphere, air density and pressure are linked by:

$$\rho(z) = \frac{\rho_{amb}}{P_{amb}} \cdot P(z) \tag{3.25}$$

Estimate of the error on the measure of Q

The error on the measure of flow rate for DUSTER-2011 instrument has been estimated in the same way as was done for the DUSTER-2009 instrument (see section 3.5.2.) The standard deviation on the flow rate measure is given by:

$$\sigma_{Qi} = \left(\frac{M}{RT}\right) \left\{ \frac{1}{\rho^2} \left(\frac{dP}{dt}\right)^2 \sigma_v^2 + \frac{v^2}{\rho^4} \left(\frac{dP}{dt}\right)^2 \sigma_\rho^2 + \frac{v^2}{\rho^2} \sigma_{dP/dt}^2 \right\}^{1/2} \tag{3.26}$$

where the standard deviations σ_v and σ_ρ computed in the section 3.5.2. From the conversion factor for these measurements, eq.3.22, we have:

$$\sigma(dP/dt) = 4 \times 10^5 \sigma(dV/dt)$$

and, from the estimates made in the section 3.5.2, we can assume $\sigma_{dV/dt} = 4\% \times (dV/dt)$.

DUSTER-2009 pumping group: results

The results are listed in tables from 3.2 to 3.5.

The flow rates obtained with the Duster-2009 flight micropumps, with (A) and (B) configurations, have been plotted for comparison; they are reported in fig. 3.22.

As we can see from plot 3.22 with the new (B) configuration the measured flow rate is substantially greater than in the case of old (A) configuration. For this reason we decided to use the new configuration (fig. 3.2 (B)) for the realization of the DUSTER-2011 instrument.

P_{amb} CONF.A	P $(mbar)$	dV/dt (V/ms)	dP/dt (Pa/s)	**Q** (m^3/h)	σ_Q (m^3/h)
acq 1	1000	0.12014	48056.4	0.72	0.04
acq 2	1000	0.12082	48326.4	0.72	0.04
acq 3	1000	0.11779	47118.0	0.70	0.04

Table 3.2: *Flow rate at ambient pressure; Fur Gut micropumps, configuration (A)*

P_{amb} CONF.B	P $(mbar)$	dV/dt (V/ms)	dP/dt (Pa/s)	**Q** (m^3/h)	σ_Q (m^3/h)
acq1	1000	0.18059	72237.6	1.08	0.05
acq2	1000	0.18996	75944.0	1.13	0.06

Table 3.3: *Flow rate at ambient pressure; Fur Gut micropumps, configuration (B)*

P_{strato} CONF.A	P $(mbar)$	dV/dt (V/ms)	dP/dt (Pa/s)	**Q** (m^3/h)	σ_Q (m^3/h)
acq1	3.0	0.000248	99.2	0.50	0.03
acq2	3.4	0.000341	136.4	0.61	0.03
acq3	4.0	0.000382	152.8	0.58	0.03
acq4	4.6	0.000513	205.2	0.67	0.04
acq5	5.4	0.000636	254.4	0.71	0.03
acq6	6.3	0.000629	251.6	0.60	0.04
acq7	7.4	0.000795	318.0	0.65	0.03

Table 3.4: *Flow rate at stratospheric pressure; Fur Gut micropumps, configuration (A)*

P_{strato} $CONF.B$	P $(mbar)$	dV/dt (V/ms)	dP/dt (Pa/s)	**Q** (m^3/h)	σ_Q (m^3/h)
acq1	3.4	0.000368	147.2	0.65305	0.03
acq2	4.0	0.000664	265.6	1.00158	0.05
acq3	4.6	0.000817	326.8	1.07162	0.06
acq4	5.4	0.000997	398.8	1.11398	0.06
acq5	6.3	0.001144	457.6	1.09563	0.06
acq6	7.4	0.001384	553.6	1.12845	0.06
acq7	8.6	0.001583	633.2	1.11061	0.06
acq8	10	0.001949	779.6	1.17595	0.06
acq8	14	0.002757	1102.8	1.18819	0.06

Table 3.5: *Flow rate at stratospheric pressure; Fur Gut micropumps, configuration (B)*

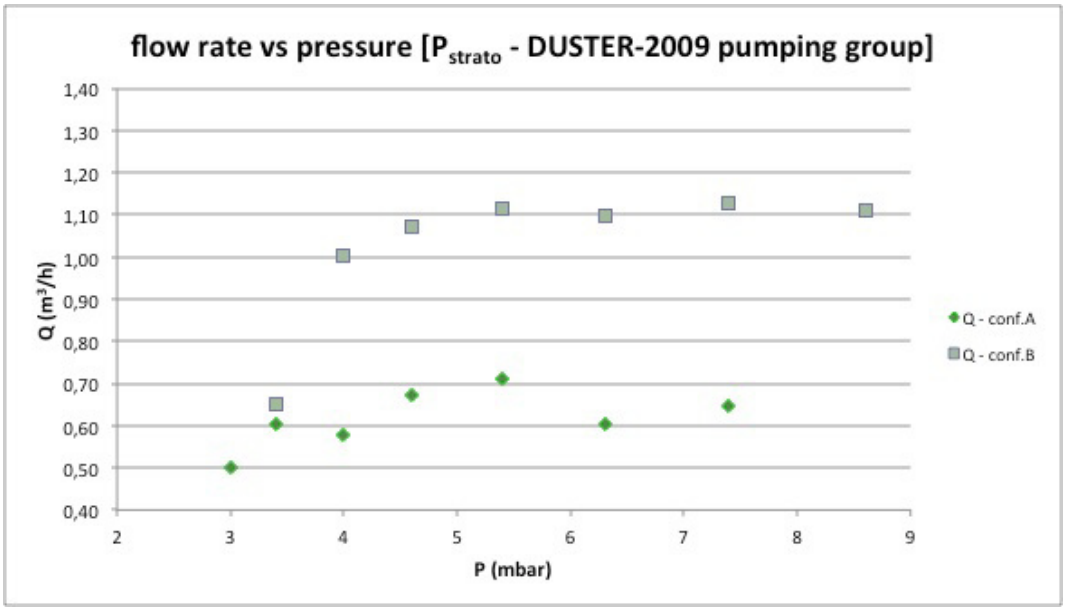

Figure 3.22: *Flow rate at stratospheric pressure: Fur Gut micropumps; (A) and (B) configuration.*

DUSTER-2011 pumping group

Using the same experimental apparatus and following the same procedure, but using a new pumping group, we performed the following measurements:

- $P_{amb} = 1013$ mbar, configuration (B) (fig. 3.2 (B)); 3 acquisitions; results in tab. 3.6;
- $P_{strato} = 100 \div 3$ mbar, configuration (B) (fig. 3.2 (B)); 11 acquisitions; results in tab. 3.7;

The new pumping group was constituted by six micropumps (*Thomas, G 12/04 EB*) supplied with +12 V DC. Measurements with new micropumps were all made only using the new configuration of electrovalves (conf.B, fig. 3.2).

DUSTER-2011 pumping group: results

In fig. 3.23 and 3.24 are plotted the waveforms obtained with the LabVIEW tool for measurements at ambient pressure and stratospheric pressure, while in fig. 3.25 the linear fit from which we determined the slope dV/dt. The results from measurements at $P_{amb} = 1013$ mbar and P_{strato} are listed in tab. 3.6 and tab. 3.7.

P_{amb} *CONF.B*	P $(mbar)$	dV/dt (V/ms)	dP/dt (Pa/s)	**Q** (m^3/h)	σ_Q (m^3/h)
acq 1	1000	0.16400	65600.0	1.47	0.05
acq 2	1000	0.16461	65.842.4	1.47	0.05
acq 3	1000	0.16812	67248.4	1.50	0.05

Table 3.6: *Flow rate at ambient pressure; Thomas G 12/04 EB - micropumps, configuration (B)*

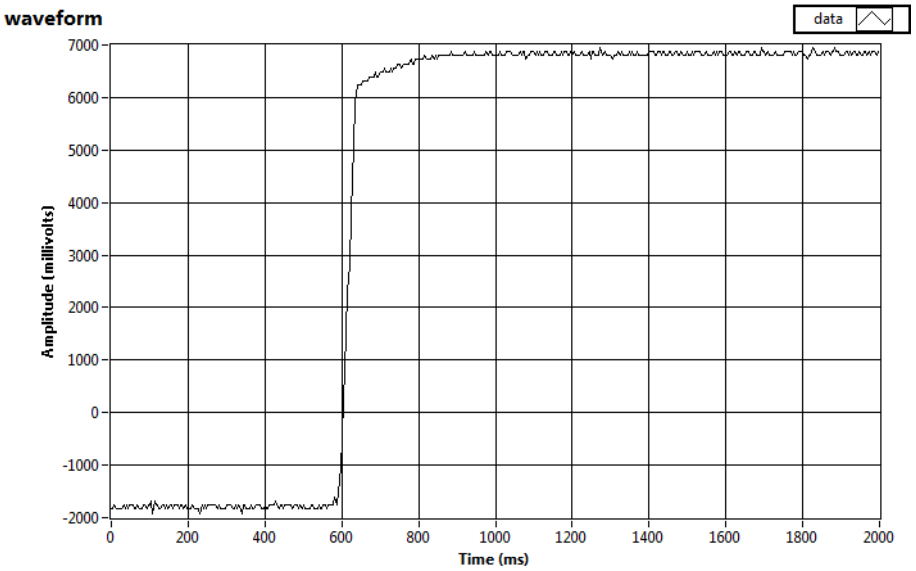

Figure 3.23: *Waveform at ambient pressure $P = 1013mbar$ (Thomas G 12/04 EB - micropumps).*

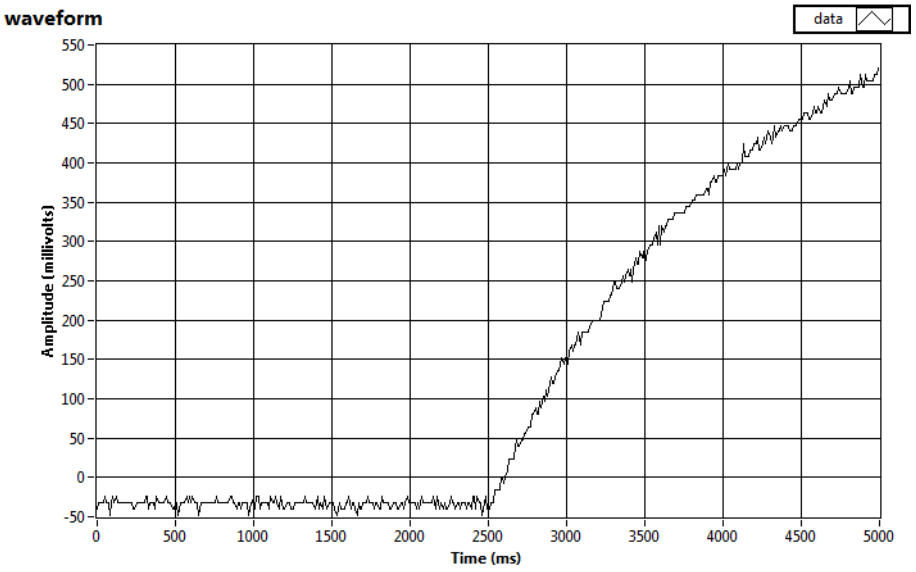

Figure 3.24: *Waveform at stratospheric pressure (Thomas G 12/04 EB - micropumps).*

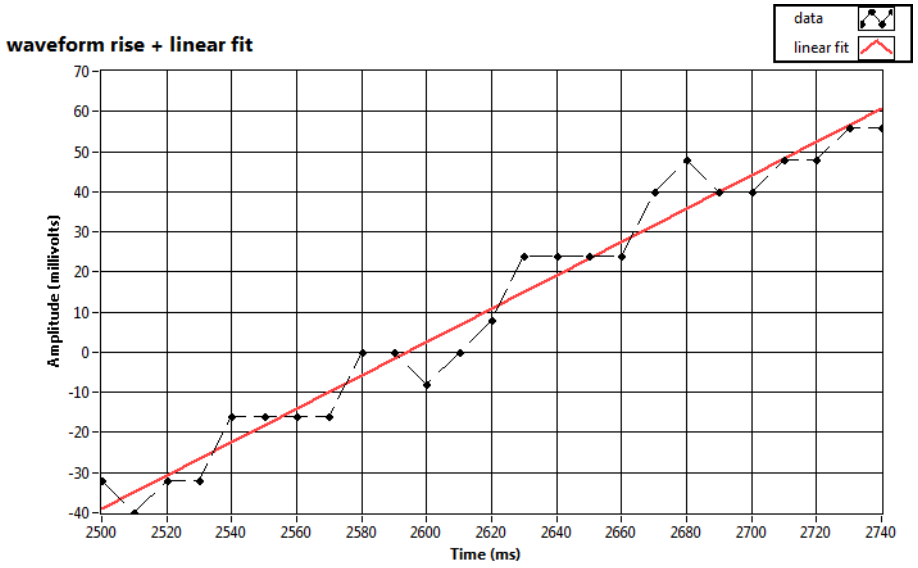

Figure 3.25: *Fit of the waveform rise at stratospheric pressure (Thomas G 12/04 EB - micropumps).*

P_{strato} *CONF.B*	P $(mbar)$	dV/dt (V/ms)	dP/dt (Pa/s)	**Q** (m^3/h)	σ_Q (m^3/h)
acq 1	3.0	0.000284	113.6	0.86	0.03
acq 2	3.4	0.000406	162.4	1.08	0.04
acq 3	4.0	0.000452	180.8	1.02269	0.04
acq 4	4.6	0.000603	241.2	1.19	0.04
acq 5	5.4	0.000802	320.8	1.34	0.05
acq 6	6.3	0.000907	362.8	1.30	0.05
acq 7	7.4	0.001049	419.6	1.28	0.04
acq 8	8.6	0.001186	474.4	1.25	0.04
acq 9	10	0.001524	609.6	1.38	0.05
acq 10	12	0.00174	696.0	1.31	0.05
acq 11	14	0.00213	852.0	1.38	0.05

Table 3.7: *Flow rate at stratospheric pressure; Thomas G 12/04 EB - micropumps, configuration (B)*

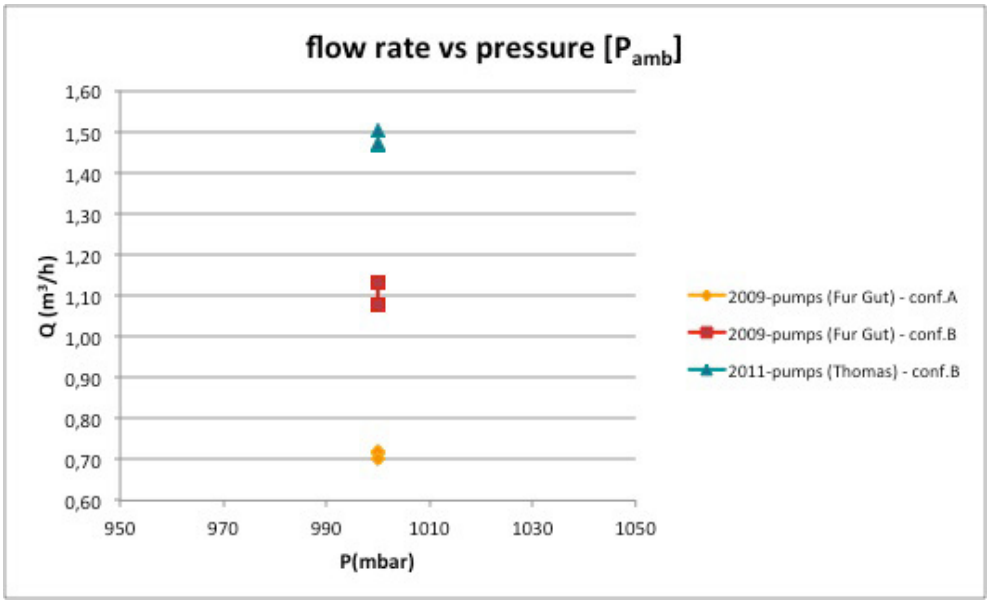

Figure 3.26: *Maximization of flow rate.*

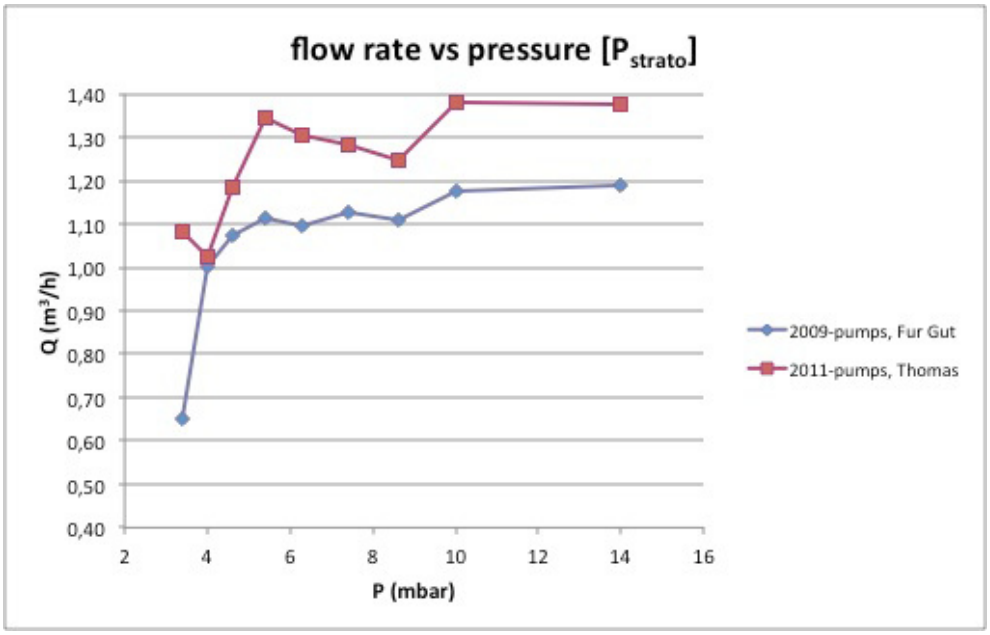

Figure 3.27: *Flow rate: 2009-micropumps vs 2011-micropumps.*

In figures 3.26 and 3.27 are plotted for comparison the flow rates of DUSTER-2009 pumping group and of the DUSTER-2011 pumping group. Summarizing, we have from tab. 3.7:

$$Q(3.4mbar) = 1.08\ m^3/h \tag{3.27}$$

and

$$Q(6.3mbar) = 1.30\ m^3/h \tag{3.28}$$

for the flow rate of the whole group. As we can see, the flow rate is maximized using the 2011-pumping group (*Thomas G 12/04 EB*) with the configuration of fig. 3.2 (B). Finally there is an increase in flow rate of $\approx 25\%$ with respect to DUSTER-2009 micropumps and configuration (A) (see eq. 3.16 for comparison).

3.6 EGSE

The task of the EGSE of DUSTER (*Electrical Ground Support Equipment*) is to allow the communication between the experimenter and the instrument during all stages of the flight. The EGSE is developed in NI-LabView (*National Instruments*) environment consisting in an intuitive laboratory interface between the user and the instrument. Whatever is the type of telemetry hardware used, the EGSE must be able to manage the communication with the instrument (with its SBC), that is to perform fundamentally two operations:

- TM packets reception (*telemetry*)
- TC packets sending (*telecommands*)

For DUSTER-2009 we used IRIDIUM telemetry system (see section 3.6.4). In this hardware configuration the instrument had to exchange TM/TC packets with the experimenter via email; so the EGSE had to be able to manage the telemetry packets sending and receiving emails through an apposite webmail account. For DUSTER-2011 we did not use the IRIDIUM telemetry system (see section 3.6.5), and there was not the need to send/receive packets via email.

3.6.1 TM packets

Telemetry packets contain all the information about the instrument functioning, its configuration, the operations it is doing, its status. There are two types of TM packets:

- *status file*
- *housekeeping*

The status file (SF) is a 24 bytes packet and contains all informations about the status of the instrument and its correct working:

- status flags
- instrument configuration (auto/slave)
- sampling status (sampling/safe)
- pumps configuration (enabled/disabled)

- pumps status (on/off)
- electrovalves status (open/closed)
- instrument parameters limit values
- time
- encoders

The status flags tell us which operation the instrument is doing; each flag is expressed by a bit configuration, to which corresponds a number between 0 and 6, and represents one of the following operations: *update, warning, transition, accepted, rejected, executed, timeout*; the last four flags refer to the reception of telecommands (TC). The sampling status can assume four values, because the instrument can be in *slave* mode and can be in sampling or in safe; otherwise it can be in *auto* mode and can be in sampling or in safe configuration. The instrument parameters limit values indicate over range parameters: T_{lim} (several components), $T_{lim}(cpu)$, I_{lim} (pumps), low battery, gate and butterfly valves closed or open. The *time* value of each packet is the number of seconds that have elapsed since a reference time t_0 until the arrive of the TM; the reference time depends on the on-board pc. In order to have a useful information on arrival time, this quantity must be converted in date and hours.

The housekeeping (HK) is a 72 bytes packet and contains all the informations regarding the physical parameters of various parts of the instrument, that is all physical values measured by the sensors; so the housekeeping packet is a sequence of values corresponding to:

- temperatures
- pump currents
- voltages
- ambient pressure
- coordinates (GPS)
- time
- measure of ΔP

3.6.2 TC packets

In addition to the reception of telemetry packets (HK and SF), the EGSE allows the possibility to send telecommands (TC). If the instrument is set in *auto* mode , it automatically and periodically sends to the user telemetry packets, with a period of few minutes; moreover it is possible to request telemetry packets simply sending the corresponding telecommands, either if the instrument is set in *slave* mode or in *auto* mode. The list of telecommands is:

- MONI: asks the instrument to send a housekeeping packet;
- STAT: asks the instrument to send a status file packet;
- SLAV: sets the instrument in slave mode;
- AUTO: sets the instrument in auto mode;
- SAMP: activates the sampling;
- SAFE: stops the sampling;
- CFDO: asks the instrument to send the *configuration file* (CF);
- CFUP: sends the CF to the instrument;
- GVON: opens the gate valve;
- GVOF: closes the gate valve;
- BVON: opens the butterfly valve;
- BVOF: close the butterfly valve;
- PnON: switches on the pump n;
- PnOF: switches off the pump n.

A further telecommand allows to quit the EGSE program and to switch off the instrument.

3.6.3 Logic of conversion of TM packets

The first stage of the managing of TM/TC is the interaction between the EGSE and the instrument and depends on the particular type of telemetry hardware used: this will be explained in the two next subsections (3.6.4 and 3.6.5). The following

operations are instead common to both versions of EGSE. In the next stage the program has first of all to recognize the type of packet received; each HK or SF packet arrives as a stream of 72 or 24 bytes, that is interpreted as a hexadecimal string. The program reads the *header*, that is the first byte of the stream: the header has at least 6 bit that are always zero and 2 bit different from zero, and it encapsules the information on the type of telemetry packet; a header whose numerical value is 2, indicates a status file, while a header whose numerical value is 3 indicates a housekeeping.

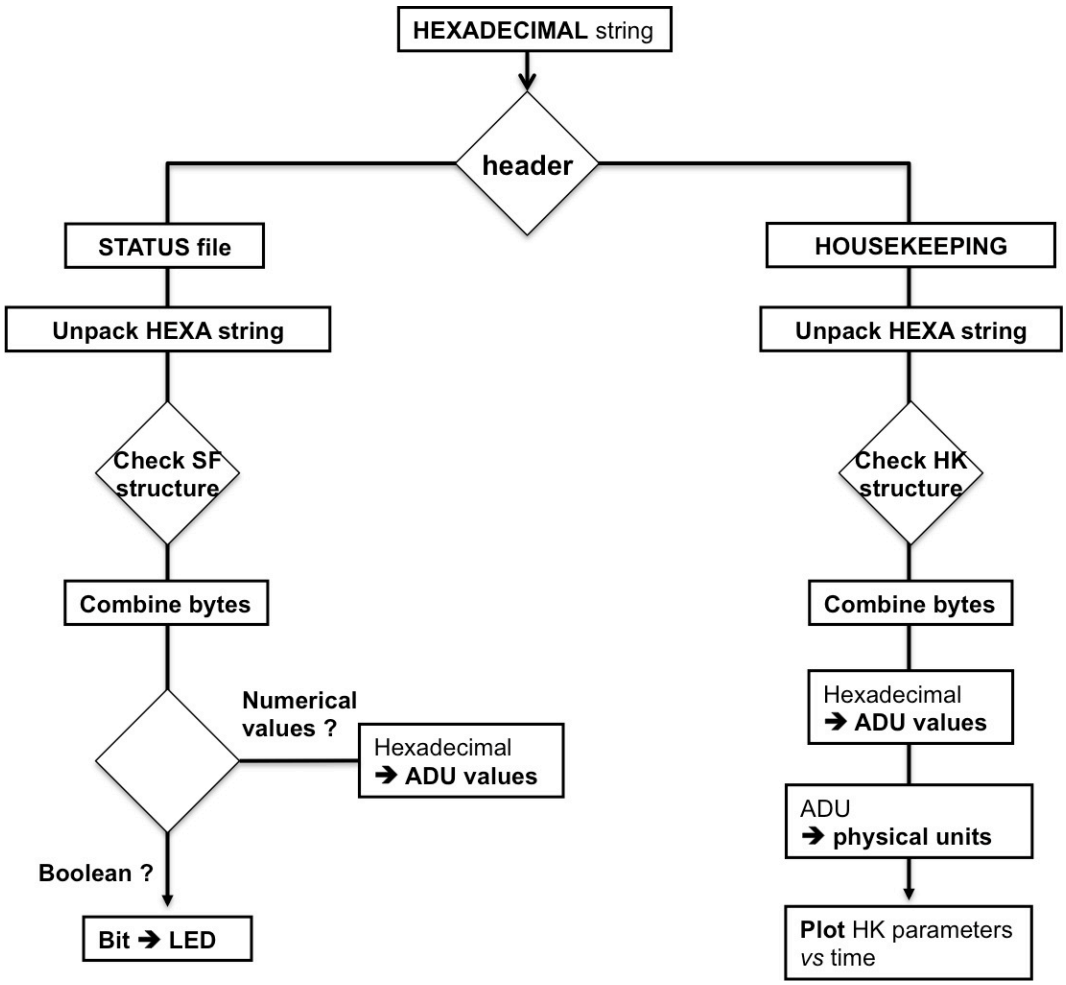

Figure 3.28: *Logic of conversion of TM packets hexadecimal strings.*

Once the program has recognized the type of packet received, the next operation is to split the packet into all significative bytes, taking into account the precise

structure of each type of packet. According to the structure of the HK packet, each parameter is constituted typically of 2, 3 or 4 bytes. The preliminary conversion from hexadecimal characters to numerical values, only gives values in ADU units (*analog to digital units*); so it is necessary a further conversion from ADU numerical values to parameters in physical units. The relation used for the conversion of the temperatures as measured by temperature sensors is:

$$T(^{\circ}C) = \left\{ T(ADU) \cdot \frac{5}{65536} \cdot 100 \right\} - 273.15^{\circ}\mathrm{C} \tag{3.29}$$

where we have taken into account the fact that these parameters are 16 bit numbers ($65536 = 2^{16}$). For the conversion of the total current we used:

$$I_{tot}(A) = I_{tot}(ADU) \cdot \frac{5}{65536} \tag{3.30}$$

while for the pumps currents:

$$I_{pump}(A) = \left\{ I_{pump}(ADU) \cdot \frac{5}{65536} \right\} \cdot \frac{1}{8} \tag{3.31}$$

For the data from the altimeters we have:

$$P(Pa) = \frac{P(ADU)}{10} \tag{3.32}$$

and:

$$T(^{\circ}C)_{altim} = \frac{T(ADU)_{altim}}{10} - 273.15^{\circ}\mathrm{C} \tag{3.33}$$

From the measurement of the differential pressure sensor we get:

$$\Delta P(Pa) = \Delta P(ADU) \cdot \frac{5}{65536} \tag{3.34}$$

Finally the conversion of the battery voltage measurement is:

$$V(Volt) = V(ADU) \cdot \frac{5}{65536} \cdot 5.36 \tag{3.35}$$

The power consuption is calculated as follows:

$$W(W) = V(V) \cdot I_{tot}(A) \tag{3.36}$$

The program computes the real time altitude of the instrument during the flight, starting from the pressure data of the altimeters. The computing of conversion from pressure data to altitude is in appendix A. In a SF packet all informations are as flags, which are translated in virtual LEDs in the front panel. The only numerical values are the two encoder readings and the time. The encoder reading value corresponds to a certain number of steps done by the motor when we open or close the gate/butterfly valve. The time value conversion from number of seconds to date (mm/dd/yyyy) is in appendix B.

3.6.4 DUSTER-2009 EGSE

The telecommand/telemetry (TC/TM) system used for the flight of the DUSTER-2009 instrument, launched from the Svalbard base, was based on the IRIDIUM satellite communication system. The IRIDIUM system consists of a constellation of 77 satellites deployed in LEO orbits (780 km altitude) and placed in 6 equally spaced orbit planes, each inclined at 86.4° to the equator (see [33]). Thanks to an IRIDIUM Modem (*9601 SBD Transceiver*) and an IRIDIUM Antenna the instrument exchanges messages with the user at ground:

- Mobile Originated (MO, from system to experimenter) messages up to 340 bytes
- Mobile Terminated (MT, from experimenter to system) messages up to 270 bytes
- Low, uniform global latency (≤ 1 min)

The exchanged messages are in SBD format, that is *Short Burst Data*. In order to send a MO-SBD, the on-board software loads the data message in the transceiver and instructs it to send the MO message (see [20]). The data message is sent to the IRIDIUM Gateway through the satellite network, and finally it is sent to the experimenter via email; the SBD data arrive as email attachments, so they are stored

for subsequent data processing. On the other side, the experimenter sends MT-SBD to the instrument via email; data messages must pass through the IRIDIUM Gateway before to be sent to the instrument (see fig. 3.29).

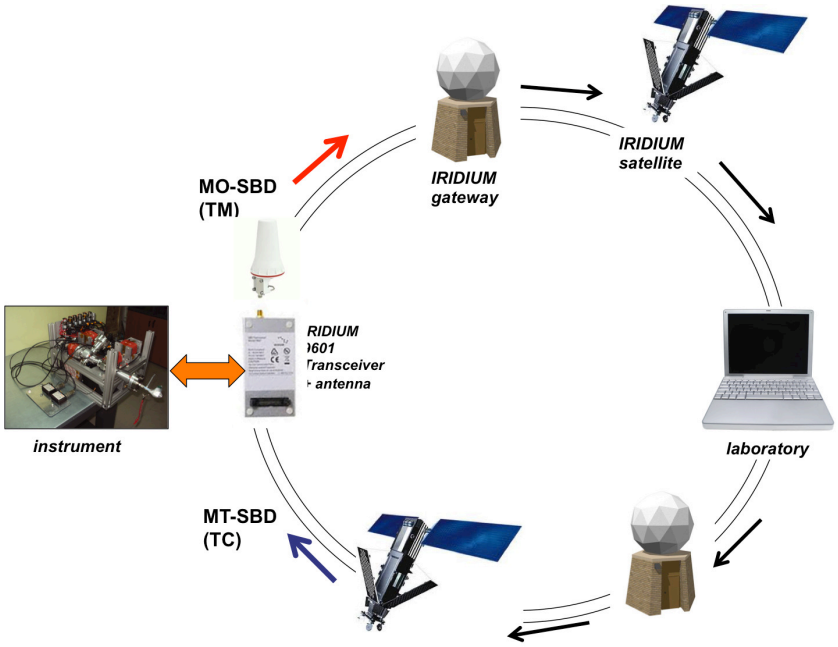

Figure 3.29: *Telemetry system scheme: IRIDIUM communication.*

The EGSE of the DUSTER-2009 instrument has been developed taking into account the type of telemetry utilized. Once that all SBD attachments have been downloaded from the email account by the experimenter and saved on the dedicated pc, the program is able to convert the telemetry packets contained in the SBD attachments. Each attachment consists of a *hexadecimal string*, that is a sequence of bytes expressed in hexadecimal units with the structure:

$$hexadecimal\ string = header + information$$

A Mobile Originated SBD attachment can be:

- *housekeeping* packet
- *status file* packet

Apart from the mode of data access of the DUSTER-2009 EGSE, the subsequent logic of conversion from hexadecimal string to single bytes, of information extraction from the bytes and of conversion from ADU units to physical units of the HK and SF packets is the same as for the EGSE of the DUSTER-2011 instrument. There are nevertheless some differences between the two versions. In the DUSTER-2009 instrument we did not use any GPS system, so we obtained the coordinates of the balloon directly from the IRIDIUM SBD packets. A text message was also included in every email, more than the SBD attachment, that contained time and position informations. The serial communication was not yet developed in this version. For the description of EGSE main structure, of the logic of conversion and of the structure of TC/TM packets, see sections 3.6.1, 3.6.2 and 3.6.3.

3.6.5 DUSTER-2011 EGSE

The DUSTER-2011 flight, which has been supported and executed by CNES, has been performed from the Esrange Centre, near Kiruna, Sweden, on April 7th 2011. The EGSE for the DUSTER-2011 instrument has been developed taking into account the fact that the interface between instrument and computer at ground depended on the telemetry system used for flight control; in this case the telemetry system was provided by the CNES launch team.

The on-board main computer communicated with the telemetry system via a RS232 serial port used in asynchronous mode, and through this system the pc communicated with a dedicate pc in the laboratory (fig. 3.30).

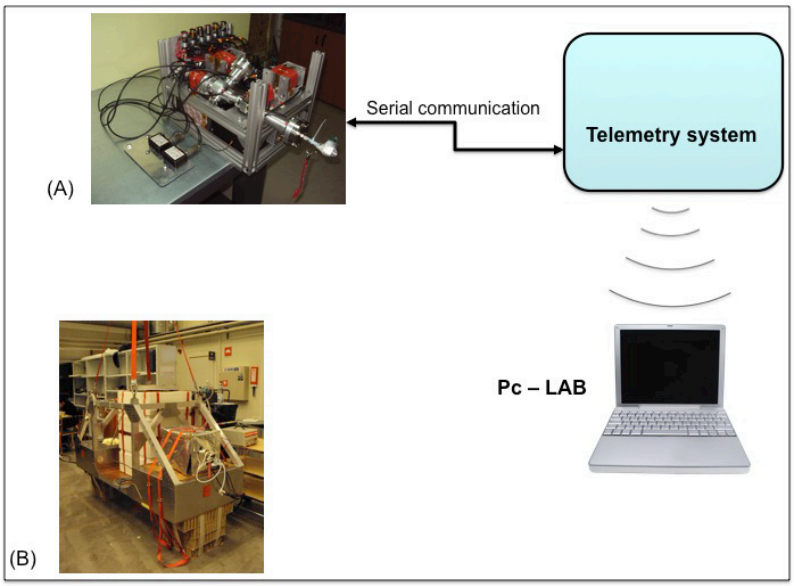

Figure 3.30: *(A): Telemetry system scheme; (B) the instrument placed on flight gondola*

The EGSE has been developed in NI-LabVIEW environment; three versions have been developed, depending on the type of input of the informations:

- serial communication
- reading from file
- reading from text string

The logic of the program is schematized in fig. 3.31 and 3.32. The initialization of the program (serial version) consists in the serial port configuration, with the setting of all necessary parameters (*baud rate, parity, number of bytes to read or write*). After that a *while* cycle runs; inside the while cycle an *event* structure allows the activation of two distinct operations by clicking with the mouse on a virtual button on the front panel: thanks to the event structure it is possible to switch between the *read* or *write* configuration. In *read* configuration the EGSE performs telemetry reception; in *write* configuration the user can send telecommands. In the write configuration, a *case* structure allows to switch between 15 possibilities, each associated to a single telecommand; in each case the write action of a TC consists in writing the corresponding byte sequence onto the serial port. In the read configuration the program reads the byte sequence on the serial port, with a 10 sec temporization; the next operation is the conversion from byte sequence (hexadecimal string) to numerical values and plots. For a description of the logic of conversion and of the structure of TC/TM packets, see sections 3.6.1, 3.6.2 and 3.6.3.

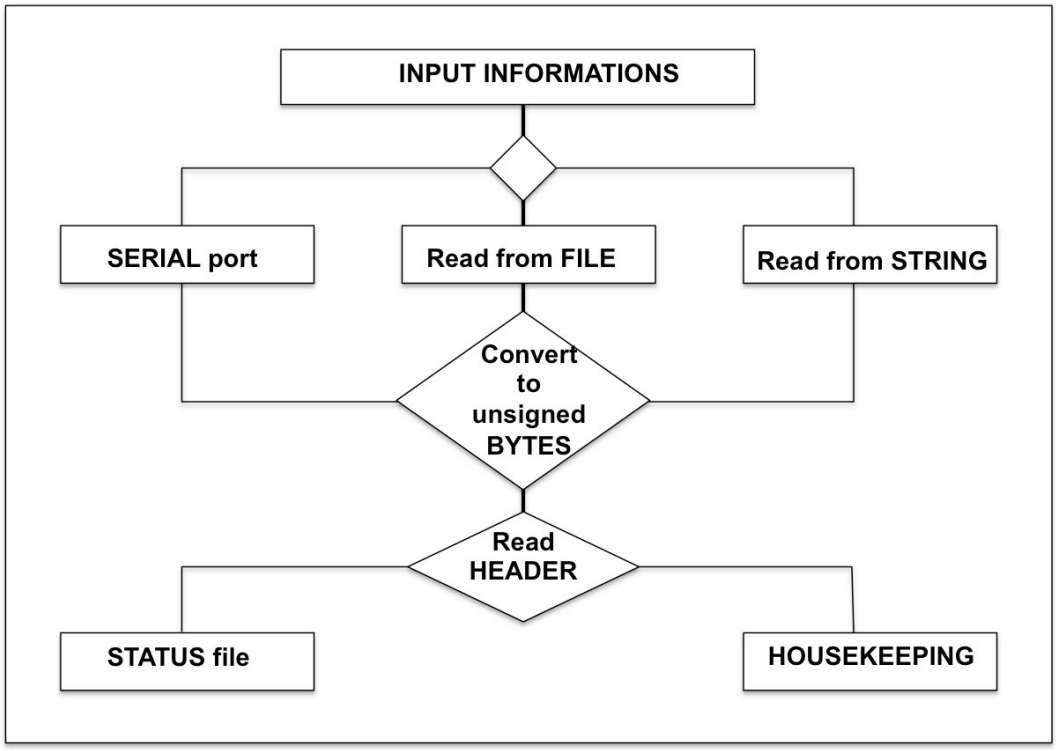

Figure 3.31: *Block diagram of the EGSE essential logic. A) Different types of input; B) conversion of telemetry packets.*

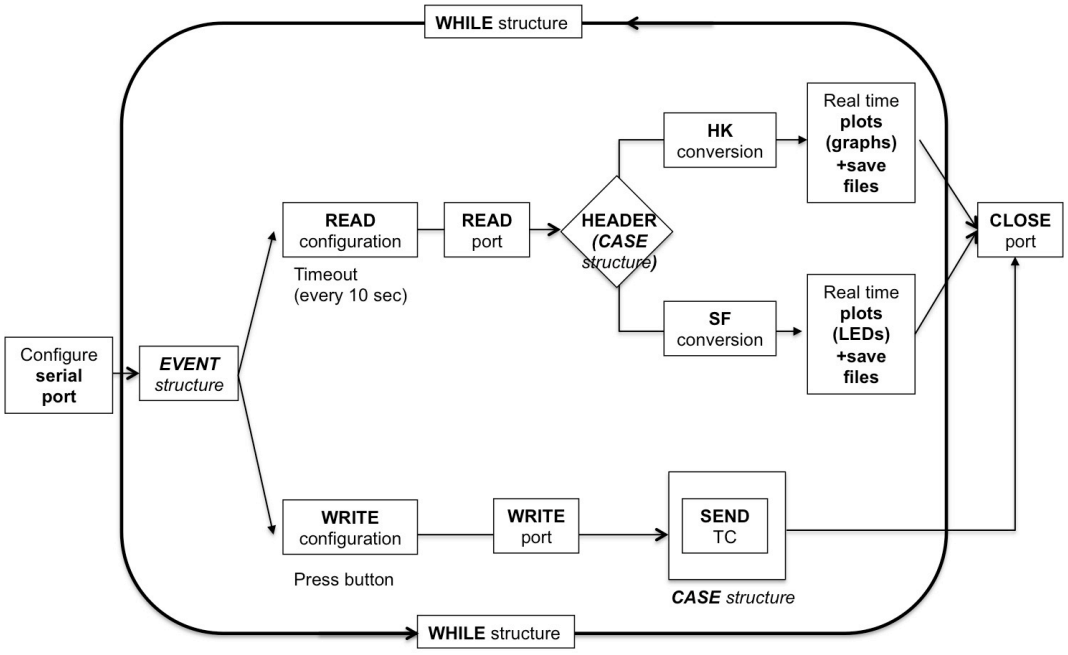

Figure 3.32: *Block diagram of the EGSE essential logic. Serial communication.*

The EGSE interface consists of a front panel that can be switched between 5 different screens; the user can switch between them pressing a button. In the first panel (see fig. 3.33) there are all the necessary controls to set the correct configuration of the program: there is a frame with the control parameters of the serial port, a frame with the control to send the telecommands, the browser to choose the folder for saved files. In the second panel (see fig. 3.34) the plots of housekeeping parameters are showed: a single plot relative to the 12 temperatures measured by the temperature sensors, a plot of the altitude, one for pumps currents and total current, one for altimeter data (2 pressure values and 2 temperature values), one for battery voltage and power consumption. All HK parameters are plotted as function of the time since 30 minutes before flight until the end of flight. In the third panel (see fig. 3.35) the altitude profile is compared with the sampling status of the instrument: this is useful to see immediately what is the sampling altitude range of the instrument. In the fourth panel (see fig. 3.36) the trajectory of the flight, with reference to the ground map, is showed. The trajectory is obtained by plotting latitude vs longitude. The fifth panel (see fig. 3.37) shows numeric converted data from HK packets, numeric data and LEDs from status file packets, number of telemetry packets. Note that all showed pictures refer to the DUSTER-2011 flight.

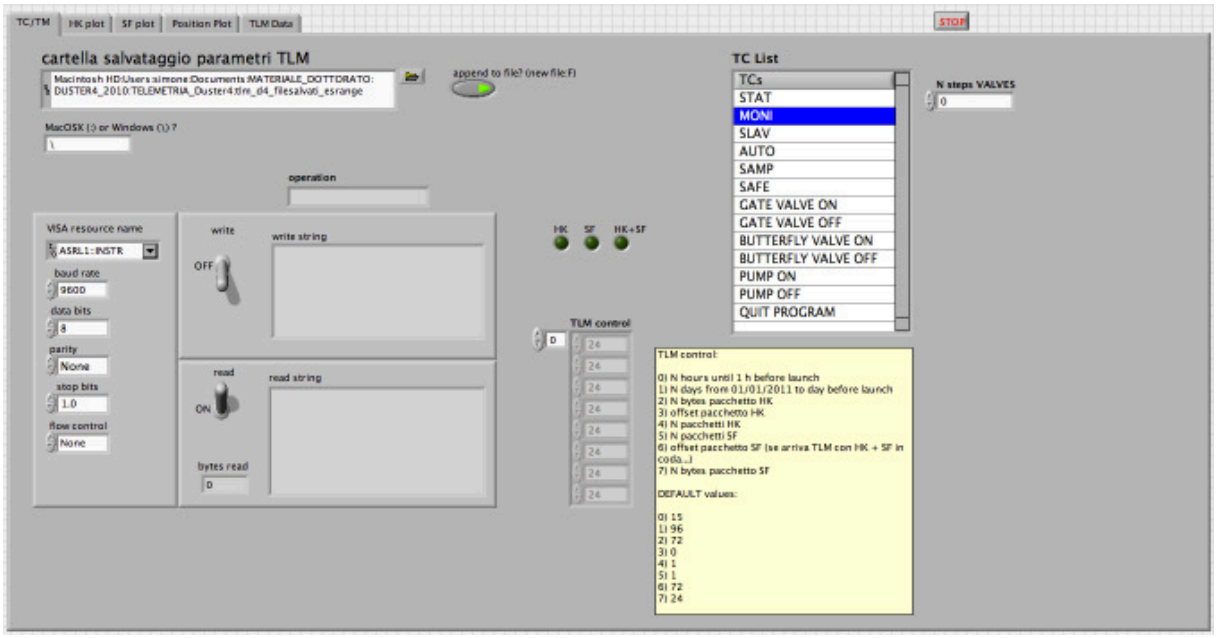

Figure 3.33: *EGSE, front panel: TLM controls.*

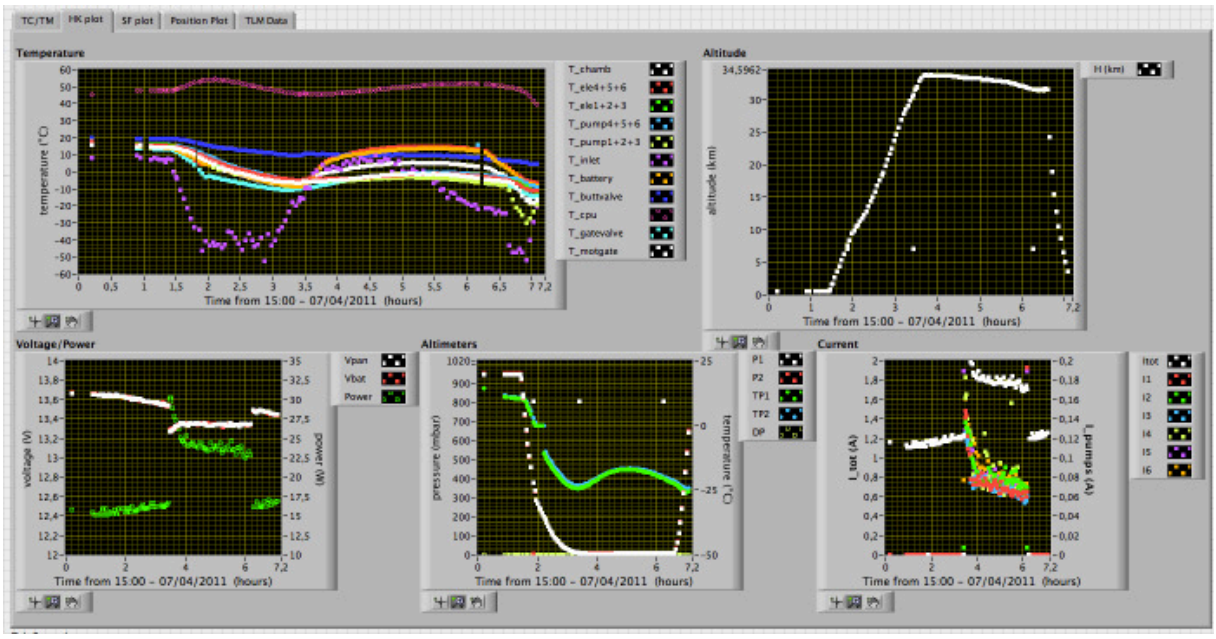

Figure 3.34: *EGSE, front panel: plots.*

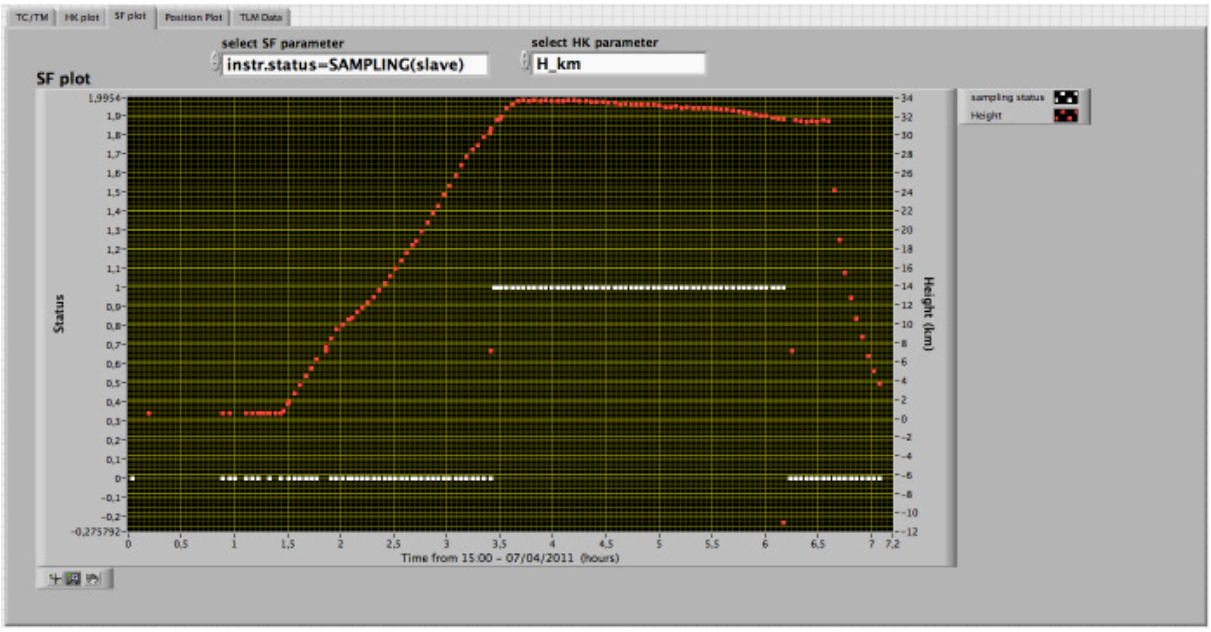

Figure 3.35: *EGSE, front panel: altitude profile vs sampling status.*

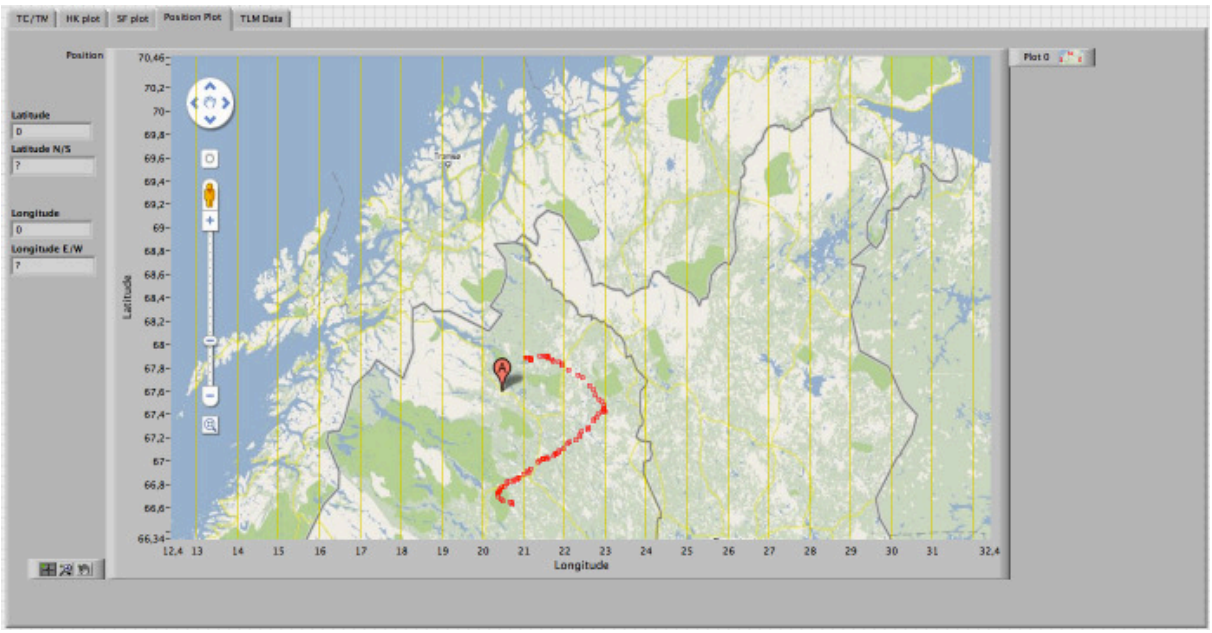

Figure 3.36: *EGSE, front panel: flight trajectory.*

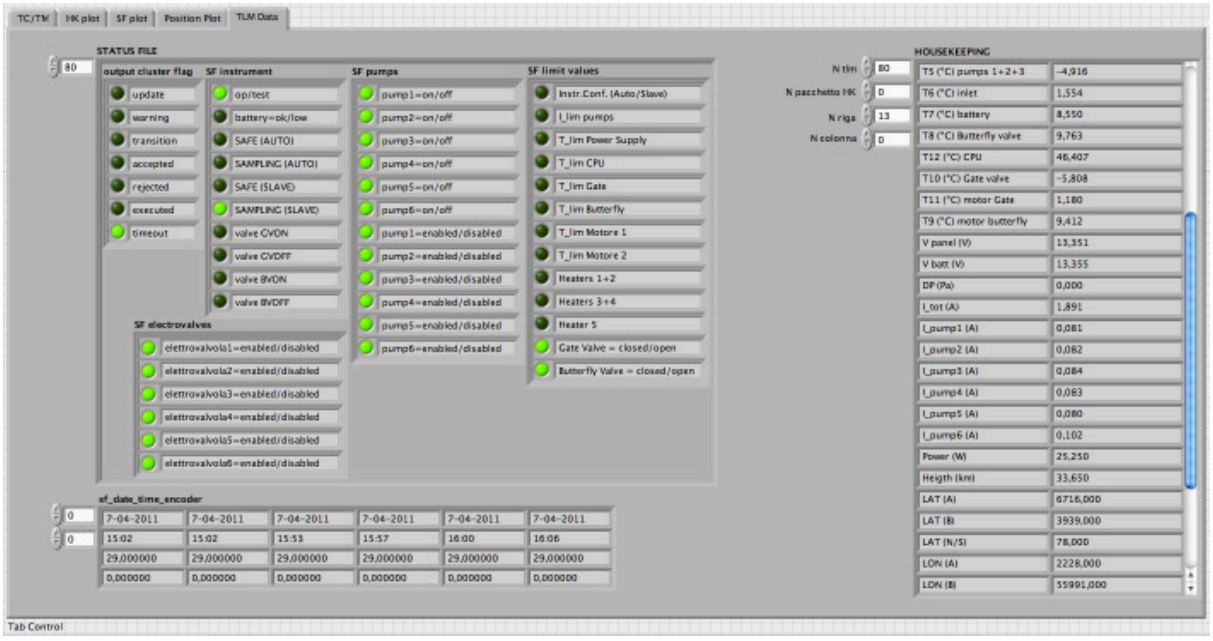

Figure 3.37: *EGSE, front panel: status file and housekeeping data.*

3.7 Thermal tests of pumping system

Thermal tests have been performed on the DUSTER-2011 instrument with the aim to check its correct working at low stratospheric temperatures. In order to perform thermal tests at low temperature, the instrument was mounted with its main mechanical components (pumping group, collection chamber, inlet tube, gate valve, butterfly valve and motors) and electronics in flight configuration. DUSTER has been placed in the environmental chamber, using the same experimental setup of flow rate measurements (fig. 3.20) in order to cool the chamber and to perform tests at stratospheric pressure. A copper cooling coil inside the chamber, in which flowed liquid nitrogen, was used to refrigerate the instrument. Once that the pressure reached a stratospheric value ($p = 3 \div 6$ mbar) inside the chamber (using the turbopump) we began to let the liquid nitrogen flow into the copper serpentine in order to cool the chamber. Meanwhile the instrument was connected to the laboratory pc through a serial cable; the communication between DUSTER and the experimenter was performed using the EGSE (2011 serial version). While the chamber was refrigerated and the internal temperature slowly decreased, the following tests were performed sending TC to the instrument:

- switching on of the instrument
- switching on of the pumping group
- opening and closing of gate valve
- opening and closing of butterfly valve
- check of correct opening/closing for both valves (encoder reading)
- switching off of the pumping group
- switching off of the instrument

DUSTER sent HK and SF packets periodically and upon request. In fig. 3.38 the plots of the temperatures of main components are showed. We can see from the plot that the minimum temperatures that we reached were $T_{chamb} = -125°\text{C}$ and $T_{Butt} = -120°\text{C}$. Even at these low temperatures the functioning of all mechanical parts of DUSTER was optimal, and we did not register any problem. All mechanic components don't need any lubrication in order to correctly work even at very low temperatures. For comparison the minimum temperature in stratosphere is typically $\approx -60°\text{C}$ at ≈ 15 km altitude, then it increases above $\approx 0°\text{C}$ at ≈ 40 km.

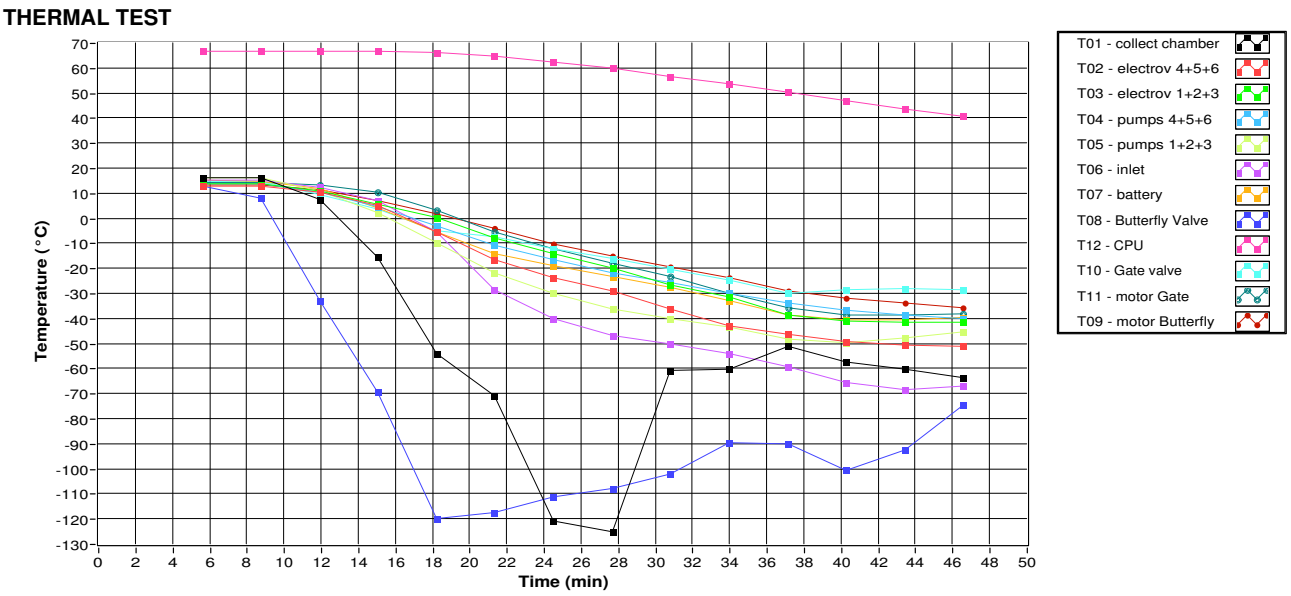

Figure 3.38: *Thermal tests: plots of temperatures of main components.*

3.8 DUSTER flights

DUSTER has performed 3 scientific flights since 2008 to date, plus a technical flight of the instrument prototype in 2006. In the tab. 3.8 are listed the principal informations about its flights.

year	***launch site***	***landing site***	H_{float}	Δt_{samp}	Q	V_{samp}
2006	Kiruna (Swe)	Kiruna	28-29 km	2 h	$< 1.62\ m^3/h$	$< 3.24\ m^3$
2008	Svalbard (Nor)	Greenland	37 km	36 h	$1\ m^3/h$	$36\ m^3$
2009	Svalbard (Nor)	Baffin Island (Can)	39 km	25 h	$1.04\ m^3/h$	$26\ m^3$
2011	Kiruna (Swe)	Kiruna	31-33 km	2.8 h	$1.30\ m^3/h$	$3.62\ m^3$

Table 3.8: *DUSTER flights.*

Chapter 4

DUSTER instrument calibration

Calibration of DUSTER instrument implies its *collection* or *sampling efficiency* to be measured, in order to fully characterize the instrument. In the following, the work performed in the direction of a complete DUSTER calibration is reported, stressing the preparatory work for a dedicated facility and the results of measurements aimed at comparing the efficiencies of different collecting techniques. For our purpose we can assimilate DUSTER to a sampling system, which aspires particles from the surrounding environment. The *inlet efficiency* η_{inlet} is defined as the product of two terms:

$$\eta_{inlet} = \eta_{asp} \cdot \eta_{transm} \tag{4.1}$$

The *aspiration efficiency* η_{asp} is the fraction of particles that enter the inlet with respect to the concentration of particles in the external environment [3]. A certain fraction of particles that are aspired through the inlet does not reach the interior of the sampling system and the collection substrate, because of losses through the sample lines due to various deposition mechanisms; so the *transmission efficiency* η_{transm} is defined as the fraction of sampled particles that reach the rest of the sampling system respect to the particles that cross the inlet. The inlet efficiency is thus the ratio of the concentration of particles that are transmitted to the aerosol transport section of the sampling system, to the original environmental particles concentration. Sampled particles while moving from the inlet to the rest of the sampling system and to the collection substrate are subject to losses. Particles losses through the sample line are due to several deposition mechanisms:

- Gravitational settling
- Diffusional deposition
- Inertial deposition (turbulent, at a bend, at flow constrictions)
- Electrostatic deposition

The *transport efficiency* $\eta_{transport}$ of the system takes into account all aerosol losses through the various sections of the sampling apparatus and the correlated deposition mechanisms. Finally the *sampling efficiency* η_{samp} is the ratio of particles reaching the collection substrate, to the external environmental concentration, and is defined as the product of the two terms:

$$\eta_{samp} = \eta_{inlet} \cdot \eta_{transport} = \eta_{asp} \cdot \eta_{transm} \cdot \eta_{transport} \tag{4.2}$$

The collection efficiency is thus:

$$\eta_{samp} = \frac{C_{sub}}{C_{env}} \tag{4.3}$$

where C_{sub} is the number concentration of particles collected on the substrate and C_{env} is the number concentration of particles in the external environment: in our case C_{env} is the concentration measured inside the environmental chamber A.

Given the measured flow rate Q of the instrument, if we know the total sampling time Δt_{samp} we can compute the air volume V_{samp} sampled during the flight:

$$V_{samp} = Q \times \Delta t_{samp} \tag{4.4}$$

Then from the count of the number of collected particles N_c, once we know the collection efficiency η_{samp} it is possible to suggest an estimate of the particle number density c_{strato} in stratosphere:

$$C_{strato} = \frac{N_c}{V_{samp} \times \eta_{samp}} \tag{4.5}$$

Calibration measurements are performed in three phases. In the first (phase I, section 4.1), a given and controlled configuration of aerosol concentration and pressure is reproduced in an environmental pressure chamber (A); the particles concentration

C_{env} is measured with a suitable technique. In the second (phase II, section 4.2) and third (phase III, section 4.3) phases, a comparison between the efficiencies of filtering and inertial collection is performed. In both cases, the same configuration as for phase I is reproduced, but the particles concentration is measured directly sampling with the DUSTER instrument using two alternative collection techniques: first, a nucleopore filter is used as a substrate, then an inertial impactor made of carbon film is used as a substrate. In the following the measure procedures are described.

4.1 Phase I: controlled particles inlet in an environmental chamber

To determine the optimal configuration necessary to reproduce a controlled aerosol inlet, several proofs have been made, using different experimental setups both for the particles inlet and for the concentration measure technique. In all the measurements aerosol droplets have been generated with monodisperse synthetic spherical particles suspended in distilled water; tests have been performed with particles of different diameters: 1, 5 and 10 μm (see tab. 4.1).

Particle diameter (μm)	*material*	*bulk density* (g/cm^3)	*type*
1.14 ± 0.05	polystyrene (latex)	1.51	MF-R-S1141
4.78 ± 0.19	SiO_2	1.90	R-97006
4.83 ± 0.12	polystyrene (latex)	1.51	MF-R-1450
9.78 ± 0.17	polystyrene (latex)	1.51	MF-R-2750

Table 4.1: *Synthetic particles used for calibration measurements.*

Measurements have been repeated keeping the environmental chamber A first at ambient pressure ($p_A = 1.013$ bar) and then at stratospheric pressure ($p_A = 3 \div 6$ mbar). In order to inlet aerosol in the chamber A at stratospheric pressure, it is necessary first to inlet the particles in a small chamber B, with higher pressure ($p_B \gg p_A$; typically $p_B \sim 10^2$ mbar) and smaller volume ($V_B \ll V_A$). The chamber B is connected to A through a gate valve, initially closed; once the valve is open, the pressure in the two chambers reaches an equilibrium value and the particles are shot from B to A. Before of describing the different experimental setups that we tested in order to determine the optimal configuration, I will describe the computing of the gravitational settling velocity of aerosol particles.

4.1.1 Settling velocity of aerosol particles

Aerosol particles that are inlet in chamber A consist of synthetic particles suspended in water droplets; after the inlet the droplets vaporize and the particles begin to fall for gravitational settling. The settling velocity of aerosol particles depends on their density, air density and other parameters; in natural atmosphere, for $\rho/\rho_p < 10^{-3}$, according to Kasten (1968) [48] the relation is:

$$v_{settl}(r) = \frac{2}{9}\frac{\rho_p r^2 g}{\eta} \cdot \left[1 + \frac{\lambda}{r}\left(A + Be^{-Cr/\lambda}\right)\right] \tag{4.6}$$

where:

- ρ = air density
- ρ_p = particle density
- r = particle radius
- g = acceleration of gravity
- η = dynamic viscosity
- λ = mean free path length
- A, B, C = dimensionless empirical constants (they depend on λ)

The values of these constants are:

$$\begin{cases} A &= 1.249 \\ B &= 0.42 \\ C &= 0.87 \end{cases}$$

The relation is valid for the Reynolds number is sufficiently small:

$$Re = \frac{2r\rho v_{settl}}{\eta} \leq 0.1$$

The Reynolds number remains < 0.1 within the whole atmosphere up to 80 km height, if $r \leq 10\ \mu m$; remembering that $Re \propto v_{settl} \propto \rho_p$ the relation for settling velocity is valid in these conditions for particles with any density up to 6 g/cm^3 [48].

In order to obtain the settling velocity of the particles that we used, we have to calibrate the relation 4.6. From Kasten (1968) we get tabulated values of v_{settl}, calculated for particles with density $\rho_p = 1\ \mathrm{g}/cm^3$ and for U.S. Standard Atmosphere, for different values of height z and particle radius r (fig. 4.1).

z (km)	r (μm) 0.003	0.01	0.03	0.1	0.3	1	3	10
0	4.1150E-06	1.4283E-05	4.8096E-05	2.3182E-04	1.4008E-03	1.3188E-02	1.1264E-01	1.2280E 00
1	4.6069E-06	1.5930E-05	5.3080E-05	2.4864E-04	1.4580E-03	1.3524E-02	1.1493E-01	1.2506E 00
2	5.1727E-06	1.7825E-05	5.8811E-05	2.6796E-04	1.5224E-03	1.3890E-02	1.1738E-01	1.2745E 00
3	5.8253E-06	2.0009E-05	6.5415E-05	2.9023E-04	1.5951E-03	1.4289E-02	1.1999E-01	1.2997E 00
4	6.5809E-06	2.2537E-05	7.3058E-05	3.1600E-04	1.6778E-03	1.4725E-02	1.2279E-01	1.3264E 00
5	7.4591E-06	2.5474E-05	8.1936E-05	3.4593E-04	1.7726E-03	1.5205E-02	1.2579E-01	1.3548E 00
6	8.4837E-06	2.8901E-05	9.2287E-05	3.8083E-04	1.8818E-03	1.5736E-02	1.2903E-01	1.3848E 00
7	9.6837E-06	3.2912E-05	1.0440E-04	4.2168E-04	2.0085E-03	1.6325E-02	1.3254E-01	1.4168E 00
8	1.1096E-05	3.7630E-05	1.1864E-04	4.6970E-04	2.1565E-03	1.6985E-02	1.3635E-01	1.4509E 00
9	1.2765E-05	4.3208E-05	1.3547E-04	5.2644E-04	2.3305E-03	1.7730E-02	1.4052E-01	1.4875E 00
10	1.4747E-05	4.9831E-05	1.5544E-04	5.9377E-04	2.5363E-03	1.8575E-02	1.4510E-01	1.5269E 00
11	1.7116E-05	5.7741E-05	1.7929E-04	6.7411E-04	2.7813E-03	1.9546E-02	1.5017E-01	1.5694E 00
12	2.0005E-05	6.7369E-05	2.0814E-04	7.6918E-04	3.0490E-03	2.0299E-02	1.5235E-01	1.5769E 00
13	2.3385E-05	7.8635E-05	2.4190E-04	8.8072E-04	3.3665E-03	2.1191E-02	1.5484E-01	1.5848E 00
14	2.7337E-05	9.1809E-05	2.8140E-04	1.0115E-03	3.7427E-03	2.2259E-02	1.5776E-01	1.5942E 00
15	3.1959E-05	1.0721E-04	3.2758E-04	1.1646E-03	4.1873E-03	2.3540E-02	1.6118E-01	1.6052E 00
16	3.7362E-05	1.2522E-04	3.8159E-04	1.3440E-03	4.7117E-03	2.5077E-02	1.6521E-01	1.6183E 00
17	4.3679E-05	1.4628E-04	4.4474E-04	1.5539E-03	5.3291E-03	2.6919E-02	1.6997E-01	1.6335E 00
18	5.1065E-05	1.7090E-04	5.1858E-04	1.7995E-03	6.0547E-03	2.9122E-02	1.7559E-01	1.6515E 00
19	5.9699E-05	1.9968E-04	6.0491E-04	2.0868E-03	6.9066E-03	3.1751E-02	1.8229E-01	1.6725E 00
20	6.9792E-05	2.3332E-04	7.0582E-04	2.4227E-03	7.9057E-03	3.4878E-02	1.9027E-01	1.6972E 00
21	8.1619E-05	2.7274E-04	8.2405E-04	2.8162E-03	9.0760E-03	3.8553E-02	1.9939E-01	1.7208E 00
22	9.5383E-05	3.1862E-04	9.6165E-04	3.2743E-03	1.0441E-02	4.2890E-02	2.1034E-01	1.7489E 00
23	1.1140E-04	3.7200E-04	1.1218E-03	3.8076E-03	1.2032E-02	4.7999E-02	2.2354E-01	1.7829E 00
24	1.3000E-04	4.3399E-04	1.3077E-03	4.4268E-03	1.3882E-02	5.3987E-02	2.3936E-01	1.8237E 00
25	1.5160E-04	5.0598E-04	1.5237E-03	5.1462E-03	1.6034E-02	6.0997E-02	2.5826E-01	1.8725E 00
26	1.7666E-04	5.8953E-04	1.7743E-03	5.9812E-03	1.8533E-02	6.9179E-02	2.8074E-01	1.9311E 00
28	2.3937E-04	7.9856E-04	2.4013E-03	8.0706E-03	2.4790E-02	8.9785E-02	3.3872E-01	2.0855E 00
30	3.2344E-04	1.0788E-03	3.2420E-03	1.0872E-02	3.3186E-02	1.1757E-01	4.1873E-01	2.3077E 00
32	4.3586E-04	1.4535E-03	4.3661E-03	1.4619E-02	4.4418E-02	1.5484E-01	5.2775E-01	2.6247E 00
34	5.8605E-04	1.9541E-03	5.8679E-03	1.9623E-02	5.9418E-02	2.0463E-01	6.7402E-01	3.0564E 00
36	7.8270E-04	2.6096E-03	7.8342E-03	2.6176E-02	7.9065E-02	2.6993E-01	8.6733E-01	3.6503E 00
38	1.0383E-03	3.4617E-03	1.0390E-02	3.4695E-02	1.0461E-01	3.5491E-01	1.1201E 00	4.4497E 00
40	1.3688E-03	4.5633E-03	1.3695E-02	4.5710E-02	1.3764E-01	4.6488E-01	1.4482E 00	5.5071E 00
42	1.7933E-03	5.9782E-03	1.7940E-02	5.9857E-02	1.8008E-01	6.0619E-01	1.8706E 00	6.8847E 00
44	2.3359E-03	7.7868E-03	2.3365E-02	7.7942E-02	2.3432E-01	7.8688E-01	2.4114E 00	8.6620E 00
46	3.0255E-03	1.0085E-02	3.0261E-02	1.0093E-01	3.0327E-01	1.0166E 00	3.0993E 00	1.0934E 01
48	3.8933E-03	1.2978E-02	3.8939E-02	1.2985E-01	3.9004E-01	1.3058E 00	3.9660E 00	1.3808E 01
50	4.9889E-03	1.6630E-02	4.9896E-02	1.6638E-01	4.9961E-01	1.6710E 00	5.0615E 00	1.7453E 01
52	6.3919E-03	2.1307E-02	6.3925E-02	2.1314E-01	6.3990E-01	2.1386E 00	6.4642E 00	2.2124E 01
54	8.1778E-03	2.7260E-02	8.1784E-02	2.7267E-01	8.1850E-01	2.7340E 00	8.2506E 00	2.8080E 01
56	1.0492E-02	3.4973E-02	1.0492E-01	3.4981E-01	1.0499E 00	3.5054E 00	1.0565E 01	3.5799E 01
58	1.3510E-02	4.5035E-02	1.3511E-01	4.5043E-01	1.3518E 00	4.5117E 00	1.3585E 01	4.5868E 01
60	1.7463E-02	5.8210E-02	1.7463E-01	5.8217E-01	1.7470E 00	5.8293E 00	1.7538E 01	5.9050E 01
62	2.2645E-02	7.5486E-02	2.2646E-01	7.5493E-01	2.2653E 00	7.5569E 00	2.2722E 01	7.6336E 01
64	2.9500E-02	9.8334E-02	2.9501E-01	9.8342E-01	2.9508E 00	9.8420E 00	2.9578E 01	9.9205E 01
66	3.8766E-02	1.2922E-01	3.8766E-01	1.2923E 00	3.8774E 00	1.2931E 01	3.8846E 01	1.3011E 02
68	5.1373E-02	1.7124E-01	5.1374E-01	1.7125E 00	5.1381E 00	1.7133E 01	5.1455E 01	1.7216E 02
70	6.8892E-02	2.2964E-01	6.8893E-01	2.2965E 00	6.8901E 00	2.2974E 01	6.8977E 01	2.3058E 02
72	9.3289E-02	3.1096E-01	9.3290E-01	3.1097E 00	9.3298E 00	3.1106E 01	9.3376E 01	3.1193E 02
74	1.2782E-01	4.2605E-01	1.2782E 00	4.2606E 00	1.2782E 01	4.2615E 01	1.2791E 02	4.2705E 02
76	1.7731E-01	5.9103E-01	1.7731E 00	5.9104E 00	1.7732E 01	5.9114E 01	1.7740E 02	5.9207E 02
78	2.4925E-01	8.3082E-01	2.4925E 00	8.3083E 00	2.4926E 01	8.3093E 01	2.4934E 02	8.3189E 02
80	3.5574E-01	1.1858E 00	3.5574E 00	1.1858E 01	3.5575E 01	1.1859E 02	3.5584E 02	1.1869E 03

Figure 4.1: *Settling velocity (cm/s) calculated for particles with density $\rho_p = 1g/cm^3$ and 1962 US Standard Atmosphere, for different heights (z) and radii (r) [From Kasten (1968), [48]].*

At sea level pressure, for particle with radius $r = 3\ \mu m$ we have $v_{settl} = 1.13 \cdot 10^{-1}$ cm/s; thus, using for the mean free path length the value $\lambda = 6.53 \cdot 10^{-6}$ cm, we obtain the dynamic viscosity $\eta = 1.78 \times 10^{-4}\ \mathrm{g}{\cdot}cm^{-1} \cdot s^{-1}$. This value of η can be

now used to determine v_{settl} for other radii. The fall speed values for the particles that we used at ambient pressure (1.013 bar) are listed in tab. 4.2.

Sea level pressure		$p = 1.013\ bar$
Particle diameter (μm)	*density* (g/cm^3)	$v_{settling}(cm/s)$
1.14	1.51	$6.90 \cdot 10^{-3}$
4.78	1.90	$1.38 \cdot 10^{-1}$
4.83	1.51	$1.12 \cdot 10^{-1}$
9.78	1.51	$4.50 \cdot 10^{-1}$

Table 4.2: *Settling velocities for synthetic particles used for calibration measurements (ambient air pressure).*

In order to determine the fall speed of aerosol particles at stratospheric pressure (6 mbar) we fit the values listed in fig. 4.1. Calling v^1_{settl} these values (they refer to unit density particles) we can write, for particles with any density ρ_p:

$$v_{settl}(r) = v^1_{settl} \times \rho_p \tag{4.7}$$

An exponential fitting procedure of these data leads to plots in fig. 4.2; from fit procedure we determined the parametric equation:

$$v_{settl}(r) = v_0 + A \times e^{r/t} \tag{4.8}$$

where v_0, A and t are fit parameters. Thus we obtained the settling velocity at stratospheric pressure for our particles, listed in tab. 4.3.

Stratospheric pressure		$p = 6\ mbar \div z = 34\ km$	$p = 2.7\ mbar \div z = 40km$
Particle diam. (μm)	$\rho_p(g/cm^3)$	$v_{settling}(cm/s)$	$v_{settling}(cm/s)$
1.14	1.51	$1.74 \cdot 10^{-1}$	$3.97 \cdot 10^{-1}$
4.78	1.90	$9.93 \cdot 10^{-1}$	2.17
4.83	1.51	$7.98 \cdot 10^{-1}$	1.74
9.78	1.51	1.80	3.69

Table 4.3: *Settling velocities for synthetic particles used for calibration measurements (stratospheric pressure).*

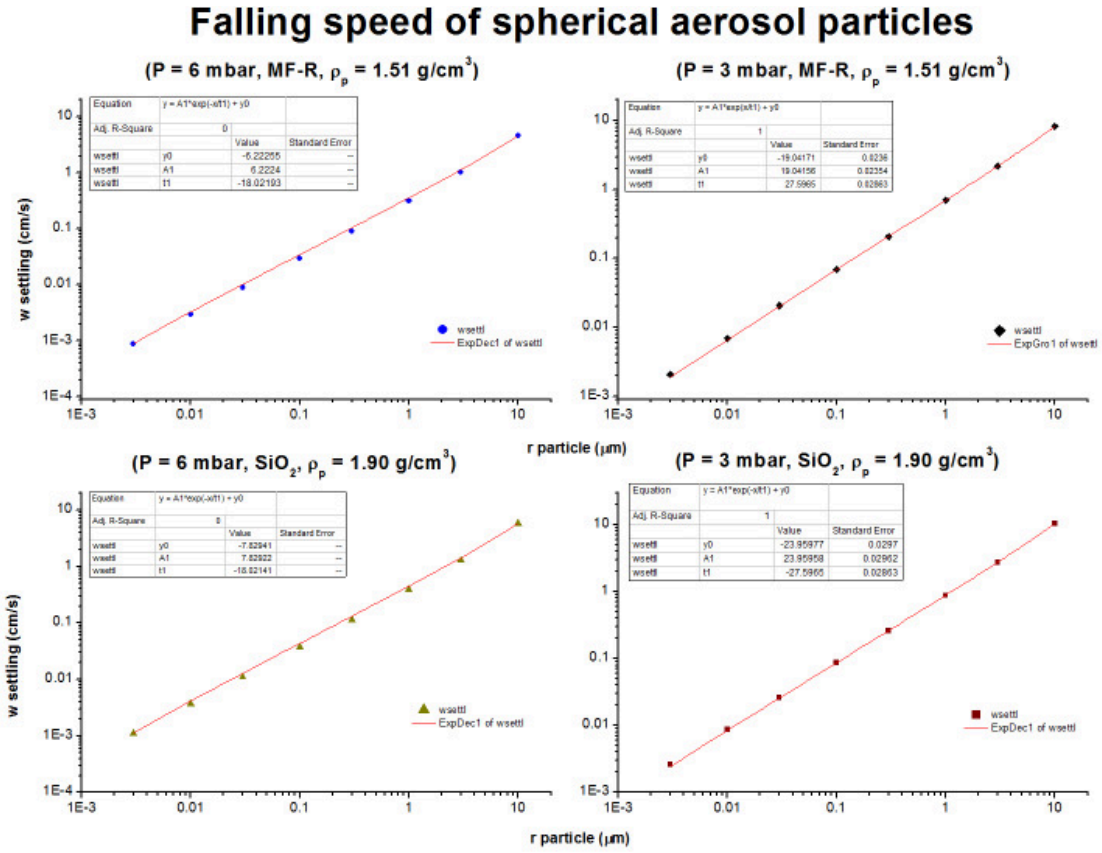

Figure 4.2: *Settling velocity of spherical particles at 6 and 3 mbar pressure.*

4.1.2 Visual preliminary measurements

In the first test aerosol droplets have been generated using compressed air to vaporize the aqueous suspension, and have been inlet in the pressure chamber through a simple sprayer (experimental setup in fig. 4.3). In this test the aerosol concentration has been measured thanks to the gravitational settling of the particles: a glass slide on the bottom of the chamber was used as a deposition substrate. The procedure has the following steps:

- inlet of aerosol droplets in the chamber, for 2-4 minutes;
- gravitational settling for few minutes;
- the glass slide has been extracted from the chamber and observed under an optical microscope for particles counting.

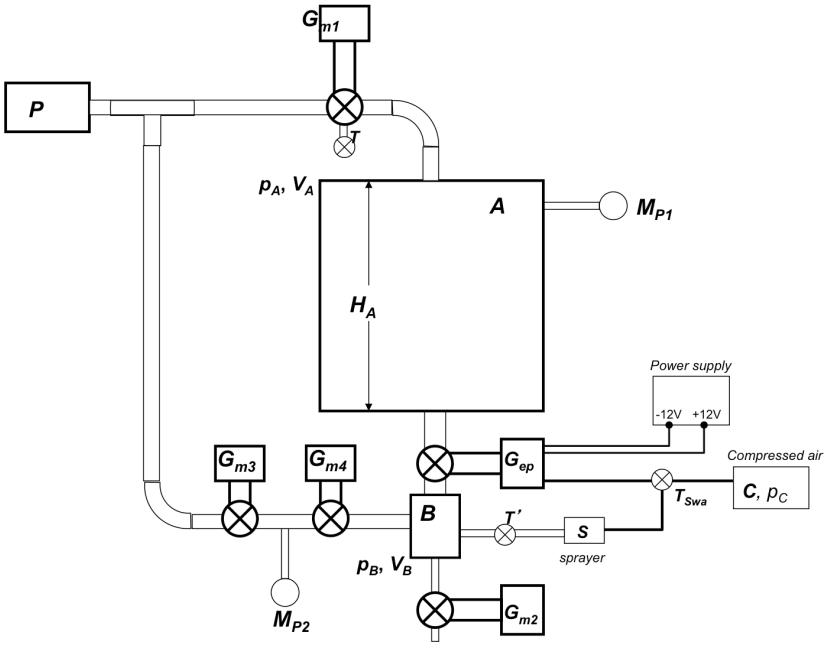

Figure 4.3: *Phase I: first experimental setup. This setup has been used for test at stratospheric pressure. A = great environmental chamber; B = small environmental chamber; P = pump; G_m = gate valves; M_P = pressure gauge; T,T' = taps; G_{ep} = electropneumatic gate valve; C = compressor. For test at ambient pressure, the particles are inlet directly in the chamber A without using the small chamber B.*

In order to inlet particles in the chamber A at stratospheric pressure (fig. 4.3), we first pump in A, lowering the pressure down to $\sim 0.1 mbar$, and keeping closed the electro-pneumatic valve G_{ep}. The volume ratio between the chambers A and B ($V_A = 27$ lt and $V_B = 0.86$ lt respectively) is such that a pressure $p_B \approx 250$ mbar in B is needed to reach a final pressure $p_A = 6$ mbar in A, once the valve is open. The same compressor (C in fig. 4.3) has been used to vaporize aerosol droplets and to control the electro-pneumatic valve G_{ep}. In this first setup the particles have been inlet in A from the bottom of the chamber. This same procedure has been repeated several times. The sprayer system used here was not very repeatable, so these preliminary results are not very reliable. In fig. 4.4 an image of a fraction of the slide grid before gravitational settling is compared with the same area after settling; the optical microscope was *Leitz - Labovert FS*.

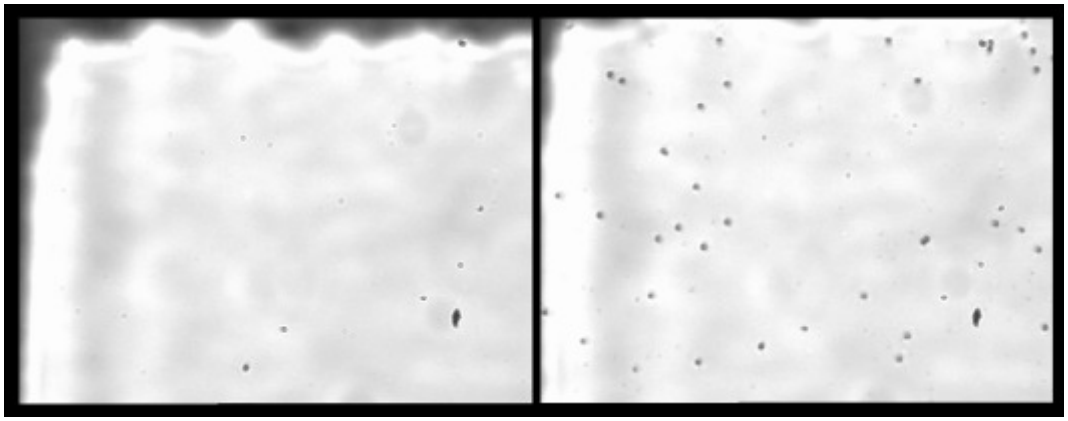

Figure 4.4: *Phase I: first experimental setup. Comparison of a portion of slide grid area between before (left) and after (right) settling. There are some spots on the microscope objective visible in both pictures.*

With this first setup we measured a volume concentration (and a standard deviation):

$$\rho_V = \langle \rho \rangle \pm \sigma_p = 40.65 \pm 30.07 \text{ particles } /cm^3 \tag{4.9}$$

with a relative standard deviation:

$$\sigma_{rel} = \frac{\sigma_p}{\langle \rho \rangle} = 78\% \tag{4.10}$$

4.1.3 OPC test and hints of Mie Theory

In a second experimental setup, an automatic aerosol generator and an optical particle counter (OPC) have been used in order to generate aerosol particles and to measure the concentration.

We used a *Grimm Aerosol Generator* coupled with a *Grimm Sky-OPC*. The main chamber A still has the volume $V_A = 27$ lt, and the small chamber B for pre-inlet has the volume $V_B = 0.86$ lt. The experimental setup is that of fig. 4.5.

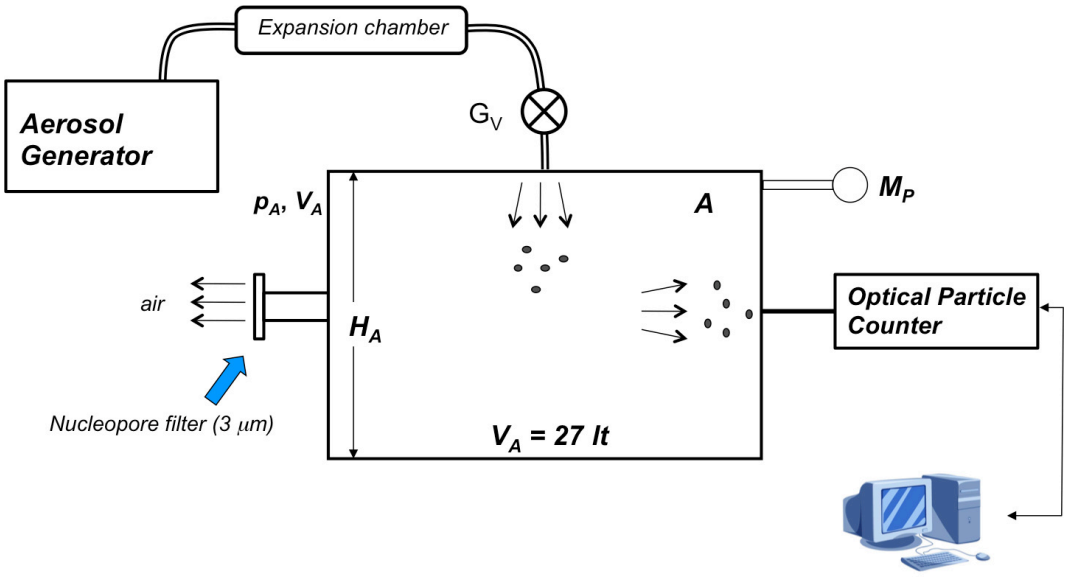

Figure 4.5: *Phase I: second experimental setup. The particles are product from the aerosol generator and are inlet in the main chamber A through an expansion chamber. The pump lowers the pressure in A. M_p is the pressure gauge. The optical particle counter measures the aerosol concentration in A, and it is connected to a pc. An open tube on the side of the main chamber, coupled with a 3 μm nucleopore filter, allows the air to exit from the chamber, keeping particles inside.*

The aerosol generator produces aerosol particles vaporizing an aqueous suspension kept in a container (*atomizer*); the atomizer can contain about ten milliliters of aqueous suspension. The aerosol production rate can be adjusted setting the air flow rate through the atomizer (Q_{air}) of the generator, and this is done regulating the pressure p_{air} of the air used to vaporize the suspension, using a rotary knob on the instrument front panel: setting the pressure in the range 100-750 mbar, the air outflow

rate varies approximately linearly from 2 to 6 l/min; an aerosol outflow rate of about 0.1 ml/min corresponds to an air flow through the atomizer $Q_{air} = 6$ l/min and a pressure $p_{air} = 750$ mbar. The generator uses the ambient air to produce aerosol: the air is first dried through a cylinder containing silica gel. The aerosol droplets produced by the generator flow in a tube and are inlet into the main chamber, after flowing through an *expansion chamber*.
The optical particle counter consists of a sensible volume, in which particle pass, a laser source and a photodetector. The OPC aspirates air and particles from the main chamber; it has a small pump inside, that guarantees a constant flow rate of about 1.2 l/min but it needs a further external pump to reach a sufficient flow rate. The sampled air flow rate is controlled by a critical orifice, based upon the measured ratio of the pressure behind and before the orifice. The laser optics and the measurement cell are protected from pollution through a rinsing air circulation. As the particles pass through the sensible volume, they are irradiated by the laser source; the scattered light is then revealed from the photodetector.
The process of scattering of light from a spherical particle (and in general from non-spherical particles) is described from the Mie Theory [5]. Analyzing the scattered light from particles it is possible to obtain information on optical and physical properties of aerosol; indeed the amount of scattered radiation depends on the physical properties and the optical constants of the particles. In particular, let us consider an ensemble of particles suspended in a *non-absorbing* medium and placed in a beam of light, between the source and a detector D; in this configuration (fig. 4.6), the detector receives the electromagnetic power U from the particles; if the particles are removed, then the detector receives the power U_0, with $U_0 > U$.

The difference $\Delta U = U_0 - U$ is due to the *extinction* of light by particles. If we consider only one particle, let A be the area of an imaginary sphere of radius r surrounding the particle; the mean power that crosses the surface A is:

$$W_a = -\int_A \mathbf{S} \cdot \hat{\mathbf{e}}_\mathbf{r} dA \tag{4.11}$$

in which $\hat{\mathbf{e}}_\mathbf{r}$ indicates the direction of propagation of the electric field, and the *Poynting vector* is given in general by:

$$\mathbf{S} = \mathbf{E} \times \mathbf{H} \tag{4.12}$$

with $\mathbf{E}$ and $\mathbf{H}$ electric and magnetic field respectively. The quantity W_a is the

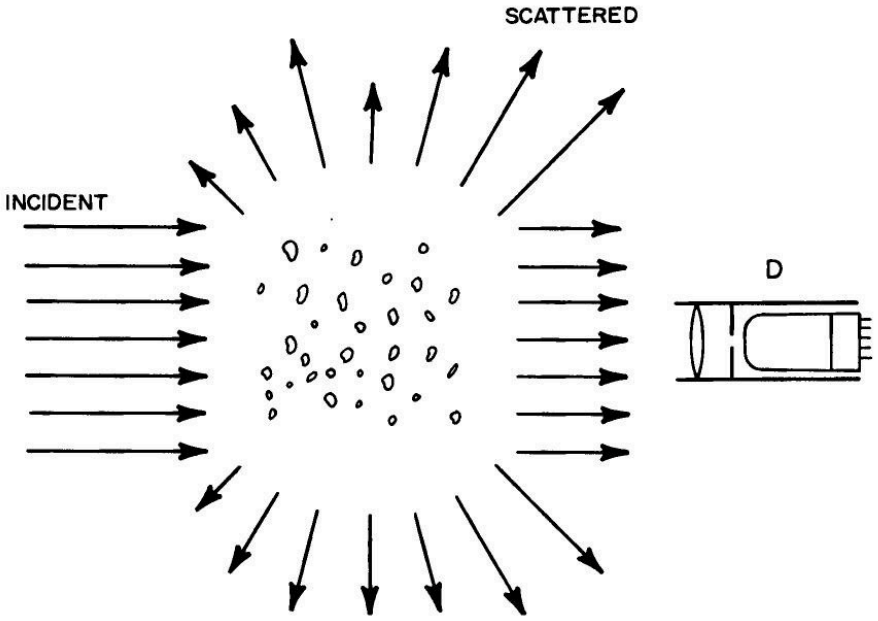

Figure 4.6: *Extinction of light by particles in a medium: absorption and scattering.*

absorbed power, and it is related to the energy extinction rate by:

$$W_{ext} = W_a + W_s \tag{4.13}$$

in which W_s is the power scattered by particles.

In the case in which the detector is collimated, and if $\hat{\mathbf{e}}_\mathbf{r}$ is not too close to the forward direction $\hat{\mathbf{e}}_\mathbf{z}$, then the detector is sensible only to the scattered power. The scattered Poynting vector is:

$$\mathbf{S_s} = \frac{1}{2}\mathrm{Re}\{\mathbf{E_s} \times \mathbf{H_s^*}\} \tag{4.14}$$

So the scattered power received by the detector D is proportional to:

$$\mathbf{S_s} \cdot \hat{\mathbf{e}}_\mathbf{r} \Delta A = \frac{k}{2\omega\mu} \frac{|\mathbf{A}|^2}{k^2} \Delta\Omega \tag{4.15}$$

where ΔA is the sensible area of the detector and $\Delta\Omega = \Delta A/r^2$ is the solid angle subtended by the detector; here μ is the magnetic permeability of the medium, k is the wave number ($k = 2\pi/\lambda$) and $\mathbf{A}$ is the area surrounding the particle. Then it is possible to calculate the *scattering cross section* [5]:

$$C_{sca} = \int_{4\pi} \frac{|\mathbf{X}|^2}{k^2} d\Omega \tag{4.16}$$

where the quantity $|\mathbf{X}|^2$ is related to the components of the incident and scattered electric field and is the *vector scattering amplitude* [5]. The differential scattering cross section (dC_{sca}) specifies the angular distribution of the scattered light. Finally the *efficiency of scattering* is defined as:

$$Q_{sca} = \frac{C_{sca}}{G} \tag{4.17}$$

in which G is the projected particle cross-sectional area; $G = \pi a^2$ for a sphere of radius a. So applying an inverse computing starting from the scattered power measured by a photodetector it is possible to obtain information about the radius a of a particle.
The procedure used for the OPC test at ambient pressure is the following (fig. 4.5):

- preparation of an aqueous suspension consisting in latex particles suspended in water (few ml); here we used 4.78 μm SiO_2 particles ($\rho = 1.90$ g/cm^3);
- the aerosol generator is switched on, allowing the inlet of particles in main chamber A for 2-4 minutes;
- after the generator is switched off, we switch on the OPC;
- the OPC measurement lasts about 10 minutes.

Because the functioning of the OPC is based on air aspiration, and in order to limit the interference between the measuring process and the gravitational settling of the particles, the OPC is only switched on every 60 sec to take a single acquisition and then switched off, each single acquisition lasting 6 sec; in this configuration the number concentration is measured as $N_{particles}$/100 ml. The OPC is controlled via serial port from the pc (using *hyper terminal*) and then the saved data are elaborated with a LabView tool; it performs measurements using 31 channels, corresponding to 31 lower limits for particle diameters, and it determines counts of particles for each size

channel (size distribution): the first channel corresponds to the range $d > 0.25\ \mu m$, the second to the range $d > 0.28\ \mu m$ and the last channel corresponds to particle sizes $d > 32\ \mu m$.
Then we compute the concentration of particles in the size range $4 < d < 7.5\ \mu m$: we chose an upper limit higher than $5\ \mu m$, taking into account possible measurement errors; in fact a sovra-estimation of particle size is possible, because the optical particle counter was calibrated with polystyrene particles ($\rho = 1.51$ g/cm^3). The measured concentration during the 60 sec time interval has an exponential decay; an exponential fit of the size distribution gives us the initial number concentration. A plot of the concentration is in fig. 4.7. The initial concentration measured for particles in the range $4 < d < 7.5\ \mu m$ is 30 particles/100 ml, that is 0.3 particles/cm^3. The different result with respect to the previous measurements (see section 4.1.2) obviously depends on the different system used to count particles, the different experimental setup, a longer or shorter chain of inlet of particles.

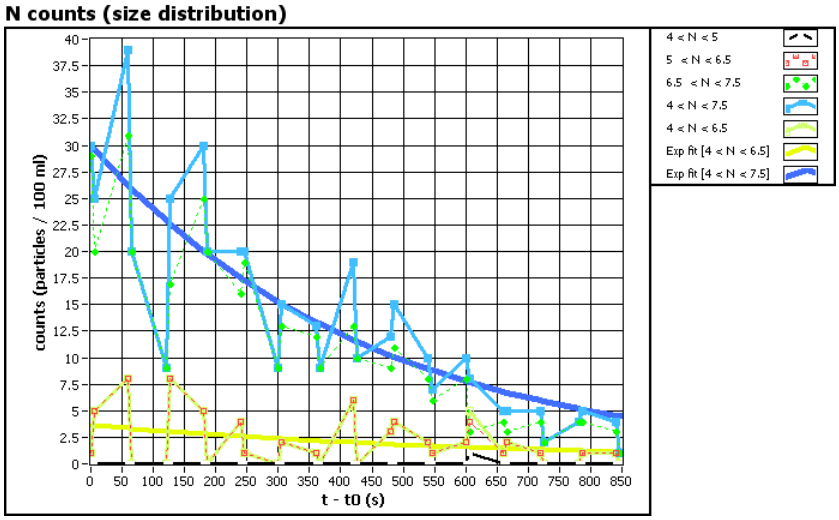

Figure 4.7: *Sky-OPC measurements of particle size distribution. The yellow exp fit corresponds to particles in the range* $4 < d < 6.5\ \mu m$*; the blue exp fit corresponds to particles in the range* $4 < d < 7.5\ \mu m$.

4.1.4 OPC and settling measurements in main chamber

The third experimental setup is based on the use of a greater main chamber for particle deposition; the main chamber has the volume $V_A = 157$ lt. We now use a larger main chamber because in the phase II and III (see section 4.2 and 4.3) the DUSTER instrument has to be put inside this chamber. The pre-inlet chamber has the volume $V_B = 0.47$ lt. Particles number concentration inside A is measured through gravitational settling onto microscope slides, and also monitored with the OPC; the optical microscope for slide analyses is a *Leica*, M205C. The aerosol generator and OPC types are described in section 4.1.3. The pump we used is *Pfeiffer Vacuum*, HiCUBE. The analyses of the slides with the optical microscopes have been performed in a cleanroom, *Terra Universal*, Class 100. The experimental setup is that of fig. 4.8.

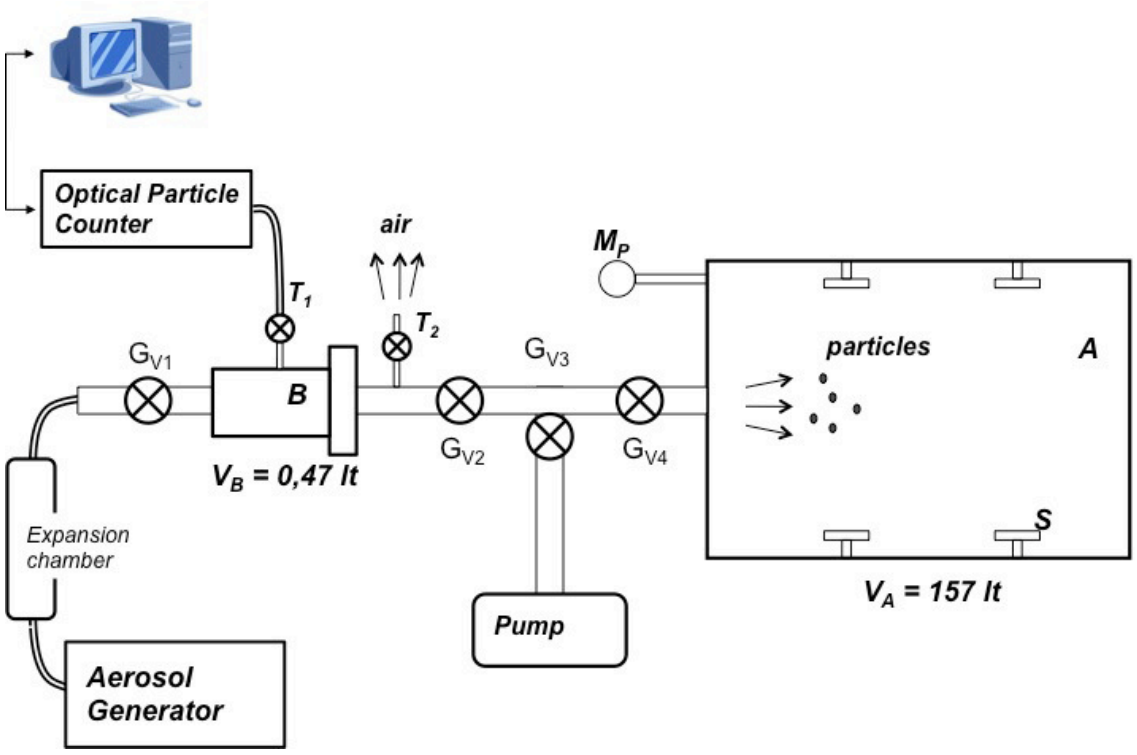

Figure 4.8: *Phase I: third experimental setup, as used for measurements. A = main chamber; B = small chamber for pre-inlet; G_V = gate valves; T = tap valves; M_P = pressure gauge; S = stub for settling.*

Experimental procedure

The procedure is as follows:

1. an aqueous suspension is created, using PSL-Latex spherical particles and water; the volume is about 10 ml; these particles have been previously observed at the optical microscope onto a reference slide, in order to allow the successive identification;
2. the aqueous suspension is put into the *atomizer*;
3. optical microscope slides are used as substrates; they must be characterized before of the settling, in order to check if any material is already on them; then, the slides are placed on the bottom of the main chamber A (see fig.4.8)
4. at the beginning, all the valves except G_{V2} must be kept open; the valve G_{V2} is only open to allow the injection of particles from B to A;
5. keeping G_{V2} closed and G_{V3}, G_{V4} open, air is pumped from the large chamber A, until the pressure drops down to about $0.1 - 0.3$ mbar;
6. after the pumping in A, the valve G_{V3} must be close;
7. at the end of the pumping, the aerosol generator is switched on: aerosol particles are injected into B for $t_{pre-inlet} = 10$ min; the valve T_2 is kept open in order to limit the pressure inside B at $p_B = 1013$ mbar during the pre-inlet phase;
8. the Sky-OPC is switched on after 5 min from the beginning of the pre-injection phase; it is maintained switched on for 5 min, in order to monitor the injection of particles into B, and it is shut down at the end of the time interval $t_{pre-inlet}$; the OPC is controlled via terminal from the pc (see section 4.1.3);
9. after the pre-inlet, the valves G_{V1}, T_1 and T_2 must be closed, and the aerosol generator is switched off;
10. the valve G_{V2} is open for 1 s, and then closed again; this is the injection phase: the aerosol particles are inlet from B to A;
11. the volume ratio between the two chambers, V_A/V_B, is such that, if the initial pressure $p_{A,i}$ in the large chamber is $0.1 - 0.3$ mbar, and the pressure in B is $p_{B,i} = 1013$ mbar, then after opening the valve G_{V2} for 1 s, the equilibrium pressure in the chamber A is about $p_A = 6$ mbar;

12. after the injection, the gravitational settling of particles on the substrates lasts several minutes, taking into account the settling velocities calculated in the section 4.1.1;
13. after $t_{settling} \approx 10$ min, air reentry inside A is performed through a small valve;
14. finally, the substrates can be extracted from A and analyzed under the optical microscope;
15. this procedure has been repeated five times: $n_{meas} = 5$.

Results for $4.83\ \mu m$ **particles**

The compute of the number concentration for particles with $d = 4.83 \pm 0.12\ \mu m$ has been determined with the following procedure, relatively to each of the 5 measurements performed. For each analyzed slide, a certain number of rectangular areas ($n_A = 10 \div 40$) have been observed, the counts being made at a microscope magnification $Mag = 12.5$ X (see fig.4.9 and 4.10). With this magnification, each single observed area (A_{LEICA}), that is visualized on the optical microscope, has sizes $a' = 54.25$ pixels and $b' = 72.25$ pixels; a particle with $d = 4.83\ \mu m$ corresponds to an average diameter $\langle d' \rangle = 0.65$ px, assuming a maximum error $\Delta d' = \Delta a' = \Delta b' = 0.05$ px; for a Gaussian distribution of the errors the standard deviation is $\sigma = \frac{1}{3}\Delta$. Thus the proportion between the dimensions in pixels and the real size is given by:

$$R = d/\langle d' \rangle = 7.43\ \mu m/px$$

so the real size is:

$$\begin{cases} a &= R \cdot a' = 403.12\ \mu m \\ b &= R \cdot b' = 536.87\ \mu m \end{cases} \tag{4.18}$$

and thus we obtain the single area $A_{LEICA} = 0.22\ mm^2$. The standard deviations on the dimensions have been calculated as follows:

$$\sigma_R = \left[\frac{\sigma_d^2}{d'^2} + \left(\frac{d^2}{d'^4} \right) \cdot \sigma_{d'}^2 \right]^{1/2} = 0.27\ \mu m/px$$

From the consideration that $A_{LEICA} = a \cdot b = R^2 a' b'$ we obtain:

$$\sigma_{A-LEICA} = \left[4a'^2 b'^2 R^2 \sigma_R^2 + R^4 (a'^2 + b'^2)\sigma_{a'}^2\right]^{1/2} = 0.02\ mm^2$$

that is:

$$A_{LEICA} = 0.22 \pm 0.02\ mm^2 \tag{4.19}$$

Here we suppose that the particles that settled onto each single area were contained in the air column of base A_{LEICA} and height $h = 250$ mm; this hypothesis can be made if we assume that there is not turbulence in the chamber A during the gravitational settling. Hence the concentration has to be referred to the volume $V_{LEICA} = h \times A_{LEICA}$; the standard deviation on this quantity is:

$$\sigma_{V-LEICA} = [h^2 \sigma_A^2 + A^2 \sigma_h^2]^{1/2}$$

Assuming $\sigma_h = \frac{1}{3}\Delta h = \frac{1}{3} \cdot 0.5$ mm, we obtain:

$$V_{LEICA} = 54.11 \pm 3.86\ mm^3 \tag{4.20}$$

For each count we have a value C_i for the particle concentration:

$$C_i = \frac{N_i}{V_{LEICA}} \tag{4.21}$$

and we associate a standard deviation:

$$\sigma_{Ci} = \left[\frac{\sigma_{Ni}^2}{V^2} + \frac{N_i^2}{V^4}\sigma_V^2\right]^{1/2} \tag{4.22}$$

where the maximum error and the standard deviation for particle counts are linked by $\sigma_{Ni} = \Delta N_i/3 = 1/3$.
Five measurements of particles concentration have been performed; for each measurement, 10 to 40 areas A_{LEICA} have been analyzed; the values C_i have been averaged over all the counts within a single measurement, and over all the five measurements, in order to obtain a final value $\langle C_A \rangle$. The values determined for each of the five measurements are listed in tab. 4.5. The final relation is:

$$\langle C_A \rangle = \frac{\langle N \rangle}{V_{LEICA}} \tag{4.23}$$

and the standard deviation on the mean:

$$\sigma_{\langle C \rangle} = \left[\frac{\sum_{i=1}^{n} \sigma_{Ci}^2}{n_{tot}^2} \right]^{1/2} \tag{4.24}$$

where n_{tot} is the total number of values determined for C_i. Finally we obtain the average value for the particles concentration:

$$\langle C_A \rangle_{4.83\mu m} = 27.68 \pm 0.64 \text{ particles}/cm^3 \tag{4.25}$$

	Pressure	***Diameter***	***Concentration***	***Standard deviation***
Meas.	$p(mbar)$	$d(\mu m)$	$C\ (part/cm^3)$	$\sigma_C\ (part/cm^3)$
I	6.3	4.83	25.64	1.03
II	6.3	4.83	24.49	1.02
III	6.3	4.83	27.26	1.05
IV	6.3	4.83	18.48	1.41
V	6.3	4.83	42.51	2.25

Table 4.4: *Mean particle concentrations, for $d = 4.83\ \mu m$, obtained for measurements from I to V.*

Results for $9.78\ \mu m$ **particles**

The compute of the number concentration for particles $d = 9.78 \pm 0.17\ \mu m$ has been determined following the same procedure as the previous section, except that here we analyzed different areas. Because the number of counts is much smaller, here we do not considerate the single areas A_{LEICA} visualized by the optical microscope, but simply considerate the whole area that is inscribed within a circle of diameter $d_O = 10.00$ mm; on each microscope slide two such reference circles are printed. The settling column has now the reference circle as a base, and height $h = 250$ mm. From the base area $A_{circle} = \pi d_O^2/4$ we determine the standard deviation:

$$\sigma_{A-circle} = \frac{1}{2}\pi d_O \sigma_{dO}$$

where the error on the diameter is $\sigma_{dO} = \frac{1}{3}\Delta d_O = \frac{1}{3} \cdot 0.01$ mm. The area is:

$$A_{circle} = 78.54 \pm 0.05 \ mm^2 \tag{4.26}$$

The volume to consider is now $V_{circle} = h \times A_{circles}$ and we obtain:

$$V_{circle} = (19.63 \pm 0.03) \ cm^3 \tag{4.27}$$

The particle counts have been performed within the entire reference circles, and the number concentration has been determined for each measurement and subsequently averaged as in the previous section. Here we performed 3 measurements. The final average number concentration is:

$$\langle C_A \rangle_{9.78\mu m} = 0.11 \pm 0.01 \text{ particles}/cm^3 \tag{4.28}$$

	Pressure	***Diameter***	***Concentration***	***Standard deviation***
Meas.	$p(mbar)$	$d(\mu m)$	$C \ (part/cm^3)$	$\sigma_C \ (part/cm^3)$
I	6.3	9.78	0.18	0.01
II	6.3	9.78	0.05	0.01
III	6.3	9.78	0.10	0.01

Table 4.5: *Mean particle concentrations, for* $d = 9.78 \ \mu m$*, obtained for meas. I - III.*

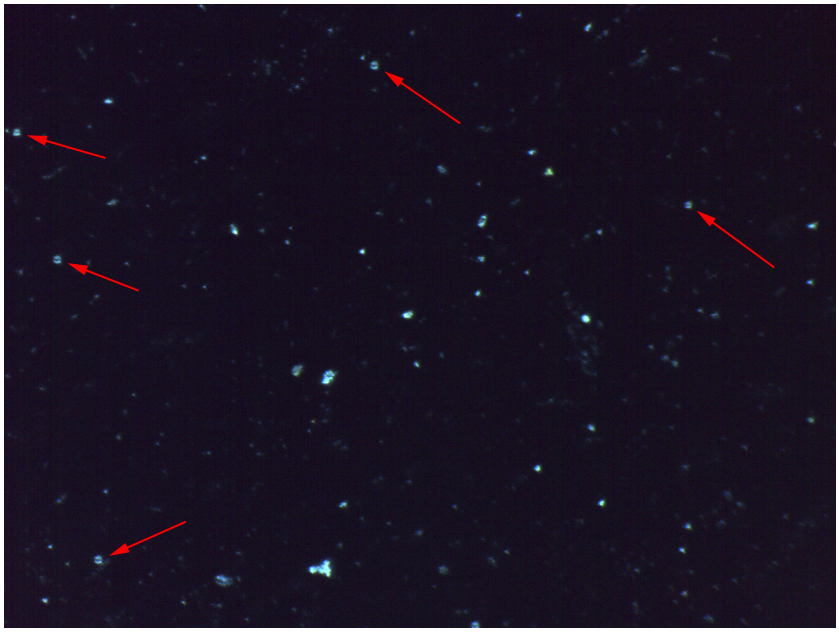

Figure 4.9: *PSL particles ($d = 4.83\ \mu m$) on a microscope slide; $Mag = 12.5$ X; image size $= 403 \times 536\ \mu m^2$.*

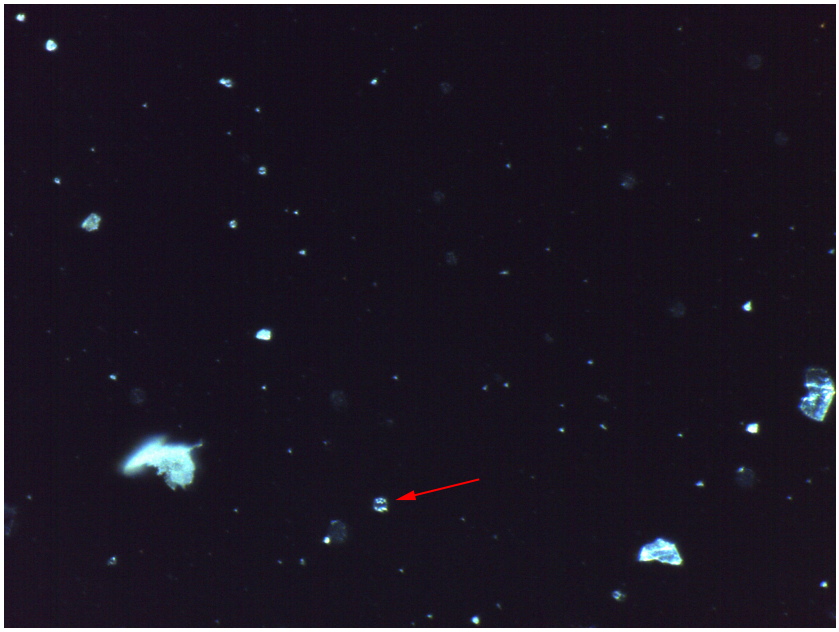

Figure 4.10: *PSL particles (9.78 μm) on a slide; $Mag = 12.5$ X; size $= 403 \times 536\ \mu m^2$.*

4.2 Phase II: collection performance evaluation measurements: nucleopore filter

In the phase II the collection efficiency η_{samp} (eq.4.3) has been measured in a configuration which uses a filter as collection substrate; scope of this measurement is comparing filtering and inertial impact collection. In this phase the DUSTER instrument has been placed into the main chamber A. Actually here we used a prototype simulator of DUSTER, consisting of a pumping group connected to an inlet; the pumping group is composed by 3 *Fur Gut* micropumps (for details see section 3.5.1), the inlet is identical to the flight one. A nucleopore filter with 3-μm holes has been used as substrate; it has been placed between the pumping line and the inlet: the drawn air passes through the holes, while the particles are retained on the substrate. The nucleopore filter is kept between two 16-mm viton gaskets and then fixed between the flange of the inlet and a flange connected to the pumping system thanks to six screws. The pumping group is connected to the power supply (+5 V) with harness feed through the main chamber A. A scheme of the instrument simulator and the used experimental setup are in fig.4.11.

4.2.1 Experimental procedure

Both the microscope slides and the nucleopore filter have been characterize with the optical microscope before of each measurement, in order to check if any particle were initially present. The procedure is the same as described in section 4.1.4 up to the point 11, then there are the following steps:

1. the instrument is switched on simultaneously with the injection from B to A, that is after $t_{pre-inlet}$;
2. the gravitational settling lasts several minutes, and the instrument pumps air for a time interval $t_{samp} = 10$ min; the measurements have been performed at pressures $p_A = 16$ mbar and $p_A = 6.3$ mbar;
3. after t_{samp}, the reentry of air into A is allowed, until $p_A = 1013$ mbar;
4. finally it is possible to open the chamber A and extract the substrates for the analysis.

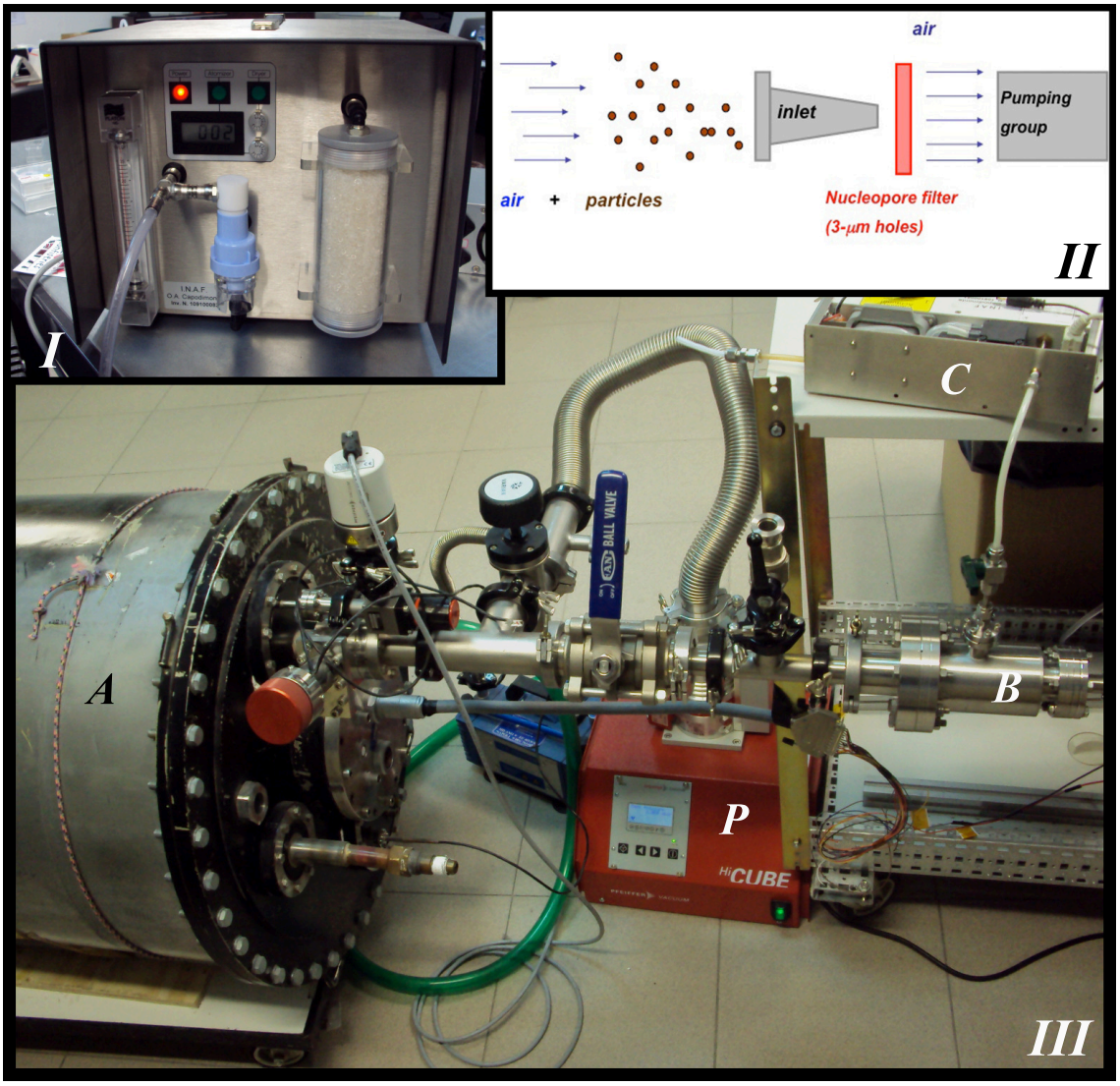

Figure 4.11: *Phase II experimental setup: (I) aerosol generator: the atomizer, the air dryer, the tube for the aerosol outflow, the two rotary knobs and the pressure display are visible; (II) the simulator of DUSTER used for the collection efficiency measurements. This instrument has been placed inside the main chamber A; (III) the main chamber A, the pre-inlet chamber B, the Sky-OPC (C) and the rotative pump P; the blue "AN-Ball Valve" corresponds to the valve G_{V2} in fig.4.8; it is only open for the injection from B to A.*

4.2.2 Results

The particles number concentration on the nucleopore filter has been determined following the same criterion as for the phase I. Each rectangular portion of the nucleopore filter, observed on the optical microscope at $Mag = 12.5$ X, has the area $A_{LEICA} = 0.22 \pm 0.02\ mm^2$. The corresponding volume to be considered, V_{LEICA}, now depends on the sampled volume. If A_{filter} is the circular area enclosed within the viton gasket, that is the total area exposed to the air flux, with diameter $d_{gask} = 16.2$ mm, then we have:

$$V_{LEICA} = V_{samp} \cdot \frac{A_{LEICA}}{A_{filter}} = x_A \cdot V_{samp} \tag{4.29}$$

having set $x_A = A_L/A_f$. Hence the particle number concentration corresponding to each analyzed area is:

$$C_i = \frac{N_i}{V_{LEICA}} \tag{4.30}$$

and the standard deviation is given by eq.4.22, but now the error on the reference volume must be computed using the eq.4.29. The total area exposed to the air flux is:

$$A_f = \pi \left(\frac{d_{gask}^2}{4} \right) = 824.48\ mm^2 \tag{4.31}$$

with:

$$\sigma_{Af} = \frac{1}{2} \pi d \sigma_d \tag{4.32}$$

and $\sigma_d = \frac{1}{3}\Delta d = \frac{1}{3} \cdot 0.01$ mm.

Taking into account the pumps flow rate and the sampling time, the sampled volume is given by:

$$V_{samp} = Q \cdot t \tag{4.33}$$

Hence we have:

$$V_{LEICA} = Q \cdot t \cdot x_A \tag{4.34}$$

and the error is:

$$\sigma_{V-leica} = \left[(t \cdot x_A)^2 \sigma_Q^2 + (Q \cdot x_A)^2 \sigma_t^2 + (Q \cdot t)^2 \sigma_{xA}^2 \right]^{1/2} \tag{4.35}$$

where σ_Q is given in tab.3.1; $\sigma_t = \frac{1}{3}\Delta s = \frac{1}{3} \cdot 1s$ and:

$$\sigma_{xA} = \left\{ \frac{\sigma_{AL}^2}{A_f^2} + \frac{A_L^2}{A_f^4} \sigma_{Af}^2 \right\}^{1/2} \tag{4.36}$$

The mean flow rate Q for a group of 3 *Fur Gut* micropumps is (see section 3.5.1, tab.3.4):

$$\begin{cases} Q = (5.00 \pm 0.4) \times 10^3 \ cm^3/min & (6 \ mbar) \\ Q = (5.33 \pm 0.3) \times 10^3 \ cm^3/min & (16 \ mbar) \end{cases} \tag{4.37}$$

Thus the reference volume is:

$$\begin{cases} V_{LEICA} = 13.3 \pm 2.0 \ cm^3 & (6 \ mbar) \\ V_{LEICA} = 14.2 \pm 2.1 \ cm^3 & (16 \ mbar) \end{cases} \tag{4.38}$$

Using the equations 4.23 and 4.24 we obtain the mean particles number concentration upon the nucleopore filter, corrected for a 6-pumps system:

$$\begin{cases} \langle C \rangle_{filter} = (6.60 \pm 0.38) \times 10^{-1} \ part/cm^3 & (6 \ mbar) \\ \langle C \rangle_{filter} = (4.64 \pm 0.29) \times 10^{-1} \ part/cm^3 & (16 \ mbar) \end{cases} \tag{4.39}$$

Finally we can determine the collection efficiency, inserting $\langle C \rangle_{filter} = C_{sub}$ and $\langle C_A \rangle = C_{env}$ into the equation 4.3:

$$\eta_{samp} = \frac{\langle C \rangle_{filter}}{\langle C_A \rangle} \tag{4.40}$$

and finally:

$$\begin{cases} \eta_{samp} = (2.38 \pm 0.15)\ \% & (6\ mbar) \\ \eta_{samp} = (1.68 \pm 0.11)\ \% & (16\ mbar) \end{cases} \tag{4.41}$$

Note that these results are not reliable as absolute values as the flux through the system should be re-calibrated as it was derived in different conditions; only purpose of this measurement is comparing two different instrument configurations. Moreover, here we used particles with diameter $d = 4.83\ \mu m$.

4.3 Phase III: collection performance evaluation measurements: carbon film substrate

In the phase three, the experimental configuration is identical as in the phase II, but for the collecting surface, as here we used a carbon film substrate instead of a nucleopore filter (see section 4.2 for details) also changing in this way the collection mechanism: inertial impact collection instead of filtering.
The fraction of observed volume is:

$$V_{LEICA} = V_{samp} \cdot \frac{A_{LEICA}}{A_{gask}} = x_A \cdot V_{samp} \tag{4.42}$$

with $A_{gask} = A_{filter} = 824\ mm^2$ and $x_A = A_L/A_g$. With the same parameters used in section **??** we obtain the mean concentration:

$$\langle C \rangle_{carbon} = (3.06 \pm 0.18)\ part/cm^3 \qquad (6\ mbar) \tag{4.43}$$

and finally the collection efficiency:

$$\eta_{samp} = (11.05 \pm 0.71)\ \% \qquad (6\ mbar) \tag{4.44}$$

In these last measurement we assumed a larger maximum error on the counts; we assumed $\Delta N/N = 20\%$. With these ultimate measurements we demonstrate that, using an inertial impactor as a substrate and the mechanism of inertial deposition, instead of using the experimental configuration with the nucleopore filter (3-μm

pores) as analyzed in the phase II, the collection efficiency is much better: we have an increase from 2% to 11%. Hence the use of an inertial impactor as a substrate is the suitable experimental configuration in order to perform a more efficient and representative sampling.

Chapter 5

Raman analyses of stratospheric particles collected during the DUSTER-2008 campaign

5.1 Raman spectroscopy

In the first part of this section the physics of the Raman effect, on which Raman spectroscopy is based, is described. In the second part a brief summary of literary results of Raman spectroscopy performed on carbonaceous (terrestrial and astrophysical) materials is reported. In the second section Raman analyses performed on stratospheric particles, collected by DUSTER-2008 instrument, are described and discussed. Finally in the third section a new NI-LabVIEW tool, developed to compute automatized fits of numerous Raman spectra, is presented.

5.1.1 Classical theory of Raman Effect

The Raman spectroscopy is based on the Raman effect: it consists in an inelastic scattering that occurs when an electromagnetic radiation beam hits a *material system*, that is an ensemble of molecules. In the classical treatment the molecules are assumed to be non-rotating and non-interacting [53]; a more realistic and detailed treatment would require a quantum-mechanical approach. Classically, the incident electromagnetic radiation is treated as a monochromatic plane wave of frequency ω_1

and irradiance $\Im$; the electromagnetic radiation scattered by a molecule is a plane wave of frequency ω_s and intensity I. When the scattered radiation has the same frequency of the incident radiation, $\omega_s = \omega_1$, we have Rayleigh Scattering; if the scattered and incident radiation have different frequencies, $\omega_s \neq \omega_1$, then we have Raman scattering.

Considering the Rayleigh scattering, the interaction between a photon and a molecule causes the transition of the molecule into an excited state and then the return to the ground state. In the case of Raman scattering, the interaction between photon and molecule causes the transition of the latter to a virtual state and then to an intermediate state (fig. 5.1).

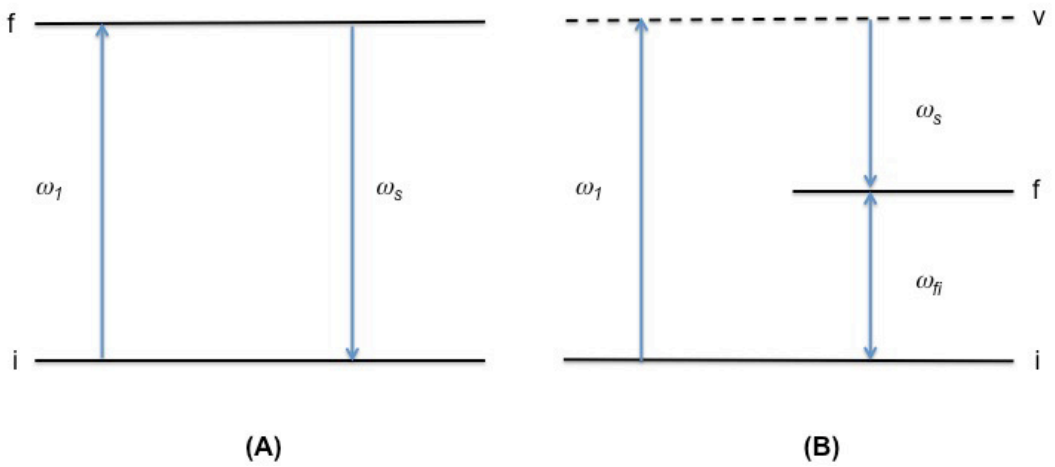

Figure 5.1: *Energy diagram showing the initial and final energy levels of a molecule in the case of Rayleigh scattering (A) and Raman scattering (B), and the frequencies of the relative transitions: "i" is the initial state, "f" the final state, and "v" the virtual state.*

In Raman scattering the frequency of the scattered wave can be greater than the incident frequency, $\omega_s = \omega_1 + \omega_M$, and the corresponding line is named *anti-Stokes band*; if the scattered wave frequency is less than the incident, $\omega_s = \omega_1 - \omega_M$, then there is a *Stokes band*. The electric field associated to the electromagnetic radiation incident on a molecule causes the oscillation of the molecule electric dipole p; the intensity radiated by the oscillating dipole is:

$$I = k'_\omega \omega_s^4 p_0^2 \sin^2 \theta \tag{5.1}$$

where:

$$k'_{\omega} = \frac{1}{32\pi^2\epsilon_0 c_0^3} \tag{5.2}$$

The intensity I is the time-averaged power per solid angle unit radiated by the oscillating dipole along the direction forming an angle θ with the dipole axis; p_0 is the dipole amplitude, ω_s is the scattered radiation frequency. The frequency is related to other parameters:

$$\omega_s = 2\pi\frac{c}{\lambda} = 2\pi\bar{\nu_s}c \tag{5.3}$$

in which $\bar{\nu_s} = 1/\lambda$ is the wavenumber, usually expressed in cm^{-1} and used in Raman spectra as independent variable. The incident electric field $\vec{E}$ causes the oscillation of the dipole:

$$\vec{p} = \underline{\alpha} \cdot \vec{E} \tag{5.4}$$

where the polarizability $\underline{\alpha}$ is a tensor, in general. Here we only consider $\vec{p}$ at the first order, that is, we neglect multipoles components.

The polarizability depends on the normal coordinates Q_k, describing the vibration of the nuclei about equilibrium positions; that is, the non-rotating molecule is fixed at the equilibrium configuration but can vibrate; a quantum of vibration is called *phonon*. The normal coordinates are in general Q_k, Q_l, ..., associated to the vibration frequencies ω_k, ω_l, ..., but we consider only one normal mode of vibration $Q_k = Q(\omega_k)$. The polarizability can be expressed, for each single component α_i, as a Taylor series at the first order:

$$\alpha_i = \alpha_{i(0)} + \left(\frac{\partial\alpha_i}{\partial Q_k}\right)_0 Q_k \tag{5.5}$$

where the subscript '0' indicates that the derivatives must be computed at the equilibrium configuration. Both the normal coordinates and the electric field have a sinusoidal time-dependence:

$$Q_k = Q_{k0}\cos(\omega_k t + \delta_k) \tag{5.6}$$

$$\vec{E} = \vec{E_0}\cos(\omega_1 t) \tag{5.7}$$

Thus we can insert the expression of Q_k into the expression for α_i obtaining:

$$\alpha_i = \alpha_{i(0)} + \dot{\alpha}_{i(0)} Q_{k0}\cos(\omega_k t + \delta_k) \tag{5.8}$$

where:

$$\dot{\alpha}_{i(0)} = \left(\frac{\partial \alpha_i}{\partial Q_k}\right)_0 \tag{5.9}$$

Using the eq. 5.7 and 5.8 the dipole (eq. 5.4) becomes:

$$\vec{p} = [\vec{\alpha}_0 + \dot{\vec{\alpha}}_0 Q_{k0}\cos(\omega_k t + \delta_k)]\vec{E}_0\cos(\omega_1 t) \tag{5.10}$$

having used the vectorial notation. We obtain:

$$\vec{p} = \vec{\alpha}_0\vec{E}_0\cos(\omega_1 t) + \dot{\vec{\alpha}}_0\vec{E}_0 Q_{k0}\cos(\omega_k t + \delta_k)\cos(\omega_1 t) \tag{5.11}$$

Using the Werner formula:

$$\cos A\cos B = \frac{1}{2}[\cos(A+B) + \cos(A-B)]$$

we finally have:

$$\vec{p} = \vec{\alpha}_0\vec{E}_0\cos(\omega_1 t) + \frac{\dot{\vec{\alpha}}_0\vec{E}_0 Q_{k0}}{2}\left\{\cos[(\omega_k+\omega_1)t + \delta_k] + \cos[(\omega_k - \omega_1)t + \delta_k]\right\} \tag{5.12}$$

that can be finally rewritten as:

$$\vec{p} = \vec{p}^{Ray} + \vec{p}^{Ram}_{anti-Stokes} + \vec{p}^{Ram}_{Stokes} \tag{5.13}$$

where the electric dipole relative to the Rayleigh effect is:

$$\vec{p}^{Ray} = \vec{\alpha}_0 \vec{E}_0 \cos(\omega_1 t) \tag{5.14}$$

the Raman anti-Stokes term is:

$$\vec{p}^{Ram}_{anti-Stokes} = \frac{\dot{\vec{\alpha}}_0 \vec{E}_0 Q_{k0}}{2} \cos[(\omega_k + \omega_1)t + \delta_k] \tag{5.15}$$

and the Raman Stokes term is:

$$\vec{p}^{Ram}_{Stokes} = \frac{\dot{\vec{\alpha}}_0 \vec{E}_0 Q_{k0}}{2} \cos[(\omega_k - \omega_1)t + \delta_k] \tag{5.16}$$

Inserting the electric dipole 5.12 in the relation 5.1 one obtains the Raman scattered intensity as a function of the frequency. The radiation-molecule interaction produces a Rayleigh component due to electric dipole oscillating at frequency ω_1, and a Raman component due to the coupling between the molecule vibrating at ω_k and the electric dipole oscillating at $\omega_k \pm \omega_1$. The rearrangement of the molecular electrons is responsible of the coupling between the motion of the molecular nuclei and the electric field. In a diatomic homonuclear molecule the quantity α can be thought as a *polarizability ellipsoid* with the principal axis, at the equilibrium, aligned with the bond direction and the other two axes at right angles. The condition so that a molecule gives Rayleigh scattering is that the polarizability α is non-zero, and this occurs for all molecules; the condition for Raman scattering instead is that at least one component α_i of the polarizability has a non-zero derivative, at the equilibrium configuration, with respect to the normal coordinates, that is:

$$\left(\frac{\partial \alpha_i}{\partial Q_k}\right)_0 \neq 0 \Longrightarrow \textit{ condition for Raman scattering} \tag{5.17}$$

For comparison the condition for IR activity is $(\partial p_i/\partial Q_k)_0 \neq 0$. In diatomic homonuclear molecules (A_2) the symmetry of the electron distribution makes the electric dipole to be zero at the equilibrium configuration, thus its derivative is zero and so there is no IR activity. Instead the polarizability in an A_2-type molecule changes with the internuclear distance, at the equilibrium distance it is not maximum ($\dot{\alpha}_0 \neq 0$) and so the molecule is Raman active. In diatomic heteronuclear molecules (AB) the asymmetry of the electronic cloud makes the electric dipole to vary with internuclear distance: it is not maximum at the equilibrium distance and so there is IR activity.

Moreover the variation of the polarizability with the internuclear distance causes Raman activity also in heteronuclear molecules.

5.1.2 Raman spectroscopy of carbonaceous materials

Raman spectroscopy is a powerful and useful tool for the investigation of chemical and mineralogical constituents of analyzed astrophysical samples, especially if used in conjunction with other laboratory techniques as for example infra-red spectroscopy, because of their complementarity character.

Carbonaceous materials have both sp^2 and sp^3 sites, depending on their structural order or disorder; sp^2 states are characterized by π and σ bonds, while sp^3 states only have σ bonds. The π and σ bonds have different behaviours, because linear σ states are two-center bond-orbitals that only involve two atoms, while π states are bond-orbitals that involve more than two atoms, they also interact with adjacent bonds. Visible Raman spectroscopy is able to probe the sp^2 content of carbonaceous materials, because visible photons excite the π bonds, that are not contained in sp^3 states. Typically the Raman scattering cross-section for visible light excitation relative to sp^2 sites is 50-230 times larger than the Raman cross-section relative to sp^3 sites (Ferrari and Robertson, 2000). Higher energy ultraviolet photons (5.1 eV) instead excite both π and σ bonds, and so UV Raman spectroscopy is a good tool to probe sp^3 sites. However visible Raman spectroscopy can be used to infer at least indirectly the sp^2/sp^3 fraction of carbonaceous materials such as the diamondlike carbon (DLC), that is amorphous carbon with a high content of sp^3 states (see the end of section 5.2).

The sp^2 and sp^3 states are indicative of the two extreme possible structures of carbonaceous materials, in that a high content of sp^2 sites implies a structural order, that is typical of graphite, in which sp^2 sites are clustered in ordered aromatic rings displaced on parallel planes. Amorphous carbons with a higher sp^3 content have a more disordered structure, in which the C atoms are disposed in distorted tetrahedral units. In a ternary phase diagram carbonaceous materials occupy different zones accounting on their sp^2/sp^3 content [28, 30]. At one extreme there is the ideal graphitic carbon, with only sp^2 content; at another extreme there is the pure diamond, with only sp^3 content; at the third vertex there are the idrocarbons (with sp^1 content). Intermediate regions in the ternary diagram are occupied by materials with different mixtures of sp^2 and sp^3 sites. For example there is the amorphous carbon (a-C) and its hydrogenated version, a-C:H, with relatively low sp^3 content. The tetrahedral

amorphous carbon (ta-C) and its hydrogenated version (ta-C:H), generally called *diamond-like carbons* (DLC), have a higher sp^3 content. A fourth dimension on the ternary diagram should be considered the level of sp^2 clustering.

Carbonaceous materials are characterized by Raman spectra that typically show two large bands: the D peak, centered at a Raman shift of about $\omega_D \approx 1360\ cm^{-1}$, and the G peak, centered at about $\omega_G \approx 1580\ cm^{-1}$. The D peak (*disorder*) is related to the A_{1g} *breathing* mode, and is present in aromatic rings. The G peak (*graphite*) is related instead to the E_{2g} *stretching* mode, and is present both in aromatic rings and in aliphatic chains (see fig.5.2) [28]. The quantities A_{1g} and E_{2g} represent symmetry groups involving phonons (a phonon is a quantum of vibration in a solid) in the molecular structure of the material. However these reference peak positions are not fixed, they depend mainly on the degree of disorder of the material structure. The Raman spectrum of ideal graphite only shows the G peak at the frequency $1582\ cm^{-1}$. The appearance of the D peak and the variations of band intensity and position relatively to D and G peaks are due to the presence of some structural disorder, that generally consists in the shape distortion of sp^2 aromatic rings (that can finally open) and sp^3 tetrahedral units, with subsequent variation of C-C bond length and angle, and in the inclusion of heteroatoms into carbonaceous materials. In the ideal graphite the transition that produces the D peak is prohibited, but in presence of disorder it becomes an allowed transition [28]; this peak is also dispersive, that is its position is shifted depending on the excitation energy. The general selection rule for the transition that originates the D peak is $\vec{k} = \vec{q}$, where $\vec{k}$ is the wave vector relative to the electronic states associated to the transition, while $\vec{q}$ is the phonon wave vector. This selection rule implies that there is a resonant Raman coupling, due to a strong enhancement of Raman cross section when electronic and phononic states are in phase ($k = q$). For example in graphite the breathing vibration mode causes a variation in the C-C bond length in aromatic rings (fig.5.2) and thus a variation of polarizability; many adjacent rings produce similar contributions, the polarizability is the sum of all these contributions, and the Raman cross section is maximum when $k = q$.

The ratio of the intensity of the D peak to G peak (I_D/I_G) is not a monotonous relation, but it depends on the graphitic domain size L_a; it is expressed by the Tuinstra-Koenig (1970) relation for $L_a > 20\ \mathring{A}$, while for $L_a < 20\ \mathring{A}$ a different relation has been proposed by Ferrari and Robertson (2000) (see discussion in section 5.2.8). The intensity ratio I_D/I_G depends on the degree of structural order, and it has not an unambiguous behaviour, but depends on the starting material and on the particular process. For example in graphite, in nano-crystalline graphite (nC-G)

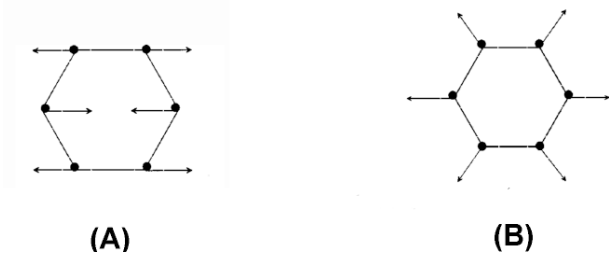

Figure 5.2: *Scheme of the vibrations of C atoms in aromatic rings, that produce the D and G peaks. (A): E_{2g} stretching mode of G peak; it is due to the relative motion of sp^2 C atoms and so it is also visible in chains; (B): A_{1g} breathing mode of D peak.*

and in general in ordered materials an increasing of I_D/I_G indicates an increasing of disorder. The increasing of I_D/I_G in very disordered amorphous carbons instead implies the increasing of order degree [1, 2, 23, 27, 28]. The process of increasing of order consists in the progressive conversion of $sp^3 \rightarrow sp^2$ sites and in the subsequent clustering of sp^2 sites. The intensity ratio is more sensitive to the clustering of sp^2 sites than to the conversion $sp^3 \rightarrow sp^2$ [27, 28]. Some astrophysical processes such as ion irradiation in interstellar and interplanetary space induce on cosmic dust particles two competitive mechanisms: graphitization and amorphization. Graphitization is a ordering mechanism, and it is due to energy release by ion collisions with target material, with subsequent $sp^3 \rightarrow sp^2$ conversion; amorphization is instead a disordering mechanism, caused by displacement collisions (Baratta et al., 2008) [2]. During these ion irradiation processes, equilibrium conditions are not possible because of small relaxation times ($\leq 10^{-12}$ s).

Annealing experiments performed through vacuum heating of amorphous carbon films up to 950°C (Dillon et al., 1984) [23] or tetrahedral amorphous carbons (ta-C) up to $>$ 1100°C (Ferrari et al., 1999) [27] show that the intensity ratio in function of the annealing temperature increases up to a maximum and then starts to decrease. The initial increasing of I_D/I_G is attributed to the increasing in number of sp^2 sites, that subsequently begin to cluster; when graphitization starts in the amorphous carbon the I_D/I_G reaches the maximum and then decreases down to zero [1, 2, 23]. In the annealing experiments of Ferrari et al. (1999) performed on ta-C the decreasing of I_D/I_G is not observed, but it increases even for temperatures $>$ 1100°C [27]. Annealed ta-C:H samples show a major sp^3 loss due to H content, than annealed ta-C, that has a major thermal stability.

The D and G band widths also vary with the structural disorder degree. When the

disorder increases, for example in amorphous carbons, the two bands become wider, and for sputtered amorphous carbons they appear as a unique large band, the D peak just appearing as a shoulder of the G peak. The widening of the D and G peaks is related to the bond angle disorder, that is the deviation from the ideal 120° bond angle in graphitic aromatic rings [1, 2, 28]

In general carbonaceous materials with different degree of structural disorder and different sp^2/sp^3 fraction are related by an ideal amorphization trajectory (Ferrari and Robertson, 2000, 2001, 2004). The amorphization trajectory, consisting in ω_G and I_D/I_G profiles in function of the sp^3 content, starts from the carbon with the higher structural order and the higher sp^2 content, the graphite, and ends with the ta-C with a high sp^3 content. The disorder increase from graphite to ta-C is caused for example by ion irradiation. This model suggests three stages characterized by different dominating processes and different types of carbons, with the sp^3 content progressively increasing from 0% to $\sim 100\%$.

The first stage comprises the evolution from ideal graphite (only sp^2, 0% sp^3) to *nanocrystalline graphite* (nc-G). There is no increasing in the sp^3 content, but the graphitic domains sizes L_a become smaller and smaller (decreasing down to ≥ 20 $\mathring{A}$); in this stage the Tuinstra-Koenig (1970) relation is valid (see discussion in section 5.2.8): the intensity ratio is inversely proportional to L_a. The D peak appears, I_D/I_G increases up to a maximum (for nc-G), and the G peak shifts from 1582 to ~ 1600 cm^{-1}. Really the G peak shift is interpreted as the appearance of a second $D2$ peak at 1620 cm^{-1} that merges with the G peak forming a large $G + D2$ band (see the end of this section).

The second stage comprises the passage from nc-G to amorphous carbon (a-C). Structural disorder is progressively introduced in the carbon structure, aromatic graphitic rings become more distorted and the sp^3 content increases. The stage ends with the formation of totally disordered a-C, with $\leq 20\%$ sp^3. The intensity ratio I_D/I_G decreases to zero, the G peak shifts from 1600 to $\sim$ 1510 cm^{-1} and the Tuinstra-Koenig relation is no longer valid, but another relation must be used (Ferrari and Robertson, 2000): here the intensity ratio is proportional to the number M of ordered aromatic rings ($\propto M \propto L_a^2$) and thus $I_D/I_G \to 0$.

The third stage includes the evolution from a-C to tetrahedral amorphous carbon (ta-C). Here the sp^3 content increases from $10 - 20\%$ up to $\sim 85\%$; most of sp^2 sites are converted from rings to chains, in which the shorter length C=C bonds produce higher frequency vibrations, and so the G peak shifts from 1510 up to $\sim 1570 - 1630$ cm^{-1}. In the third stage the intensity ratio is $I_D/I_G \approx 0$.

An ideal *ordering trajectory* (obtained for example with thermal annealing of disordered carbons or high temperature deposition of ta-C) inversely would lead from ta-C to graphite. Nevertheless, in the third and second stage of the ordering trajectory there is *hysteresis*, that is, there is not a unique relation between I_D/I_G and the sp^3 content. This is due to the fact that during the ordering, there are two processes: $sp^3 \rightarrow sp^2$ conversion, and sp^2 rings clustering. During room temperature deposition the two processes occur simultaneously, while during high temperature deposition or annealing they occur separately, with clustering occurring at lower temperature. This is the *hysteresis* mechanism: the exact sp^3 content should be determined independently with other techniques than visible Raman spectroscopy, even if an estimate can be made.

Laboratory experiments of ion irradiation on different cosmic material analogues (Baratta et al., 2004, 2008) show that starting from both pure frozen hydrocarbons (for example pure CH_4, C_4H_{10}, C_6H_6 ices) and from organic mixtures (for example H_2O+CH_4+N_2), after irradiation with He^+ or Ar^+ ions with increasing fluence (ions/cm^2), the resulting material is an organic residue mainly consisting of amorphous carbon containing hydrogen. These organic residues are called *ion produced hydrogenated amorphous carbons* (IPHAC) and are considered plausible laboratory analogues of cosmic materials such as those constituting the surface of comets, asteroids, IDPs and interstellar grains, which are subject to ion irradiation during their sojourn in space [1, 2]. Ion irradiation experiments performed on different samples (Baratta et al., 2004) also show different behaviours of carbonaceous materials, depending on which process (amorphization or graphitization) dominates. The irradiation of HOPG and a-C grains leads to a complete amorphization and disordering of the material, indicated by the increase of I_D/I_G in HOPG and the decrease of I_D/I_G in a-C grains. The ion irradiation of hydrogenated graphitic carbon (HGC), that is a highly ordered amorphous carbon (80% sp^3), and of an IPHAC, that is on the contrary very disordered (30% sp^3) lead to a similar amorphous material, intermediate between the two extremes, independently from the beginning material, with about $65 - 70\%$ sp^3 content [1]. In the first case (HGC $\rightarrow$ *amorphous structure*) the amorphization dominates; in the second case (IPHAC $\rightarrow$ *amorphous structure*) the graphitization dominates. Ion irradiation of nanodiamonds (Brunetto et al., 2004) and of aromatic and aliphatic soots (Brunetto et al., 2009) also leads to highly disordered carbonaceous materials [11, 12]. Ion irradiated a-C grains and IPHAC, differently from ion irradiated HOPG, represent well the different degrees of order showed by cosmic materials such as IDPs and meteorites, and they fix an upper limit to the ion implanted dose that cosmic particles have suffered in space [1, 2].

Raman spectra of astrophysical samples are often characterized by the presence of carbonaceous materials with different degrees of structural order. In certain cases only amorphous carbon D and G features are clearly detectable in IDPs and cometary grains Raman spectra (as for Wopenka, 1988; Quirico et al., 2005; Baratta et al., 2008; Rotundi et al., 2007, 2008), and this fact does not indicate necessarily that only a-C is present, but could be due to the opaque nature of carbonaceous materials, the small penetrating depth of laser radiation, and the Raman cross-section higher for a-C than for silicates [2, 63, 79, 80, 90]. In other cases also silicates (crystalline or amorphous) and other minerals are detected in Raman spectra of cosmic particles, as for example iron oxides such as magnetite, maghémite and hematite (Rotundi et al., 2007), or silicates (pyroxenes and olivines) and iron sulfides (Brunetto et al., 2011) [13, 79].

Raman spectra of carbonaceous materials are generally fitted only considering the two D and G first order major bands, although this is an approximation of a more complex situation, the D and G representing the convolution of several other features, as showed in Sadezky et al. (2005), which performed Raman analyses on graphite (disordered and highly ordered), soot and PAH samples [83]. A more realistic fit is obtained for example considering the "G" band actually as the convolution of a G peak (at 1580 cm^{-1}), a D_2 peak (at 1620 cm^{-1}, as suggested by Ferrari and Robertson, 2000) and a D_3 peak (at 1500 cm^{-1}). The "D" band is instead interpreted as the convolution of a D_1 peak (at 1360 cm^{-1}) and of a D_4 peak (at 1180 cm^{-1}). The best fit corresponds to a Lorentzian shape for G, D_1, D_2 and D_4 peaks, and to a Gaussian curve for the D_3 peak. Finally second order Raman bands (indicated as 2^*D_1, 2^*D_2, 2^*D_4 and $G + D_1$) appear in the region $2000 - 3000$ cm^{-1}. However in this work I only fitted the two principal D_1 and G peaks.

5.2 Raman measurements

5.2.1 Experimental setup and procedure

Raman analyses on three stratospheric particles, collected by DUSTER in the 2008 flight, have been performed in the Laboratorio di Astrofisica Sperimentale at the Osservatorio Astrofisico di Catania (INAF-OACT, Italy), under the supervision of Dr Giuseppe Baratta.

The Raman spectroscope we used consists of:

- Ar ion laser source ($\lambda = 514.5$ nm)
- optical confocal microscope (DILOR)
- triplemate spectrometer (SPEX)
- 1200 gr/mm holographic diffraction grating
- CCD detector

The light beam from the Ar^+ ion laser source enters, thanks to a plane mirror, the confocal microscope in a direction perpendicular to its optical axis, then through several mirrors the beam is reflected along the optical axis up to a beamsplitter. This beamsplitter transmits the laser beam, through another mirror, in the microscope and finally onto the sample. The laser beam is finally focused by the confocal microscope through the objective on the sample to be analyzed. The same objective collects the scattered light from the sample (Raman signal), which is then collimated in order to follow back a path parallel to the original laser beam; the beamsplitter reflects the scattered collimated radiation at 90° along the optical axis. This scattered light beam is finally focused on a diaphragm and on the entrance slit S_1 of the triplemate spectrometer, equipped with a holographic grating and the CCD detector.

In the spectrometer, three different diffraction gratings are used, in conjunction with two slits and a system of plane mirrors, in order to detect the Raman signal. This signal is much weaker than the Rayleigh one and it is mixed with the *stray light* caused by the dust grains and scratches present on the optical surfaces (gratings, mirrors and lens). The stray light do not follow the dispersion given by the grating and would mask the weak Raman signal (most of the stray light have the laser wavelength) without a suitable filter.

The gratings G_1 and G_2 are used as a filter: G_1 separates the scattered beam into its spectral components; the slit S_2 discards the components due to stray light selecting only a limited spectral range (the Raman signal); the grating G_2 recombines the components of appropriate wavelength into a non-dispersed filtered beam, which through the slit S_3 arrives on the grating G_3 (1200 gr/mm), which finally disperses the non-monochromatic beam onto the CCD detector.

On the CCD detector (1024×128 pixel, corresponding to 1024 columns $\times$ 128 rows) arrives the radiation dispersed by the last grating; all spectral components of the Raman signal are dispersed along a direction in the horizontal plane, and the X axis of the CCD is parallel to this direction of dispersion. The X axis of the CCD represents the spectral information along the wavenumber: a single wavelength is associated to each column (1024 columns) of the CCD; on the Y axis there are the images produced by the last slit (S_3); each pixel carry the information about the signal intensity. The Raman signal does not occupy the whole area of the CCD detector: we select an horizontal rectangular area of 20 points of height along the Y axis, centered at $Y = 73$. A smaller sensible area on the detector allows to decrease the noise, thus increasing the S/N ratio.

The confocal illuminator is equipped with three objectives: 10X (*working distance* = 10 mm), 50X (wd = 0.457 mm), and 100X (wd = 0.3 mm); we used the 10X objective to focus the sample, not to perform Raman analyses.

As preliminary operations, we first had to calibrate the grating position of the spectrometer. This is done acquiring a spectrum of the mercury line at $\nu_0 = 546.07$ nm, using as a source the fluorescence lamp in the laboratory room. If the Hg line in the spectrum occurs at $\nu_0 \pm \Delta\nu_0$ then the spectrometer has to be shifted of the amount $\mp\Delta\nu_0$.

Second, we check the alignment of the laser beam by watching the Raman signal on the CCD, using a silicon solid sample. While the laser beam has to be softened with a filter when irradiating the sample (see below), during the calibration with the Si sample this is not necessary. The Si sample gives a very strong spectral line at ~ 500 nm, with a maximum measured signal of $\approx 800 - 1000$ counts per second (c.p.s.). The signal is optimized if it occupies the minimum possible number of columns, and if the maximum intensity occurs in the minimum possible number of pixel.

The calibration of spectra in the region of frequencies of the amorphous carbon (aC) was done acquiring spectra of a sample of *highly ordered polycrystalline graphite* (HOPG) (see 5.2.2).

Before of the acquisition of spectra directly on the samples, we first acquired *blank* spectra, without irradiating the sample with the laser, and keeping the room light turned off. These blank spectra are used to subtract the background signal from the spectra obtained on the samples. A shutter allows to direct the laser beam onto the sample or not; a second CCD is used in order to visualize on a screen in real time the laser spot on the sample while focusing.

When the sample is illuminated by the laser beam, in order to avoid any possible surface thermal alteration, especially for micrometer-sized particles, we use a neutral filter which is able to soften the laser beam power; the filter is characterized by the parameters *density*, d, and *softening*, $A = 10^d$. If the emitted power is P_{laser}, the incident power on the filter is $P_{filter} = \eta P_{laser}$, with the factor $\eta < 1$; then the incident power on the sample is:

$$P_{sample} = \frac{P_{filter}}{A} = \eta P_{laser} \times 10^{-d}$$

In order to measure the effective laser light power focused on the sample we used a small (pen size) calibrated detector placed at the sample position. With an emitted power $P_{laser} = 60$ mW, an incident power $P_{filter} = 6$ mW on the filter, using a filter of density $d = 2$, we irradiated the samples with a power $P_{sample} = 60 \div 70\ \mu W$, that did not produce any surface alteration on the particles. The laser beam spot on the analyzed sample was typically of the order of 2 μm, for an acquisition time for each spectrum $\Delta t_{acq} = 60$ s x 10 scan. For each analyzed particle, several spectra were taken both on the *front* side and on the *back* side, in several different sites: the two sides are defined in fig. 5.9. Moreover, for each side, the spectra were taken both in the amorphous carbon (aC) region, that is centering the spectra at the frequency $\nu_0 = 1450\ cm^{-1}$, and in the silicates region, centering the spectra at $\nu_0 = 850\ cm^{-1}$. All the spectra in the carbon region for the three analyzed particles have been fitted with the Microcal Origin software, using two Lorentzian curves. A tool has been developed in NI-LabVIEW environment in order to compute many automatized fit of the spectra in the carbon region (see section 5.3); with this tool the fits have been performed using two Lorentzians, two Gaussians or two BWF (Breit Wigner Fano) curves in order to find an optimum fit for the D and G bands (see app.C); the Raman band parameters (peak position, width, intensity, area and their ratios, listed in tab.5.3 and 5.4) have been then averaged among these four fit models. In this section spectra fitted with MicroCal Origin are reported; in the carbon spectral region, for each picture there are two spectra: the original spectrum with raw data, on the bottom a straight baseline has been subtracted to the spectrum in the range

$1000 - 1800\ cm^{-1}$, in order to take into account the contribution of the fluorescence continuum background, and it has been cut and fitted only in this selected range of Raman shifts. The baseline equation is calculated as follows:

$$y_{base} = y_1 + \frac{y_2 - y_1}{x_2 - x_1} \cdot (x_{raw} - x_1) \tag{5.18}$$

in which x_{raw} are the Raman shift original data, (x_1, y_1) and (x_2, y_2) are the two extreme points of the straight baseline; generally they are chosen to be conventionally at $x_1 = 1000\ cm^{-1}$ and $x_2 = 1800\ cm^{-1}$, in order to obtain spectra that can be compared among different laboratories. Once the two points have been chosen and the baseline calculated, the spectrum is cut, selecting only Raman data in the range $1000 - 1800\ cm^{-1}$. The baseline is subtracted from the raw data obtaining the cut spectrum $y_{cut} = y_{raw} - y_{base}$:

$$y_{cut} = y_{raw} - y_1 - \frac{y_2 - y_1}{x_2 - x_1} \cdot (x_{raw} - x_1) \tag{5.19}$$

Finally the fits are computed on the points (x_{raw}, y_{cut}) in the range $1000 < x_{raw} < 1800\ cm^{-1}$.

5.2.2 Calibration of spectra with HOPG

In order to perform a better and more precise calibration of the spectra obtained in the aC region, we acquired spectra of a sample of *highly ordered pyrolitic graphite* (HOPG): the Raman spectrum of the HOPG is indeed characterized by the single strong G peak centered at $\nu_0 = 1582\ cm^{-1}$. If there is some surface structural disorder on the HOPG (e.g. sample surface can be easily damaged by rubbing), then in the spectrum the D peak also appears at $\sim 1360\ cm^{-1}$ (fig. 5.3). After exfoliating the surface of the graphite, by using the adhesive tape technique, the D peak disappears (fig. 5.4).

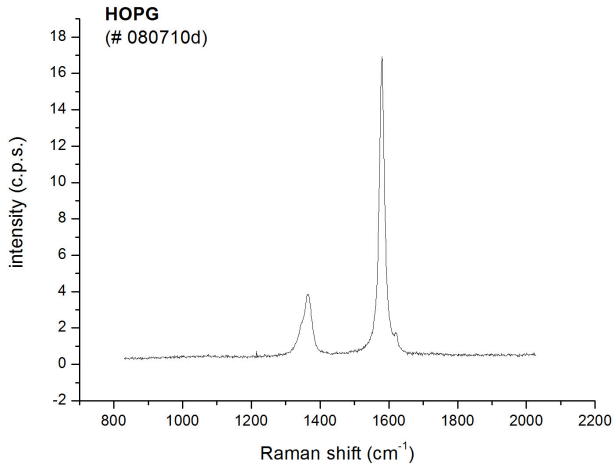

Figure 5.3: *Highly Ordered Pyrolitic Graphite (HOPG) used to calibrate Raman spectra. The G peak of the graphite is at 1582 cm^{-1}. The presence of the D peak at 1360 cm^{-1} indicates that there is some surface structural disorder.*

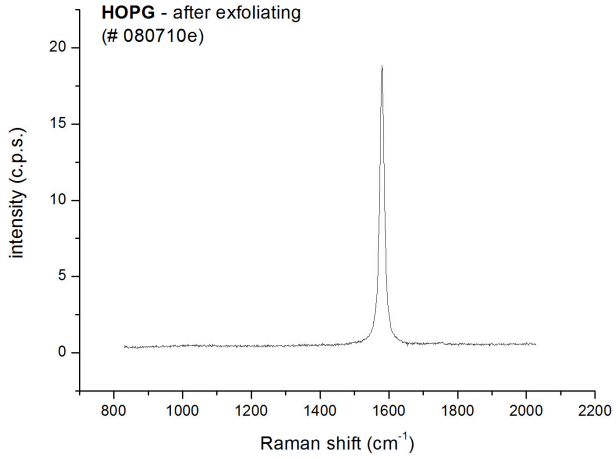

Figure 5.4: *Raman spectrum of the HOPG taken after the exfoliation of the graphite surface: the structural disorder and the D peak have disappeared.*

5.2.3 Analyzed particles

The three particles are *D08C_006* (size 3.09 × 2.06 μm), *D08C_008a* (small fragment, size 5.01 μm) and *D08C_008b* (large fragment, size 6.771 × 16.44 μm). The three particles have been collected by DUSTER during the summer-2008 flight from Longyearbyen (Svalbard Islands, Norway) to Greenland, in the upper stratosphere at a mean altitude of 37 km [15, 16, 20]. The SEM/EDX characterization of these particles is described in Ciucci, PhD Thesis (2010; note that in my work the nomenclature for the particles *D08C_008a* and *D08C_008b* is inverted with respect to this reference) [15]. Raman analyses on these particles have not been performed directly onto the collection substrate (TEM grids and holey carbon film, see section 3.2.3) used during the flight: in order to get an easier transport, to keep the particles shielded from external contamination, and to perform transmission infrared analyses, some of the particles were relocated to a FIB-copper grid (fig. 5.9), by means of a FIB (*Focused Ion Beam*) [15, 88].

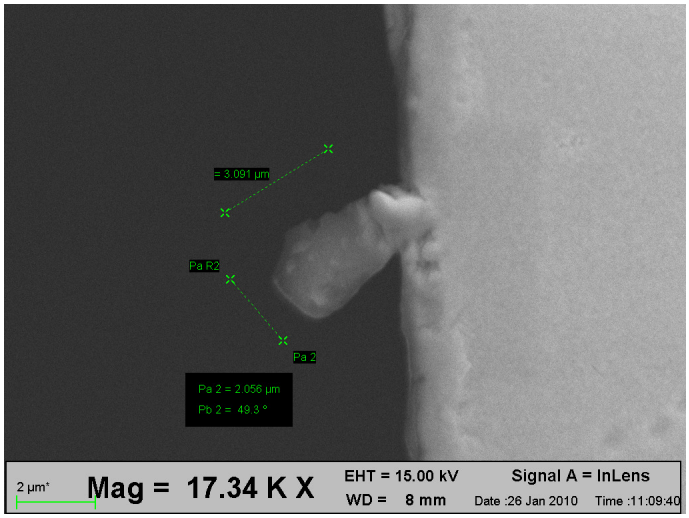

Figure 5.5: *SEM image of particle D08C_006, front side [15].*

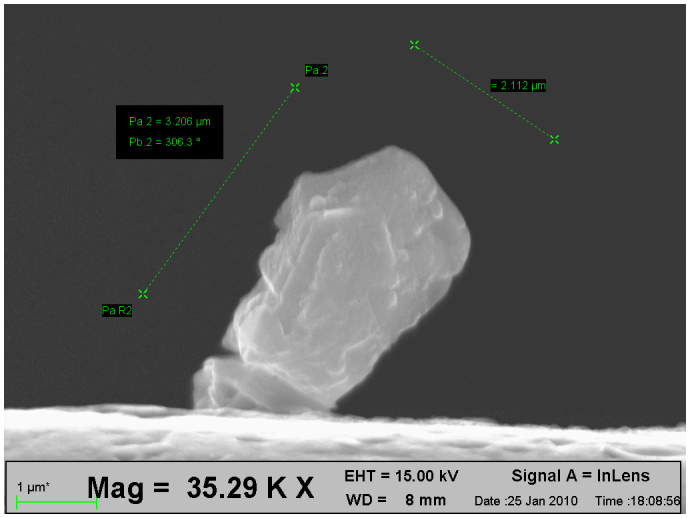

Figure 5.6: *SEM image of particle D08C_006, back side [15].*

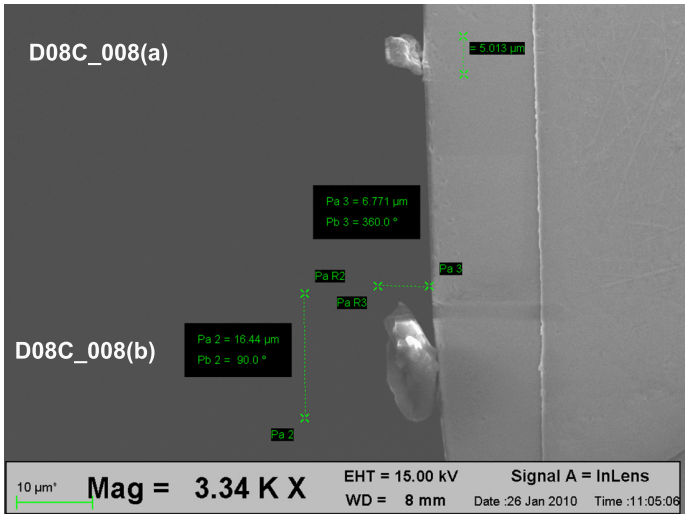

Figure 5.7: *SEM image of particles D08C_008a and D08C_008b, front side [15].*

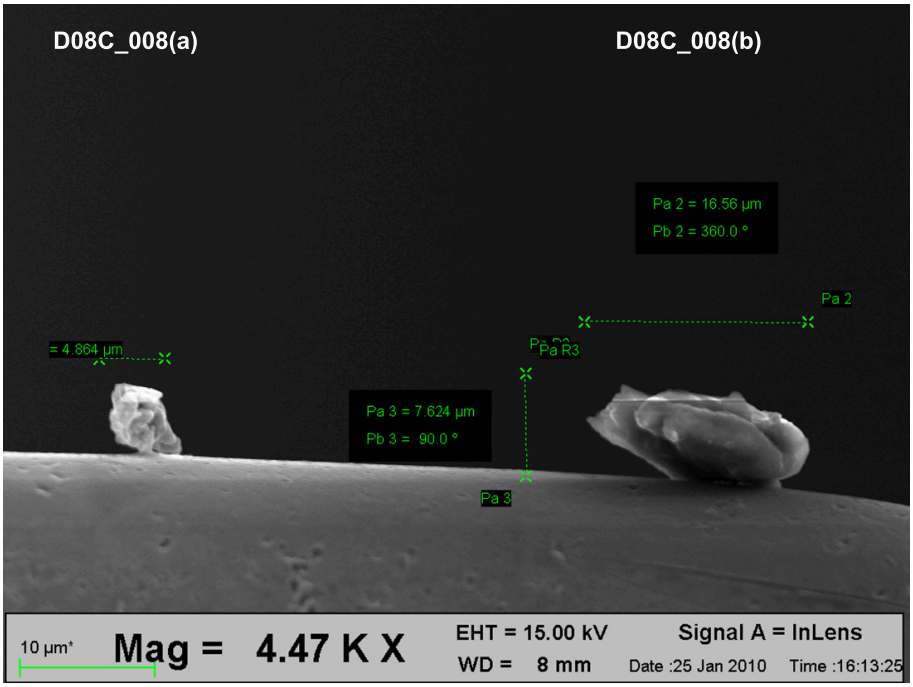

Figure 5.8: *SEM image of particles D08C_008a and D08C_008b, back side [15].*

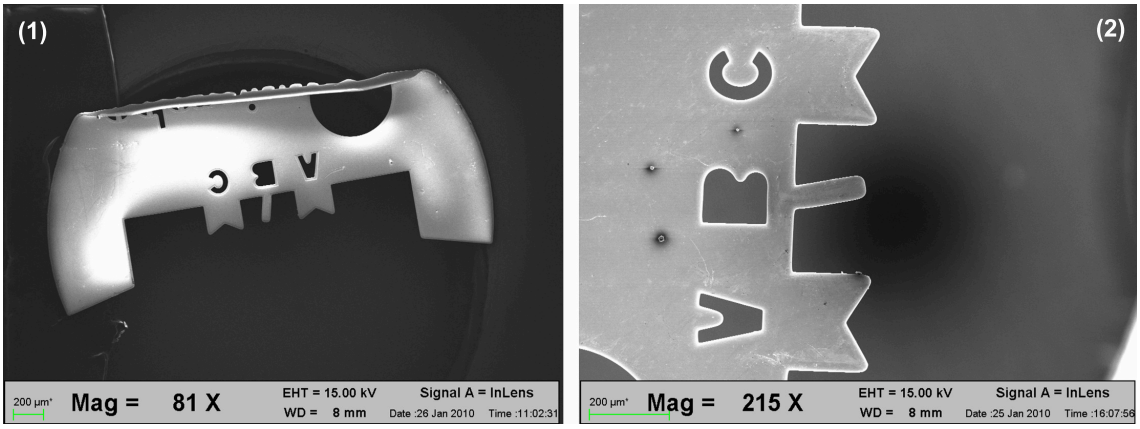

Figure 5.9: *FIB-deposited copper grid used for Raman analyses. (1): front side, the letters 'A', 'B' and 'C' are readable; (2): back side, the letters are seen in mirror way. The particle D08C_006 is welded near the 'C' on the edge; the particles D08C_008a and D08C_008b are welded near the 'A' on the edge. Particles have been welded on the FIB-copper grid using the focused ion beam procedure [15].*

5.2.4 Raman spectra of particle D08C_006

Carbon region

The Raman spectra of the particle D08C_006 in the carbon region (fig.5.11 and 5.12) are characterized by the two very strong D and G bands, at $\sim 1360\ cm^{-1}$ and $\sim 1580\ cm^{-1}$ respectively, typical of the amorphous carbon (aC). The exact band parameters (peak position (ν_0), band width ($FWHM$), peak intensity ($I(c.p.s.)$) and intensity ratio (I_D/I_G)) are listed in tab.5.3 for all analyzed samples. Spectra in the aC region have been acquired in one position on the front side and in two positions on the back side. The mapping performed on this particle in the aC region is in fig. 5.10 for front and back side: the laser spot is $< 2\ \mu m$. All the three spectra (here we reported only two) show the unique predominant features due to the aC. The D band does not occur as a separate band, rather it appears as a shoulder of the G band. The rather high level of noise and the very strong signal due to the presence of the amorphous carbon, prevent the detection of other weaker bands, e.g. due to silicates or oxides, possibly present.

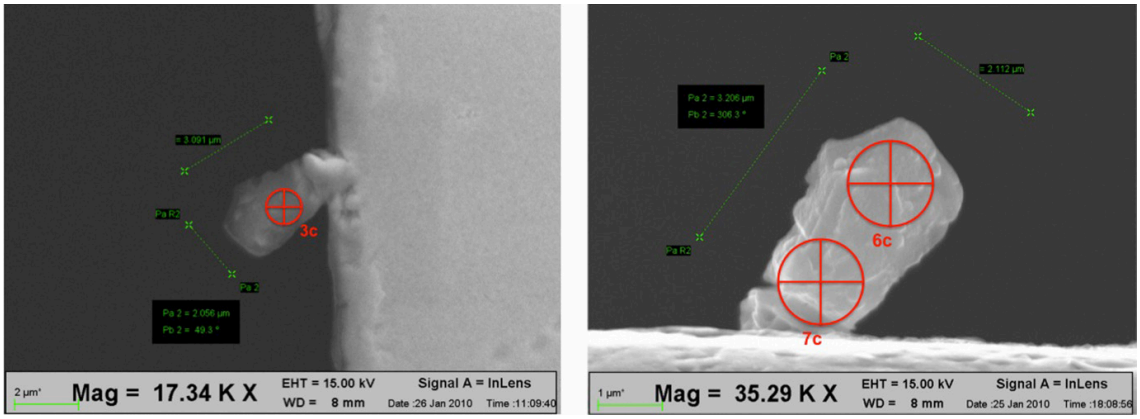

Figure 5.10: *Image of the Raman mapping performed on the particle D08C_006. Amorphous carbon region. Left: front side; right: back side.*

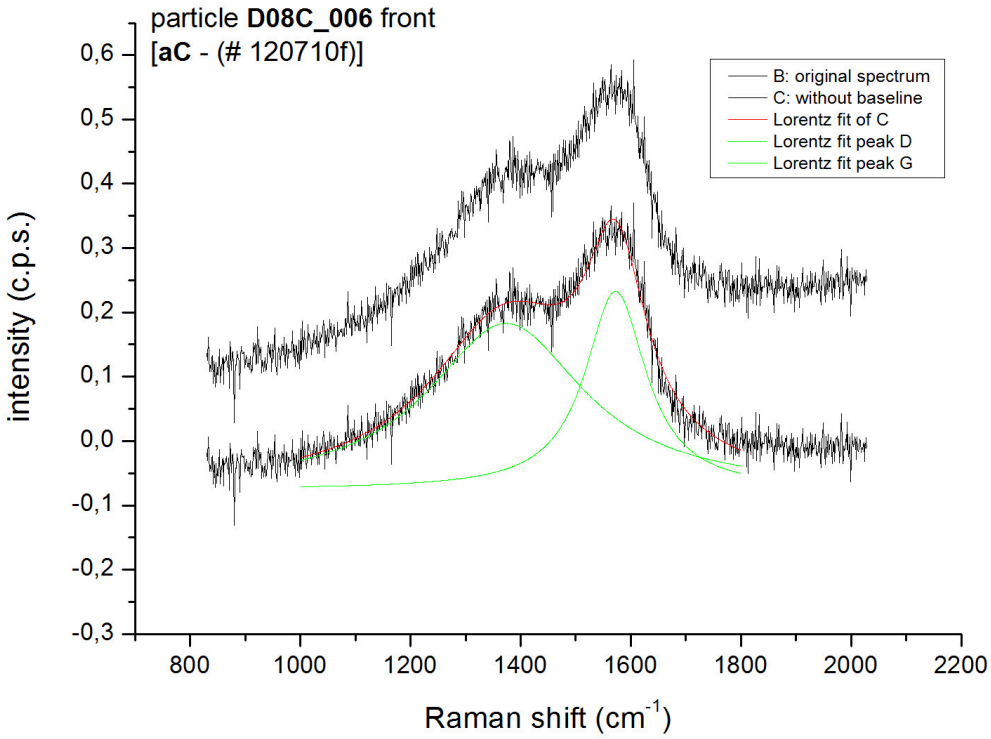

Figure 5.11: *Raman spectrum of particle D08C_006. Amorphous carbon region (Front side). The spectrum (# 120710f) has been acquired in the position 3c, fig.5.10. The D (1361 cm^{-1}) and G (1580 cm^{-1}) peaks are very strong; they appear almost joined in a unique large band with two peaks.*

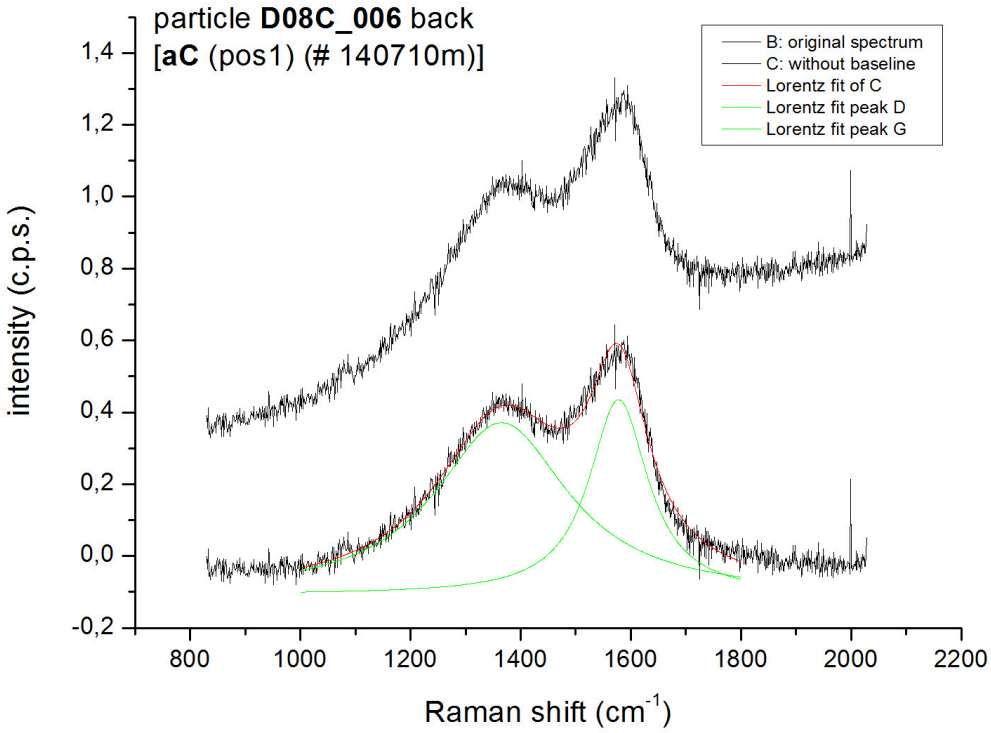

Figure 5.12: *Raman spectrum of particle D08C_006. Amorphous carbon region (Back side). The spectrum (# 140710m) has been acquired in the position 6c, fig.5.10. The D and G aC peaks are very strong and almost joined, also if a bit less than in the spectrum of fig.5.11.*

Silicates region

The mapping in the silicates region performed on the particle D08C_006 is schematized in fig. 5.13, with a laser spot $< 2\ \mu m$. The spectra are characterized by the fluorescence background continuum, onto which at larger Raman shift the aC signal is superimposed and dominant; in some spectra, among the noise, some weak peaks are detectable. The spectrum on the front side (#120710c in fig. 5.14) is very noisy and it is difficult to reveal the presence of possible weak bands. The spectrum in the back side (#130710m in fig. 5.15) shows a weak feature at a Raman shift $\sim 1080 cm^{-1}$ superimposed onto the fluorescence continuum background: the peak at $1080 cm^{-1}$ could be due to the presence of calcium carbonate ($CaCO_3$, *calcite* or *aragonite*) [81]. This interpretation is supported by the EDX analyses [15]: calcium 29.76 ± 0.30 wt%, carbon 13.79 ± 0.15 wt% and oxygen 14.14 ± 0.43 wt%. In the same spectrum two very faint and broad bands seem to appear centered at ~ 400 and $\sim 750\ cm^{-1}$.

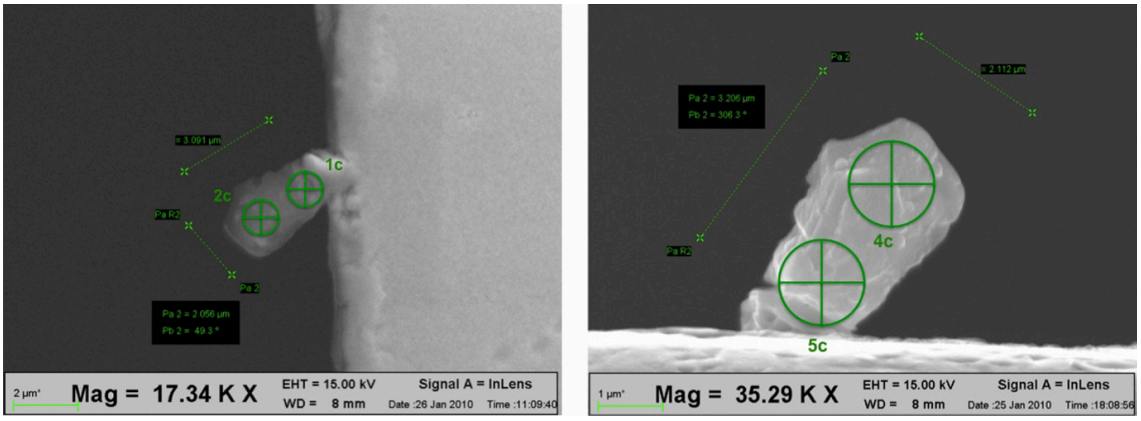

Figure 5.13: *Image of the Raman mapping performed on the particle D08C_006. Silicates region. Left: front side; right: back side.*

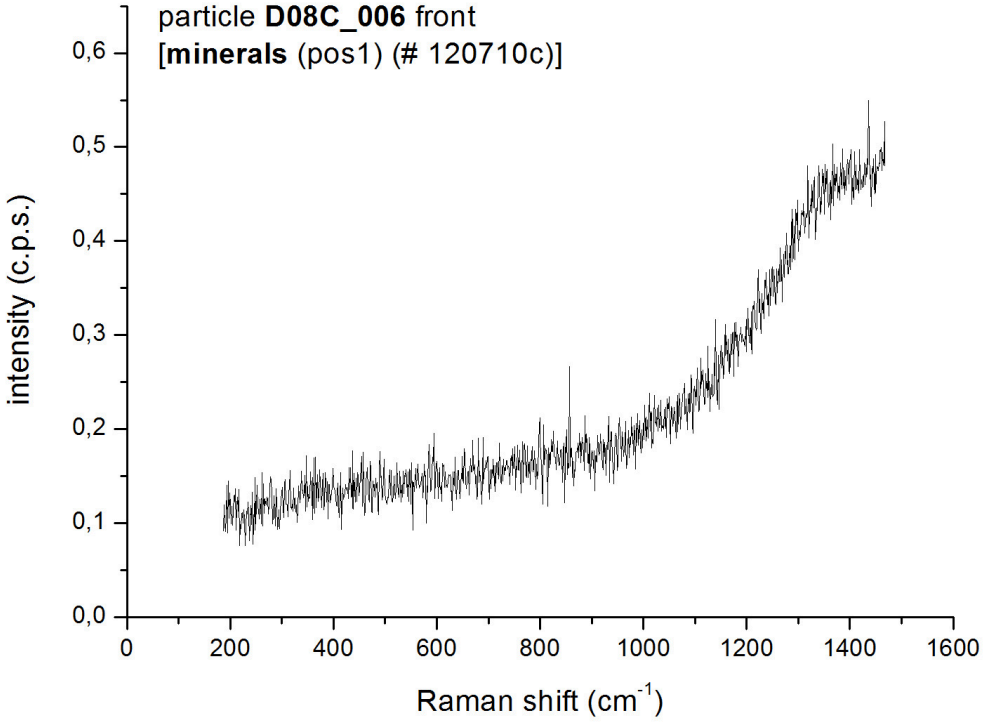

Figure 5.14: *Raman spectrum of particle D08C_006. Silicates region (Front side). The spectrum (# 120710c) has been acquired in the position 1c, fig.5.13. Because of the high level noise it is difficult to detect any eventually present band of an appreciable intensity, beyond the strong presence in surface of the amorphous carbon.*

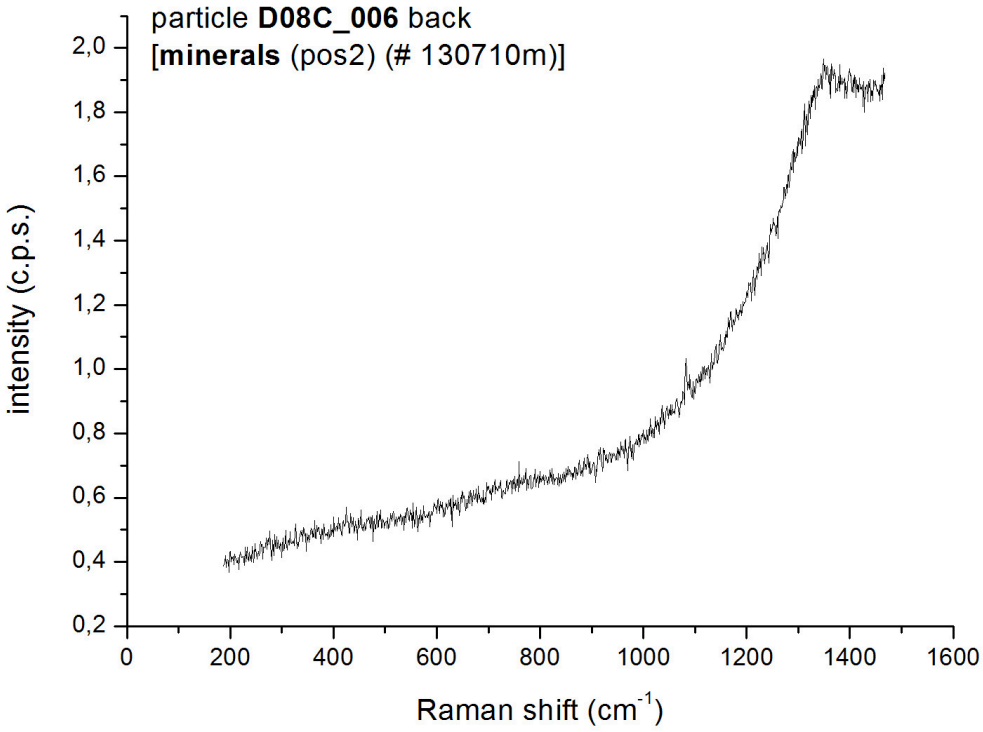

Figure 5.15: *Raman spectrum of particle D08C_006. Silicates region (Back side). The spectrum (# 130710m) has been acquired in the position 5c, fig.5.13. It is evident the weak peak at* $\sim 1086\ cm^{-1}$ *superimposed onto the fluorescence background; this peak could be due to the presence of calcite or aragonite* ($CaCO_3$) *grains [81]. The other peak due to calcium carbonate, at* $280cm^{-1}$*, is quite immersed in the noise. Two very weak and broad bands seem to appear, centered at* $\sim 400\ cm^{-1}$ *and* $\sim 750\ cm^{-1}$.

5.2.5 Raman spectra of particle D08C_008a

Carbon region

Three spectra in the carbon region have been acquired, one on the front side and two on the back side. The mapping of this particle in the carbon region is schematized in fig. 5.16; the laser spot is $< 2\ \mu m$. The spectrum in position 1a (front side, spectrum in fig. 5.17) is characterized by a high level of noise, and the only strong features are the D and G bands at $\sim$ 1360 and $\sim$ 1580 cm^{-1} respectively. In this point the two bands are almost welded in an unique large band; it is evident that here the carbon has a highly amorphous structure. The spectrum in position 9a (back side, #140710i in fig. 5.18) has a lower level of noise; the D and G bands are the two stronger features immediately apparent, they are almost joined. A weak peak appears at the Raman shift $\sim$ 1080 cm^{-1} (spectrum 5.18).

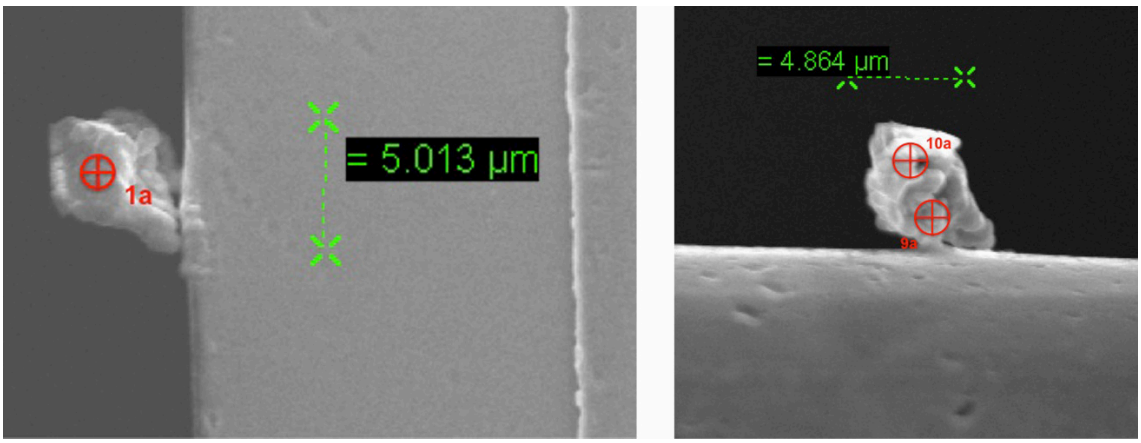

Figure 5.16: *Image of the Raman mapping performed on the particle D08C_008a. Amorphous carbon region. Left: front side; right: back side.*

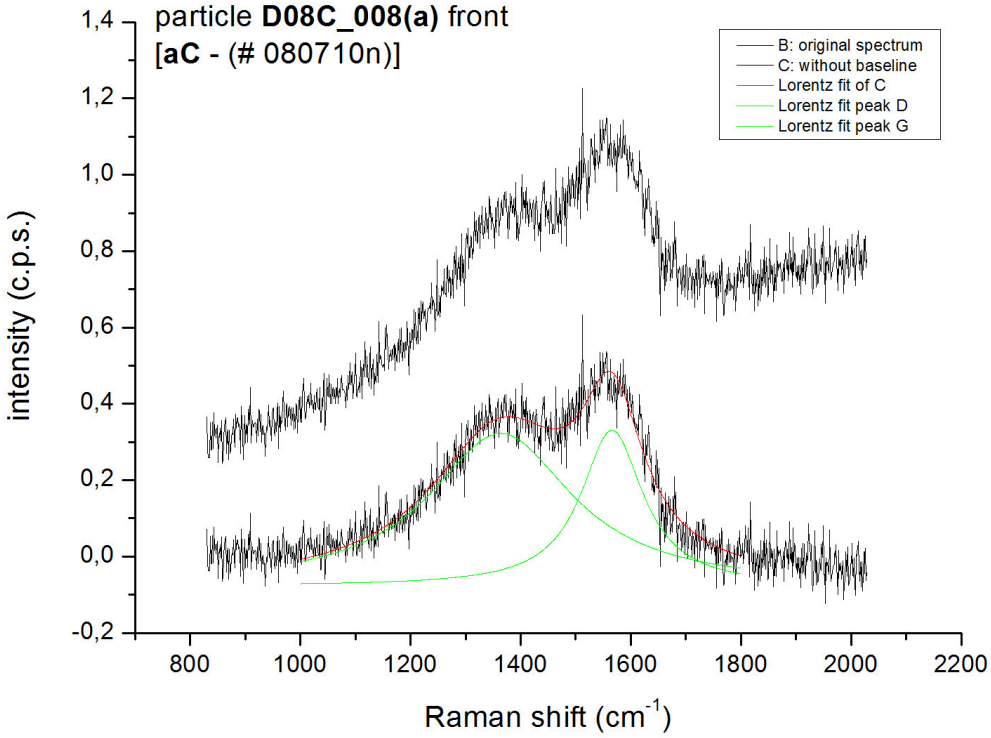

Figure 5.17: *Raman spectrum of particle D08C_008a. Amorphous carbon region (Front side). The spectrum (# 080710n) has been acquired in the position 1a, fig. 5.16. It is evident the strong presence of amorphous carbon, characterized by the two D and G bands at* ~ 1360 *and* ~ 1580 cm^{-1}.

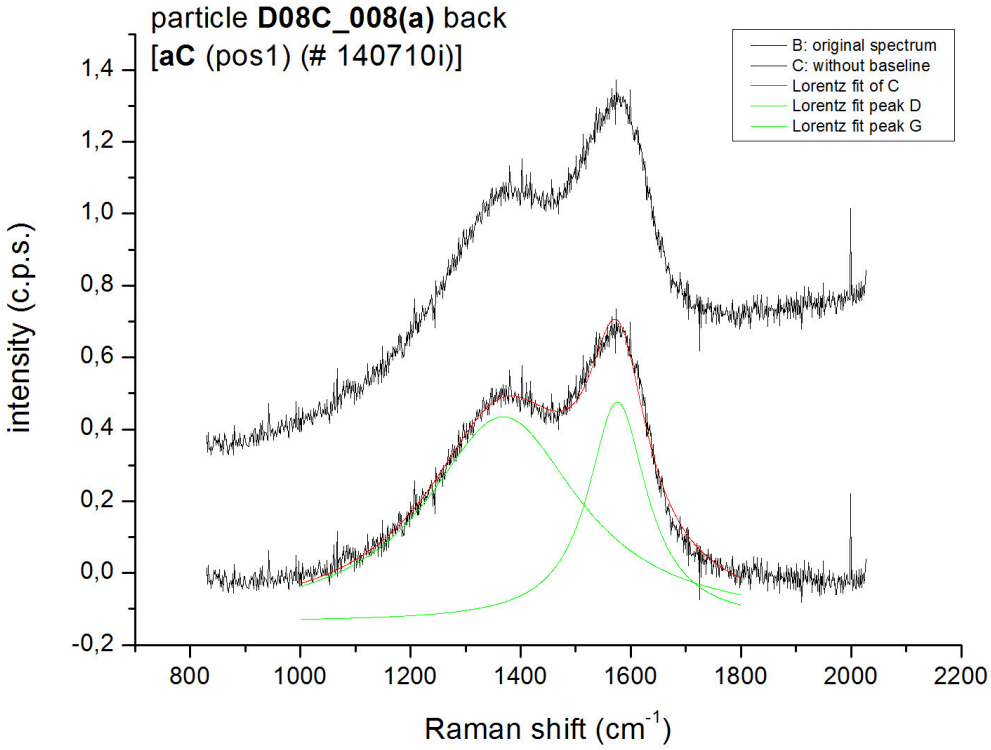

Figure 5.18: *Raman spectrum of particle D08C_008a. Amorphous carbon region (Back side). The spectrum (# 140710i) has been acquired in the position 9a, fig.5.16. The strong and almost welded D and G aC bands reveal the presence of amorphous carbon in surface; moreover, a weak peak is visible at the Raman shift* $\sim 1080\ cm^{-1}$*, though the noise level it is not small with respect to the peak intensity.*

Silicates region

Seven spectra have been acquired on the particle D08C_008a in the silicates/minerals region, three on the front side and four on the back side. The mapping is schematized in fig. 5.19. The spectrum in position 2a (#080710p in fig. 5.20) presents a weak peak at $\sim 1080\ cm^{-1}$. The spectrum in position 3a (#090710b in fig. 5.21) also shows a weak peak at $\sim 1080\ cm^{-1}$ though it is immersed in a very noisy signal. The spectrum in position 7a (#130710g in fig. 5.22) shows a peak at $\sim 1080\ cm^{-1}$. Two faint and broad bands seem to be centered at ~ 410 and $\sim 800\ cm^{-1}$.

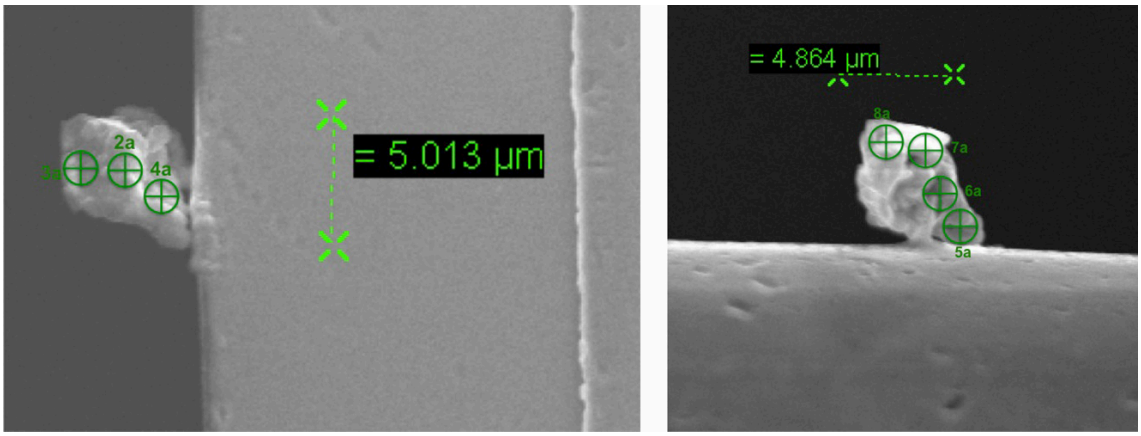

Figure 5.19: *Image of the Raman mapping performed on the particle D08C_008a. Silicates region. Left: front side; right: back side.*

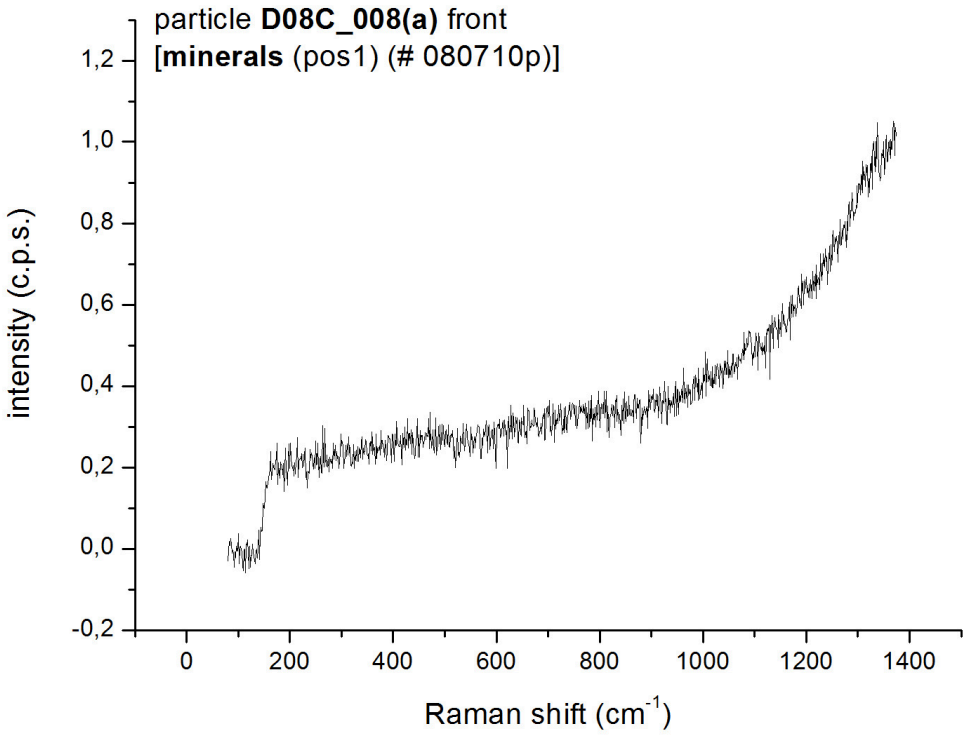

Figure 5.20: *Raman spectrum of particle D08C_008a. Silicates region (Front side). The spectrum (# 080710p) has been acquired in the position 2a, fig. 5.19. Only a weak disturbed peak is detectable at the Raman shift* $\sim 1080\ cm^{-1}$.

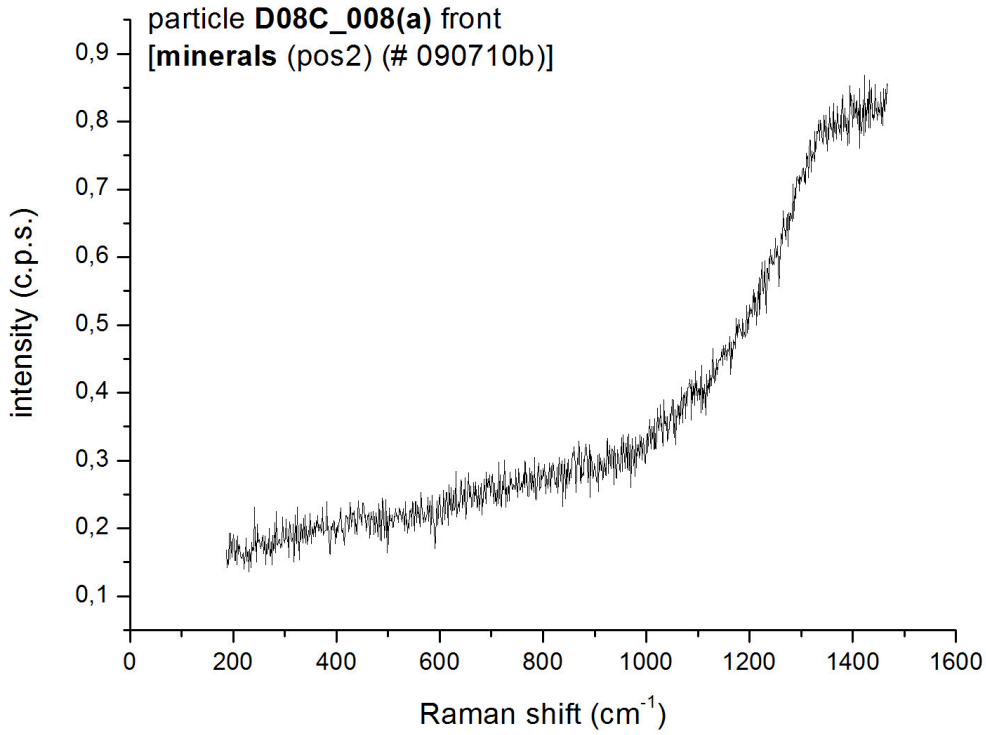

Figure 5.21: *Raman spectrum of particle D08C_008a. Silicates region (Front side). The spectrum (# 090710b) has been acquired in the position 3a, fig. 5.19. A weak peak, immersed in a noisy signal, appears at* $\sim 1080\ cm^{-1}$.

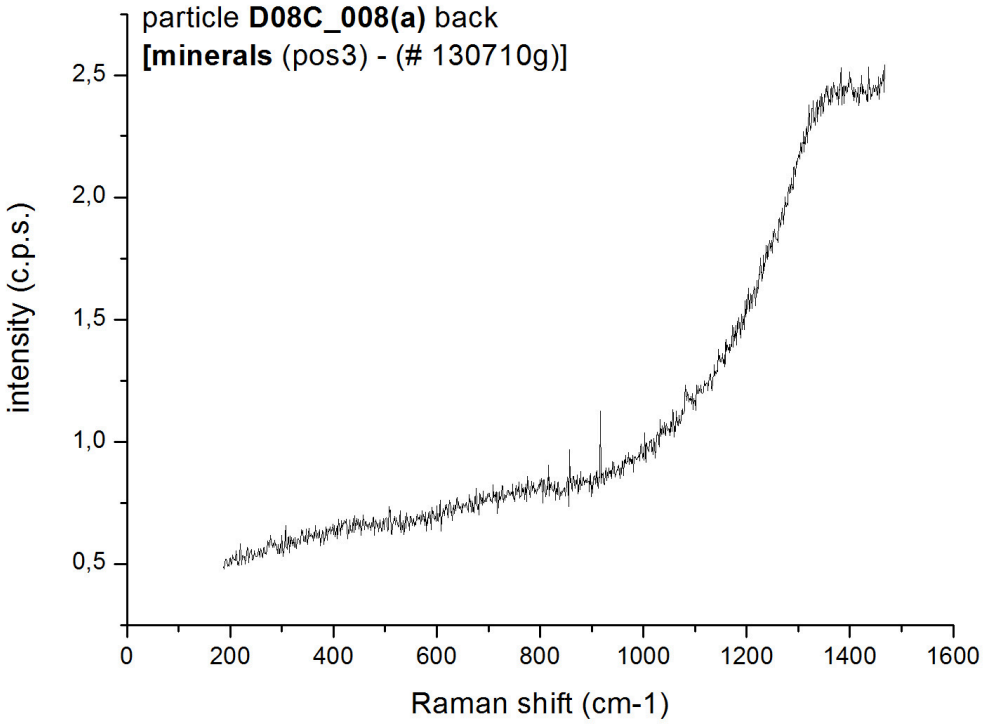

Figure 5.22: *Raman spectrum of particle D08C_008a. Silicates region (Back side). The spectrum (#130710g) has been acquired in position 7a, fig. 5.19. The peaks at* ~ 280 *and* ~ 1080 cm^{-1} *appear; two faint and broad bands are visible centered at* ~ 400 *and* ~ 800 cm^{-1}.

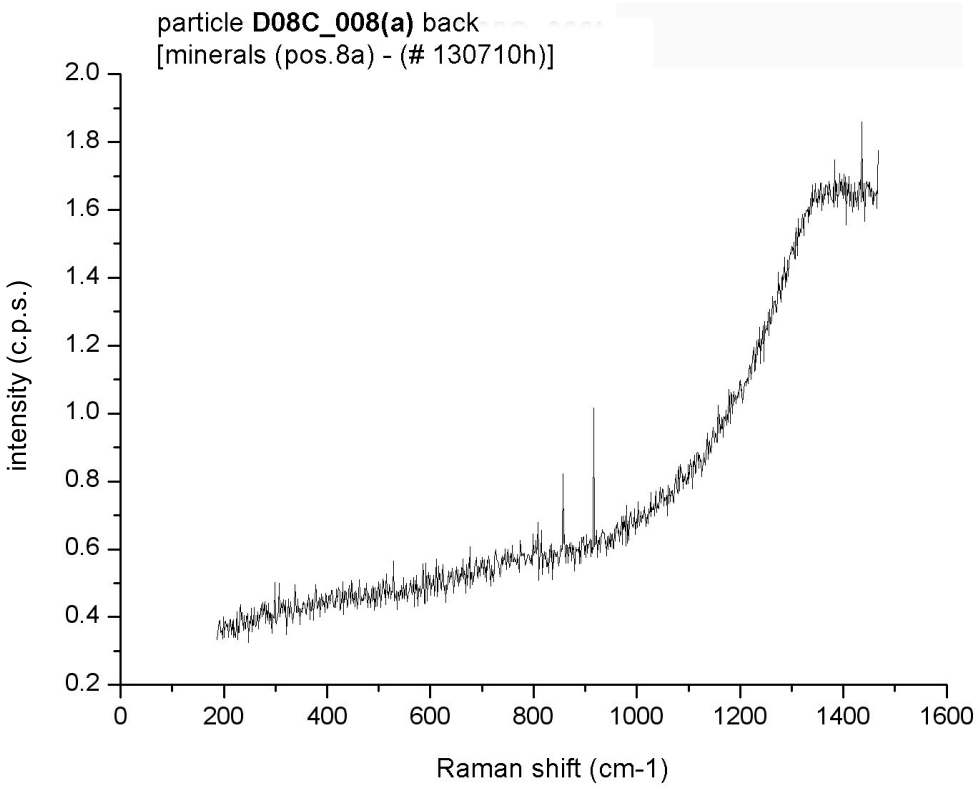

Figure 5.23: *Raman spectrum of particle D08C_008a. Silicates region (Back side). The spectrum (#130710h) has been acquired in position 8a, fig. 5.19. A weak peak appears at 280 cm^{-1}, though it is of the same order of magnitude of the noise level. A faint and broad band appears to be centered at about 800 cm^{-1}.*

5.2.6 Raman spectra of particle D08C_008b

Carbon region

Nine spectra have been acquired on this particle in the spectral region of carbon, four on the front side and five on the back side; the mapping image is in fig. 5.24; the laser spot is always $< 2\ \mu m$. The spectrum in position 2b (#080710g in fig. 5.25) is characterized by the presence of the two very strong D and G bands of the amorphous carbon at ~ 1360 and $\sim 1580\ cm^{-1}$; a small peak also seems to appear at $\sim 940\ cm^{-1}$. The spectrum in position 3b (#080710h in fig. 5.26) is dominated by the strong D and G carbon bands. In the spectrum obtained in position 12b (#140710d in fig. 5.27) the dominating presence of the amorphous carbon is revealed by the D and G bands; though immersed in the high noise, a weak feature seems visible at $\sim 980\ cm^{-1}$.

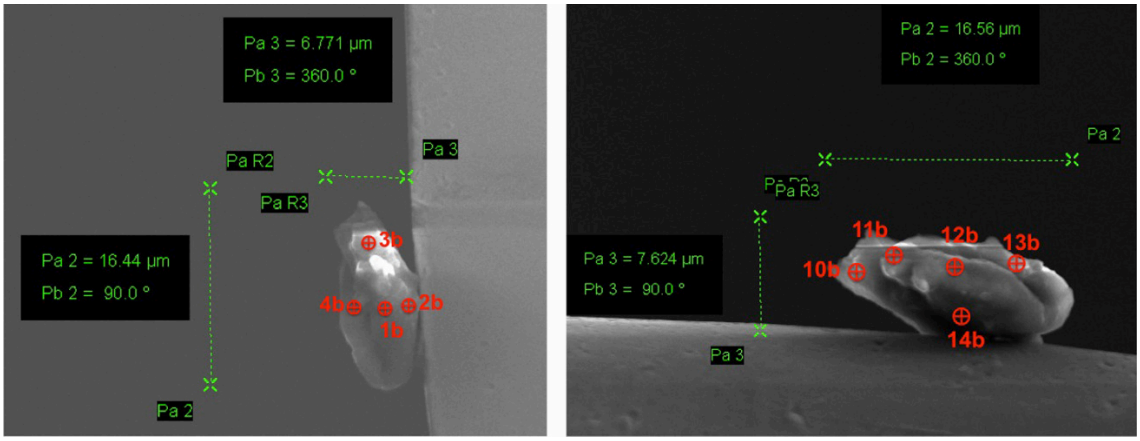

Figure 5.24: *Image of the Raman mapping performed on the particle D08C_008b. Carbon region. Left: front side; right: back side.*

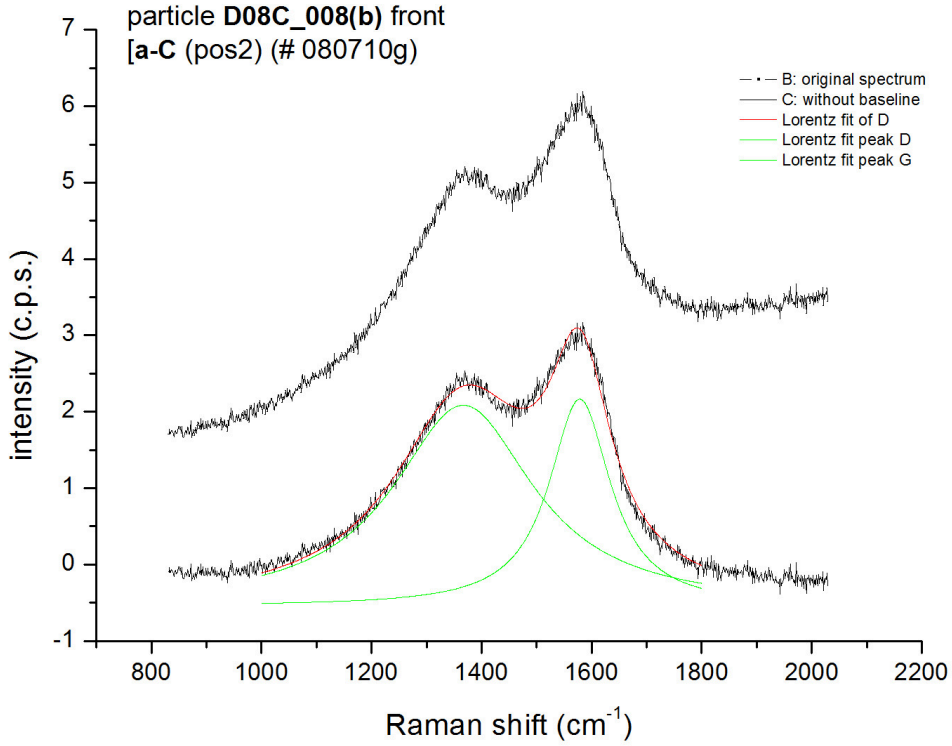

Figure 5.25: *Raman spectrum of particle D08C_008b. Amorphous carbon region (Front side). The spectrum (# 080710g) has been acquired in the position 2b, fig. 5.24. The two almost joined D and G carbon bands dominate the Raman signal, denoting the strong contribution of surface amorphous carbon. A small peak appears at about* $\sim 940\ cm^{-1}$*, nevertheless its intensity is comparable with the noise level.*

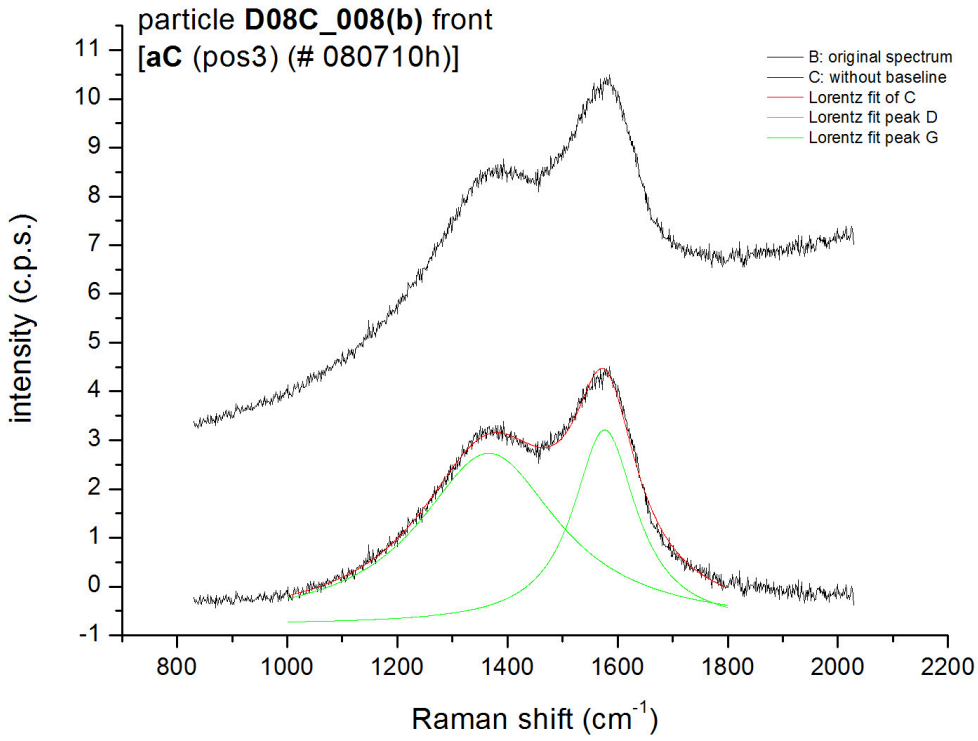

Figure 5.26: *Raman spectrum of particle D08C_008b. Amorphous carbon region (Front side) The spectrum (# 080710h) has been acquired in the position 3b, fig. 5.24. Only the two D and G carbon bands at* ~ 1360 *and* ~ 1580 cm^{-1} *are evident, the former band appearing as a shoulder of the latter.*

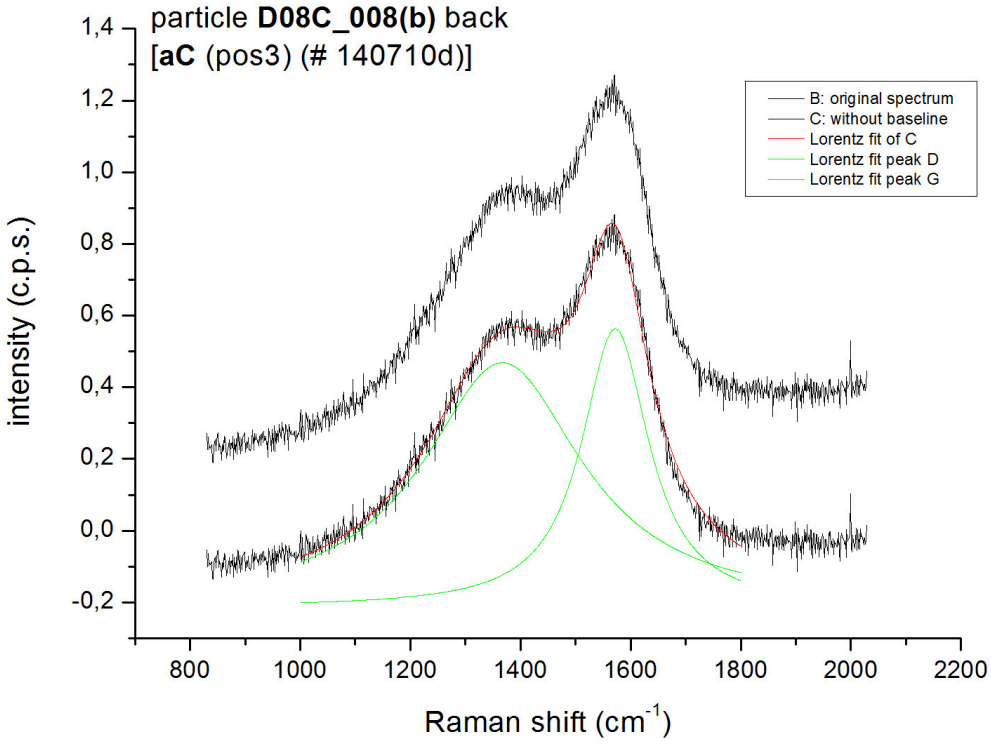

Figure 5.27: *Raman spectrum of particle D08C_008b. Amorphous carbon region (Back side). The spectrum (# 140710d) has been acquired in the position 12b, fig. 5.24. The presence of surface amorphous carbon is revealed by the two D and G almost joined bands. A very weak and confused peak seems to appear at about 980* cm^{-1}.

Silicates region

Five spectra have been acquired on the particle D08C_008b in the silicates spectral region, two on the front side and three on the back side. In the spectrum obtained in position 5b (#090710d in fig. 5.29) two faint and broad bands appear centered at about 440 and 700 cm^{-1}, the latter being approximately in the range 600-800 cm^{-1}. The spectrum in position 8b (#130710c in fig. 5.30) has a high noise level, that prevent an easy identification of eventually present spectral features; the weak and broad band in the range 600-800 cm^{-1} seems to be present. In the spectrum obtained in position 9b (#130710d in fig. 5.31) two very weak and broad bands can be seen in the range 380-440 cm^{-1} and 600-800 cm^{-1}. These two bands could be interpreted as the L_1 and L_2 peaks appearing in Raman spectra of sputtered amorphous carbon with low sp^3 content (Ferrari and Robertson, 2001): the two bands are clearly visible in spectra obtained with exciting laser energy of 785 nm, while increasing the laser energy they progressively disappear; at 514 nm they are very faint and only the L_2 peak at around 800 cm^{-1} is detectable (as in fig.5.29), while at 244 nm they disappear at all [29].

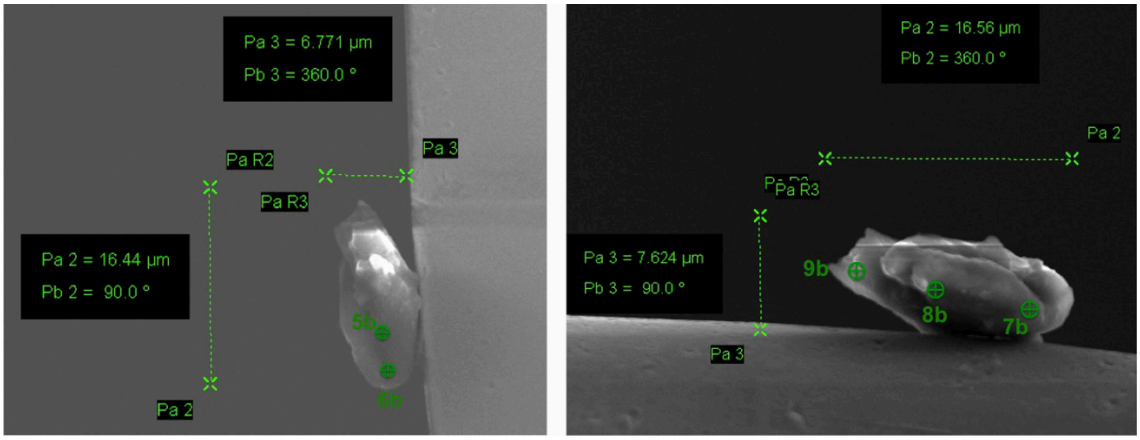

Figure 5.28: *Image of the Raman mapping performed on the particle D08C_008b. Silicates region. Left: front side; right: back side.*

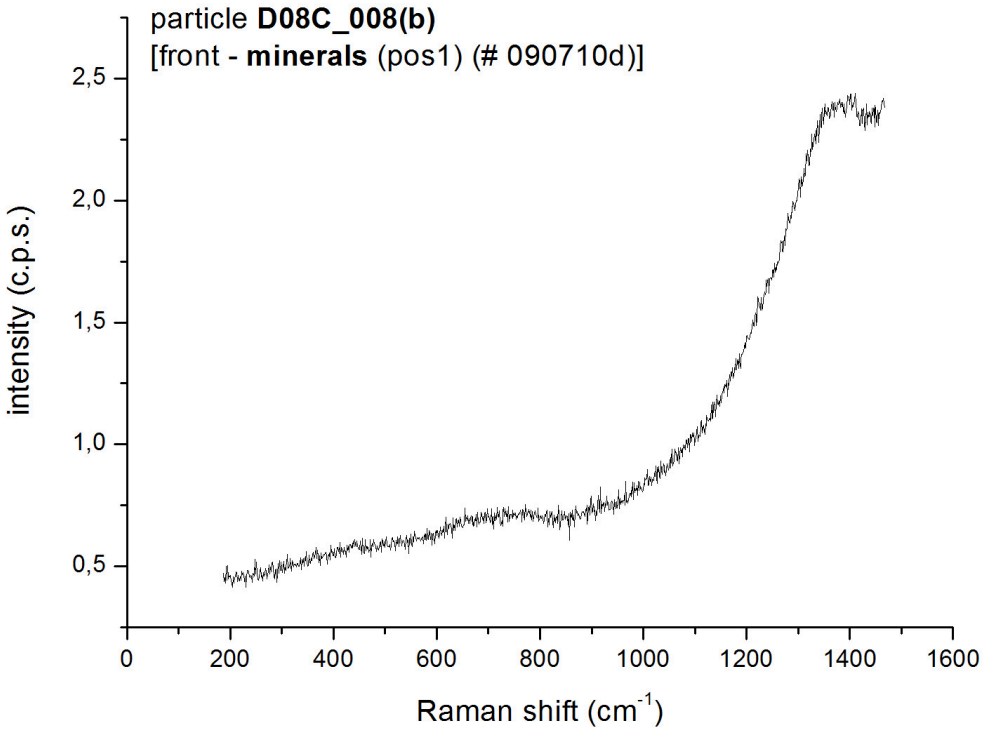

Figure 5.29: *Raman spectrum of particle D08C_008b. Silicates region (Front side). The spectrum (#090710d) has been acquired in the position 5b, fig. 5.28. A broad band appear in the range 600-800 cm^{-1}, centered at about 700 cm^{-1}; another small peak seems evident, centered at about 440 cm^{-1}.*

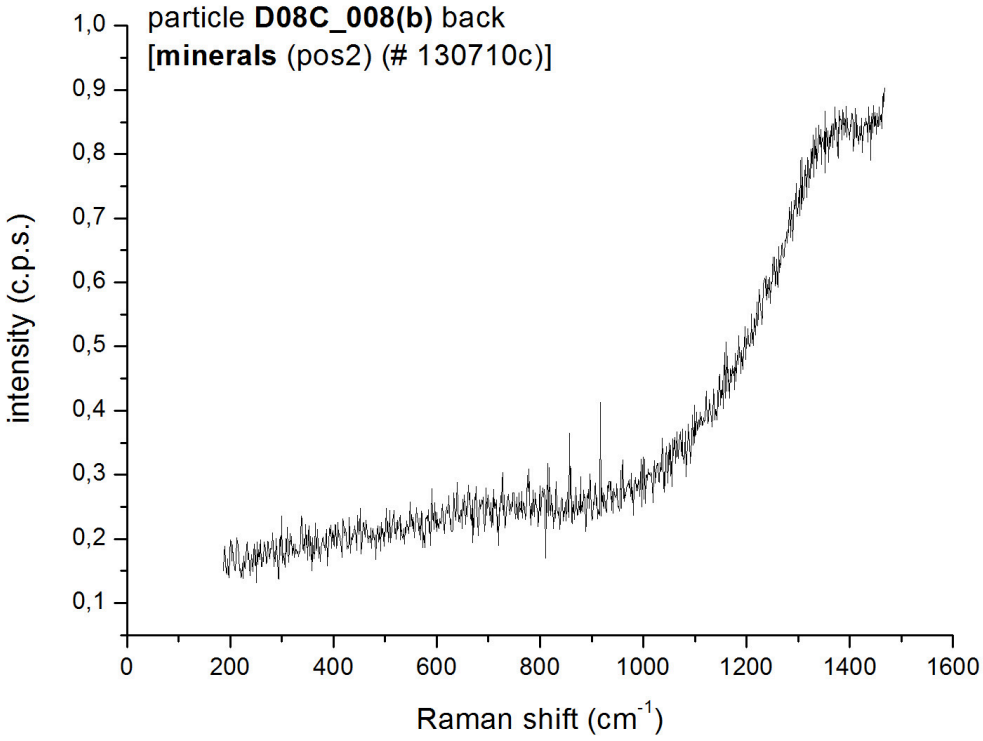

Figure 5.30: *Raman spectrum of particle D08C_008b. Silicates region (Back side). The spectrum (#130710c) has been acquired in the position 8b, fig. 5.28. Here the noise level is high and the aC signal dominates with respect to other sources eventually present.*

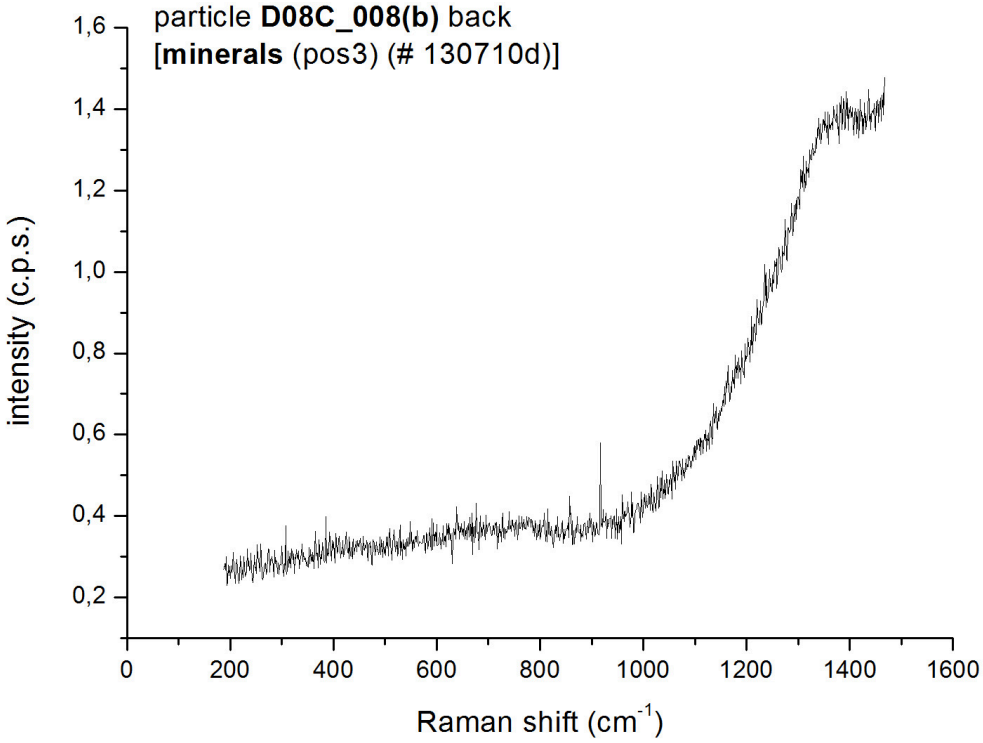

Figure 5.31: *Raman spectrum of particle D08C_008b. Silicates region (Back side). The spectrum (#130710d) has been acquired in the position 9b, fig. 5.28. Two faint and broadened bands at 380-440 cm^{-1} and 600-800 cm^{-1} are detectable.*

5.2.7 Checks for possible Carbon Contamination

Several Raman spectra have been acquired on the holey carbon film in order to establish if the amorphous carbon found on the surface of all particles was due to some contamination: the particles are collected onto the carbon film within the TEM grids (see section 3.2.3 for details), and so part of it could have contaminated the particles during the collection. One spectrum of the carbon film is in fig. 5.32: it is evident that, in this case, the carbon film has a more amorphous structure than the carbon present on the surface of the analyzed particles. In this case indeed the two D and G bands are not resolved separately, but appear completely joined in a unique broad band: here the structural disorder is higher. Thus the two carbons have definitely different degrees of structural disorder, so the amorphous carbon that is present on the particles likely is not originated from the holey carbon film.

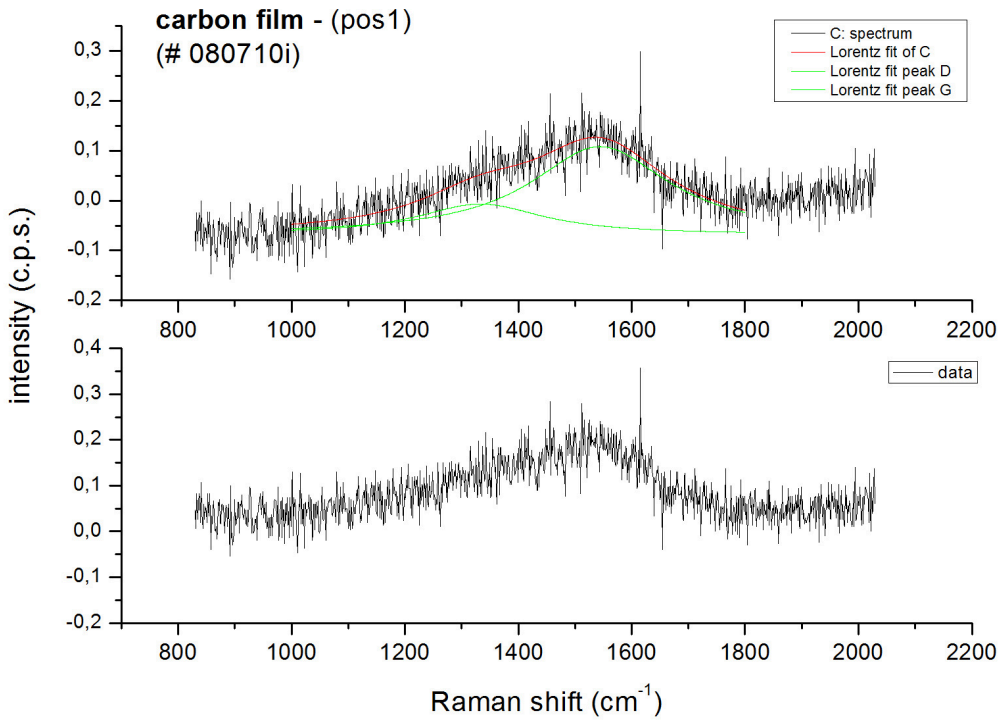

Figure 5.32: *Raman spectrum of holey carbon film analogue to that used as flight substrate.*

In order to check if the amorphous carbon was due to some post-flight contamination process due for example to the focused ion beam welding procedure, we acquired many spectra directly on the FIB-copper grid, both near the welding point of each particle, and in several positions on the grid at different distances from the welding points. The resulting spectra, relative to the point where the particle D08C_006 had been welded, are reported in fig.5.33. Eight spectra are reported: they have been acquired from a *position 1* to a *position 8*, shifting the laser spot along the grid with increasing distance from the particle welding point. Six spectra are characterized by the presence of amorphous carbon. The plot clearly shows that the shape of the two D and G bands gradually evolves from pos.1 to pos.8: their intensity decreases, they become more joined, and in the spectra 7 and 8, the farthest two, they completely disappear. This is an evidence that at least part of the amorphous carbon on the particles is related to the FIB welding procedure, being aC present also on the welding point and on the grid at short distance. In the next session, the contamination issue is assessed in more detail.

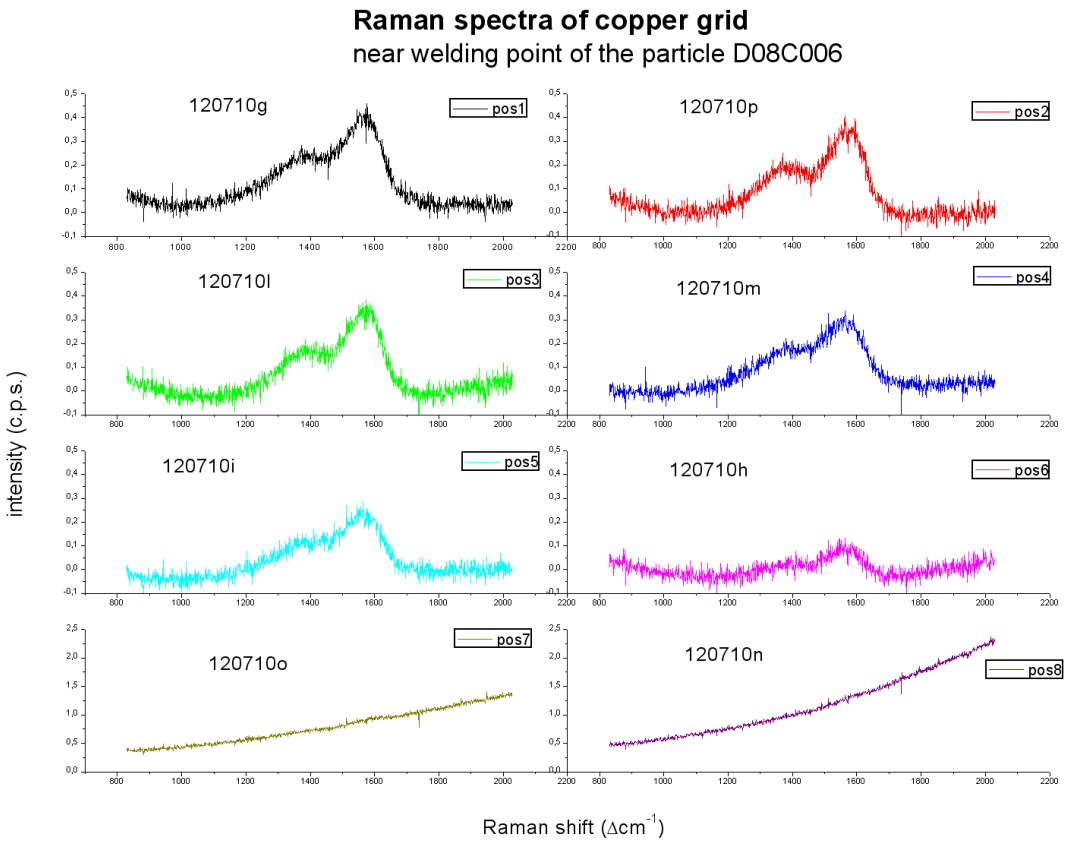

Figure 5.33: *Raman spectra of the copper grid onto which particles were welded with FIB. These spectra are relative to the point where particle D08C_006 was attached. The spectra were taken on the grid at various positions with respect to the welding point of the particle ('C' letter in fig. 5.9): positions from 1 to 8 are at increasing distance from the welding point. The D and G peaks gradually disappear.*

5.2.8 Discussion

Micro-Raman analyses on the 3 DUSTER particles detected the presence of amorphous carbon, with a variable degree of structural order, in different positions of the particles surfaces. It seems that part of the amorphous carbon found may not be indigenous of the particles, occurring as a non-uniform coating that covers their surface. This item needs to be confirmed by further tests. On the other hand, a fraction of the detected amorphous carbon is intrinsic to the particles. Also other minerals (silicates, oxides) could be present but not detected because embedded into a carbonaceous matrix. The presence of a surface layer of amorphous carbon prevents or at least makes very difficult the detection of other compounds, minerals, silicates eventually present, essentially for two reasons [2, 28, 63, 90]:

1. the laser penetration depth on the material is a few hundred angstroms, and the surface aC coating detected could prevent the detection of other minerals possibly present underneath;

2. the Raman cross section of the amorphous carbon is considerably larger than the Raman cross section of other minerals and silicates, so the presence of aC results in a strong signal that covers other possible sources.

The Raman parameters have been obtained fitting the D and G bands in the Raman spectra in the carbon region (centered at $\nu_0 = 1450\ cm^{-1}$) with four different fit modes, that is with the MicroCal Origin Lab software (Lorentzian curve) and with an ad-hoc tool in LabVIEW environment (Lorentzian, Gaussian and BWF curve), and then taking the average values of the four fitting modes. Raman band parameters are listed in tab. 5.3 and 5.4. The D-peak position, relatively to DUSTER particles, varies in the range $1362.96 < \omega_D < 1378.89\ cm^{-1}$, while the G-peak position is in the range $1562.18 < \omega_G < 1576.64\ cm^{-1}$; the *full width at half maximum* of the D peak (FWHM-D) varies in the range $205.28 < \Gamma_D < 261.97\ cm^{-1}$, and the FWHM-G is in the range $103.63 < \Gamma_G < 131.74\ cm^{-1}$. For each of the D and G bands, intensity, area and their relative ratios have been calculated (tab.5.3 and 5.4).

The Raman spectra acquired on the FIB-copper grid near the particles welding points clearly show that a small amount of aC is also present on the grid (fig.5.33). A plot of the intensity ratio I_D/I_G, and of the area ratio A_D/A_G, in function of the distance from the welding point (fig.5.34, relative to particle D08C_006), depicts an almost monotone decrease of the ratios, as the distance from the particle welding point increases. Thus a minor amount of amorphous carbon is present on the FIB grid near the welding points, and it decreases at large distance up to disappear

completely.

This can be a hint to interpret the amorphous carbon detected on the particle surfaces as a post-flight contamination due to the FIB welding procedure. The focused ion beam mechanism typically uses Ga ions and precursor gases (generally containing Pt and carbon) in order to produce the welding of the samples. Several conditions such as temperature rising, the presence of vapors in the ambient and of seeds on the surface subject to the ions beam, can cause the deposition of ions and materials and the adsorption of precursor gases on the material surface [88]. But to prove the FIB contamination scenario further analyses have to be performed.

The very different spectra of holey carbon film with respect to the spectra of DUSTER particles (fig.5.32), both with the fact that in fig.5.35-A and -C the different sample regions do not overlap with each other, discard the possibility that carbon film could have contaminated stratospheric particles during the collection.

The Γ_D vs ω_D has been plotted for DUSTER particles, FIB-copper grid and holey carbon film (fig.5.35-A) and for DUSTER particles alone (fig.5.35-B); the Γ_G vs ω_G has been plotted for DUSTER particles, HOPG, carbon film and FIB-copper grid (fig.5.35-C) and for DUSTER particles alone (fig.5.35-D). From the plots in fig.5.35-A and 5.35-C it appears that most of the band parameters relative to the different analyzed samples spread in different regions of the plots, without a substantial overlapping; this could indicate that at least part of the detected amorphous carbon is really intrinsic of the collected particles. The plot in fig.5.35-B relative to the D-peak, shows a general tendency of increasing FWHM-D with increasing ω_D. The plot in fig.5.35-D relative to the G-peak reveals the tendency of decreasing FWHM-G with increasing ω_G. These two latter plots seem to be consistent with the trends of Γ_D *vs* ω_D and Γ_G *vs* ω_G that are reported for example in [1], relatively to extraterrestrial samples (IDPs and meteorites) and IPHAC.

The Γ_G vs ω_G plot has been reported by many authors as a tool to investigate the nature of carbonaceous materials in extraterrestrial samples collected both at the Earth surface [2, 63], in the stratosphere [2, 13, 63, 79] and in space missions (for example the Stardust mission, [80]), as far as in cosmic dust laboratory analogues [1, 2]. The Γ_G vs ω_G plot here reported is consistent for example with that reported in Baratta et al. (2004) and in Rotundi et al. (2008) [1, 80]: the general tendency of a decreasing Γ_G with increasing ω_G observed in DUSTER particles is somewhat analogue to that observed for carbonaceous materials in extraterrestrial samples; the quite decreasing trend is similar to that of carbonaceous materials found in terrestrial meteorites; primitive meteorites are characterized by large G-peaks occurring

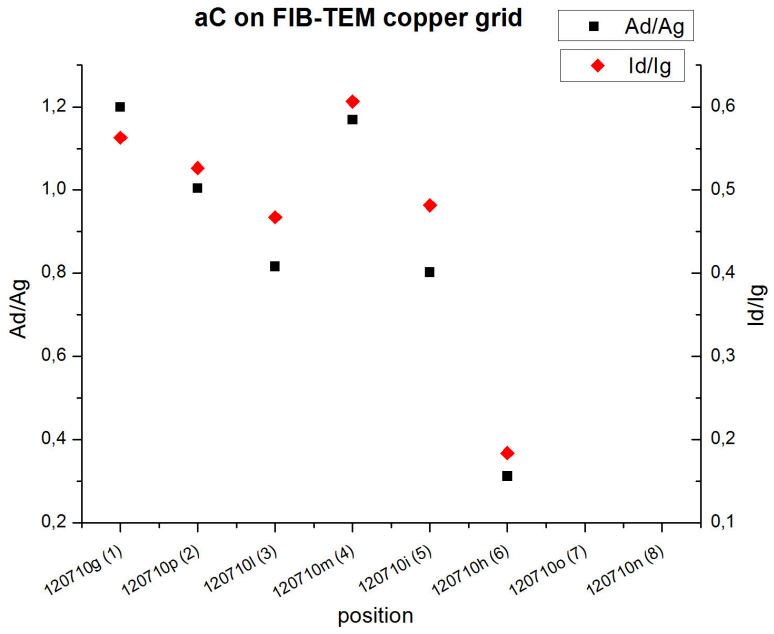

Figure 5.34: *Plot of the D and G peaks area ratio and intensity ratio vs position, relative to spectra obtained on the FIB copper grid, near the welding point of the particle D08C_006. On the X axis there are the spectra names with relative positions (from 1 to 8 with increasing distance) with respect to the welding point. A small amount of aC is also present on the grid, but it decreases moving along the grid going away from the welding point. In the spectra obtained in positions 7 and 8, no D and G bands are present.*

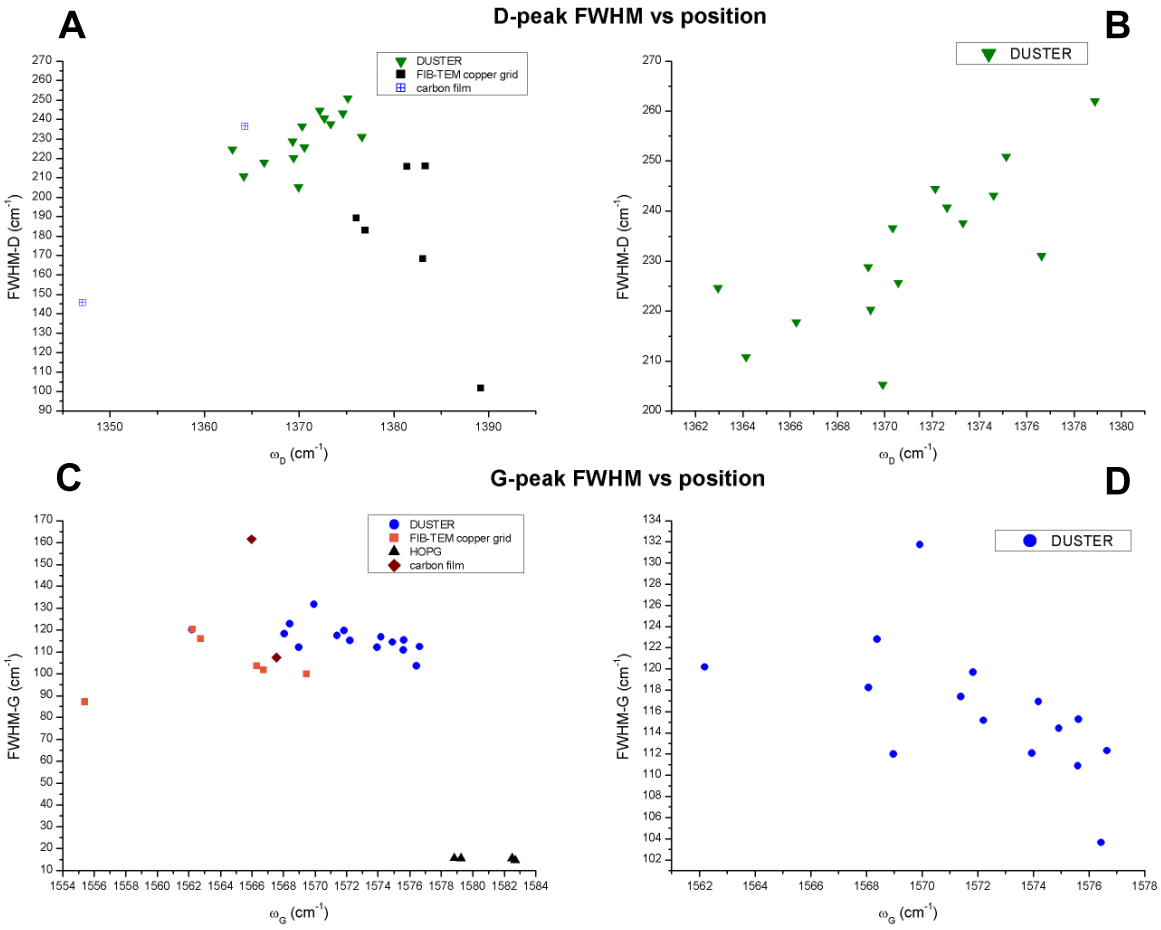

Figure 5.35: *FWHM vs peak position plotted for D-peak (A,B) and G-peak (C,D). In plot A, Raman parameters for DUSTER particles, carbon film and FIB-copper grid are plotted, while in plot B only data relative to collected particles are evidenced; in plot C, Raman parameters for DUSTER particles, carbon film, FIB-copper grid and HOPG are graphed, while in plot D there are only data relative to collected particles. The plots A and C show that the Raman parameters spread in different and non-overlapping regions in the* $\Gamma vs\omega$ *plot: this could be an indication that surface carbon on collected particles is mainly intrinsic.*

at small ω_G, while processed meteorites are characterized by narrow G-peaks occurring at high ω_G [80]. If we try to compare Raman band parameters obtained for DUSTER particles, with Raman band parameters determined for stratospheric IDPs and cometary grains collected by Stardust, we can see that the former lie well along the meteorites line, rather shifted towards the more primitive meteorites extreme (fig.5.36).

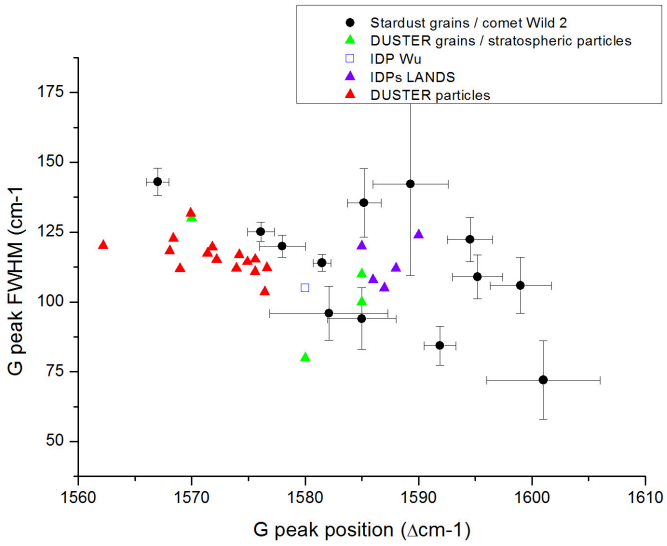

Figure 5.36: *Raman band parameters for DUSTER particles (red triangles) compared with that of Stardust grains (black circles) and stratospheric IDPs collected by NASA (green and purple triangles) [79, 80].*

The intensity ratio, I_D/I_G, has been calculated and plotted in function both of the D-peak position and of the G-peak position, for DUSTER particles and for spectra obtained on the copper grid (fig.5.37). From the two plots in fig.5.37 we can see that the intensity ratios calculated for DUSTER particles and those calculated for the FIB-copper grid, spread in different non-overlapping regions. The intensity ratio calculated for the collected particles are in the range $0.68 < I_D/I_G < 0.99$, while those calculated for the copper grid are in the range $0.18 < I_D/I_G < 0.61$. The intensity ratio is typically another parameter useful to investigate and characterize carbonaceous materials, in addition to the G-peak FWHM and position, although it is not unambiguous. The I_D/I_G ratio in general depends on the size L_a of the graphitic domains of the carbonaceous structure, but the dependence is not monotonous, indeed both highly disordered amorphous carbons and very ordered materials can have a

similar value of the intensity ratio. For $L_a < 20$ $\mathring{A}$ the intensity ratio is proportional to the square of the domain size (Ferrari and Robertson, 2000):

$$\frac{I_D}{I_G} = C'(\lambda) \cdot L_a^2 \tag{5.20}$$

where the parameter C' depends on the laser wavelength; here $C'(514nm) = 0.0055$ $\mathring{A}^2$. For $L_a > 20$ $\mathring{A}$ the intensity ratio is proportional to the inverse of the domain size (Tuinstra-Koenig, 1970):

$$\frac{I_D}{I_G} = \frac{C(\lambda)}{L_a} \tag{5.21}$$

where the parameter is $C(515nm) = 44$ $\mathring{A}$. Thus determining the intensity ratio can give an insight about the structural disorder of carbons. Considering the *amorphization* trajectory described by Ferrari and Robertson (2000), we can make the hypothesis that DUSTER particles carbons lie in the stage 2, that is from *nanocrystalline graphite (nC-G)* $\Longrightarrow$ *amorphous carbon*. The intensity ratio is indeed in the range $0.68 < I_D/I_G < 0.99$ (see fig.5.37). For the three particles we obtain the average values $\langle I_D/I_G \rangle = 0.80, 0.80, 0.83$. We can determine the domain size L_a using the Ferrari-Robertson relation (eq.5.20) which is valid in the stage 2:

$$L_a = \sqrt{\frac{1}{C'(\lambda)} \cdot \frac{I_D}{I_G}} \tag{5.22}$$

thus we obtain the average value of the domain size for the three particles: $\langle L_a \rangle = 12.14$ $\mathring{A}$; finally the corresponding average sp^3 content is $11 - 12\%$, as can be determined on the amorphization trajectory [19, 28].

In addition to the amorphous carbon, among all the revealed peaks, the other unique compound detected and likely identified is the calcium carbonate $CaCO_3$, though yet there is ambiguity between the two forms: calcite or aragonite. The calcium carbonate is revealed by the two peaks at ~ 280 cm^{-1} and ~ 1080 cm^{-1} found in the Raman spectra of particles D08C_006 and D08C_008a (small fragment). Micrometer-sized single grains of calcite have been found in stratospheric IDPs by Brownlee et al. (1980) [9]. Calcite micrometer-sized globules have also been detected with micro-Raman techniques in meteorites, such as for example in the Vaca Muerta mesosiderite found in the Atacama Desert (Chile), by Rull Perez and Martinez-Frias (2003) [81].

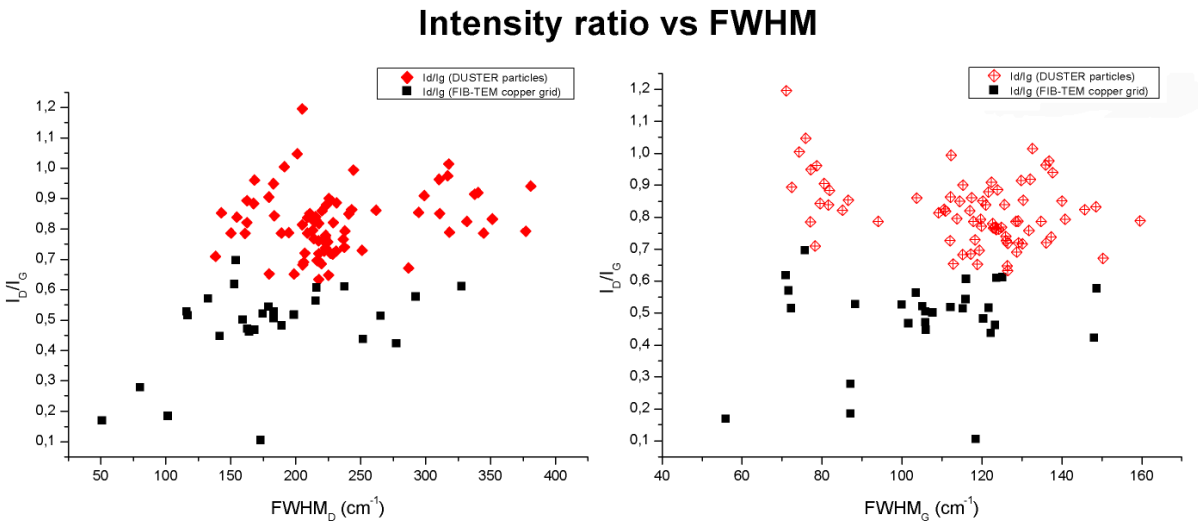

Figure 5.37: *Intensity ratio I_D/I_G in function of D-peak FWHM (left) and of G-peak FWHM (right). Red rhombs are relative to DUSTER particles, black squares are data relative to FIB-copper grid. The two set of data in each plot do not overlap, they spread in two distinct regions.*

The Raman spectrum of calcite is characterized by a peak at 286-288 cm^{-1}, a very small peak at 713-716 cm^{-1} and a major peak at 1086-1092 cm^{-1} [25, 81, 38]. Here we only detected the peaks at 286 and 1086 cm^{-1} (fig. 5.15, 5.18, 5.20, 5.21, 5.22 and 5.23), while the very small peak at 713 cm^{-1} is not visible within the high noise caused by aC in our spectra; the intensity of the peak at 713 cm^{-1} is generally $< 1/2$ of the intensity of the peak at 286 cm^{-1}, and so it is immersed within the noise [81]. Scanning electron microscope and EDX analyses performed by Ciucci (2010) reveal a high calcium content in these two particles, up to 29.76 ± 0.30 $wt\%$ within the particle D08C_006, and up to 27.28 ± 0.25 $wt\%$ within the particle D08C_008a [15, 16] (note that the nomenclature of the particles -08a and -08b here are reversed). Moreover the infrared spectra of calcite-type minerals are characterized by peaks at 712 cm^{-1} (symmetric CO_3 deformation), 874-876 cm^{-1} (asymmetric CO_3 deformation) and 1400-1435 cm^{-1} (asymmetric CO_3 stretching) (see fig.5.38) [25, 38]. The infrared spectrum of particle D08C_008a (small) [15] indeed shows three peaks at about 710, 875 and 1400 cm^{-1}, thus the presence of calcite would be confirmed also by IR measurements.

All these considerations support the idea that submicrometer-sized grains of calcium carbonate are really present in these stratospheric particles collected by DUSTER.

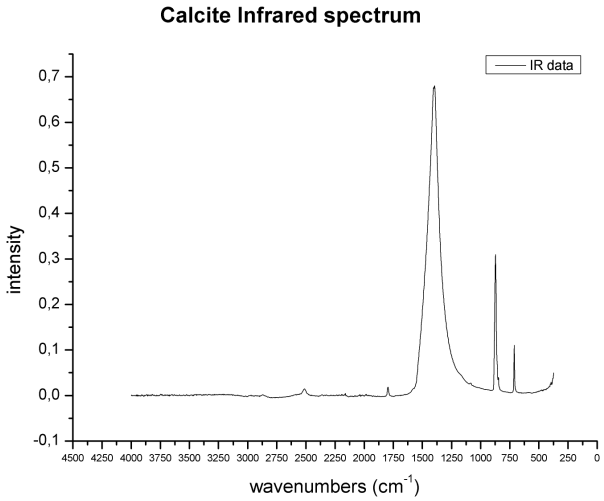

Figure 5.38: *Infrared spectrum of calcite [25].*

Typically stratospheric Ca-rich particles are likely extraterrestrial in nature, rather than terrestrial. Ca-rich particles of terrestrial origin (for example from Arctic geological environments) like *mono-hydrocalcite* ($CaCO_3 \cdot H_2O$) or *ikaite* ($CaCO_3 \cdot 6(H_2O)$) have different composition and morphology with respect to DUSTER particles [15]. Other arguments suggest that these particles could be of cosmic origin, rather than of terrestrial origin. Carbonaceous materials are often the most abundant compounds that are detected in many extraterrestrial samples, like IDPs and meteorites; many IDPs collected in stratosphere indeed present Raman spectra only dominated by the strong D and G carbon Raman bands (see for example Wopenka, 1988, Quirico et al., 2005, Rotundi et al., 2007) [63, 79, 90]. The "Γ vs ω" plots for D and G-peak here reported show trends that are consistent with those reported by Baratta et al. (2004) and Rotundi et al. (2008). Another reasonable argument is the collection altitude of these particles, that is $\sim$ 37 km [15, 16, 20]: solid dust particles of extraterrestrial origin generally are the main population above $\sim$ 20 km, and above $\sim$ 30 km extraterrestrial particles dominate [67, 87] (see also chapter 2). Finally another argument is that these particles were collected in the free-volcanic stratosphere, that is during a period (June 21-24, 2008) in which no large volcanic eruptions occurred, except the eruption of the Chaitén volcano (Chile) on May 2, 2008: but this volcano, whose ashes reached an altitude of < 30 km, is located in the southern hemisphere, and so there is a small probability that DUSTER could have collected particles from the Chaitén volcano. In conclusion the analyzed particles are likely of extraterrestrial origin, though more analyses are needed in order to establish with

more accuracy their origin. Successive TEM and isotopic analyses are needed to derive further conclusion on the origin of these particles. In addition, the analyses of microtomed slices of these particles will reveal details also of their internal composition by means of micro-Raman and micro-infrared spectroscopy as also TEM observations. Micro-Raman spectroscopic analyses on other stratospheric samples collected by DUSTER in the future must be possibly performed directly onto the collection substrates.

particle	***peak frequency*** (cm^{-1})	***compound***
D08C_006	$1366 - 1376$	aC D-peak
	$1568 - 1576$	aC G-peak
	280	$CaCO_3$
	1080	$CaCO_3$
	400	aC L_1 peak (?)
	750	aC L_2 peak (?)
D08C_008a	$1364 - 1374$	aC D-peak
	$1562 - 1573$	aC G-peak
	280	$CaCO_3$
	1080	$CaCO_3$
	400	aC L_1 peak (?)
	800	aC L_2 peak (?)
	800; 860; 920	(?)
D08C_008b	$1363 - 1379$	aC D-peak
	$1568 - 1577$	aC G-peak
	940	(?)
	400	aC L_1 peak (?)
	400	aC L_1 peak (?)

Table 5.1: *Principal peak frequencies detected in the Raman spectra of the three analyzed particles, with possible associated materials; some peaks have not been yet assigned.*

particle	$\langle I_D/I_G \rangle$	$L_a(\mathring{A})$	sp^3 *content*
D08C_006	0.80	12.08	$\sim 12\%$
D08C_008a	0.80	12.05	$\sim 12\%$
D08C_008b	0.83	12.29	$\sim 11\%$

Table 5.2: *Average intensity ratio for each particle, calculated graphitic domain size and estimated sp^3 content of the amorphous carbon.*

particle	$\langle\nu_{0(D)}\rangle$	$\langle\nu_{0(G)}\rangle$	$\langle\Gamma_D\rangle$	$\langle\Gamma_G\rangle$	$\langle I_D\rangle$	$\langle I_G\rangle$	$\langle I_D/I_G\rangle$
D08C_006	(cm^{-1})	(cm^{-1})	(cm^{-1})	(cm^{-1})	$(c.p.s.)$	$(c.p.s.)$	
$(120710f-3c)$	1376.63	1568.97	231.02	111.99	0.2006	0.2780	0.7272
$(140710m-6c)$	1366.27	1575.60	217.81	110.87	0.4047	0.4954	0.8187
$(140710n-7c)$	1369.41	1576.44	220.25	103.63	0.5329	0.6215	0.8603
D08C_008a							
$(080710n-1a)$	1364.15	1562.18	210.81	120.21	0.3281	0.3888	0.8503
$(140710i-9a)$	1374.61	1573.95	243.14	112.07	0.4710	0.5526	0.8634
$(140710l-10a)$	1369.93	1572.21	205.28	115.15	0.1931	0.2828	0.6825
D08C_008b							
$(080710f-1b)$	1372.14	1576.64	244.47	112.31	6.7306	6.8761	0.9937
$(080710g-2b)$	1370.58	1575.61	225.67	115.29	2.2111	2.4698	0.9004
$(080710h-3b)$	1369.32	1574.18	228.80	116.95	2.9588	3.6203	0.8203
$(080710m-4b)$	1372.65	1574.91	240.70	114.43	2.3453	2.7907	0.8494
$(140710b-10b)$	1375.14	1568.07	250.93	118.27	0.3722	0.5175	0.7294
$(140710c-11b)$	1378.89	1571.40	261.97	117.41	1.1332	1.3475	0.8611
$(140710d-12b)$	1370.34	1568.39	236.60	122.85	0.5300	0.6979	0.7658
$(140710e-13b)$	1362.96	1569.92	224.59	131.74	0.3108	0.4109	0.7583
$(140710f-14b)$	1373.33	1571.83	237.63	119.68	0.4000	0.5080	0.7935
HOPG							
$(140710r)$		1582.50		15.52		0.3612	
$(140710s)$		1582.70		14.74		3.3297	
Copper grid							
$(120710g-1)$	1381.39	1566.32	215.72	103.55	0.1828	0.3261	0.5628
$(120710p-2)$	1376.97	1569.46	183.09	99.97	0.1753	0.3331	0.5263
$(120710l-3)$	1383.02	1566.73	168.39	101.63	0.1532	0.3274	0.4673
$(120710m-4)$	1383.33	1562.73	216.01	116.04	0.1458	0.2414	0.6064
$(120710i-5)$	1376.05	1562.23	189.19	120.39	0.1084	0.2235	0.4817
$(120710h-6)$	1389.14	1555.39	101.60	87.19	0.0172	0.0905	0.1837
$(120710o-7)$							
$(120710n-8)$							
Carbon film							
$(080710i)$	1347.06	1565.97	145.83	161.44	1.5850	1.8315	0.4459

Table 5.3: *Raman band parameters relative to the three analyzed particles, HOPG, FIB-copper grid and holey carbon film. In the first left column there are particle name, spectrum name and the mapping position. Values listed here have been obtained averaging the results of the fits computed both with MicroCal Origin software (Lorentzian) and with the LabVIEW tool (Lorentzian, Gaussian and BWF).*

particle	$\langle A_D \rangle$	$\langle A_G \rangle$	$\langle A_D/A_G \rangle$
D08C_006	(cm^{-1})	(cm^{-1})	
$(120710f-3c)$	64.79	39.46	1.54
$(140710m-6c)$	115.19	68.19	1.62
$(140710n-7c)$	153.20	80.17	1.85
D08C_008a			
(140710i-1a)	152.31	78.22	1.95
$(140710l-9a)$	54.32	42.08	1.24
$(080710n-10a)$	92.99	57.10	1.50
D08C_008b			
$(080710f-1b)$	2109.50	980.37	2.89
$(080710g-2b)$	654.12	356.06	1.79
$(080710h-3b)$	887.05	530.17	1.63
$(080710m-4b)$	754.37	400.49	1.84
$(140710b-10b)$	131.03	77.75	1.61
$(140710c-11b)$	409.09	203.36	2.02
$(140710d-12b)$	175.82	109.52	1.50
$(140710e-13b)$	94.77	68.46	1.31
$(140710f-14b)$	126.10	76.71	1.62
HOPG			
$(140710r)$		8.8	
$(140710s)$	101.19	42.67	2.45
Copper grid			
$(120710g-1)$	52.38	41.02	1.20
$(120710p-2)$	43.12	40.73	1.00
$(120710l-3)$	36.20	41.45	0.81
$(120710m-4)$	41.08	35.29	1.17
$(120710i-5)$	29.49	34.14	0.80
$(120710h-6)$	4.98	12.09	0.31
$(120710o-7)$			
$(120710n-8)$			

Table 5.4: *Raman band parameters (band areas and their ratio) relative to the three analyzed particles, HOPG and FIB-copper grid. In the first left column there are particle name, spectrum name and the mapping position. Values listed here have been obtained averaging the results of the fits computed both with MicroCal Origin software (Lorentzian) and with the LabVIEW tool (Lorentzian, Gaussian and BWF).*

5.3 A LabView tool for automatized fitting of spectra

A useful tool has been developed in NI-LabVIEW environment in order to perform automatized fits of many Raman spectra in the carbon region ($800 < x < 2000\ cm^{-1}$, with $x_{0,aC} = 1450\ cm^{-1}$). Spectra acquired in the minerals region ($200 < x < 1400\ cm^{-1}$, with $x_{0,Si} = 850\ cm^{-1}$) are plotted and not fitted. Synthetically the program performs a cycle relatively to all the raw spectra that are saved within a folder, that typically can be several hundreds of spectra, recorded as *.*csv* or *.*txt* files. The main operations foreseen on each single spectrum are: to read raw data, to compute a continuum baseline, to subtract the baseline, to cut the spectrum tails outside a selected range, to calculate non-linear fit of the D and G peaks, to compute the fit parameters (peak intensity, position, FWHM and area), and to plot (see diagram of the logic operations of the program, fig.5.40). At each iteration (*for loop*), the program opens a spectrum file, reads the data, searching for the minimum value x_{min} of each spectrum; if $x_{min} < 700\ cm^{-1}$, then the spectrum is centered in the minerals region and so it is not fitted; if $x_{min} \geq 700\ cm^{-1}$ then the spectrum is centered in the carbon region, and thus it is fitted (*case structure*). Several *control buttons* on the *front panel* interface allow the user to set different parameters or to enable/disable some operations: these settings must be performed before the program is running. Two control buttons allows to fit or not the spectra and to subtract or not a baseline: in case of no fit, only the raw spectrum is plotted; in both cases the raw spectrum is also plotted for comparison. Another control button allows the user to perform a smoothing of the y-data, setting the smoothing order $n \geq 1$. Then it is possible to choose the baseline curve, switching between a straight line or a polynomial baseline. In the first case one range $\Delta x = x_1 - x_2$ has to be selected, which extremes are typically $x_1 \approx 1000\ cm^{-1}$ and $x_2 \approx 1800\ cm^{-1}$. In the second case two ranges have to be selected, typically $\Delta x_1 \approx 900 - 1200\ cm^{-1}$ and $\Delta x_2 \approx 1850 - 2000\ cm^{-1}$. After computation and subtraction of the baseline, the user can cut or not the spectrum, limiting to study only a selected interval of data, generally the range 1000-1800 cm^{-1}. Successively on the front panel the user has the possibility to switch between three types of data fitting curve: the D and G peaks can be fitted with a sum of two Lorentzian, two Gaussian or two BWF curves (see app.C). After the setting of all parameters and controls, once the program is running, it recursively makes all these operations on all spectra, visualizing on a graphic output the original raw spectrum, the corrected spectrum (cut + baseline subtraction) and the fit curve. The fitting procedure has as output several parameters

for each spectrum: peak intensity, peak position, FWHM, area and fit residue, that is calculated as the reduced chi-squared:

$$\frac{\chi^2}{DoF} = \sum_{i=1}^{N} \frac{(y_{i,fit} - y_{i,raw})^2}{N\sigma^2} \tag{5.23}$$

Some other quantities are computed such as the intensity ratio I_D/I_G and the area ratio A_D/A_G; moreover FWHMs of D and G bands in function of peak positions are plotted. Finally the program creates a new file (*.xls and *.txt) in which it saves in columns all original (x_{raw}, y_{raw}) data, computed fitting curves (y_{fit}), and all calculated parameters. A frequency histogram of the output fit residues has been computed for all the four types of fitting (see fig.5.39): the majority of calculated fits have residues around the value 0.007.

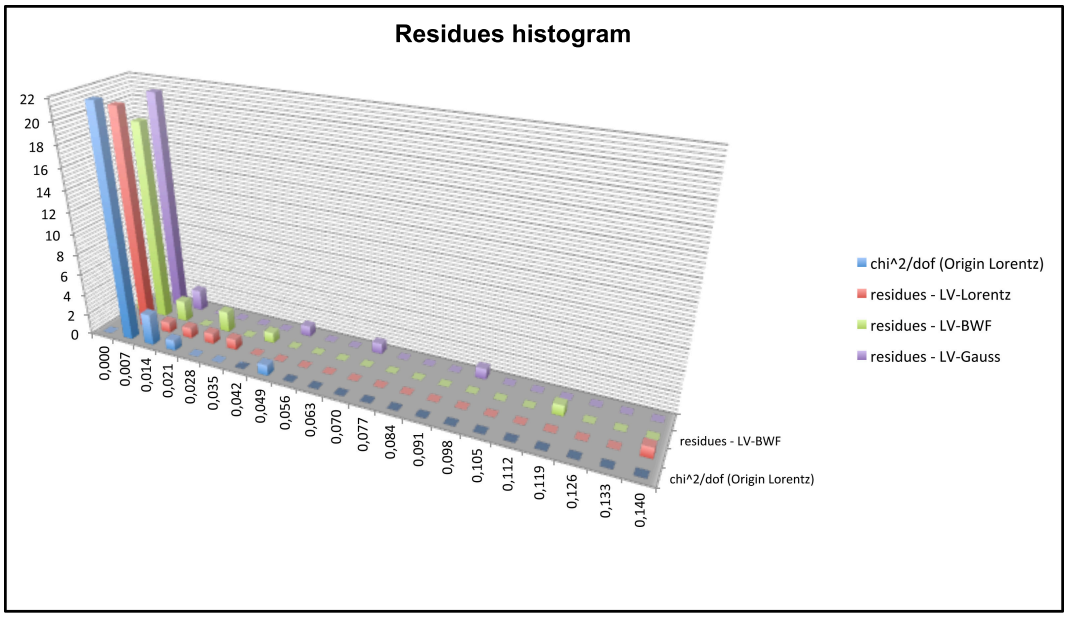

Figure 5.39: *Frequency histogram of the output fit residues for all types of data fitting. Most of the residues (reduced χ^2) have values around 0.007.*

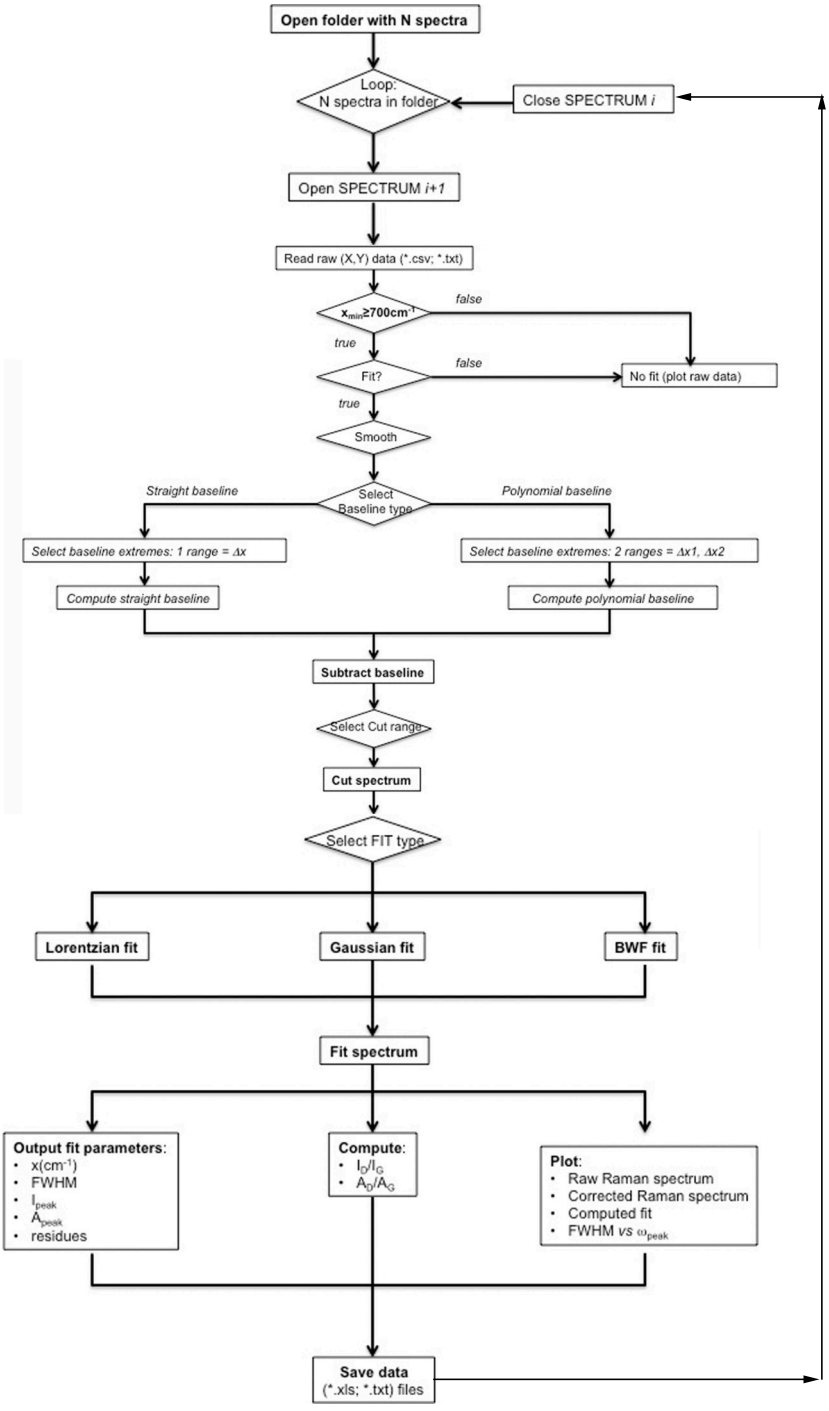

Figure 5.40: *Flux diagram of the logic operations computed by the developed tool for the automatized fitting of Raman spectra.*

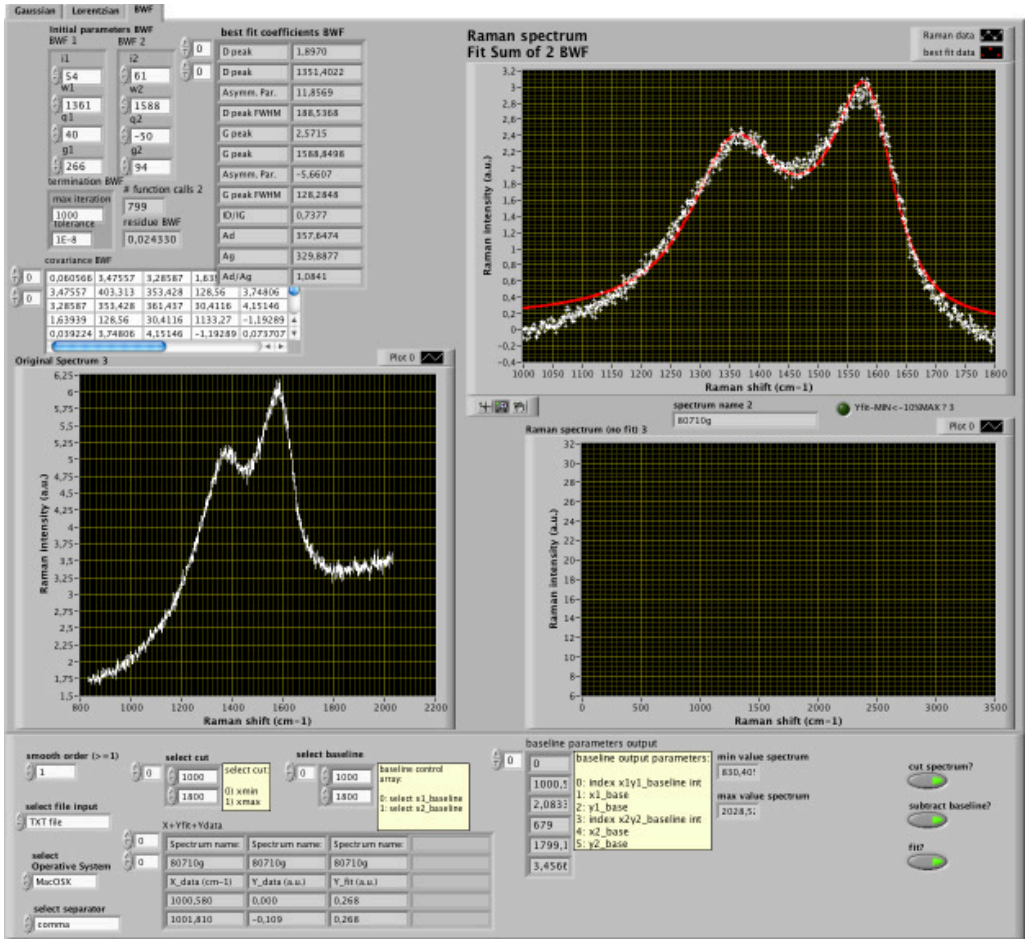

Figure 5.41: *Front panel (user interface) of the LabVIEW tool. On the top of the panel, three tab controls allows the user to switch among the three curve-types of fitting. The three graph windows are relative to the raw spectrum, the spectrum after cut and baseline correction, and the corrected and fitted spectrum. In the top left box, there are the controls to set the initial parameters for the fit, on the right box there are the best fit output coefficients. On the bottom there are controls to set the file to read, the desired smoothing level, the cut and baseline ranges. Finally on bottom right there are three press buttons (boolean controls) to choose the possibility of cut, subtract the baseline and to fit the spectrum: when the button lights are on, these operations are activated; when the buttons lights are off, they are not.*

Conclusions

My work focused both on technical and scientific aspects of the DUSTER project. With regard to different technical aspects of the instrument, I performed flow rate measurements on the instrument pumping group used for the 2009 and 2011 flight campaign, obtaining for the DUSTER-2009 instrument the value $Q_{2009} = 1$ m$^3/h$, and for the DUSTER-2011 instrument a better flow rate, $Q_{2011} = 1.3$ m$^3/h$, about 30% larger than that of the DUSTER-2009 instrument. Other technical aspects of my work concerned the development of the EGSE (Electrical Ground Support Equipment), in NI-LabVIEW environment, for the management of some flight operations and the decoding of telemetry packets, providing a laboratory real-time virtual interface between the experimenter and the instrument on board the balloon during the flight. The EGSE has been developed both for DUSTER-2009 and DUSTER-2011 instruments, in several versions; in the 2011-instrument versions the possibility to send telecommands (TC) has also been implemented. Other technical works regarded thermal tests and the main electronics of the instrument, in particular concerning the realization of PC-104 electronic boards for the supply of micro-electrovalves and for the conditioning of micro-pumps and temperature sensors, both on DUSTER-2009 and DUSTER-2011 instruments. Calibration measurements allowed the determination of the collection performance of the instrument: a laboratory system, for the controlled injection of synthetic μm-sized particles into an environmental chamber (at controlled pressure and temperature), has been developed, in order to compare different techniques (filtering and inertial impact deposition) of sampling. The environmental chamber simulates the stratospheric pressure conditions; a certain number concentration of synthetic micrometer-sized particles, of dimensions similar to that of cosmic particles that we want to collect, is reproduced in the chamber, and measured thanks to gravitational settling onto microscope slides and also using an optical particle counter. Once in the chamber, the instrument is put in similar working conditions as in the stratosphere. Actually here we performed collection performance measurements with an instrument characterized by a similar functioning principle

with respect to DUSTER: it was demonstrated that particles collection with inertial impactors gives a much better collection efficiency ($\eta = 11\%$ for 5-μm particles) than using a filter as a substrate ($\eta \approx 2\%$). Future works on calibration and collection efficiency measurements, could involve the true DUSTER instrument as a whole; a laboratory instrument spare, identical to the flight instrument, could be realized and used in order to determine the collection efficiency. Measurements could be done inside a very large chamber, much larger than the instrument typical size (40 cm); finally, flight spare collection substrates (TEM grids and holey carbon film) could be used for sampling, allowing the particles detection to be made with the electron microscope.

With regard to scientific aspects, micro-Raman analyses allowed to determine the mineralogical characterization of three particles collected during the DUSTER-2008 flight campaign (particles *D08C006*, *D08C008a* and *D08C008b*). The three particles are characterized by the dominant presence of amorphous carbon (aC), with different degrees of structural order from one particle to another, and also within the same particle. The only other detected feature is the presence of calcium carbonate ($CaCO_3$) in two particles (*-006* and *-008a*). The presence of surface aC prevented the detection of possible other minerals eventually present. There are indications that part of the aC is intrinsic of the particles. Several considerations lead to the conclusion that the particles *D08C006* and *D08C008a* could be of extraterrestrial origin, such as for example the fact that carbonates are generally found in cosmic particles [in IDPs (Brownlee et al., 1980) or in meteorites (Rull Perez and Martinez-Frias, 2003); see also Ciucci, 2011, PhD Thesis]; the high altitude (37 km) at which these particles have been collected, well above the aerosol layer and in a region (the upper stratopshere) in which the terrestrial contamination is minimum, and the aerosols are dominated by extraterrestrial materials; the fact that during the collection period (June, 2008) there were not large volcanic eruptions in the North Hemisphere; finally, the similarity between the Raman spectra of DUSTER samples and the Raman spectra of many IDPs reported in literature (for example Wopenka, 1988; Quirico et al., 2005; Rotundi et al., 2007), only characterized by carbonaceous materials. On the other side, for the particle *D08C008b* no conclusion about its origin can be done. The analysis of Raman parameters of the spectra obtained for the particles has been performed with the help of a LabVIEW tool, developed in order to compute automatized fits of numerous Raman spectra of carbonaceous materials. Further micro-Raman investigations are certainly needed, in order to better characterize the mineralogy of these samples; future analyses must be performed directly onto the collection substrates.

Appendix A

Pressure - Height conversion: Atmospheric Standard Model

According to the *Standard Atmosphere Model* it is possible to obtain the relationship between altitude and pressure; this relation is not unique because of the correlation between temperature, pressure and altitude; in different altitude ranges there are different relations $H\ vs\ P$ because we have to consider also T:

$$\begin{cases} T = T(H) \\ P = P(T) \end{cases}$$

So for each range we have the following relationships:

$$H < 11km \Rightarrow \begin{cases} T = 288.15K - \left(6.5\frac{K}{km}\right) \cdot H \\ P = 101.325kPa \cdot \left(\frac{288.15K}{T}\right)^{5.255877} \end{cases} \tag{A.1}$$

$$11km < H < 20km \Rightarrow \begin{cases} T = 216.55K \\ P = 22.632kPa \cdot e^{-0.1577 \cdot (H-11)} \end{cases} \tag{A.2}$$

$$20km < H < 32km \Rightarrow \begin{cases} T = 216.65K + \frac{1K}{km} \cdot (H - 20km) \\ P = 5.4749kPa \cdot \left(\frac{216.65K}{T}\right)^{34.16319} \end{cases} \tag{A.3}$$

$$32km < H < 47km \Rightarrow \begin{cases} T = 228.65K + 2.8K/km \cdot (H - 32km) \\ P = 0.868kPa \cdot \left(\frac{228.65K}{T}\right)^{12.2011} \end{cases} \tag{A.4}$$

Combining in each range we obtain the following $H = H(P)$ relationships:

$$[H < 11km] \Rightarrow H = 44.33km \cdot \left[1 - \left(\frac{1013.25mbar}{P(mbar)}\right)^{-\frac{1}{5.255877}}\right] \tag{A.5}$$

$$[11km < H < 20km] \Rightarrow H = 11km + \frac{1}{0.1577} ln \left[\frac{226.321mbar}{P(mbar)}\right] \tag{A.6}$$

$$[20km < H < 32km] \Rightarrow H = 20km + 216.65km \cdot \left[\left(\frac{P(mbar)}{54.749mbar}\right)^{-\frac{1}{34.16319}} - 1\right] \tag{A.7}$$

$$[32km < H < 47km] \Rightarrow H = 32km + 81.66km \cdot \left[\left(\frac{P(mbar)}{8.68}\right)^{-\frac{1}{12.2011}} - 1\right] \tag{A.8}$$

Appendix B

Time conversion in HK and SF packets

The ADU time value, both for housekeeping and status file packages, consists of the number of seconds elapsed since a given instant t_m to today, t_f; for the particular SBC that we used, this instant corresponds to t_m = 01/01/1970, at 00:00; we call this number of seconds N_1. A particular function in LabView converts the number of seconds in date (mm/dd/yyyy), but it needs that the number of seconds is calculated since t_i = 01/01/1904 at 00:00. We call N_0 the total number of seconds elapsed since t_i to t_m. So we have:

- t_i = 01/01/1904 at 00:00
- t_m = 01/01/1970 at 00:00
- t_f = today

Then we have:

$$N_0(s) = t_m - t_i$$

and

$$N_1(s) = t_f - t_m$$

So the total number of seconds elapsed since t_i to t_f is:

$$N_f = N_0 + N_1 \tag{B.1}$$

The LabView function converts the quantity N_f in date.

Appendix C

Curves used for the fit of Raman D and G peaks

Three curves have been used in order to compute the fits of the D and G bands in Raman spectra: a sum of two Lorentzians, a sum of two Gaussians and a sum of two Breit-Wigner-Fano (BWF). The Lorentzian curve is given by:

$$I(\omega) = \frac{I_D}{1 + \left[\frac{2(\omega - \omega_D)}{\Gamma_D}\right]^2} + \frac{I_G}{1 + \left[\frac{2(\omega - \omega_G)}{\Gamma_G}\right]^2} \tag{C.1}$$

where:

- $I_{D,G} = D$ and G peak intensity respectively
- $\omega_{D,G} = D$, G peak position
- $\Gamma_{D,G} = D$, G band width (FWHM)

The Gaussian curve is:

$$I(\omega) = a_D \cdot e^{-\frac{(\omega - m_D)^2}{\sigma_D^2}} + a_G \cdot e^{-\frac{(\omega - m_G)^2}{\sigma_G^2}} \tag{C.2}$$

where the parameters are:

- $a = \frac{1}{\sigma\sqrt{2\pi}}$

- σ = standard deviation
- $m = \langle\omega\rangle$

The asymmetric BWF curve is:

$$I(\omega) = \frac{I_D\left[1+\frac{2(\omega-\omega_D)}{Q_D\Gamma_D}\right]^2}{1+\left[\frac{2(\omega-\omega_D)}{\Gamma_D}\right]^2} + \frac{I_G\left[1+\frac{2(\omega-\omega_G)}{Q_G\Gamma_G}\right]^2}{1+\left[\frac{2(\omega-\omega_G)}{\Gamma_G}\right]^2} \tag{C.3}$$

in which Q is called *asymmetry parameter*; Q^{-1} is the BWF coupling coefficient. The Lorentzian line is obtained for $Q^{-1} \to 0$.

Bibliography

[1] Baratta G.A., Mennella V., Brucato J.R., Colangeli L., Leto G., Palumbo M.E., and Strazzulla G.: *Raman spectroscopy of ion-irradiated interplanetary carbon dust analogues*, Journal of Raman Spectroscopy, 35, 487-496, 2004

[2] Baratta G.A., Brunetto R., Leto G., Palumbo M.E., Spinella F., and Strazzulla G.: *Raman spectroscopy of ion-irradiated astrophysically relevant materials*, Journal of Raman Spectroscopy, 39, 211-219, 2008

[3] Baron P.A., Willeke K.: *Aerosol Measurements. Principles, Techniques and Applications*, Second Edition, Wiley Interscience, 2001

[4] Bigg E.K., Ono A., and Thompson W.J.: *Aerosols at altitudes between 20 and 37 km*, Tellus, vol.22, issue 5, 550-563, 1970

[5] Bohren C.F., Huffman D.R.: *Absorption and Scattering of Light by Small Particles.* John Wiley & Sons, Edition 1998

[6] Borovicka J., and Charvát Z.: *Meteosat observation of the atmospheric entry of 2008 TC_3 over Sudan and the associated dust cloud*, Astronomy & Astrophysics, 507, 1015-1022, 2009

[7] Brownlee D.E., Horz F., Vedder J.F., Gault D.E., and Hartung J.B.: *Some physical parameters of micrometeoroids*, Proceedings of the Fourth Lunar Science Conference (Suppl.4, Geochimica et Cosmochimica Acta), vol.3, 3197-3212, 1973

[8] Brownlee D.E., Horz F., Tomandl D.A., and Hodge P.W.: *Physical properties of interplanetary grains*, in NASA, Goddard Space Flight Center, The Study of Comets, Part 2, 962-982, 1976

[9] Brownlee D.E., Pilachowski L., Olszewski E., and Hodge P.W.: *Analysis of interplanetary dust collections*, in *Solid particles in the solar system*, Proceedings

of the Symposium, Ottawa, Canada, August 27-30, 1979. Dordrecht, D. Reidel Publishing Co., p.333-341, 1980

[10] Brownlee D.E.: *Cosmic dust: collection and research*, Annual Review of Earth and Planetary Science, 13, 147-173, 1985

[11] Brunetto R., Baratta G.A., and Strazzulla G.: *Raman spectroscopy of ion irradiated diamond*, Journal of Applied Physics, vol.96, n.1, 380-386, 2004

[12] Brunetto R., Pino T., Dartois E., Cao A.-T., d'Hendecourt L., Strazzulla G., and Bréchignac Ph.: *Comparison of the Raman spectra of ion irradiated soot and collected extraterrestrial carbon*, Icarus, 200, 323-337, 2009

[13] Brunetto R., Borg J., Dartois E., Rietmeijer F.J.M., Grossemy F., Sandt C., d'Hendecourt L.L.S., Rotundi A., Dumas P., Djouadi Z., and Jamme F.: *Mid-IR, Far-IR, Raman micro-spectroscopy, and FESEM-EDX study of IDP L2021C5: clues to its origin*, Icarus, 212, 896-910, 2011

[14] Charlson R.J., Schwartz S.E., Hales J.M., Cess R.D., Coakley J.A., Hansen J.E., and Hofmann D.J.: *Climate forcing by anthropogenic aerosols*, Science, New Series, vol.255, n.5043, 423-430, 1992

[15] Ciucci A.: *Stratospheric Dust Collection by DUSTER (Dust in The Upper Stratosphere Tracking Experiment and Retrieval), a balloon-borne instrument, and laboratory analyses of collected dust.* PhD Thesis, 2010

[16] Ciucci A., Palumbo P., Brunetto R., Della Corte V., De Angelis S., Rotundi A., Rietmeijer F.J.M., Zona E., Colangeli L., Esposito F., Mazzotta Epifani E., Mennella V., Inarta S., Peterzen S., Masi S., and Ibba R.: *DUSTER: Preliminary Analysis.* Mem. S.A.It. Suppl. Vol.16, 119-124, SAIt 2011

[17] Cziczo D.J., Thomson D.S., and Murphy D.M.: *Ablation, flux, and atmospheric implications of meteors inferred from stratospheric aerosol*, Science, vol.291, 1772-1775, 2001

[18] Danilin M.Y., Shia R.-L., Ko M.K.W., Weisenstein D.K., Sze N.D., Lamb J.J., Smith T.W., Lohn P.D., and Prather M.J.: *Global stratospheric effects of the alumina emissions by solid-fueled rocket motors*, Journal of Geophysical Research, vol.106, Issue D12, 12727-12738, 2001

[19] De Angelis S., Della Corte V., Baratta G.A., Rietmeijer F.J.M., Brunetto R., Palumbo P., Ciucci A., and Rotundi A.: *Raman Micro-Spectroscopy per-*

formed on Extraterrestrial Particles, Spectroscopy Letters, 44, Issue 7-8, 549-553, http://dx.doi.org/10.1080/00387010.2011.610424, 2011

[20] Della Corte V., Palumbo P., De Angelis S., Ciucci A., Brunetto R., Rotundi A., Rietmeijer F.J.M., Zona E., Bussoletti E., Colangeli L., Esposito F., Mazzotta Epifani E., Mennella V., Peterzen S., Masi S., and Ibba R.: *DUSTER: a balloon-borne dust particle collector.* Mem. S.A.It. Suppl. Vol.16, 14-21, 2011

[21] Deshler T., Hervig M.E., Hofmann D.J., Rosen J.M., and Liley J.B.: *Thirty years of in situ stratospheric aerosol size distribution measurements from Laramie, Wyoming (41° N), using balloon-borne instruments*, Journal of Geophysical Research, vol.108, n.D5, 4167, doi:10.1029/2002JD002514, 2003

[22] Deshler T.: *A review of global stratospheric aerosol: measurements, importance, life cycle, and local stratospheric aerosol*, Atmospheric Research, 90, 223-232, 2008

[23] Dillon R.O., Woollam J.A., and Katkanant V.: *Use of Raman scattering to investigate disorder and crystallite formation in as-deposited and annealed carbon films*, Physical Review B., vol.29, n.6, 1984

[24] Dorschner J. and Henning T.: *Dust metamorphosis in the galaxy*, The Astronomy and Astrophysics Review, 6, 271-333, Springer-Verlag, 1995

[25] Downs R.T.: *The RRUFF Project: an integrated study of the chemistry, crystallography, Raman and infrared spectroscopy of minerals*, Program and Abstracts of the 19th General Meeting of the International Mineralogical Association in Kobe, Japan. O03-13, 2006

[26] Dutton E.G., and Christy J.R.: *Solar radiative forcing at selected locations and evidence for global lower tropospheric cooling following the eruptions of El Chichón and Pinatubo*, Geophysical Research Letters, vol.19, n.23, 2313-2316, doi:10.1029/92GL02495, 1992

[27] Ferrari A.C., Kleinsorge B., Morrison N.A., Hart A., Stolojan V., and Robertson J.: *Stress reduction and bond stability during thermal annealing of tetrahedral amorphous carbon*, Journal of Applied Physics, vol.85, n.10, 1999

[28] Ferrari A.C. and Robertson J.: *Interpretation of Raman spectra of disordered and amorphous carbon*, Physical Review B, vol.61, n.20, 2000

[29] Ferrari A.C. and Robertson J.: *Resonant Raman spectroscopy of disordered, amorphous, and diamondlike carbon*, Physical Review B, vol.64, 075414-1:13, 2001

[30] Ferrari A.C. and Robertson J.: *Raman spectroscopy of amorphous, nanostructured, diamond-like carbon, and nanodiamond*, Phil. Trans. R. Soc. Lond. A, 362, 2477-2512, 2004

[31] Flynn G.J.: *Atmospheric entry heating: a criterion to distinguish between asteroidal and cometary sources of interplanetary dust*, Icarus, vol.77, issue 2, 287-310, 1989

[32] Flynn G.J., Sutton S.R.: *Cosmic Dust Particle densities: evidence for two populations of stony micrometeorites*, Proceedings of Lunar and Planetary Science, Lunar and Planetary Institute, vol.21, 541-547, 1991

[33] Fortescue P., Stark J., Swinerd G.: *Spacecraft Systems Engineering.* Softback, 2003

[34] Fromm M.D., and Servranckx R.: *Transport of forest fire smoke above the tropopause by supercell convection*, Geophysical Research Letters, vol.30, n.10, 1542, doi:10.1029/2002GL016820, 2003

[35] Fueglistaler S., Wernli H., and Peter T.: *Tropical troposphere-to-stratosphere transport inferred from trajectory calculations*, Journal of Geophysical Research, vol.109, Issue D3, 2004

[36] Goldstein A.H., Koven C.D., Heald C.L., and Fung I.Y.: *Biogenic carbon and anthropogenic pollutants combine to form a cooling haze over southeastern United States*, Proceeding of the National Academy of Sciences, www.pnas.org/cgi/doi/10.1073/pnas.0904128106, PNAS, vol.106, n.22, 8835-8840, 2009

[37] Grun E., Levasseur-Regourd A.-C., McBride N., Palumbo P., Srama A.: *Cosmic Dune: an observatory for the study of interstellar and interplanetary dust*, ESA-SCI(2001)5, Mission Definition Report Draft, October 2001

[38] Gunasekaran S., Anbalagan G., and Pandi S.: *Raman and infrared spectra of carbonates of calcite structure*, Journal of Raman Spectroscopy, 37, 892-899, 2006

[39] Hemenway C.L., Fullam E.F., and Phillips L.: *Nanometeorites*, Nature, n.4779, vol.190, 897-898, 1961

[40] Hunten D.M., Turco R.P., Toon O.B.: *Smoke and Dust Particles of Meteoric Origin in the Mesosphere and Stratosphere*, Journal of Atmospheric Sciences, vol.37, 1342-1357, 1980

[41] Immler F., Engelbart D., and Schrems O.: *Fluorescence from atmospheric aerosol detected by a lidar indicates biogenic particles in the lowermost stratosphere*, Atmospheric Chemistry and Physics, 5, 345-355, 2005

[42] Iwasaka Y., Hayashi M., Kondo Y., Koike M., Koga S., Yamato M., Aimedieu P., and Matthews W.A.: *Chemical state of polar stratospheric aerosols*, Proceedings National Institute of Polar Research, Symp. Polar Meteorol. Glaciol., 5, 1-8, 1992

[43] Jablonska M., Rietmeijer F.J.M., and Janeczek J.: *Fine-grained barite in coal fly ash from the Upper Silesian Industrian Region*, Environmental Geology, 40, 941-948, 2001

[44] Jackman C.H., Considine D.B., and Fleming E.L.: *A global modeling study of solid rocket aluminum oxide emission effects on stratospheric ozone*, Geophysical Research Letters, vol.25, n.6, 907-910, 1998

[45] Jost H.J., Drdla K., Stohl A., Pfister L., Loewenstein M., Lopez J.P., Hudson P.K., Murphy D.M., Cziczo D.J., Fromm M., Bui T.P., Dean-Day J., Gerbig C., Mahoney M.J., Richard E.C., Spichtinger N., Vellovic Pittman J., Weinstock E.M., Wilson J.C., and Xueref I.: *In-situ observations of mid-latitude forest fire plumes deep in the stratosphere*, Geophysical Research Letters, vol.31, L11101, doi:10.1029/2003GL019253, 2004

[46] Joswiak D.J., Brownlee D.E., Pepin R.O., and Schlutter D.J.: *Densities and mineralogy of cometary and asteroidal interplanetary dust particles collected in the stratosphere*, Proc. 'Dust in Planetary Systems', Kauai, Hawaii, USA, 26–30 September 2005 (ESA SP-643, January 2007)

[47] Junge C.E., Chagnon C.W., and Manson J.E.: *Stratospheric aerosols*, Journal of Meteorology, vol.18, 81-108, 1961

[48] Kasten F.: *Falling Speed of Aerosol Particles*, Journal of Applied Meteorology, vol.7, 944-947, 1968

[49] Klekociuk A.R., Brown P.G., Pack D.W., ReVelle D.O., Edwards W.N., Spalding R.E., Tagliaferri E., Yoo B.B., and Zagari J.: *Meteoritic dust from the atmospheric disintegration of a large meteoroid*, Nature - Letters, vol.436, 1132-1135, doi:10.1038/nature03881, 2005

[50] Labitzke K., and McCormick M.P.: *Stratospheric temperature increases due to Pinatubo aerosols*, Geophysical Research Letters, vol.19, n.2, 207-210, doi:10.1029/91GL02940, 1992

[51] Lee S.H., Reeves J.M., Wilson J.C., Hunton D.E., Viggiano A.A., Miller T.M., Ballenthin J.O., and Lait L.R.: *Particle formation by ion nucleation in the upper troposphere and lower stratosphere*, Science, vol.301, 1886-1889, 2003

[52] Lin N.H., Saxena V.K.: *Changes in stratospheric aerosol parameters over 105-135°E longitude due to eruption of Mount Pinatubo*, Journal of Aerosol Science, vol.28, N.4, 697-712, 1997

[53] Long D.E.: *The Raman effect: a unified treatment of the theory of Raman scattering by molecules*, John Wiley & Sons Ltd, 2002

[54] MacKinnon I.D.R., Goodling J.L., McKay D.S., and Clanton U.S.: *The El Chichón stratospheric cloud: solid particulates and settling rates*, Journal of Volcanology and Geothermal Research, vol.23, Issues 1-2, 125-146, 1984

[55] Mateshvili N., Mateshvili G., Mateshvili I., Gheondjian L., and Avsajanishvili O.: *Vertical distribution of dust particles in the Earth's atmosphere during the 1998 Leonids*, Meteoritics & Planetary Science, 34, 969-973, 1999

[56] Mateshvili N., Rietmeijer F.J.M.: *Stratospheric dust loading from early 1981 to September 1985 based on the twilight sounding method and stratospheric dust collections*, Journal of Volcanology and Geothermal Research, 120, 55-69, 2002

[57] Mateshvili N., Fussen D., Vanhellemont F., Bingen C., Kyrola E., Mateshvili I., and Mateshvili G.: *Twilight sky brightness measurements as a useful tool for stratospheric aerosol investigations*, Journal of Geophysical Research, vol.110, 2005, D09209, doi:10.1029/2004JD005512

[58] Murphy D.M., Thomson D.S., and Mahoney M.J.: *In situ measurement of organics, meteoritic material, mercury, and other elements in aerosols at 5 to 19 kilometers*, Science, vol.282, 1664-1669, 1998

[59] Nier A.O., and Schlutter D.J.: *Helium and Neon isotopes in stratospheric particles*, Meteoritics, 25, 263-267, 1990

[60] Okada K., Wu P.M., Tanaka T.: *A light balloon-borne sampler collecting stratospheric aerosol particles*, Journal of the Meteorological Society of Japan, vol.75, n.3, 753-760, 1997

[61] Palumbo P., Della Corte V., Rotundi A., Ciucci A., Aronica A., Brucato J.R., Colangeli L., Esposito F., Mazzotta Epifani E., Mennella V., Battaglia R., Ferrini G., Rietmeijer F.J.M., Flynn G.J., Renard J.B., Stephens J.R., Zona E., and Inarta S.: *DUSTER, Aerosol Collection in the Stratosphere.* Mem. S.A.It. Vol.79, 853-857, SAIt 2008

[62] Penner J.E., Andreae M., Annegarn H., Barrie L., Feichter J., Hegg D., Jayaraman A., Leaitch R., Murphy D., Nganga J., and Pitari G.: *Aerosols, their direct and indirect effects*, In *Climate change 2001: The scientific basis. Contribution of Working Group I to the Third Assessment Report of the Intergovernmental Panel on Climate Change*, [Houghton J.T., Ding Y., Griggs D.J., Noguer M., van der Linden P.J., Dai X., Maskell K., and Johnson C.A. (eds.)]. Cambridge University Press, Cambridge, United Kingdom and New York, NY, USA, 881pp., 2001

[63] Quirico E., Borg J., Raynal P-I., Montagnac G., and d'Hendecourt L.: *A micro-Raman survey of 10 IDPs and 6 carbonaceous chondrites*, Planetary and Space Science, 53, 1443-1448, 2005

[64] Qun X.: *Influences of Pinatubo volcanic clouds on large scale climate in 1992*, Q. J. Appl. Meteor., 6(1), 35-42, 1995

[65] Ray E.A., Rosenlof K.H., Richard E.C., Hudson P.K., Cziczo D.J., Loewenstein M., Jost H.-J., Lopez J., Ridley B., Weinheimer A., Montzka D., Knapp D., Wofsy S.C., Daube B.C., Gerbig C., Xueref I., and Herman R.L.: *Evidence of the effect of summertime midlatitude convection on the subtropical lower stratosphere from CRYSTAL-FACE tracer measurements*, Journal of Geophysical Research, vol.109, D18304, doi:10.1029/2004JD004655, 2004

[66] Renard J.-B., Ovarlez J., Berthet G., Fussen D., Vanhellemont F., Brogniez C., Hadamcik E., Chartier M., and Ovarlez H.: *Optical and physical properties of stratospheric aerosols from balloon measurements in the visible and near-infrared domains. III. Presence of aerosols in the middle stratosphere*, Applied Optics, vol.44, n.19, 2005

[67] Renard J.-B., Brogniez C., Berthet G., Bourgeois Q., Gaubicher B., Chartier M., Balois J.-Y., Verwaerde C., Auriol F., Francois P., Daugeron D., and Engrand C.: *Vertical distribution of the different types of aerosols in the stratosphere: detection of solid particles and analysis of their spatial variability*, Journal of Geophysical Research, vol.113, D21303, doi:10.1029/2008JD010150, 2008

[68] Renard J.-B., Berthet G., Salazar V., Catoire V., Tagger M., Gaubicher B., and Robert C.: *In situ detection of aerosol layers in the middle stratosphere*, Geophysical Research Letters, vol.37, L20803, doi:10.1029/2010GL044307, 2010

[69] Rietmeijer F.J.M.: *Bromine in Interplanetary Dust Particles (IDPs): evidence for stratospheric contamination*, Meteoritics, vol.27, n.3, 280-281, 1992

[70] Rietmeijer F.J.M., and Janeczek J.: *An analytical electron microscope study of airborne industrial particles in Sosnowiec, Poland*, Atmospheric Environment, vol.31, n.13, 1941-1951, 1997

[71] Rietmeijer F.J.M.: *Interrelationships among metals, meteors, interplanetary dust, micrometeorites, and meteorites*, Meteoritics & Planetary Sciences, 35, 1025-1041, 2000

[72] Rietmeijer F.J.M.: *Identification of Fe-rich meteoric dust*, Planetary and Space Science, 49, 71-77, 2001

[73] Rietmeijer F.J.M.: *The earliest chemical dust evolution in the Solar Nebula*, Chemie der Erde - Geochemistry, vol.62, issue 1, 1-45, 2002

[74] Rietmeijer F.J.M., and Flynn G.J.: *A cosmic iron/nickel signature associated with dust between 34-36 kilometer altitude during may 1985*, 63rd Annual Meteoritical Society Meeting, 2000

[75] Robock A., and Mao J.: *The volcanic signal in surface temperature observations*, Journal of Climate, vol.8, 1086-1103, 1995

[76] Rose W.I., Durant A.J.: *Fine ash content of explosive eruptions*, Journal of Volcanology and Geothermal Research 186, 32-39, 2009

[77] Rosen J.M.: *The boiling point of stratospheric aerosols*, Journal of Applied Meteorology, vol.10, 1044-1046, 1971

[78] Rosinski J., and Snow R.H.: *Secondary particulate matter from meteor vapors*, Journal of Meteorology, vol.18, 736-745, 1961

[79] Rotundi A., Ferrini G., Baratta G.A., Palumbo M.E., Palomba E., and Colangeli L.: *Combined micro-infrared (IR) and micro-Raman measurements on stratospheric interplanetary dust particles*, Proc. "Dust in Planetary Systems", Kauai, Hawaii, USA. 26–30 September (ESA SP-643, January 2007)

[80] Rotundi A., Baratta G.A., Borg J., Brucato J.R., Busemann H., Colangeli L., D'Hendecourt L., Djouadi Z., Ferrini G., Franchi I.A., Fries M., Grossemy F.,

Keller L.P., Mennella V., Nakamura K., Nittler L.R., Palumbo M.E., Sandford S.A., Steele A., and Wopenka B.: *Combined micro-Raman, micro-infrared, and field emission scanning electron microscope analyses of comet 81P/Wild 2 particles collected by Stardust*, Meteoritics & Planetary Science, 43, Nr 1/2, 367-397, 2008

[81] Rull Perez F., and Martinez-Frias J.: *Identification of calcite grains in the Vaca Muerta mesosiderite by Raman spectroscopy*, Journal of Raman Spectroscopy, 34, 367-370, 2003

[82] Russell J.M.III, Tuck A.F., Gordley L.L., Park J.H., Drayson S.R., Harries J.E., Cicerone R.J., and Crutzen P.J: *HALOE Antarctic observations in the spring of 1991*, Geophysical Research Letters, 20, 8, p.719-722, doi:10.1029/93GL00497

[83] Sadezky A., Muckenhuber H., Grothe H., Niessner R., and Poschl U.: *Raman microspectroscopy of soot and related carbonaceous materials: spectral analysis and structural information*, Carbon, 43, 1731-1742, 2005

[84] Salpeter E.E.: *Formation and destruction of dust grains*, Ann. Rev. Astron. Astrophys., 15, p.267-293, 1977

[85] Saxena V.K., Shaocai Y., and Anderson J.: *Impact of stratospheric volcanic aerosols on climate: evidence for aerosol shortwave and longwave forcing in the southwestern U.S.*, Atmospheric Environment, vol.31, n.24, 4211-4221, 1997

[86] Stephens J.R., and Kothari B.K.: *Laboratory analogues to cosmic dust*, The Moon and the Planets, 19, 139-152, 1978

[87] Testa J.P., Stephens J.R., Berg W.W., Cahill T.A., Onaka T., Nakada Y., Arnold J.R., Fong N., and Sperry P.D.: *Collection of microparticles at high balloon altitudes in the stratosphere*, Earth and Planetary Science Letters, 98, 287-302, 1990

[88] Tripathi S.K., Shukla N., and Kulkarni V.N.: *Correlation between ion beam parameters and physical characteristics of nanostructures fabricated by focused ion beam*, Nuclear Instruments and Methods in Physics Research B, 266, 1468-1474, 2008

[89] Whipple F.L.: *The theory of micro-meteorites. Part I. In an isothermal atmosphere*, Proceedings of the National Academy of Sciences, vol.36, n.12, 687-695, 1950

[90] Wopenka B.: *Raman observations on individual interplanetary dust particles*, Earth and Planetary Science Letters, 88, 221-231, 1988

[91] Wu P.M., Okada K., Tanaka T., Sasaki T., Nagai T., Fujimoto T., and Uchino O.: *Balloon observation of stratospheric aerosols over Tsukuba, Japan, two years after the Pinatubo volcanic eruption*, Journal of Meteorological Society of Japan, vol.72, n.3, p.475-480, 1994

[92] Xu L., Okada K., Iwasaka Y., Hara K., Okuhara Y., Tsutsumi Y., and Shi G.: *The composition of individual aerosol particle in the troposphere and stratosphere over Xianghe (39.45°N, 117.0°E), China*, Atmospheric Environment, 35, 3145-3153, 2001

Contents

Acknowledgements

I wish to thank Prof Pasquale Palumbo and Prof Alessandra Rotundi for their great support and for the chance they gave to me; Ing Della Corte for his invaluable help for everything; Dr Giuseppe Baratta for great help in Raman analyses, and Dr Rosario Brunetto for long and useful discussions about Raman spectroscopy; the group of the Laboratory of Cosmic Physics at "Parthenope" University (Alessandra C., Mario, Roberto, Ernesto and all the others) and the whole group of "Cosmic Physics and Planetology" at OAC (Naples) for many good moments and feelings (Sergio, Michele, Fabio and all the others). A particular thank to Prof Antonio Moccia, for his availability.
Finally I wish to thank my family, for their unique support during these years, Verena, for her patience, and Giovanna and Peppe, mates of life.